Stony Brook University

Plasma Sprayed Magnetic Composites

Process, Microstructure and Properties

A Dissertation Presented

by

Shanshan Liang

to
The Graduate School

in Partial Fulfillment of the

Requirements

for the Degree of

Doctor of Philosophy

in

Materials Science and Engineering

Stony Brook University

December 2008

Stony Brook University
The Graduate School

Shanshan Liang
We, the dissertation committee for the above candidate for the
Doctor of Philosophy degree,
hereby recommend acceptance of the dissertation.

Professor Richard J. Gambino, Advisor
Department of Materials Science and Engineering

Professor Sanjay Sampath, Co-Advisor
Department of Materials Science and Engineering

Professor David O. Welch, Member
Department of Materials Science and Engineering

Professor Jon P. Longtin
Department of Mechanical Engineering

This dissertation is accepted by the Graduate School

Lawrence Martin
Dean of the Graduate School

Abstract of the Dissertation

Plasma Sprayed Magnetic Composites
Process, Microstructure and Properties

By
Shanshan Liang
Doctor of Philosophy
In
Materials Science and Engineering
Stony Brook University
2008

The dissertation presents research results from integrated studies of process, structure and magnetic properties of plasma-sprayed ferrite-metal composites. These magnetic composites are considered as the core materials for miniaturized high frequency planar inductors, thick film magnetoresistive sensors and potentially as magnetostrictive sensors. Offering the advantages of low substrate temperature during processing, high throughput production capability, cost efficiency and minimizing the interfacial reaction between the ferrite and metal phases, plasma spraying can be considered as a promising route for fabricating magnetic composites with industrial applications. A multitude of experimental techniques, including phase analysis, microstructure observation, magnetic property and electrical property measurements and numerical modeling have been applied for this investigation.

A number of fundamental attributes in terms of process-microstructure-property relationships have been investigated by a systematic processing approach through the frame work of process maps. Such studies can provide insight into process control and optimization.

Three types of magnetic composites have been fabricated using plasma spraying. Rocksalt structured monoxides form in the as-sprayed coatings due to deoxidation of ferrite as well as the oxidation of metallic particles. Random cation distribution and the presence of monoxides and microstructural defects, degrade the magnetic and electrical properties of the composites. Low temperature air annealing can improve these properties by means of forming insulating trivalent oxides (Hematite) and ordering the cations. Functional properties such as magnetoresistance and magnetostriction of comparable value to bulk materials can be obtained after annealing.

A salient finding is the transition form a giant magnetoresistance (GMR) to anisotropic magnetoresistance (AMR) at the percolation threshold which has been reported for the first time in magnetic composites. Thermally sprayed composites coatings are found to have a much smaller percolation threshold due to the anisotropy of splats. Using the effective medium approximation, the relationship between the percolation threshold and aspect ratio has been derived. The experimental results are in good agreement with simulation results. This is the first time that the percolation phenomenon in thermally sprayed composites has been studied quantitatively and compared with theory.

Dedicated to my Family
献给我挚爱的亲人

Table of Contents

List of figures

Acknowledgement

I would like to give my most sincere thanks to my dear advisor Prof. Richard. J. Gambino and co-advisor, Prof. Sanjay Sampath for their guidance and support in preparing and executing this work. Without their inspiring advices and constant encouragement, this work would not have been possible.

I would like to thank my dissertation committee members, Professor Jon P. Longtin and Professor David O. Welch for their enlightening discussions and suggestions.

I am indebted to Mr. Glenn Bancke, Dr. Vasudevan Srinivasan, Dr. AlfredoValarezo and my CTSR colleagues Jose Colmenares and Eduardo Mari for preparing samples and process map study collaborations.

I am indebted to Dr. Qingyu Yan who has been the role model in the study of plasma sprayed functional oxide, I am also thankful for his teaching in magnetic measurement and many other measurements.

I am indebted to Dr. B. G. Ravi for many good suggestions I received from him.

I am thankful to Dr. L. Li, Dr. X. Guo, Dr. A. Sharma, Dr. B. W. Choi and Dr. N. Srinivasan for teaching me the operation of the instruments that I used throughout my Ph.D. study.

I am thankful to Dr. Jim Quinn for his help in SEM experiments and other laboratory advices and supports.

I am grateful to Dr. Y. Wu, Dr. Y. Li, Dr. W. Zhang, Dr. Y. Tan, Dr. W. Chi and other CTSR members for all their help.

I would like to extend my thanks to financial support provided by the U.S. National Science Foundation under award DMI-0428708, and the Materials Research Science and Engineering Center (MRSEC) program of the National Science Foundation to the Center for Thermal Spray Research (CTSR) under Award No. DMR-0080021.

Finally, I want to thank my family, my dearest mother and husband, for their unconditional loves and encouragements.

Chapter 1 Introduction

1.1. Magnetic composites in modern technology

Magnetic composites consisting of one or two magnetic phases have been receiving significant research interests in recent years. For example, alternating Fe-Cr multilayered system has been found to have a magnetoresistance ratio of 50%, a magnitude larger than other known magnetoresistive materials at the time of discovery [1]. These giant magnetoresistive devices based on magnetic metal/nonmagnetic metal (or insulator) nanoscale composites are now the base of the high density memory industry. Another hot spot of recent research is multiferroics which will be the next generation memory. Materials with simultaneous ferromagnetic and ferroelectric ordering have potential applications in multiple state memory and direct control of polarization by magnetic field or vise versa. Due to chemical incompatibility, multiferroic materials are scarce in nature. Composites consisting of a ferromagnetic phase and a ferroelectric phase such as a composite of $CoFe_2O_4$ and $BaTiO_3$ are found to have magnetoelectricity due to the elastic coupling between the two phases [2].

Traditionally, magnetic ferrites are fabricated by ceramic sintering method including (1) Powder preparation [(a) Raw materials selection, (b) Weighing and blending, (c) granulation]r, (2) Pressing and (3) Firing. The sintering method is not only a lengthy process but also presents difficulties in performing required miniaturization for complex geometrical devices. To solve these problems, fabrication techniques for making thin film/thick film devices have been utilized, i.e. pulse laser deposition (PLD), ion beam sputtering, co-evaporation, spin coating, Molecular Beam Epitaxy (MBE) and thermal spraying.

1.2. Plasma spraying as a new route for making magnetic composite devices

Among the above mentioned techniques for making magnetic composites, thermal spraying has certain advantages [3] that are suitable for industrial applications, including (1) bulk productivity: it can easily deposit large area samples with varied thickness (50 μm~2 mm), (2) low substrate temperature during process (<200 °C), (3) simple process: no need for vacuum or special gas (oxygen, nitrogen) environments, (4) cost efficiency. For making thick film magnetic composites, thermal spraying offers a particular advantage over sintering method, which is that in thermal spraying, particles of two species melt individually and solidify rapidly, therefore the interface reaction between different phases is minimal. This is almost impossible in ceramic sintering which requires long duration of high temperature heat treatment, allowing interdiffusion between two phases. The objective of the study is to utilize the advantage that thermal spray offers to explore the potential of plasma spray in making magnetic composites with application in magnetostrictive sensors, magnetoresistive sensors and planar inductors.

-

1.3. Potential challenges in plasma spraying magnetic composites

Thermal spraying is a simple process in the sense of simpler powder preparation or no need of vacuum controlling. It is, on the other hand, a complex process technique; because there are a numerous factors that can vary the process condition and resultantly change the microstructure and properties of the deposits. The high temperature flame not only melts the powder but also changes the composition of magnetic materials due to oxygen loss or phase decomposition, etc. Great impact on the substrate as well as large thermal gradients and rapid quenching, will result in a highly defected structures and leave a large residual stress in the deposits. The process is not uniform; each individual particle may have totally different history in the plasma plume, leading to compositional or other kinds of inhomogeneity. Thermally sprayed materials are built up by splats with large diameter to thickness ratio. Therefore, their microstructure and properties are very anisotropic. Powders with difference in size or density may be segregated in the plasma plume, failing to produce a macroscopically homogeneous composite. All these issues need to be studied to contribute to our knowledge in process engineering and scientific understanding of magnetic composites or fundamental magnetism.

Chapter 2 Background and literature survey

Since thermally sprayed magnetic composites for high frequency inductor or magnetostrictive sensors or magnetoresistive sensors are the main topic of this research. Understanding the mechanism of magnetization and thermal spraying science is essential to study these materials. Therefore, in this chapter, the physics of magnetostriction, magnetoresistance, percolation theory and thermal spraying process will be discussed in details while the physical properties of materials under this study will be briefly introduced.

2.1 Magnetic Ferrite

Modern technology has been boosted by the development of the semiconductor industry, however semiconductor devices would not be possible without the usage of accompanying magnetic components [4]. Magnetic materials can be found in many modern devices such as inductors, transducers, microwave devices, recording media and magnetic read/write heads, etc, without these devices, modern technology especially information technology wouldn't have existed.

While all materials are magnetic to some degree, many of them fall under the category of paramagnetic or diamagnetic materials possessing only weak and relatively undetectable magnetic properties, as such, they are not used in practical devices but have great scientific importance. More practically useful materials are those possessing strong magnetic properties such as ferromagnetic, ferrimagnetic materials and antiferromagnetic materials. All matter possesses diamagnetism but in most materials, the diamagnetism is obscured by paramagnetism or ferromagnetism. Diamagnetism is a result of Larmor procession of orbiting electrons in an external magnetic field. If the electron spins are not completely paired, the unpaired electron spins will result in a net magnetic response to the external field, this response is called paramagnetism. Both paramagnetism and diamagnetism are important in the study of atomic and molecular structure but these effects are very weak and have no practical significance, large scale magnetic effects resulting in commercially important materials occur in only a few metals like Fe, Co, Ni and some rare earth metals or in alloys or oxides containing such elements and some neighboring ions such as Mn. In these metals or alloys, the atomic spin effect are enhanced due to the cooperative interaction of large numbers (10^{13}-10^{14}) of these atomic spins producing a region where all atomic spins within it are aligned parallel by positive exchange interaction, these materials are therefore called ferromagnetic. Other technically important magnetic materials are ferrimagnetic materials such as Fe_3O_4, $(MnZnFe)_3O_4$, $BaFe_{12}O_{19}$, etc. In these oxides, the presence of oxygen provides an alternative exchange interaction – a negative superexchange interaction. The spins of an ion are aligned antiparallel to the next-nearest iron through the nearest anion such as oxygen. If the spins in both sides of the anion are equal such as in the case of FeO or MnO, then the net magnetic moment is zero, hence the material is antiferromagnetic. If the spins are not equal then the material will have a net magnetic moment, hence the material is ferrimagnetic.

2.1.1 Superexchange and ferrimagnetism

Figure 2-1 illustrates a simple picture of superexchange. Two transition metal (T) ions are separated by a *p* ion, i.e. an oxygen ion. The *p* orbital, which is filled in the ground state, can exchange an electron with each of the adjacent 3d orbitals, making the bonding mostly ionic. But some hopping is allowed between the T^{2+} and O^{2-}. The doubly occupied p_x orbital has two electrons of opposite spin. The 3d and p orbitals exchange electrons in order to lower the energy to achieve a ground state, that is, some of the excited states of the system must be partially occupied. A simpler electronic state picture is shown in the lower part of Figure 2-1. One of the p_x electrons is excited into an empty d state to form a $(p-d)\sigma$ or σ^* bond, it leaves behind an electron of opposite spin, being exchanged with the d states of the other T species coupled to this p_x orbital. If the two d ions have the same ground-state electronic configuration, the net effect is an effective antiferromagnetic coupling between the two T ions.

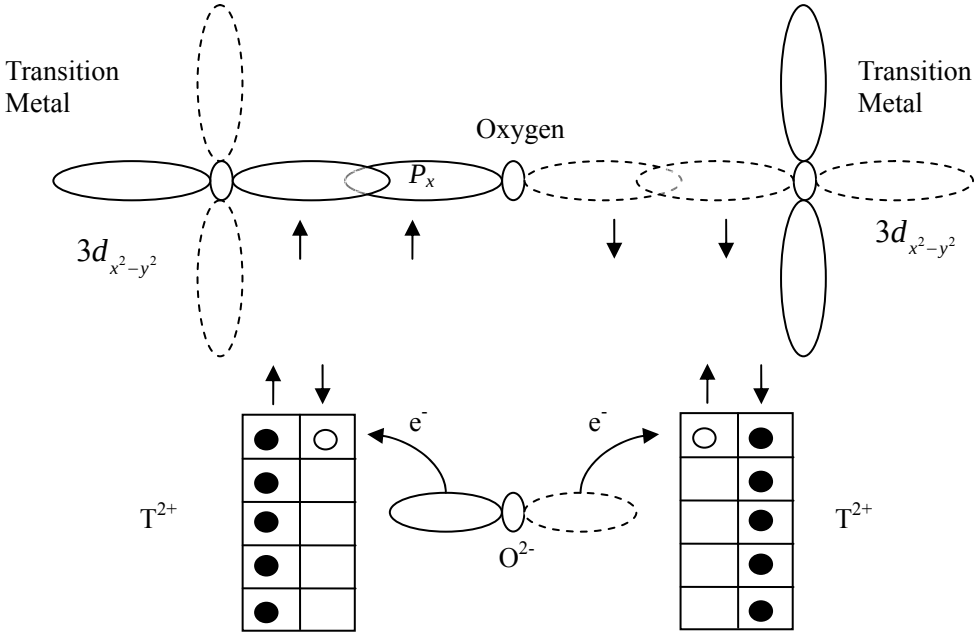

Figure 2-1, schematic of superexchange interaction. When an electron is exchanged or shared by the overlapping orbitals between two sites, the spin is conserved as the electron hops from the p-like to the d-like orbitals. The result is that the two T ions must have opposite directions. Figure is adapted from O'Handley [5].

Transition metal monoxides, fluorides and chlorides with rocksalt structure are often antiferromagnetic. As shown in Figure 2-2, the spins on some nearest neighbor transition metal ions are parallel, such as (a) and (b), or antiparallel on some other nearest neighbor transition metal ions, such as (b) and (c). But next nearest neighbors always have antiparallel spins: (a) and (c) or (b) and (d). Thus the spins within a given (111) plane are parallel to each other and antiparallel to those on the two adjacent (111) planes. The preferred direction of magnetization of a given sublattice is along the [100] crystal direction.

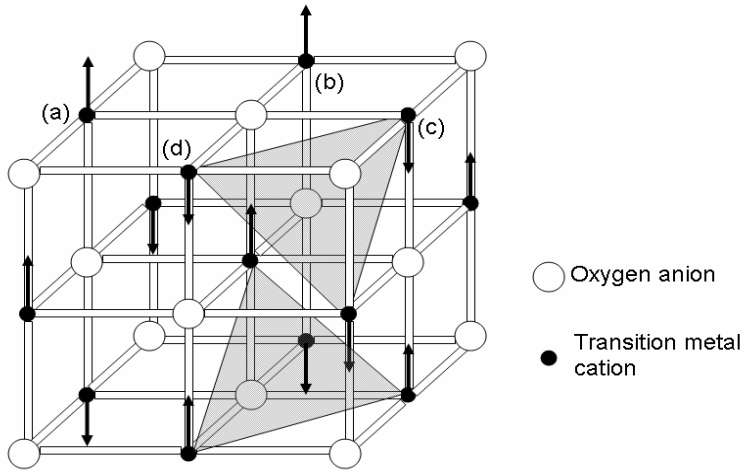

Figure 2-2, Spin structure of rocksalt structure transition metal monoxide. Figure adapted from O'Handley [5].

Now take $CoFe_2O_4$ as an example to illustrate ferrimagnetism. $CoFe_2O_4$ is of spinel structure (space group 227: Fd3m). A unit cell of the spinel lattice has 8 $CoFe_2O_4$ formula units, so there are 32 O^{2-}, 8 Co^{2+} and 16 Fe^{3+} ions respectively. As illustrated in Figure 2-3, a unit cell of spinel structure consists of 8 small cubes, oxygen anions are closed packed and occupy the four vertices of each small cube. Oxygen ions are closed-packed and forms a face center cubic (FCC) structure. Therefore there are 64 tetrahedral sites (A site) and 32 octahedral sites (B site) in a spinel unit cell. In a spinel lattice, only 8 out of 64 A sites and 16 out of 32 B sites are filled. If all the divalent cations are filled in the tetrahedral A sites, and all the trivalent cations are filled in the octahedral B sites, then this type of spinel is called normal spinel. If all the divalent cations are in the B sites, half of trivalent cations are in A site and half are in B site, then this type of spinel is called complete inverse spinel. Mixed spinels are those divalent and trivalent cations are in both sites. The cation distribution in the A, B sites depends on the ionic radii of the ions, the size of the interstices, temperature and the orbital preference for specific coordination. Generally, divalent cations have larger ionic radii so they prefer B site which has a larger size. The exceptions are Zn^{2+} and Cd^{2+}, since their electronic configurations are favorable for tetrahedral bonding to the oxygen ions. Thus, MnZn ferrite has a normal spinel structure. Cobalt ferrite has an inverse spinel structure [6] in which the Co^{2+} occupy B site and half of Fe^{3+} occupy B site and half Fe^{3+} occupy A site. The magnetic exchange interactions between 3d cations in ionic solids are antiferromagnetic superexchange coupling. The strongest coupling is where the two transition metal cations and oxygen anion are collinear [5]. Since the bonding angles are 125° between A-O-B, 90° between B-O-B and there are no A-O-A bonds, so the strongest superexchange in spinel is antiferromagnetic A-B coupling. B sites also exhibit a weak 90° antiferromagnetic coupling among themselves. These interactions are best accommodated if all A moments are parallel to each other and antiparallel to all the B moments.

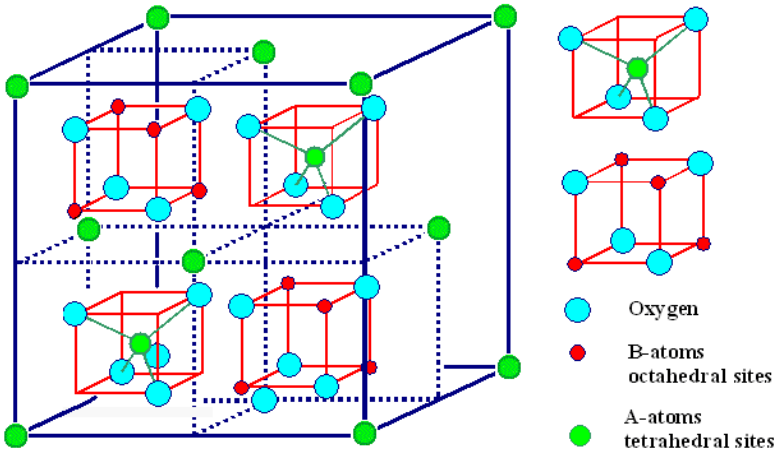

Figure 2-3, Crystal structure of AB_2O_4 spinel, the red cubes are also contained in the back half of the unit cell.

2.1.2 Ferrite in modern technology

Ferrites can be found in numerous applications. A few are listed in Table 2-1.

Table 2-1, Applications of ferrites in modern technology.

Applications/Devices	Requirements on materials	Ferrite materials for this application
Inductors and transformers for low power applications, such as PC, internet access, image scanner, cellular phone, ATM machine, etc	• No need for high saturation magnetization • Medium to high initial permeability • Low loss factor at relevant frequencies • High stability of inductance to changes in operating conditions (temperature, DC bias, AC signal level, etc.) • Low disaccommodation (decrease of permeability with time)	Soft ferrites such as MnZn ferrite
EMI (electromagnetic interference) suppression	• High permeability at frequencies where interference and disturbance take place • Pass the lower frequencies with sufficient inductor	Soft ferrites. NiZn ferrite more used in high frequencies (Megahertz to Gigahertz) while MnZn ferrite more used from Kilohertz to lower Megahertz.
Entertainment applications- radio and TV The second column list a few ferrite devices used in TV and radio applications	• Ferrite TV picture tube deflection yokes	MnZn ferrite and MgZn ferrite (better for HDTV)
	• Flyback transformers	MnZn ferrite
	• Ferrite antennas for radios	NiZn ferrite, doped with Cobalt for higher frequencies
High power applications	• Large flux density • Low core losses • Large resistivity • High amplitude permeability	MnZn ferrite and NiZn ferrite
Magnetic recording	• Magnetic recording tapes	Υ-Fe_2O_3 Ba ferrite
	• Magneto-optical recording media	Bi doped Garnets Co-Ti doped Ba ferrite Undoped or doped Cobalt ferrite
	• Colossal magnetoresistive recording media	$LaCaMnO_3$ etc.
Microwave applications Such as Radar invisible combat planes	• Ferromagnetic resonance frequency in the Gigahertz range	Garnet

2.1.3. MnZn Ferrite and Cobalt ferrite

As can be seen from the Table 2-1, MnZn ferrite is widely used in inductor or transformers in LC circuits for high frequency range, in EMI suppression, TV and radio devices, readout head for magnetic recording, etc, due to its unique properties such as high resistivity, high saturation magnetization, low coercivity, and low eddy-current losses. Cobalt ferrite finds some other interesting applications in magnetic recording applications, magnetostrictive sensors and transducers due to its high magnetic anisotropy, large coercivity, and large remanence magnetization.

2.1.3.1 Structure

MnZn ferrite and Co ferrite are both of spinel structure (space group 227: fd-3m) which has been shown in Figure 2-3. Since Mn^{2+} and Zn^{2+} strongly preferred A site over B site than Fe^{3+}, thus under equilibrium conditions, Mn^{2+} and Zn^{2+} occupy the A sites and expel Fe^{3+} to B sites, resulting in an normal spinel structure for $Mn_{0.5}Zn_{0.5}Fe_2O_4$. Co^{2+} favors B site over A site, therefore, under equilibrium, Co ferrite is inverse spinel which is also confirmed by neutron diffraction experiments [7].

2.1.3.2 Saturation magnetization

The saturation magnetization of a magnetic material is a result of the sum of the unpaired spins of cations. The negative interaction or exchange force between the moments of two metal ions on different sites depends on the distance between these ions and the oxygen ion that links them. The angle between the three ions is also important. The interaction is greatest for an angle of 180 degree and also where the inter-atomic distances are the shortest. In case of MnZn ferrites and Co ferrite, the interaction between the A-A sites and B-B sites is small (both are 90° bonding angle) [8]. The main interaction is the superexchange coupling [9] of the spins between A sites and B sites (125° bonding angle) , which results in antiparallel alignment of the spins in these two sublattice sites. Thus the saturation magnetization of the MnZn ferrite or Co ferrite results from the difference of the number of unpaired spins between the A sites and B sites. For the case of MnZn ferrite with the chemical formula $(Mn_xZn_{1-x})Fe_2O_4$, the magnetic moment per formula unit, μ, is calculated to be

$$\mu = 2\mu_{Fe^{3+}} - x\mu_{Zn^{2+}} - (1-x)\mu_{Mn^{2+}} \qquad \text{(Equation 2-1)}$$

where $\mu_{M^{N+}}$ is the magnetic moment of different cations, *i.e.* $\mu_{Zn^{2+}} = 0\ \mu_B$, $\mu_{Fe^{2+}} = 4\ \mu_B$ and $\mu_{Fe^{3+}} = 5\ \mu_B$. Increasing the concentration of zinc can increase the net magnetization of the MnZn ferrite. The above equation is valid only for small values of x, as the increase of zinc concentration above some critical value; the magnetic moment decreases due to the fact that the interactions between cations in A-B sites are no longer dominant in the ferrite system. As shown in Figure 2-4 [5], the magnetization of MnZn ferrite increases to a maximum value of 7.5 μ_B then falls to paramagnetism. Since Co^{2+} has 3 μ_B and Fe^{3+} has 5 μ_B, the theoretical magnetic moment of $CoFe_2O_4$ is calculated as $\mu = \mu_{Fe^{3+}} + \mu_{Co^{2+}} - \mu_{Fe^{3+}}$ which gives 3 μ_B. The

experimental value is 3.7 μ_B.

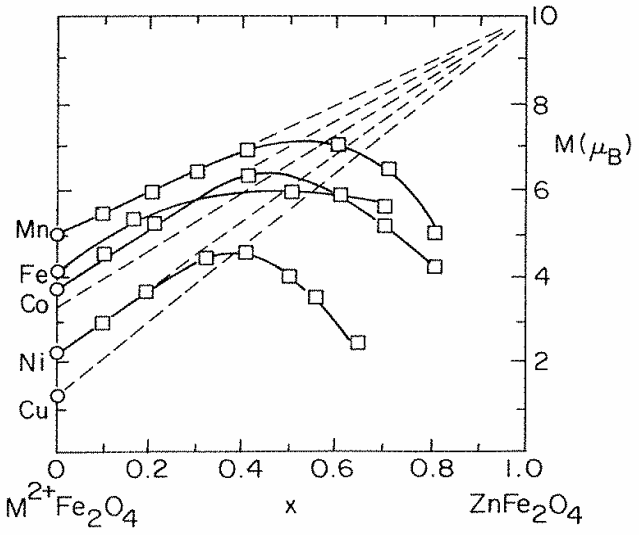

Figure 2-4, the number of Bohr magnetron per unit formula as a function Zn concentration for various ferrites [5].

2.1.3.3 Magnetic anisotropy

The preference for the magnetization to lie in a particular direction in a sample is called *magnetic anisotropy*. Magnetic anisotropy can have its origin in sample shape (shape anisotropy), crystal symmetry (magnetocrystalline anisotropy), stress (magnetostrictive anisotropy), or directed atomic pair ordering (exchange anisotropy). The shape anisotropy is a result of dipole interaction from free poles at surfaces. Stress anisotropy is an inverse effect of magnetostriction where the state of stress can modify the domain structures and magnetization process. Exchange anisotropy is that the exchange coupling in the interface of two magnetic phases can pin or couple the magnetization in one direction and can make it difficult or easier to magnetize than the other directions. Here we will describe the magnetocrystalline anisotropy in details since it is the origin of magnetostriction and anisotropic magnetoresistance.

Magnetocrystalline anisotropy arises from the fact that ferromagnetic materials have specific easy or hard crystallographic directions for magnetization, e.g. , bcc Fe is easier to magnetize in [100] directions but harder to magnetize in [111] directions. The magnetocrystalline anisotropy in cubic systems can be written as:

$$E_a = K_1(\alpha_1^2\alpha_2^2 + \alpha_2^2\alpha_3^2 + \alpha_3^2\alpha_1^2) + K_2\alpha_1^2\alpha_2^2\alpha_3^2 + \ldots \quad \text{(Equation 2-2)}$$

where α_i are directional cosines for the angles between magnetization vector with the 3 orthogonal axes, K_1 and K_2 are the first and second order anisotropic constants, respectively. The magnetocrystalline anisotropy depends critically on composition. For MnZn ferrite, at a slightly Fe rich, Zn deficient region from $Mn_{0.5}Zn_{0.5}Fe_2O_4$, K_1 can be zero. The K_1 values of MnZn ferrite is about 10^4 erg/cm^3 [10] and is 2.7×10^6 erg/cm^3 for stoichiometric Co ferrite

[11].

The origin of magnetocrystalline anisotropy lies in two coupling effects. Fist is the spin-orbit interaction (SOI) that links the orientation of spin to that of orbit, and second is the crystal field splitting effect that links the orbit to particular direction in the lattice. These coupling effects result in a strong preference of spin orientation to lattice direction. Generally speaking, 3d metals and ferrites have less magnetocrystalline anisotropy than that of 4f metal whose 4f electrons are screened from the crystal electric field thus the angular momentum is not quenched. However, Co ferrite is an exception showing large magnetocrystalline anisotropy. Slonczewski [12], [13] explained why the substitution of Fe^{2+} with Co^{2+} can greatly increase the magnetic anisotropy using a single ion model. In his model, the energy splitting due to cubic crystal electric field (CEF) and trigonal CEF are both considered. In a spinel unit cell, Co^{2+} with $3d^7$ configuration sits in the octahedral site, due to cubic CEF (6 nearest neighbors of oxygen anions), the 5-degenerate 3d orbitals split into a triply degenerate t_{2g} (d_{xz}, d_{yz} and d_{xy}) and a doubly degenerate e_g (d_{z^2} and $d_{x^2-y^2}$) states. If there is only cubic CEF, then the electronic configuration of Fe^{2+} in B site is $(t_{2g})^4(e_g)^2$, while $(t_{2g})^5(e_g)^2$ for Co^{2+}, which leads to $< L_z >= -1$ for Fe^{2+} and $< L_z >= -2$ for Co^{2+}, this does not explain the significant increase in magnetocrystalline anisotropy from Fe_3O_4 ($K_1 = -0.9\times10^5 erg/cm^3$) to $CoFe_2O_4$ ($K_1 = 2.7\times10^6 erg/cm^3$). So what is responsible for the large jump in magnetocrystalline anisotropy is the trigonal CEF splitting (Figure 2-5). The six second nearest neighbors of Co^{2+} cations have a trigonal arrangement about the <111> axis, and it can lower the crystal electric field symmetry and break down the degeneracy of the t_{2g} states (figure 2-6). The three d_{xy} like states recombine to form three new orbitals compatible with the trigonal symmetry and form one singlet state with charge distribution concentrated along the trigonal axis and a doublet state with charge distribution in the plane perpendicular to the trigonal axis. For Fe^{2+} ($3d^6$) in a trigonal environment, the electrons first fill up the 3 t_{2g} orbitals and 2 e_g orbitals, the remaining one electron fill the singlet state, so the angular momentum is $< L_z >= 0$. Thus, for Fe^{2+}, there is no significant spin-orbit interaction and consequently low magnetic anisotropy and small magnetostriction. For Co^{2+} ($3d^7$) in a trigonal environment, the remaining 2 electrons first fill into a singlet state and then one of the doubly degenerate state (Figure 2-6), thus the degeneracy is still kept and $< L_z >\neq 0$, so the spin-orbit interaction couples the spin to crystal directions, giving rise to high anisotropy.

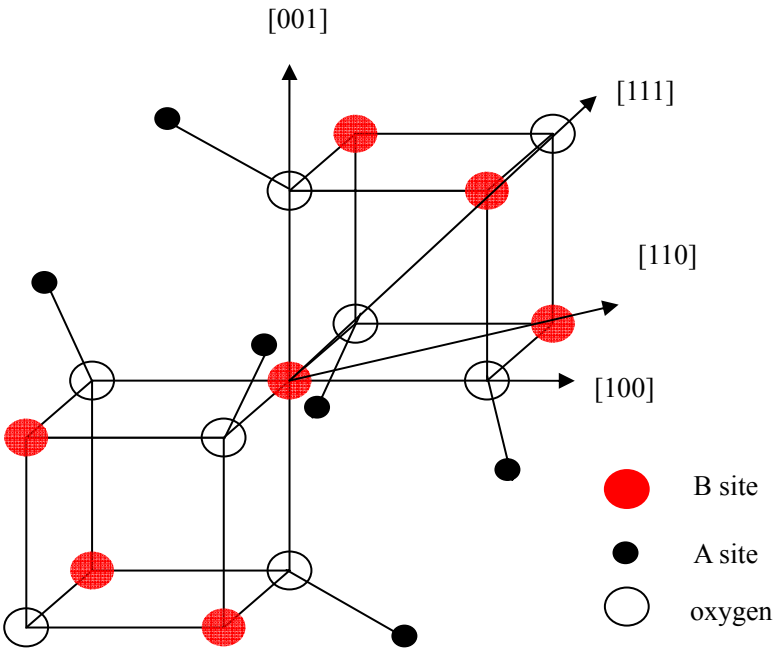

Figure 2-5, cation in spinel structures is octahedrally coordinated by nearest-neighbor-anions and trigonally coordinated by next-nearest-neighbor-cations [12].

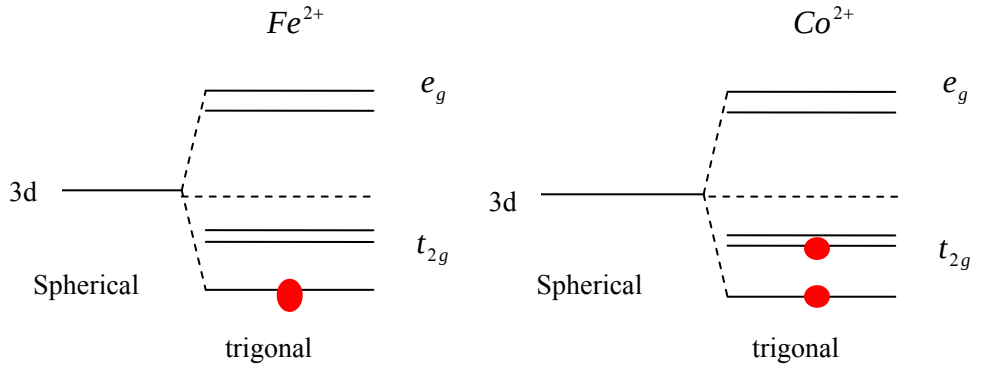

Figure 2-6, crystal field splitting of anti-bonding 3d levels in trigonal sites symmetry. Minority spin states of Fe^{2+} (left) and Co^{2+} (right). Figure adapted from O'Handley (2000) [5].

2.1.3.4 Magnetic domains and coercivity

To reduce the magnetostatic energy, magnetic materials break down into regions with different magnetization orientations. The region where the magnetic moments are lined up in one direction is called a magnetic domain. The transitional area between two neighboring magnetic domains is called a domain wall. Coercivity is the extra magnetic force to fully demagnetize magnetic materials after being magnetized. The existence of magnetic domains and coercivity results in hysteresis in magnetization curves, magnetostriction curves, and magnetoresistance curves, etc. A micromagnetic theory of coercivity based on domain wall pinning by sharply defined defects was developed by Friedberg and Paul in 1975 [14] and extended by Paul in 1982 [15]. The model is micromagnetic because it considers the boundary conditions on the magnetization at the matrix/defect interfaces and takes exchanges into account. In this model the defects, of width D, can be larger or smaller than the domain wall thickness. Figure 2-7 outlines the geometry that distinguishes the anisotropy K_1, exchange A_1, and magnetization M_1 in the matrix from those parameters in the defects. The theory gives the coercivity of a magnetic material with well-defined defects (grain boundaries, voids, antiphase boundaries and dislocations) as

$$H_c = \frac{h_c K_u}{M_s} \qquad \text{(Equation 2-3)}$$

where K_u is the effective anisotropy constant and h_c is a coefficient related to the defect size and normalized defect domain wall energy. The value of h_c has been numerically calculated by Paul [14]. Therefore, low values of K_u and h_c will result in low values of H_c with all other things being equal. The effective anisotropy constant K_u includes contribution from the crystalline anisotropy, magnetoelastic anisotropy and magnetostatic anisotropy.

Usually, MnZn ferrite has low coercivity due to its low magnetocrystalline anisotropy energy. As $MnFe_2O_4$ and $ZnFe_2O_4$ have opposite signs of crystalline anisotropy, the net anisotropy constant decreases when zinc is doped into the $MnFe_2O_4$ lattice and low coercivity can be achieved. $MnFe_2O_4$ and $FeFe_2O_4$ have opposite signs of magnetostriction constant [16]. Thus the existence of Fe^{2+} in MnZn ferrites system may also help to reduce the coercivity. On the other hand, Co ferrite has high magnetostriction and high crystalline anisotropy so high coercivity ranging from a few hundred Oersteds to thousands of Oersteds, depending on chemistry, microstructure and processing conditions. The extra surfaces inside the ferrites can increase the magnetostatic anisotropy. Thus dense ferrite samples are desired to decrease the magnetostatic anisotropy.

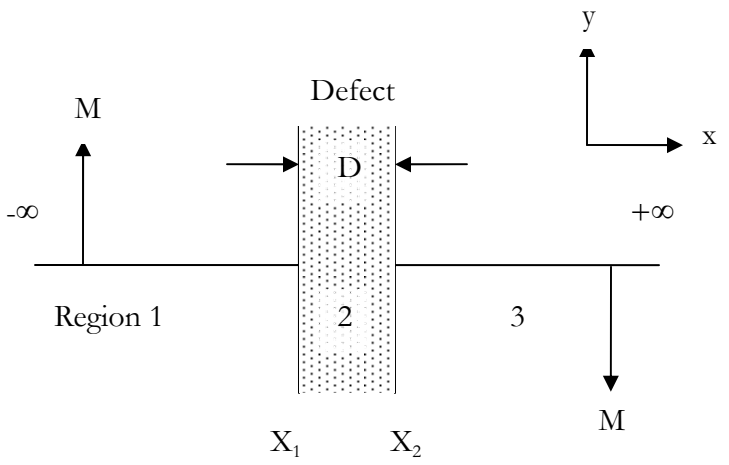

Figure 2-7, division of a magnetic material into three regions: (1) to the left of a planar defect; (2) inside the planar defect; (3) to the right of the defect. Material properties are the same in region (1) and (3). Defect width is $D=X_2-X_1$, and magnetization values at infinity indicate that a domain wall exists somewhere in between [15].

2.1.3.5 Permeability

The magnetic flux density *B* is related to the magnetization *M* and magnetic filed *H* by the equation:

$$B = \mu H = \mu_0 \left(H + M \right) = \mu_0 \left(H + \chi H \right). \quad \text{(Equation 2-4)}$$

Permeability, μ, is defined as the ratio of induction **B** to magnetic field **H**, it is equal to $\left(1+\chi\right)\mu_0$, where χ is magnetic susceptibility, and μ_0 is vacuum permeability and equal to $4\pi \times 10^{-7} H/m$. Relative permeability, μ_r, is defined as $1+\chi$. Permeability can be measured under different sets of conditions. For example, if the magnetizing field is very small, approaching zero, the ratio will be called the initial permeability μ_0. It is an important parameter in telecommunication applications where very low drive levels are involved. High permeability is preferred in inductor applications as the inductance L is equal to $\frac{N^2 \mu A}{l}$, where *N, A, l* are the number of turns, area and length of magnetic core. However, in an AC magnetic field, as the frequency increases, the generation of eddy currents may cause the damping of the domain wall movement [5] and significantly decreases the permeability. Therefore, for medium- or high-frequency applications, instead of using conductive permalloy NiFe (relative permeability is about 10000), people use MnZn ferrite or NiZn ferrite due to their relatively high resistivity which can inhibit the generation of eddy current.

2.1.3.6 Electrical resistivity

The power loss of ferrite materials used as inductor cores is the sum of three terms: the *hysteresis loss*, the *eddy current loss* and *residual loss* [17]. The hysteresis loss is defined as the energy per unit volume that is lost per cycle in magnetizing the material, which is the area inside a quasistatic B-H loop. The hysteresis loss has a linear dependence on the frequency while the eddy current loss is proportional to the square of the frequency. The eddy current loss Pe can be expressed as [5]:

$$P_e = \frac{4\omega^2 B_m^2 V}{2\pi^3 \rho} \qquad \text{(Equation 2-5)}$$

where ω is angular frequency of the current passing through the induction, Bm is the maximum magnetic flux, V is the volume of the core and ρ is the resistivity of the ferrite core. Therefore high value of ρ can lead to low eddy current losses. The physical origin of residual loss is less well understood. Magnetic resonance processes, which are associated with any change of applied field, are said to be responsible for the residual losses [18].

The electrical conductivity in ferrite is due to electron hopping between the Fe^{2+} and Fe^{3+} cations that coexist in the B sites [19]. The hopping rate of electrons, P, depends on the temperature through the following equation [20]

$$P = N\exp(-E/kT) \qquad \text{(Equation 2-6)}$$

Where E is the height of the potential energy barrier, N is the characteristic atomic vibration frequency, k is the Boltzmann constant and T is the absolute temperature. A decrease of the Fe^{2+}/Fe^{3+} ratio can greatly decrease the value of P, which leads to the increase of resistivity. In high frequency applications, yttrium iron garnets (YIG) are used even though the magnetic properties are not as good as MnZn ferrites. There is no Fe^{2+} in YIG, so no electron hopping takes place and results in high resistivity.

2.1.3.7 Other properties

Some other physical properties $CoFe_2O_4$ and MnZn ferrite are listed in the following Table 2-2 and Table 2-3, respectively.

Table 2-2, some physical properties of $CoFe_2O_4$.

Physical property	Values and remarks
Magnetic anisotropy	$K_1 = 2.7\times10^6 erg/cm^3$ at room temperature [5]
Magnetostriction	$\lambda_{100} = -670\times10^{-6}$, $\lambda_{111} = 120\times10^{-6}$, by reference [5], $\lambda_s = -210\times10^{-6}$ for polycrystals, by reference [5],[21]
Curie temperature	520°C [22]
Melting point	1570°C [2]

Electrical resistivity	In the paper by Na et. al.[23], the resistivity of Cobalt ferrite is found to be dependent on cation distribution, heat treatment condition and composition. For $CoFe_2O_4$, the resistivity is found to be around $100\Omega \cdot cm$.
Elastic modulus (E) and Poisson ratio (ν)	E=141.6GPa [24] ν =0.24
Coefficient of thermal expansion (CTE)	$8.7\times10^{-6}/K$ at room temperature [25] , CTE as a function of temperature is also given by the same reference [25]

Table 2-3, some physical properties of $(MnZn)Fe_2O_4$.

Physical property	Values and remarks
Magnetic anisotropy	$K_1 \sim 10^4 erg/cm^3$ at room temperature [5]
Magnetostriction	λs is less than 10ppm for selected compositions
Curie temperature	520°C by DTA/TGA measurement
Melting point	1550-1590°C
Electrical resistivity	1-20 Ω.m
Elastic modulus and Poisson ratio	E=145-200 GPa ν =0.11-0.16
Coefficient of thermal expansion (CTE)	8.5~9 $\times10^{-6}$ K^{-1} [4]

2.1.3 Magnetic composites containing MnZn ferrites or Co ferrites

Magnetic composites, two phase mixtures, consisting of one or two magnetic phases have been receiving significant research interests in recent years. Some examples are the newly developed magnetostrictive-ferroelectric composites for multiferroic devices applications [24, 26], multilayered giant magnetoresistive (GMR) devices, nanostructured granular magnetic metal/nonmagnetic metal or metal/insulator GMR devices [27], enhanced high frequency permeability ferrite-permalloy composites [28, 29], and metal/native oxide multilayer (MNOM) systems for gigahertz bandwidth shielding applications [28].

MnZn ferrites are used in high frequency transformers due to their large resistivity. However, the initial permeability of MnZn ferrites at high frequency is limited by the Snoek's law in which the product of real permeability μ' and FMR frequency f_r is

proportional to saturation magnetization (Ms). Ferromagnetic metallic materials such as Fe, NiFe, NiCo alloys, on the other hand, having high permeability and saturation magnetization making them good for high frequency applications, however, due to their low resisitivity, eddy-current losses at high frequency is inevitable. In order to find a material suitable for high frequency application, composites of ferrite and metal have been sought. These composites combine the merit of high resistivity of ferrite and high permeability, high saturation magnetization of ferromagnetic metal. Composites of high permeability permalloy with MnZn ferrite or with NiZn ferrite fabricated by spark-plasma-sintering (SPS) technology [29], and ferrite plating wet process [30, 31], have shown improved permeability and Q factor which is useful for Gigahertz applications.

Cobalt ferrite, having a very large saturation magnetostriction of about -170×10^{-6}, is second only to terfonol alloys (Terbium-Iron-Dysprosium alloy, or Terfenol-D). Besides its large saturation magnetostriction, its high sensitivity, relatively cheap cost, high mechanical strength and good corrosion resistance make it a very attractive candidate for the application of magnetostrictive sensors. Researchers in the Ames laboratory, Iowa State University, have been working on a magnetostrictive torque sensor made from cobalt ferrite and Co or NiAg composites since 1996. The addition of a small fraction of metallic phase is to enhance the magnetoelastic response and the mechanical strength. The torque sensors which are 1/4-inch-thick rings could be used to regulate the steering power provided to a car's wheels by an electric motor. This would enable automakers to eliminate the heavy, energy-draining hydraulic system currently used in power-steering assists and improve the fuel efficiency of a car by about 5 percent. As shown in Figure 2-8, when a driver turns the wheel, the magnetization of the cobalt-ferrite ring would change in proportion to the amount of force applied by the driver. The change would be detected by a nearby field sensor that would interpret how much force should be applied to turn the wheels and then relay the information to an electrical power-assist motor. The magnetomechanical effects under torsional stress showed a hysteresis of $\pm 0.5 N\cdot m$ and a sensitivity of 65A/m per $N\cdot m$ (Figure 2-8). By doping cobalt ferrite with Mn [32], they can decrease the Curie temperature and therefore decrease the hysteresis. Lo [33] also showed that magnetic annealing at 300°C for 36 hours with a dc field of 4 kOe can result in magnetic easy axis lying along the annealing field direction. The magnetic annealing can increase the saturation magnetostriction in the hard axis from -200×10^{-6} to -252×10^{-6}.

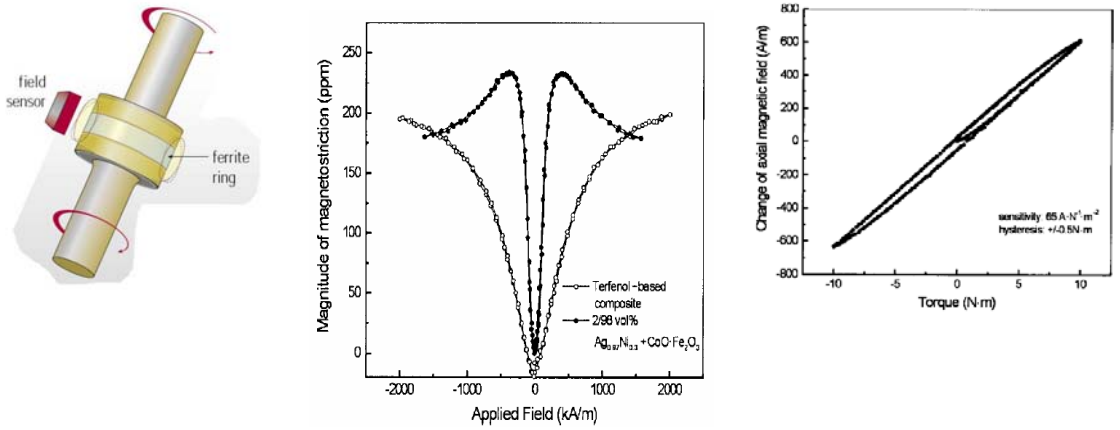

Figure 2-8, left, Cobalt ferrite torque sensor in an automobile's steering system; middle, Magnetostriction of Terfenol-based composites and cobalt ferrite based composite; right, Magnetomechanical effects under torsional stress of cobalt ferrite-AgNi composite.

Besides the application to magnetic sensors or actuators, cobalt ferrite is also widely used as magneto-anisotropic recording media due to its high magnetocrystalline anisotropy, and recent years, cobalt ferrite and piezoelectric materials such as barium titanate [24] ($BaTiO_3$), strontium titanate ($SrTiO_3$) are being intensively studied for their interesting magnetoelectrical coupling effects.

2.2 Magnetostriction

2.2.1. Magnetostriction phenomena

In 1842, James Joule discovered that a ferromagnetic substance changes its length when it is magnetized (Figure 2-9). This magnetization induced stressing or straining effect is called the Joule effect. The inverse effect, change of magnetization caused by stress, was discovered by Villari in 1865, and was defined as the Villari effect or piezomagnetism. These observations suggest that there is a coupling between magnetization and mechanical strain, this magneto-mechanical coupling effect is therefore called magnetostriction.

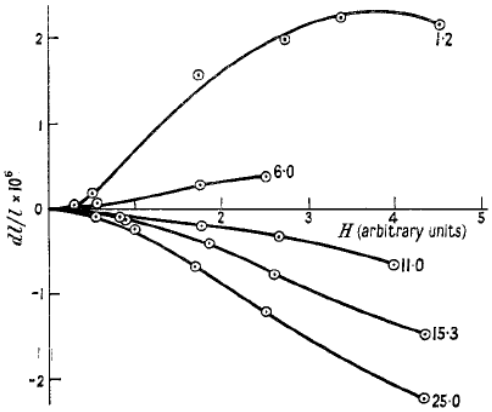

Figure 2-9, Joule's original measurements of the magnetostriction of iron (1842). The figure gives the applied tension in kg mm^{-2} [34].

There are two kinds of magnetomechanical effects, one is the direct effects in which the change of magnetization state changes the mechanical state of a ferromagnetic material, and the other one is the inverse effect in which the change of mechanical state changes the magnetization state. The direct effects include volume magnetostriction, Joule magnetostriction, dipolar magnetostriction (form effect), direct Wiedemann effect, ΔE effect, while the inverse effects include pressure dependence of σ_s and T_c, Villari effect, and

inverse Wiedemann effect, etc. [35]. In the application of torque and stress sensor, Joule effect and Wiedemann effect and their inverse effects (Villari and inverse Wiedemann effect) are of interests.

2.2.2. Origin of magnetostriction

The energy of a ferromagnetic substance includes exchange, anisotropy and magnetostatic (demagnetizing) energies. These three energies all vary with the state of strain of the substance and so it will deform spontaneously if the deformation reduces the total energy (equal to the sum of the magnetic energy and the elastic energy). These three magnetic energies are responsible for the volume magnetostriction, the linear magnetostriction and the form effect which are three major parts of magnetostriction.

(1) The contribution of spin-spin interaction to volume magnetostriction

A typical illustration of volume magnetostriction is the thermal expansion anomaly in a ferromagnet (Figure 2-10). At the Curie temperature where the spontaneous magnetization disappears, there is an abrupt change in thermal expansion coefficient. This kind of magnetostriction (volume magnetostriction) is related to the spatial dependence of the exchange interaction or spin-spin interaction. Since spin-spin interaction is isotropic, thus the volume magnetostriction is also isotropic.

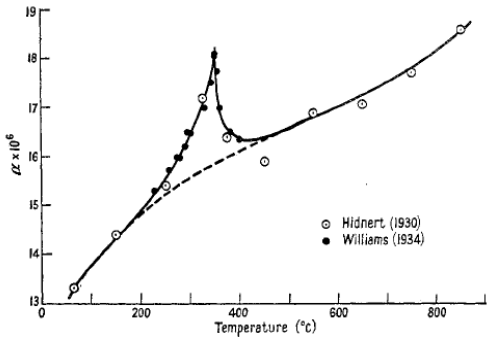

Figure 2-10, coefficient of thermal expansion of Nickel.

(2) The contribution of Spin-orbit interaction and crystal electric field to linear magnetostriction

Atoms possess two main sources of magnetic moment: the orbital electronic motion around the nucleus, which gives rise to the orbital angular momentum, $\vec{L}$, and the spin, $\vec{S}$. The orbital current produces a magnetic field, $\vec{B} = \frac{1}{emc^2}\frac{1}{r}\frac{\partial V}{\partial r}\vec{L}$, and the potential energy of the spin moment $\mu_S = -g\mu_B\vec{S}/h$ in this magnetic field is

$U = -\mu_S \cdot B = \frac{g\mu_B}{emc^2 h}\frac{1}{r}\frac{\partial V}{\partial r}\vec{L}\cdot\vec{S}$. This links the spin to orbit. On the other hand, there exists a strongly inhomogeneous electric field in magnetic solids, called the crystal electric field (CEF). The interaction of CEF and ion magnetic electrons, gives rise to a splitting of the ion energy levels while still keeping some degeneracy. This splitting is purely dictated by symmetry, e.g. in cubic symmetry the levels are e_g (doubly degenerate) and t_{2g} (triply degenerate). In the solid, orbital wave-functions, ψ_{ml}, of 3d or 4f electrons in CEF, are determined by the symmetry entourage of the ionic site and is very anisotropic. This remaining degeneracy is very important for magnetostriction, because otherwise $< L_Z >$ is zero and there is no spin-orbit coupling hence no magnetocrystalline anisotropy. In the ferromagnets or antiferromagnets, the spontaneous magnetization $\vec{M}_s$ is coming from the exchange energy $E_{ex} = -2J\sum_{i<j}^{nn} S_i \cdot S_j$. Therefore when $\vec{M}_s$ is rotated within the crystal by the torque $\vec{\Gamma}$ exerted by magnetic field, the ionic charge cloud is dragged and distorted, so the crystal is deformed. This deformation is the so-called single-ion CEF magnetostriction and it requires the rotation of $\vec{M}_s$ in some way: either by rigid vector rotation or by domain wall displacements. Since the CEF is anisotropic so the magnetostriction caused by spin-orbit interaction is very anisotropic.

(3)Form effects

Since the demagnetizing factor depends on the shape of material, magnetic energy also depends on the shape of material. For example, a sphere of ferromagnetic material will tend to increase in length along the direction of magnetization and decrease in length in the other directions which can lower the demagnetizing energy by lowering the demagnetization factor. This effect gives rise to an additional magnetostriction known as the form effect. Beck et. al. [36] showed that the magnetostriction due to form effects can be expressed by the following equations:

Longitudinal magnetostriction due to the form effect is $(\frac{dl}{l})_f = \frac{1}{2}NI^2(\frac{1}{3k}+\frac{a}{2n})$

The accompanying transverse contraction is $(\frac{dl}{l})_{f,trans} = \frac{1}{2}NI^2(\frac{1}{3k}-\frac{a}{4n})$.

Here N is the demagnetizing factor, *I* is the magnetization, *k* and *n* are the bulk and shear moduli, respectively, and *a* is a constant involving the geometry of the demagnetized state.

2.2.3. Measurement techniques

The magnetostriction can be measured by direct and indirect methods. Direct methods include measurements with strain gages, cantilever[37], capacitance transducers, interferometers, X-ray diffraction [21, 38-41] and X-ray absorption spectroscopy [42] . For crystalline materials the use of strain gages is most common. The most sensitive method is the capacitance method. Indirect methods include the Becker-Kersten (stress dependence of the hysteresis loop) method, small angle magnetization rotation (SAMR) method, traverse susceptibility methods, and ferromagnetic resonance methods (FMR)[43]. For amorphous

ribbon, the SAMR measurement gives very accurate results. Table 2-4 lists various methods for measuring magnetostriction.

Table 2-4, comparison of some methods to measure magnetostriction

Method	Manner	Sensitivity	Remarks
Strain gage	direct	$\pm 1\times 10^{-6}$	Determine $\lambda_{//}$ and $\lambda_{\perp}$ independently
capacitance	Direct	$\sim 10^{-10}$	Most sensitive method but also difficult
cantilever	Direct		Can be measured by the light deflection, capacitance and or methods.
Interferometer	Direct		
X-ray diffraction	Direct	$\sim 10^{-5}$	
X-ray absorption spectroscopy (EXAFS)	Direct	$\sim 10^{-6}$	EXAFS can measure the change of interatomic space in the magnitude of 0.01Å to 0.001 Å, but with differential magnetostriction measurements, it can detect femtometer scale of interatomic displacement
Stress dependence of hysteresis loop	Indirect	$\sim 10^{-8}$	Good for negative and very small value of λ_s
SAMR	Indirect	$\sim 10^{-9}$	High sensitivity, suitable for ribbons, usable at all temperature to determine λ_s
Transverse susceptibility	Indirect	$\sim 10^{-9}$	Variation of SAMR (small angle magnetic resonance) method
Strain modulated FMR	Indirect		Modulating the state of strain or stress, the change in FMR position can be used to calculate magnetostriction coefficient.

2.3 Magnetoresistance

Magnetoresistance (MR) is the change of resistance of a material subject to an external magnetic field. It is first discovered by William Thomson (Lord Kelvin) in 1856. He discovered that the resistance of an iron piece increases when the current is in the same direction as the magnetic force and decreases when the current is at 90° to the magnetic force. He also found the same effect in a Nickel piece but with a bigger effect. This is the ordinary MR effect. The presence of external magnetic field causes a change in resistance of a substance because the Hall Effect deflects charge carriers from the current direction. Kohler discovered that the ordinary MR is scaling with H / ρ, which is know as the *Kohler's rule*, expressed as:

$$\frac{\Delta\rho}{\rho} \propto \left(\frac{H}{\rho}\right)^2 \qquad \text{(Equation 2-7)}$$

In ferromagnetic materials the "ordinary" anisotropic transport effects are present but are accompanied by stronger phenomena having similar geometrical dependences and symmetries. This galvanomagnetic effects (electronic transport properties involving magnetic fields) associated with ferromagnetic materials is called "extraordinary", "spontaneous" or "anomalous" magnetoresistance effect. The extraordinary galvanomagnetic effect arises from the internal field which is proportional to magnetization.

But ordinary magnetoresistance does not have much practical applications. Two types of MR effects are more generally used in modern technology, namely, the anisotropic magnetoresistance (AMR) and giant magnetoresistance (GMR). And these MR effects will be discussed in more details in the following sections.

2.3.1 AMR

The magnetoresistance of ferromagnet depends on the angle between the current direction and the magnetization, therefore is called anisotropic magnetoresistance (AMR). Figure 2-11 shows the MR effect of Permalloy when current is parallel ($J//H$) and perpendicular ($J \perp H$) to the applied magnetic field. The magnetoresistance also shows hysteresis corresponding to the hysteresis of M-H loop, confirming that the origin of AMR is in the state of magnetization rather than the applied field. The AMR effect is observed in many systems to vary as $\frac{\Delta\rho(H)}{\rho_{av}} = \frac{\Delta\rho}{\rho_{av}}\left(\cos^2\theta - \frac{1}{3}\right)$, where θ is the angle between $\boldsymbol{J}$ and $\boldsymbol{M}$, ρ_{av} is the average resistance. The AMR effect is analogous to magnetostriction effect. The low field dependence of the anisotropic magnetoresistance resembles that of magnetostriction. Both effects are quadratic in a hard-axis applied field below the anisotropic field, H_a, and both show the same zero field dependence on domain structures.

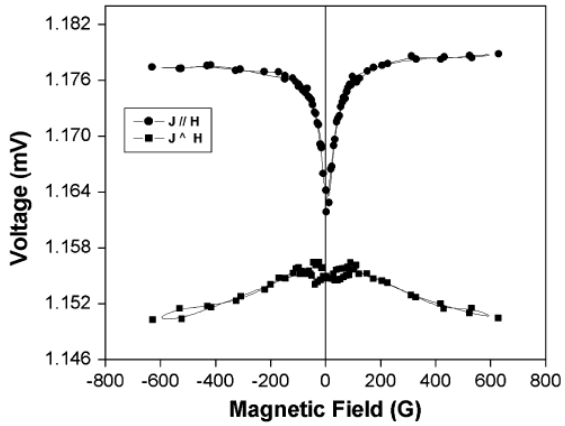

Figure 2-11, magnetoresistance of Permalloy [44].

The AMR effect is a result of spin-orbit interaction (SOI). The SOI creates holes in 3d states where 4s electrons can scatter into. However, s electrons can only scatter into the 3d

hole states if the conduction electron momentum ***k*** (the direction of current) is in the plane of the classical orbit of the empty d state which is favored when current is parallel to magnetization. Therefore, the electrical resistance has maximum value when the direction of current is parallel to the applied magnetic field. AMR ratio is usually as a low as a few percent, however, AMR up to 50% has been observed in some ferromagnetic uranium compounds. AMR has been widely applied to magnetic sensors and read-out heads for magnetic disks.

2.3.2 GMR

In 1988, Albert Fert and Peter Grünberg independently discovered that a much greater MR ratio can be obtained in FeCr multilayers. This discovery is now commercially used in hard-disk and magnetic sensors industry, enables tiny electronics such as ipod, and initiates the new filed of science – spintronics. Fert and Grünberg were awarded the Nobel Prize for Physics in 2007 for their discovery. Besides in multilayer structures, GMR also exists in a system containing granular ferromagnetic metallic precipitates in a nonmagnetic matrix.

These multilayered GMR systems essentially consist of an alternate stack of ferromagnetic (e.g., Fe, Co, Ni, and their alloys) and non-ferromagnetic (e.g., Cr, Cu, etc.) metallic layers. Each individual layer in these multilayers is only a few atomic layers thick. In the absence of external magnetic field, the ferromagnetic layers are antiparallel (AP) aligned, but become parallel (P) aligned under the application of an external field, as shown by the left part of Figure 2-12. Contrary to AMR where the electron scattering mechanism is spin-orbit scattering, here in GMR, the mechanism is spin-dependent scattering. Charge carriers are less scattered if they are of the same spin with the ferromagnetic layer. When the ferromagnetic layers are antiparallel coupled, conduction electrons of either spin will sample a series of strong and weak scattering layers. When the ferromagnetic layers are parallel coupled, electrons of the same spin direction as that of the magnetic layers will sample a series of weakly scattering, while the other ones will sample a series of strongly scattering, therefore it results in a short circuit in the ferromagnetic coupled configuration. The electrical resistance is highest at zero field and achieves a minimum upon magnetic saturation.

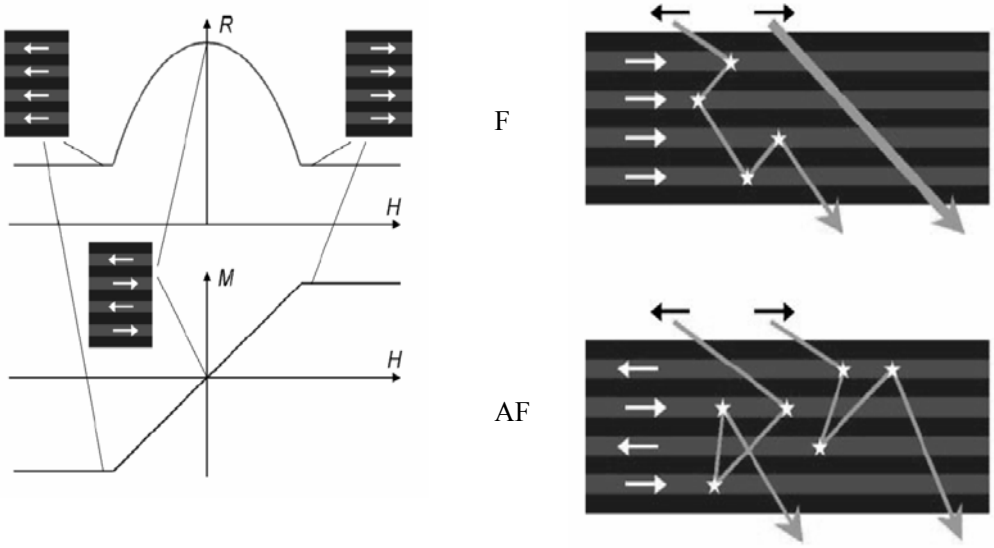

Figure 2-12, Schematic description of GMR effect. Upper left, electrical resistance of the multilayer; bottom left, magnetization of the multilayer versus applied magnetic field. The insets indicate the magnetic configuration of the multilayer in zero field and at positive and negative saturation fields. Right side illustrates the spin-dependent scattering mechanism for GMR effect. Electrons are strongly scattered in magnetic layers with magnetizations (white arrows) antiparallel to their spin (black arrows), and weakly scattered in magnetic layers with magnetizations parallel to their spin. This results in a short-circuit effect in the Ferromagnetic (F) configuration, where half of the electrons are seldom scattered, yielding a lower net resistance. Figures adapted from a webpage[45].

GMR is also found in granular magnetic solids, consisting of single domain ferromagnetic particles embedded in an immiscible medium such as Co in Cu [46], Fe in SiO_2 and Ni in Al_2O_3. The moments of the granular magnetic particles are randomly dispersed in demagnetized state, but become aligned to the magnetic field direction under an external field. Figure 2-13 shows the magneto-transport properties in various materials.

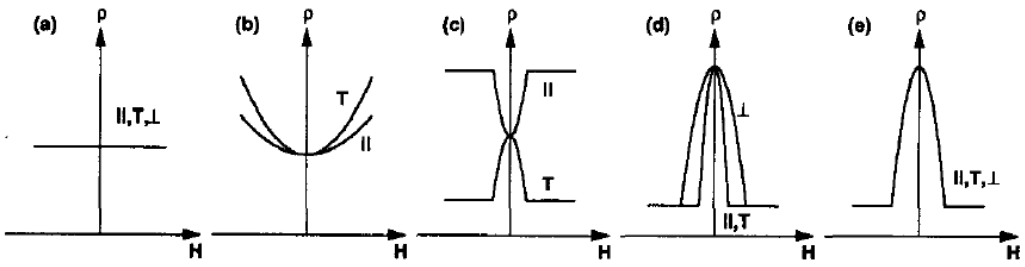

Figure 2-13, schematic representation of various MR behaviors: (a) the absence of MR in a Drude metal, (b) ordinary MR in a non-magnetic metal due to Hall effect, (c) AMR in a ferromagnetic metal, (d) negative GMR in a multilayer, and (e) negative GMR in a granular solid. Symbols $//$, T and $\perp$ represents the direction of current is parallel to both magnetic field and sample plane, perpendicular to magnetic field but parallel to sample plane, and perpendicular to both the magnetic field and sample plane, respectively. Figure is from Chien '93 [47].

2.3.3 CMR

Magnetoresistance of a change of orders of magnitude has been found in several manganese-based perovskite, such as LaBaMnO [48], and $LaCaMnO_3$ [49]. It is called colossal magnetoresistance (CMR) due to the extremely large MR ratio. Currently, there is not a theory completely explains the mechanism of CMR, CMR still remains a focus for both theoretical and experimental ongoing research.

2.4 Exchange bias

Exchange coupling refers to a preference for specific relative orientations of the moments of two different magnetic materials when they are in intimate contact with each other or are separated by a layer thin enough (≤ 60Å) to allow spin information to be communicated between the two materials. One of the magnetic materials is generally softer (a soft ferromagnet or a hard ferromagnet) while the other one is harder (a hard ferromagnet or an antiferromagnet). Ferromagnetic-antiferromagnetic (F/AF) form of exchange coupling is first discovered by Meiklejohn and Bean[50] in 1956, when they observed that if cobalt particles were cooled in a magnetic field (field cooling), the M-H loops of the particles could be displaced on the field axis by more than 1 kOe due to the presence of a thin antiferromagnetic CoO layer on the surface of the particles. Many models have been developed to explain the origin of exchange bias, including a direct exchange model by Meiklejohn and Bean, an AFM spring model by Mauri [51], a random field exchange model by Malozemoff [52], a spin-flop coupling model by Koon [53]. In a intuitive model by Meiklejohn and Bean, when the F/AF bilayer is cooled through the Néel point of the AF phase, the magnetic moment of AF phase is pinned to the cooling field direction, therefore it will require an extra field to break down the interface exchange coupling, resulting in a displacement of the M-H loop of the softer material along its field axis, as illustrated by Figure 2-14 (c).

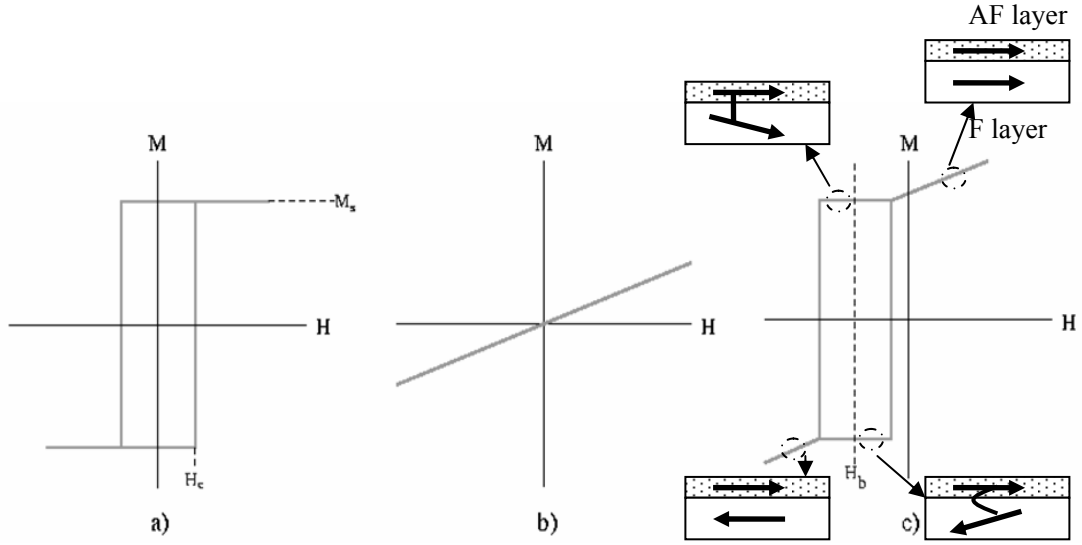

Figure 2-14, Easy-axis magnetization curves of (a) a soft ferromagnetic film, (b) an antiferromagnetic film and (c) an exchange-biased bilayer consisting of (a) and (b).

Exchange bias is widely used in magnetic recording industry, to stabilize the magnetization of soft ferromagnetic layers in readback heads based on the AMR effect or more recently to pin the harder reference layer in spin valve readback heads and MRAM memory circuits that utilize the giant magnetoresistance or magnetic tunneling effect. Because without the stabilization of magnetic domain state of the head or the ferromagnetic states of magnetic particles that will be superparamagnetic otherwise, the performance of

read head or memory could be unpredictable, leading to reliability problems. Desirable properties for an exchange bias material include: (1) high Néel temperature, (b) large magnetocrystalline anisotropy, and (c) good chemical and structural compatibility with NiFe or Co, the most important ferromagnetic films. The most technologically significant exchange bias materials have been the rocksalt-structure antiferromagnetic oxides like NiO, CoO and their alloys and the rocksalt-structure intermetallics like FeMn, NiMn, IrMn and their alloys.

2.5 Percolation

Consider a composite material made of homogeneously distributed insulator and conductor phases. When the composite is of purely insulator or purely conductor, i.e. the volume fraction of conductor is 0 or 1, the effective conductivity of the material is as low as the insulator or as high as the conductor phase, respectively. For composites of conductor volume fraction between 0 and 1, the effective conductivity changes from that of insulator to that of conductor. However, the change is not linear, when the volume fraction of conductor increases to a certain value, at which the macroscopic sample of the composite material can be traversed from one side to the other on a path covered entirely by the conductor particles [54]. This phenomenon is called percolation and the critical value is called percolation threshold, below this value, the conductor particles are scattered or at best forming only clusters, the effective conductivity of the composite is low, above this value, the conductor particles form a path for current, the effective conductivity rise abruptly up to a very high value, as shown in Figure 2-15.

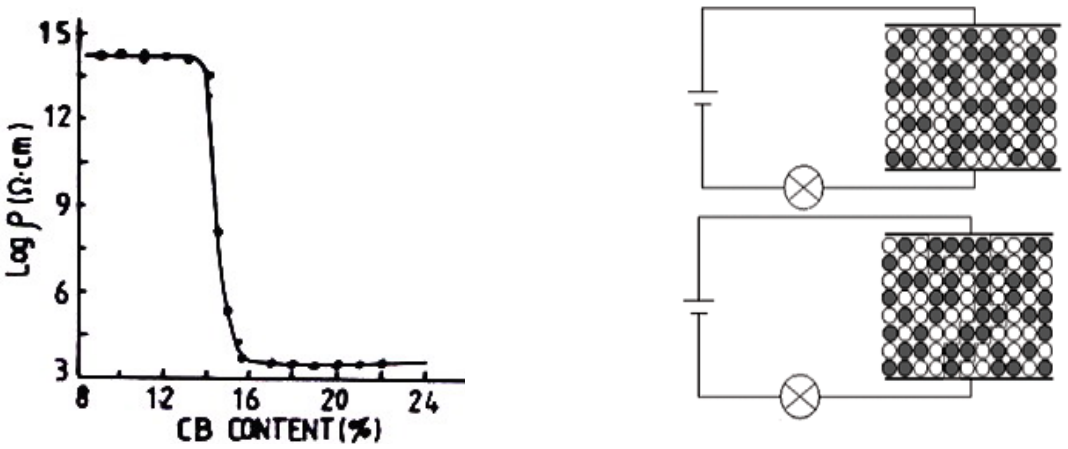

Figure 2-15, illustration of electrical percolation. Left, resistivity of a ceramic-carbon black (CB) composite as a function pf volume fraction of CB. Right, top, below the percolation threshold; bottom, above the percolation threshold, the white line indicate a short circuit by interconnecting conductor particles.

Disordered resistance networks have been studied by analog [55] and numerical simulations. But a simpler and very powerful, theoretical description of conduction in disordered resistance networks is provided by effective-medium theory (EM). This theory, originally formulated to describe the conductivity of binary mixtures, has been extended and

adapted to treat general disordered resistance networks and gives very accurate results under a wide range of conditions. Below is a brief description of EM theory.

2.5.1 Effective Medium Approximation (EMA)

In a random mixture of two types of ***spherical*** grains A and B with volume fractions ϕ and $1-\phi$, conductivities of σ_A and σ_B, respectively. To calculate the effective conductivity σ_e of this composite, we imagine that each grain *i*, instead of being embedded in its actual random environment, is instead immersed in a homogeneous effective medium of conductivity σ_e which will be determined self-consistently. Then the electric field inside grain *i* is uniform and given by the elementary result of electrostatics:

$$E_{in} = E_0 \frac{3\sigma_e}{\sigma_i + 2\sigma_e} \qquad \text{(Equation 2-8)}$$

where $\sigma_i = \sigma_A$ or σ_B and E_0 is the electric field for the grain.

The self-consistency condition required by the EMA is that the average electric field within the grain shall equal E_0, therefore,

$$\phi E_0 \frac{3\sigma_e}{\sigma_A + 2\sigma_e} + (1-\phi) E_0 \frac{3\sigma_e}{\sigma_B + 2\sigma_e} = E_0 \qquad \text{(Equation 2-9)}$$

Eliminating the common factor E_0, one will get

$$\phi \frac{\sigma_A - \sigma_e}{\sigma_A + 2\sigma_e} + (1-\phi) \frac{\sigma_B - \sigma_e}{\sigma_B + 2\sigma_e} = 0 \qquad \text{(Equation 2-10)}$$

The quadratic equation has two solutions. One is generally identified as the physically sensible solution, the other is typically negative, or has other unphysical features such as a discontinuous variation with the volume fraction ϕ, or incorrect limiting behavior as $\phi \to 1$ or $\phi \to 0$ [56].

In a conductor-insulator network where $\sigma_A \to \infty$ and σ_B is finite, one can calculate that:

$$\sigma_e = \frac{1}{3}\sigma_B (\phi - \phi_c)^{-1} \quad (\phi < \phi_c) \qquad \text{(Equation 2-11)}$$

$$\sigma_e = \infty \quad (\phi > \phi_c) \qquad \text{(Equation 2-12)}$$

The percolation threshold ϕ_c is $\frac{1}{3}$. In general, in d–dimensional random networks made up by spherical particles, the EMA gives a percolation threshold of $\frac{1}{d}$.

Since the EM approximation assumes that all the grains are located in an equivalent mean field, however, it is not the case when it is close to the percolation threshold where the system is governed by the largest cluster of conductors; therefore the mean field theory is no longer valid. To solve this problem, one must incorporate the percolation theory. The classical percolation equation is given as [57]:

$$\sigma_{eff} = \sigma_B (\frac{\varphi - \varphi_c}{1-\varphi_c})^t, \varphi > \varphi_c$$

$$\sigma_{eff} = \sigma_A (\frac{\varphi_c - \varphi}{\varphi_c})^{-s}, \varphi < \varphi_c \quad \text{(Equation 2-13)}$$

Where the fitting parameters s and t are critical exponents characterizing the conductivity in the conducting region and insulating region, respectively [57]. It is believed that the critical exponents are universal and depend only on the dimensions of the problem [58]. The most widely accepted universal values of s and t in three dimension problems are s=0.87 and t=2.00 [57]. Therefore, a physically based percolation model is governed by [57]:

$$\phi \frac{\sigma_A^{1/s} - \sigma_e^{1/s}}{\sigma_A^{1/s} + 2\sigma_e^{1/s}} + (1-\phi) \frac{\sigma_B^{1/t} - \sigma_e^{1/t}}{\sigma_B^{1/t} + 2\sigma_e^{1/t}} = 0 \quad \text{(Equation 2-14)}$$

2.5.2 Percolation in anisotropic systems

In 3-d spherical random networks, the percolation threshold is about 33% given by the effective medium approximation. When the particles are anisotropic, i.e., they are not spherical (such as fibers, wires or spheroids) and their symmetry axes are oriented in a certain way, the percolation is expected to take place in a lower volume fraction. Several studies have pointed out that in highly shape-anisotropic system, the percolation threshold can be as low as a few volume percent of the metallic phase, contrasting to around 30 percent in the classic spheroidally dispersed systems [59, 60], as shown by Figure 2-16 (a).

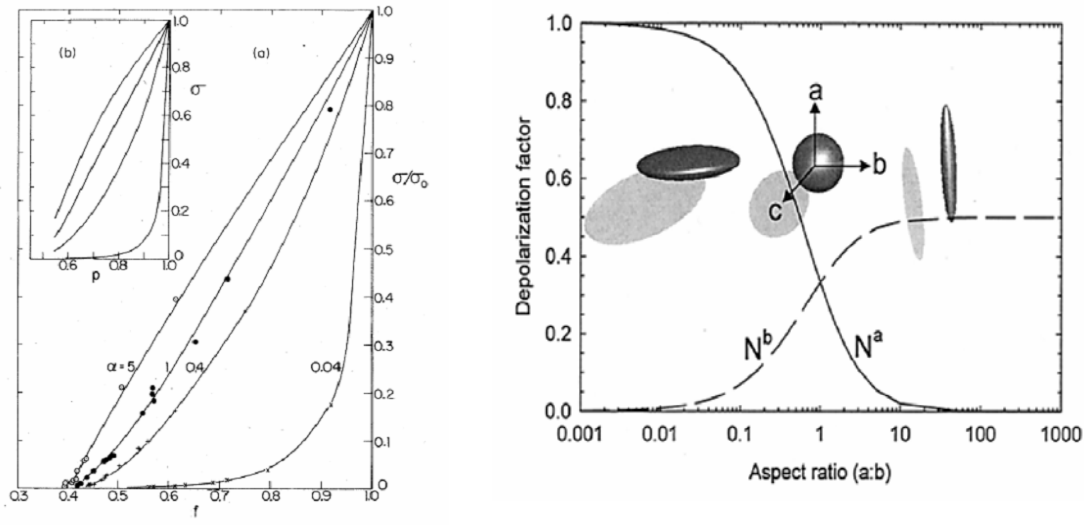

Figure 2-16, (a), electrical percolation in a 2-d percolation system. Normalized conductivity vs metal area fraction. The solid curves are a guide to the eye. The inset is result of Monte Carlo calculations on a square lattice with the same degrees of anisotropy as the data in the bigger plot. α is the aspect ratio. Figure is from Smith '79 [59]. (b), Depolarization factor as a function of aspect ratio and axial-electrical field alignment, where N^a is the depolarization factor for a particle whose rotation axis *a* is aligned parallel to the electrical field and N^b is the depolarization factor with respect to

the common axes. From Jones '00 [61].

According to an effective medium model of a macroscopically anisotropic composite consisting of M different types of unidirectionally aligned isotropic ellipsoidal inclusions of the same shape, an equation can be deduced as [62]:

$$\sum_{j=1}^{M} \phi_j (\sigma_j - \sigma_e) \cdot R^{(je)} = 0 \qquad \text{(Equation 2-15)}$$

Where

$$R^{(je)} = [I + A^* \cdot \sigma_e^{-1} \cdot (\sigma_j - \sigma_e)]^{-1} \qquad \text{(Equation 2-16)}$$

here A^* is the depolarization tensor for an ellipsoid in a matrix with an effective conductivity of σ_e. For simplicity, consider the filling particles as the identical rotational ellipsoidal particles with aspect ratio R=a/b, where the lengths of three semi-axis a_i are $a_1 = a$ and $a_2 = a_3 = b$, respectively. Then according to Doyle '92 [63] , the depolarization factors for particle filled composites are separately given by:

$$A_{i,1} \begin{cases} \dfrac{1}{1-R^2}\left[1 - \dfrac{1}{2\chi_b}\ln\left(\dfrac{1+\chi_b}{1-\chi_b}\right)\right], R>1 \\ = \quad 1/3, \text{ R=1} \\ \dfrac{1}{1-R^2}\left[1 - \dfrac{1}{2\chi_a}\tan^{-1}(\chi_a)\right], R<1 \end{cases} \qquad \text{(Equation 2-17)}$$

$$A_{i,2} = A_{i,3} = \frac{1 - A_{i,1}}{2}$$

Where $\chi_a^2 = -\chi_b^2 = \dfrac{1}{R^2} - 1$

For spherical particles, the depolarization tensor is $\begin{bmatrix} \frac{1}{3} & 0 & 0 \\ 0 & \frac{1}{3} & 0 \\ 0 & 0 & \frac{1}{3} \end{bmatrix}$, while for disk-shaped particles with large diameter to thickness ratio, the depolarization tensor can be approximated as $\begin{bmatrix} 0 & 0 & 0 \\ 0 & 0 & 0 \\ 0 & 0 & 1 \end{bmatrix}$.

2.6. Synthesis of MnZn ferrites and Co ferrites

Ferrites have been conventionally made from single crystal growth and sintering techniques. In the past few decades, thin film techniques such as sputtering, pulse laser deposition, molecular beam epitaxy, etc., have been used to fabricate ferrite thin films for

various applications and research. Below is an effort to list a few widely used synthesis methods in making ferrites, especially Co ferrites.

2.6.1. Bulk single crystal

Single crystals of Cobalt ferrite [64] or various metal substituted cobalt ferrites [65] were grown from flux technique. Cobalt zinc ferrite bulk single crystals were grown by flame fusion [41] method. The single crystals of cobalt ferrite were mostly used to study the fundamental properties of cobalt ferrite such as magnetocrystalline anisotropy, magnetic domain structure, magnetostriction at various crystallographic directions.

2.6.2. Ceramic sintering

Cobalt ferrites of different ratio of Co/Fe are fabricated by ceramic sintering techniques. In this method, powders containing Co and Fe (usually CoO and Fe_2O_3) were mixed and sintered at 1100°C for several hours following by grinding and pressing in a mold with application of certain pressures, then sintering at 1100°C for several hours. Alternative powder sources of $CoCO_3$, Co_2O_3, FeO, Fe_2O_3, were used by Pines and Gumen [39] in their X-ray study of magnetostriction. The ceramic sintering technique is also used by Chen et. al. [66] to make cobalt ferrite magnetostrictive torque sensors.

2.6.3. Thin film techniques

1. Sputtering

Okuno et. al. [67] studied the preferred orientation of cobalt ferrite using ion bombardment techniques. In this work, the primary ion beam sputtered the sintered target of $Co_xFe_{3-x}O_4$ and a second ion beam bombarded the growing surface of the film. He found that the film grown without ion bombardment was randomly oriented and almost amorphous. With ion bombardment during deposition, the crystallization improved and took preferred orientation. For $0.8 < x < 1.0$, the preferred orientation is [110], for $1.15 < x < 1.8$, the preferred orientation is [111].

Na [68] fabricated metal/cobalt ferrite composite thin films by reactive sputtering using metal iron disk and cobalt chips as source materials. The cobalt content of ferrite thin films was controlled by adjusting the number of cobalt chips attached on the iron disks. The saturation magnetization and coercivity can be adjusted by the composition of the target composite and by controlling the oxygen concentration in the sputtering gas, and substrate temperature.

Thin film of cobalt ferrite by RF magnetron sputtering was synthesized by Gu [69] using sintered cobalt ferrite with composition of $Co_{0.5}Fe_{2.5}O_4$ as target material. He found that the preferred orientation of as-deposited film is [311]. After heat treating, the saturation magnetization increased and this increase was attributed to Co^{2+} cation migration to tetrahedral sites during annealing. Gillies and coworkers have studied the magnetic properties of RF sputtered MnZn ferrite films [70].

2. Pulse laser deposition (PLD)

Cobalt ferrite pulse laser deposited on a MgO single crystal substrate from a polycrystalline cobalt ferrite target was studied by Dosey [71]. The PLD system was operated

for 5000 shots at a laser repetition rate of 5 Hz and an energy density of 2.5 J/cm^2. The substrate was heated and held at a constant temperature during annealing. The as-deposited thin film had a [100] orientation and high crystalline quality. The saturation magnetization increased with substrate temperature, the easy magnetization direction changed from in plane to perpendicular to the plane as substrate temperature increased.

Magnetic anisotropy of epitaxial cobalt ferrite films grown by pulse laser deposition on $SrTiO_3$ or $MgAl_2O_4$ substrates with 500 -1000 Å $CoCr_2O_4$ buffer layer was studied by Suzuki [72]. It is found that the film has a very high anisotropy energy coming from stress which is a result of lattice mismatch. As the film thickness increased, the stress was released, the anisotropy field decreased.

In general, thin films deposition techniques can be applied to make downsized ferrite parts. However, the processing requirements are expensive, e.g. high vacuum, substrate temperature control. The production may be low because the limited chamber space and each time the loading of the substrates need long time pumping to achieve good vacuum.

2.6.4. Sol-gel method

Sol-gel technique offers an alternative way of making ferrite thin films, it has some advantages: good homogeneity, easy composition control, lower sintering temperature, large area of thin film and lower cost [73].

Cobalt ferrite nanoparticles recently received much interest due to its potential in recording media application. Generally these nanoparticles are fabricated by a variety of sol-gel techniques. Sato [74] reported a synthesis of cobalt ferrite powder with average diameter of a few tens of nanometers by adding NaOH solution into mixed solution of $FeCl_3$ and $CoCl_2$ at pH value of 13. The magnetic moment of the synthesized nanoparticles is lower than the bulk value. The decrease in magnetic moment is a result of superparamagnetism.

To produce thin film coating by sol-gel technique, one can spin coat the solution onto suitable substrates. A typical procedure is briefly illustrated in Figure 2-17 [75], sol precursor are made by dissolving Co^{2+} and Fe^{3+} salts in proper solvent, then the precursor is spin-coated on substrate, the as-deposited film was pyrolyzed and heat treated for crystallization.

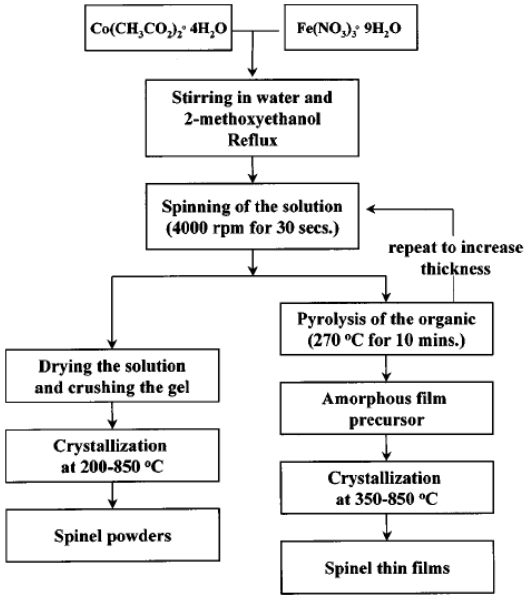

Figure 2-17, Preparation process for cobalt ferrite powders and thin films[75].

2.7. Thermal spraying

2.7.1. Overview

Harris et al. [76] first introduced the idea of plasma spraying of ferrite materials in the 1970's, some other researchers followed the idea and successfully fabricated ferrite coatings by plasma spraying [77] [78] [79] [80]. Thermal spraying offers some advantages [3] over conventional ceramic sintering technique and other thin film techniques such as: (1) low substrate temperature, (2) atmospheric environment (3) large productivity (4) low cost, making thermal spraying a good candidate for ferrite coating in the application of electric devices and sensors.

The plasma torch consists of a cone-shaped cathode and an annular anode separated by a small gap, which form the nozzle. DC power is applied to the cathode and arcs across to the anode, which is water-cooled. The plasma gas (generally, argon or other inert gas, complemented by a few percent of an enthalpy enhancing gas such as hydrogen) is introduced at the back of the gun interior, the gas swirling in a vortex and out of the front exit of the anode nozzle. The powerful electrical arc is sufficient to strip the gases of their electrons, and the state of matter known as plasma is formed. As the unstable plasma recombines back to the gaseous state, thermal energy is released. At the point of recombination, temperatures can reach up to 16,600 °C. Injection of powder into the gas plume causes it to melt and be propelled towards the target component.

2.7.2. Important parameters

The parameters involved in plasma spraying are numerous such as gun current, carrier

gas, plasma gas components, powder injection angle, substrate temperature, substrate roughness, etc. Many of the parameters are coupled and the achievement of optimal conditions is difficult.

Yan [80] studied the effects of spray process on the properties of MnZn ferrite coatings, the correlations are summarized briefly here. These research findings are the guidelines for this current research.

2.7.2.1 (a) Spray distance

The spray distance is the distance between the nozzle and the substrate. The temperature and velocity of particles changes during flight and are functions of flight distance. Figure 2-18 show the simulated results and experimental results of particle temperature and velocity at different flight distance [81].

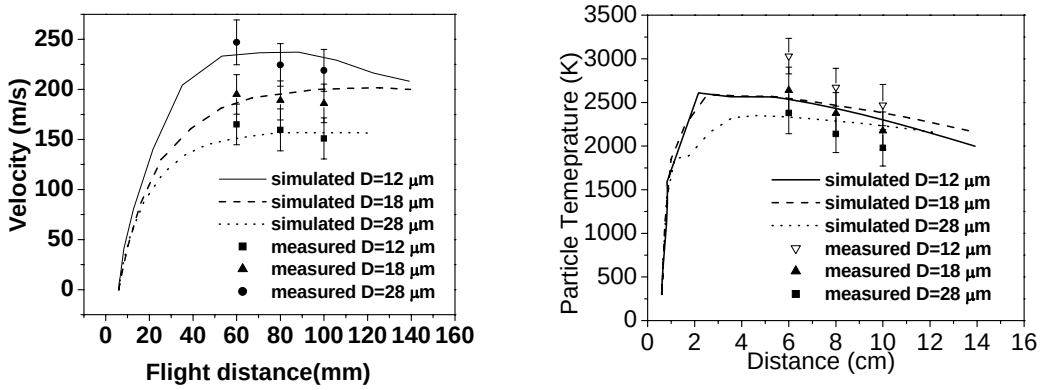

Figure 2-18, (left), average velocity for MZF particles of different sizes. The lines are simulated data and the points are measured data. D is the diameter of particles, (right), Average temperature for MZF particles of different sizes. The lines are simulated data and the points are measured data. D is the diameter of particles.

It can be seen that increasing spray distance above 60 mm leads to the drop of the particle temperature (still above melting temperature so the particle is still molten), which results in the decrease of the quenching process so that the cation distribution is relatively more ordered thus the saturation magnetization is higher (shown in left part of Figure 2-19). The coercivity is also affected by spray distance but the effect is not significant. This can be explained by the kinetic energy of molten particles. The kinetic energy has two opposite effects, one is to increase the density of the coating which is good for lowering the structural barrier to domain motion, i.e. lower the coercivity, however the other one is to increase the Reynolds number which will result in the fragmentation of the splats, this is bad from the point of view of having more structural barriers to the domain motion, i.e., higher coercivity. Since the particle velocity also starts to decrease when the spray distance is greater than 60mm, so the longer the spray distance, the lower the particle velocity, the more porous the deposited coating, so the coercivity increases, but the change is not insignificant.

Spray distance also affects the resistivity of as-deposited MnZn ferrite coatings. Since the reaction of $Fe_3O_4 \rightarrow FeO + O_2$ is favored as the temperature increases, so as the spray

distance increases, the temperature drops, resulting in the favor of the reaction of FeO + O_2 → Fe_3O_4. This recombination results in the increase of resistivity in as-deposited coating as the spray distance increases as shown in the right part of Figure 2-19.

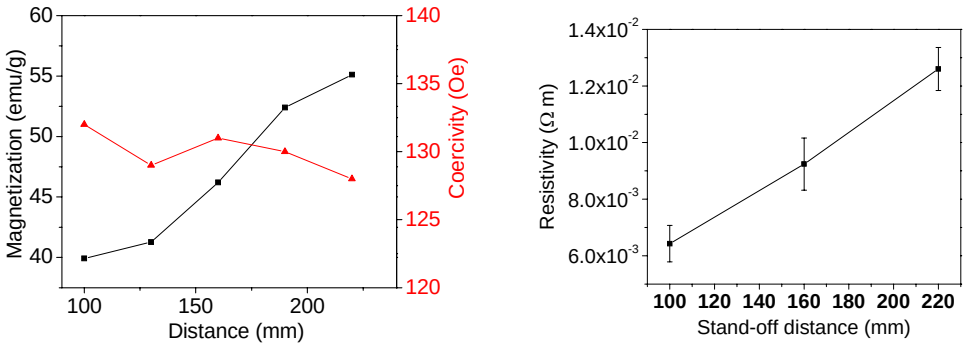

Figure 2-19, (left), Magnetization of plasma sprayed MnZn ferrite films collected at different stand off distances. The gun current and the hydrogen flow rate are fixed at 550 A and 4 L/min. Figure 2-19 (right), Resistivity of MnZn ferrite films collected at different stand off distance. The gun current and hydrogen flow are fixed at 550 A and 4 L/min.

2.7.2.2 (b) Gun current and hydrogen flow

Gun current is one of the key factors that determine the plasma temperature. Increasing gun current will increase the plasma temperature. The plasma gas used in Yan's research [80-86] is a ternary mixture of Ar-He-H_2. Ar gas increases the momentum of the plasma gas. He gas can increases both the thermal conductivity of the plasma gas and its viscosity in high temperature region [82, 83] while the H_2 can increase the enthalpy of the plasma. The plasma gas components not only can affect the particle temperature [84] but also may affect the final phase components in the as-sprayed films. The increase in plasma temperature will result in more quenching which in turn will increase the degree of disorder of cation distribution, giving rise to the decrease in saturation magnetization. Higher temperature will increase the zinc evaporation thus creating crystalline anisotropy which is a barrier to domain movement. High plasma temperature will also cause more oxygen loss which will cause more hopping conduction between Fe^{2+} and Fe^{3+}, which will give rise to lower resistivity. Table 2-5 listed the ferrite properties at various gun current and hydrogen flow conditions.

Table 2-5, Properties of ferrite films sprayed with various currents and H_2 flow rate (in the plasma gas). The spray distance is fixed at 120 mm.

Sample#	I (A)	H_2 Flow Rate (L/min)	Ms (emu/g)	Hc (Oe)	ρ (Ω·m)
1	400	0	57.9	73.2	2.84×10^{-2}
2	400	2	57.7	80.5	2.00×10^{-2}

3	400	4	51.8	98.9	1.34×10^{-2}
4	500	2	55.6	91.1	1.57×10^{-2}
5	500	4	51.3	107.4	1.13×10^{-2}
6	600	6	49.2	124.6	0.97×10^{-2}

2.7.2.3 (c) Particle size

The effects of particle size on particle temperature and velocity have been shown in Figure 2-18. It can be seen that a smaller particle has higher velocity and higher temperature under the same conditions. Since the zinc evaporation increases when temperature increases, combining the fact that zinc evaporation rate depends critically on the surface area of the particle, smaller particles has more zinc evaporation, leading to more zinc loss. Yan [81] showed that the zinc loss is inversely proportional to the surface to volume ratio, namely 1/r (shown in Figure 2-20).

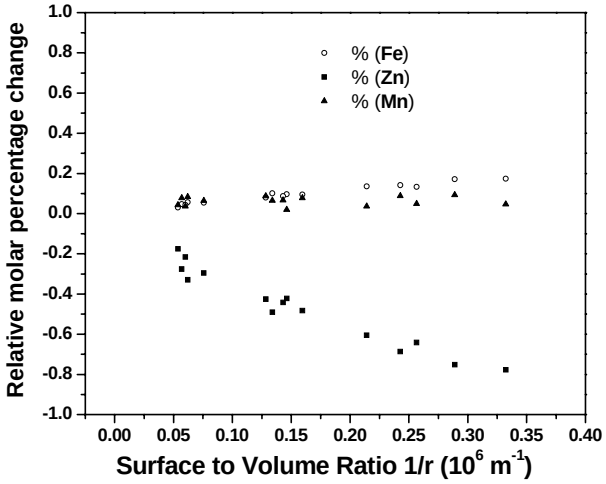

Figure 2-20, Relative molar composition changes of metallic elements for particles with different surface to volume ratio. The relative molar percentage change is given by $\frac{\text{final molar percentage-starting molar percentage}}{\text{starting molar percentage}}$ and r is the radius of the particle.

2.7.3. Structure and morphology of plasma sprayed coating

2.7.3.1 Formation, solidification and morphology

In thermal spraying, the deposit is built up by continuous impacting of molten droplets

[85]. Upon impacting, the sudden deceleration of the particle causes a pressure buildup at the particle-surface interface. The high pressure buildup at the particle forces the molten droplet to flow laterally to the substrate, which spreads outward from the point of impact and forms splats. The spreading kinetics of the impacting droplets governs the splat shape and thickness. The process of splat formation depends on the velocity, size, molten state and chemistry [85]. It is also subjected to the surface topography of the substrate and substrate temperature.

Bhat [86] have studied phase evolution and microstructure of plasma-sprayed iron-/nickel-based alloy coatings. Martensitic stainless steel powder was plasma sprayed onto a copper substrate cooled with liquid nitrogen. It was found that increase quenching rates give rise to finer grain and increase the amount of austenite phase in the as-sprayed coatings, which enhances the micro-hardness and tensile adhesion strength[87].

2.7.3.2 Residual stress

As the particles impinge on the substrate, they undergo a large temperature drop. The thermal contraction of the splats is constrained by the underlying solid. This introduces tensile quenching stress in the deposit. The difference in the thermal expansion coefficient between the substrate and the deposit material leads to the residual stress. The sign of the residual stress depends on the relative magnitudes of the respective thermal expansion coefficients. If the coatings have lower thermal expansion coefficient than that of the substrate, it will lead to compressive thermal stress in the coating. Otherwise, tensile stress will be introduced in the coatings. The magnitude of the quenching stress varies significantly with the coating material and spraying conditions [88]. The quenching stress can be relieved by various mechanisms [89] such as micro cracking, plastic yielding and creep. In case of the study of plasma-sprayed cobalt ferrite films, the residual stress is an very important issue because it has effects on the magneto-elastic anisotropy, which may affect magnetostriction and hence coercivity [90].

2.7.3.3 Structural and chemical stability

Yan [80, 81, 90-93] found that the as-deposited MnZn ferrite coating contained not only spinel phase but also wuestite phase. He also found that by air annealing wuestite transformed to hematite which can increase the resistivity of the ferrite coating. The formation of wuestite FeO is a result of oxygen loss at high temperature during spray. Since wuestite FeO is a metastable phase [91] in the binary Fe-O phase diagram (Figure 2-21), low temperature annealing will transform it into Fe and Fe_3O_4 magnetite; further air annealing can transform both Fe and Fe_3O_4 into Fe_2O_3 hematite. The entire MZF particle melting-solidifying process can be viewed as three steps: (1) oxygen loss upon heating the MZF to above its melting point ($T>1570$ °C), (2) the precipitation of spinel phase ferrite from the liquid precursor (1400 °C$<T<1570$ °C), (3) a eutectic reaction occurs to form spinel ferrite and wuestite FeO ($T<1400$ °C), which are retained in the as-sprayed coatings down to room temperature due to the rapid quenching of the molten droplets.

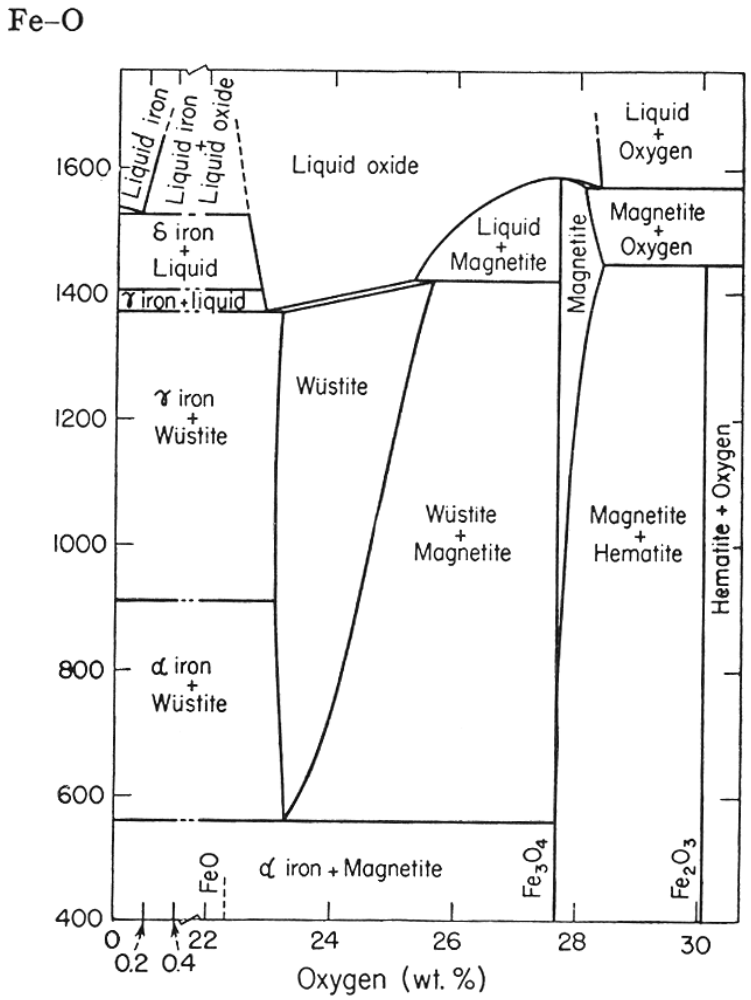

Figure 2-21， binary phase diagram of Fe-O.

2.7.3.4 Zinc loss in plasma spraying MnZn ferrites

For MnZn ferrites, Zn prefers to take the tetrahedral sites in the spinel structure [92], forcing the Fe^{3+} cation to move to octahedral sites and thereby increasing the total magnetic moment per ferrite formula. Certain Zn/Mn atomic ratios in MZF can reduce the overall magnetostriction and anisotropy constant [16], which fosters desirable low coercivity and high magnetic permeability. However, Zn loss during the high-temperature spraying process is found to create an inhomogeneous spatial compositional profile in the as-sprayed MZF coatings as well as a departure from the nominal initial powder composition [80] [81]. These changes deteriorate the soft magnetic properties, which adversely affect the performance of the ferrite devices.

As studied by Yan [80] [81], the total zinc mole loss during the spray process is $\Delta M_{Zn} = N_{Zn} A t = 4\pi r^2 N_{Zn} t$, where A is the surface area, t is the flight time and N_{Zn} is average zinc molar evaporation rate per unit surface area during the time period t. Then the

molar percentage of zinc in a single splat is given by $Zn_{final}(mole)\% = \frac{C_{Zn}V - \Delta M_{Zn}}{(C_{Zn} + C_{Mn} + C_{Fe})V - (\Delta M_{Zn} + \Delta M_{Mn} + \Delta M_{Fe})}$, where C is molar concentration of metallic elements in the initial powder, ΔM_{Fe}, ΔM_{Zn} and ΔM_{Mn} are the mole loss of Fe, Zn and Mn individually. The values of C_{Zn}, C_{Mn} and C_{Fe} are calculated from the powder composition provided by the supplier and are confirmed by the EDS measurements. Since the molar percentage changes of Fe and Mn after spraying is small (noted in Figure 2-20), implying that ΔM_{Fe} and ΔM_{Mn} can be neglected. Then the zinc molar ratio in the final deposit can be written as

$$Zn_{final}(mole)\% = \frac{C_{Zn}V - 4\pi r^2 N_{Zn} t}{(C_{Zn} + C_{Mn} + C_{Fe})V - 4\pi r^2 N_{Zn} t} = 1 - \frac{C_{Mn} + C_{Fe}}{C_{Zn} + C_{Mn} + C_{Fe} - \frac{3N_{Zn}t}{r}} \quad \text{(Equation 2-18)}$$

Therefore, the zinc molar percentage in the splat is determined by N_{Zn}, t and $\frac{1}{r}$ (surface to volume ratio). As $C_{Zn} + C_{Mn} + C_{Fe} - \frac{3N_{Zn}t}{r} > 0$, increasing the value of N_{Zn}, t and $\frac{1}{r}$ will decrease the value of $Zn_{final}(mole)\%$.

Table 2-6 lists the average zinc evaporation rate N_{Zn} and in-flight time t for MZF particles of three different sizes [80]. As can be seen from Figure 2-20 and Table 2-6, larger particles (smaller 1/r) tend to have smaller zinc loss. Also it can be seen from Table 2-6, that large particles have an increased in-flight time and low average evaporation rate. The product of N_{Zn} and t, which provides the amount of evaporated Zn per surface area, is close to 0.02 mole·m^2 for all three particle sizes and does not increase as the particle diameter decreases. Thus it is concluded that the significant decrease in Zn content found in small particles may be attributed mainly to the high surface-to-volume ratio. Zinc evaporation from particles after impacting the substrate has not been studied due to the large cooling rate making the zinc loss occurring during particle cooling negligible compared to that incurred during flight.

Table 2-6. Average N_{Zn} of particles with diameters $D_{particle}$.

$D_{particle}$ (μm)	Zn_{final} (mole)%	t (ms)	N_{Zn} (mole·s^{-1}·m^{-2})	N_{Zn}·t (×10^{-3} mole·m^{-2})
28.50	*12.78*	*0.84*	*23.4*	*18.9*
18.18	*11.09*	*0.72*	*27.9*	*23.3*
11.74	*6.93*	*0.66*	*29.4*	*19.3*

* N_{Zn} is the average Zn molar evaporation rate during the time period of t.

2.7.3.5 Microstructural defects

The microstructure of plasma-sprayed coatings may have many sub features [93] including pores, cracks and splat boundaries as shown in Figure 2-22. The intrinsic properties of individual splats and connections between them are believed to be affected by the conditions of the impacting particles; e.g. the particle size, particle temperature, phase condition, velocity, and the conditions of the substrate or previously solidified particles [94-97]. The structure of the splats determines the microstructure and the adhesion of the coatings, which consequently affects the properties and functionalities of the coatings.

The entrapped gas in the coating may introduce voids [98]. The generation of the voids and crack networks may reduce the mechanical strength and provides locations of stress concentration [99]. On the other hand, the voids and cracks may also reduce the thermal conductivity [100] and increase the strain tolerance.

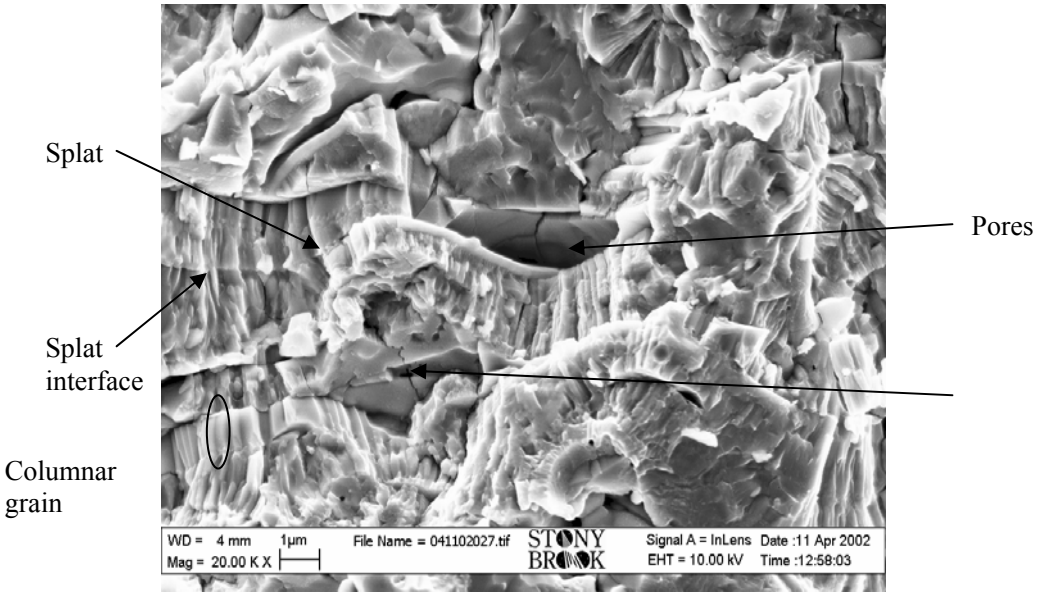

Figure 2-22, Typical microstructures of plasma-sprayed ceramic coatings

2.7.4. Post-deposition heat treatment --- annealing

The functional properties of ferrites was considered deficient after the plasma spray process [78, 101]. The inhomogeneous spatial compositional profile in the as-sprayed MZF coatings and a departure from the nominal starting powder composition results in an increase of coercivity. The non-equilibrium cation distribution results in the decrease of the saturation magnetization. The existence of additional low valence iron-based phase results in an increase of electrical conductivity.

Air annealing may be an effective route to improve the properties of plasma-sprayed ferrites. Annealing can homogenize the composition of the coating by cation diffusion [102] and release the residual stress [103], although it is unable to convert the composition of the as-sprayed MnZn ferrite coatings to that of the starting powder. The diffusion length of cations in the lattice is estimated from $\sqrt{2Dt}$ [104], where D is the diffusion coefficient of cations and t the annealing time. For example, in MnZn ferrite, at T=500 °C, D is ~2.0×10^{-8} $cm^2 \cdot s$ [105]. Thus for 120 minutes annealing, the diffusion length is about 500 μm. The actual value of D could be higher for the plasma-sprayed ferrite system due to the large amount of structural defects. The typical diameter and thickness of ferrite splats are about 20-50 μm and 0.8-1.5 μm, respectively. Cation diffusion can proceed through hundreds of

splats in the vertical direction and several of tens of splats in the lateral direction. Cation diffusion can decrease the variation of the crystalline anisotropy within the ferrite thick films. Thus, it can lower the coercivity by decreasing the energy barriers [106] that pin domain wall movement during the magnetization process. The annealing process may redistribute the cations in the spinel lattice toward their equilibrium state. In plasma-sprayed MnZn ferrites, the annealing process can bring about an ordered cation distribution at a relatively low temperature (~500 °C). As a result, the magnetic moment per ferrite unit increases, which leads to the increases of saturation magnetization.

Annealing allows oxygen diffusion through grain boundaries in MnZn ferrite [107]. During annealing, the low valence iron-based phases, e.g. FeO and Fe, can be oxidized to high-valence iron compounds, e.g. Fe_2O_3, which is normally of high resistivity. Other effects of annealing include relief of the residual stress and grain growth may also affect the properties of plasma sprayed ferrites such as change of magnetostriction and coercivities [90]. The surface of the ferrite coatings, as well as the voids and cracks inside the coatings, can act as oxygen diffusion sources.

Chapter 3 Statement of the Problem

There has been growing interests in magnetic composites in the past few decades, these research activities have resulted in development in magnetic devices. Offering advantages such as simple process, no interfacial reaction between the two distinct phases and potentially useful unique properties such as anisotropy and exchange coupling through monoxide layers, plasma spraying is proposed as a promising route for making magnetic composites devices. In this dissertation research, with the aim of synthesis magnetic composites devices through plasma spraying process, we focus on several aspects of this challenging mission:

(1) As non-percolating magnetic composites are more desired in devices applications (this will de explained later), a percolation phenomenon in thermally sprayed composites should be critically examined as it is different from bulk materials and has not been studied before.

(2) The magnetic and electrical properties of the two phases (ferrite and ferromagnetic metal) will degrade from their bulk counterparts as a result of oxygen loss, zinc loss, random cation distribution as well as defected structure. These important issues should be carefully studied.

(3) Post deposition annealing has been proved to be effective in the improvement of the functional properties of plasma sprayed ferrite [80, 108], it will be applied to plasma sprayed magnetic composites, and its effect on property improvement will be investigated.

(4) An integrated study of the process-structure-properties relationships in plasma spraying of ferrite-metal composites. An integrated set of relationships linking process, structure and properties, called process maps, will be constructed. The process maps have significance in process control and optimization.

The above four aspects are essential to the success of plasma spraying magnetic composites. Figure 3-1 illustrates their relationship, with the top box representing the motivation of this research.

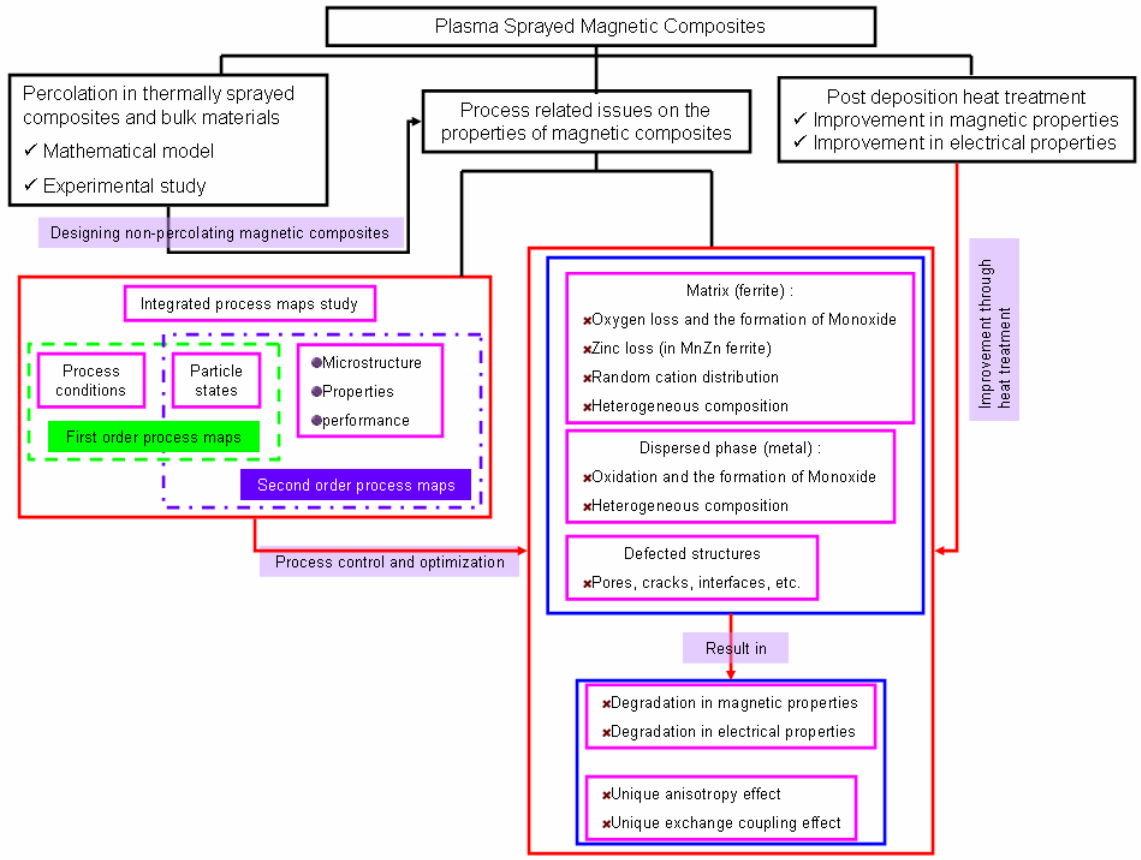

Figure 3-1, the interrelationship between composite design, plasma sprayed composites, process optimization and post deposition heat treatment.

3.1 The motivation in plasma sprayed magnetic composites

One major goal of this research is to develop thick film magnetic sensors or inductors for industrial applications. MnZn ferrite-NiFe composites, MnZn ferrite-NiCo composites and Co ferrite-Co composites are of special interests and become the focus of our study.

In a previous research on MnZn ferrite, it was shown that the plasma sprayed ferrite had improved resistivity, Q factor [109] and magnetization after low temperature annealing making it suitable to high frequency applications (~500MHz). However, the initial permeability of MnZn ferrites at high frequency is limited due to its relatively low saturation magnetization as predicted by the Snoek's law. To improve the high frequency performance of MnZn ferrite, a composite of MnZn ferrite and Permalloy $Ni_{80}Fe_{20}$, an alloy with highest permeability and nearly zero magnetostriction in the Ni-Fe binary system, is sought in this research.

$Ni_{80}Co_{20}$ anisotropic magnetoresistive sensors were directly deposited on alumina or spinel coated FR-4 (Flame Retardant #4 epoxy) substrates by plasma spraying. An impressive 2.48% longitudinal MR effect and 0.2% traverse MR effect were achieved in the

as-deposited material, resulting in an AMR of 2.68% [44]. However, the small change in resistance (ΔR) due to the intrinsic low resistivity (ϱ) of the $Ni_{80}Co_{20}$ makes a small electronic signal difficult to measure. To improve the sensor performance, increasing the resistance at zero magnetic field by dispersing the metal in insulating matrix is one of the motivations of this current study. Since using a diamagnetic insulator like Al_2O_3 increase the magnetic field needed to saturate the sensor and thus degrade the magnetic field sensitivity, a magnetic insulator should be used. In this work, by using a high resistivity ferrite instead of the diamagnetic insulator we can gain three additional improvements in sensor performance: (1) a smaller demagnetizing field because the flux is carried by both the ferrite and the ferromagnetic metal and (2) an enhanced ΔR/R because of the greater anisotropic magnetic scattering at the metal ferrite interfaces and (3) the exchange coupling at the interface of ferrite and metal may help to increase the AMR ratio, as indicated by a previous study by Lin [110], where it was observed that in ion-beam deposited $Ni_{80}Fe_{20}$-$Ni_xFe_{1-x}O$ composite films, the exchange coupling at the interface between ferromagnetic $Ni_{80}Fe_{20}$ and $NiFe_2O_4$ helps to increase the AMR ratio by a factor of 8. Therefore, MnZn ferrite with high resistivity (1-100 Ω•m) is selected as the insulating matrix.

Magnetostrictive torque sensor made from Co ferrite and Co or NiAg composites is able to be used to regulate the steering power and improve the fuel efficiency of a car. These Co ferrite composite rings are currently made by sintering method which is not cost efficient. We propose to make Co ferrite composite thick films by thermal spraying as an alternative route as it is simple and easy and is able to avoid interfacial reaction. The challenge we will be facing is the formation of the undesired CoO phase. We will seek to understand how this phase is formed and how it will affect the magnetic properties and magnetostriction of plasma sprayed coating, and how annealing can help to improve the performance of the coatings.

3.2 Composite design and percolation study

The ultimate goal of making magnetic composites suitable for high frequency applications requires that the composites possess high resistivity. The resistivity of metal-insulator composite depends critically on its microstructure and composition. The percolation threshold, ϕ_c, depends on the resistivities of each phase of the composite, the size and shape of the particles, and the orientation of the particles. Thermal sprayed coatings are built up of disk shape splats with a significant aspect ratio and as such result in highly anisotropic microstructures [111, 112]. The thickness to diameter ratio of the splats usually varies from 1/10 to 1/50, depending on the properties of the materials and the process method and conditions. Several studies have pointed out that in highly shape-anisotropic system, the percolation threshold can be as low as a few volume percent of the metallic phase, contrasting to around 30 percent in the classic spheroidally dispersed systems [59, 60]. To date, a specific study on the percolation phenomenon in thermal sprayed metal-insulator composites has not been conducted. Therefore, a detailed study on the transport properties around the percolation threshold in thermally sprayed magnetic composites is important for composite design.

3.3 Functional magnetic thick film composites

3.3.1. The degradation of functional properties due to thermal spray

During the plasma spraying process, the ferrites and metals are heated to a temperature well above their melting temperature to get fully or partially molten, at such a high temperature, ferrites will loose oxygen while metals will oxidize. Although there is no interfacial reaction between the two distinct phases, the oxide layer forms due to deoxidation of ferrite and oxidation of metal will be present in the as-sprayed deposits. The oxides, antiferromagnetic in natural, will result in a decrease in saturation magnetization, an increase in coercivity and a decrease in electrical resistivity. This oxide layer can also exchange coupled with metallic phase and ferrite phase thus act as a mediating layer, which might be useful to help aligning the magnetic moments in a favorable way. The exchange coupling may result in unique magnetization process and magnetostrictive behavior, thus it is important to study the exchange coupling mechanism between the antiferromagnetic phase and the ferrimagnetic phase.

The random cation distribution in the ferrite phase resulting from rapid quenching process also result in magnetic moment deviation from the bulk value. In case of MnZn ferrite, disordered phase has a lower saturation magnetization than the ordered phase. But in the case of Co ferrite, the disordered phase has a higher saturation magnetization than the ordered phase. The defected microstructure intrinsic to thermally sprayed coatings will also result in high coercivity and low permeability. Feedstock powders for thermal spray inevitably have a finite size distribution, this variation in particle size, combining with the three dimensional temperature and velocity gradient in plasma flame, will lead to totally different thermal histories of each individual particles. Therefore, the chemistry, microstructure and stress-strain vary from splat to splat. This inhomogeneity will result in an increase in coercivity and degradation in magnetic field response.

In this research, we will seek to understand how the above mentioned issues affect the functional properties of plasma sprayed composites, and how these issues are related to the processing conditions.

3.3.2. Post-deposition annealing effect on the improvement of functional properties

In plasma sprayed single phase of ferrite, low temperature air annealing can provide enough thermal energy for cations redistribution, compositional homogenization; it also forms insulating layers and densifies the microstructure. These factors contribute to the regaining of functional properties which are degraded by the thermal spraying process. For a ferrite-metal composite, the improvement of functional properties is also expected from the point that the magnetic and electrical properties of ferrite phase can be improved by low temperature air annealing. However, annealing in air can oxidize the metallic phase to form monoxide layer which can degrade the functional properties. Also, annealing can lead to interfacial reaction between the two magnetic phases; this is not a favorable effect. Therefore, an optimum annealing condition should be chosen to achieve a balance between the favorable and unfavorable effects.

3.4 An integrated study on the relationship between process, microstructure and coating properties – Process Maps

It has long been appreciated that plasma spray offers a spectrum of process conditions and parametric states allowing the "tuning" of the microstructure. And as a consequence of different microstructural features, coatings exhibits different properties. The differences in coating microstructure can arise due to the many process variables that affect the plasma flame. As shown in

Table 3-1, a large number of variables (both controllable and non-controllable) exist in the plasma spray process [113].

Table 3-1, feedstock and process variables for plasma spray

Feedstock variables	Torch variables	Plasma forming variables	Deposition variables	Measured outcomes
✓ Powder morphologies ✓ Manufacturing methods ✓ Particle size distribution ✓ Carrier flow and injection location	✓ Torch type ✓ Nozzle type: Laminar vs. swirl ✓ Nozzle size ✓ Powder injection type: Angle of injector	✓ Primary gas type: Ar, N_2, H_2 ✓ Primary gas flow rate ✓ Secondary gas type: He or H_2 ✓ Secondary gas flow rate ✓ Gun current	✓ Spray distance ✓ Substrate conditions: temperatures, roughness, etc. ✓ Robotic trajectory and speed	✓ Particle states (temperature, velocity, size distribution) ✓ Coating thickness and buildup rate ✓ Phases and Compositions ✓ Magnetic and electrical properties

As has been mentioned in Chapter 2, the functional properties of ferrites such as magnetization, coercivity, electrical resistivity are greatly dependent on the process conditions, such as particle size, gun current and spray distance, etc. In the previous study by Yan [80, 81], *process-microstructure-properties* relationships has been looked at an preliminary stage, relationship between magnetic properties, electrical properties have been linked with spray distance, gun current and hydrogen flow rate. Important issues such as oxygen loss, zinc loss have been correlated to the feedstock characteristics. However, issues such as the relationship between oxygen loss or zinc loss and the particle temperature and velocity which are the results of process operating conditions are not studied. Also, a quantitative study between the process conditions and the coating properties and microstructures, linking through the in-flight particle states, has not been explored yet. Therefore, in this dissertation, we aim to get a more detailed understanding on the *process-microstructure-properties* relationships, with the aide from advanced in-flight diagnostics tools and process map methodologies.

3.4.1. Generation of process map

A process map is an integrated set of relationships that link materials and processes to

microstructures, ultimately to properties and performance [113]. The map can consist of experimental, analytical and computational information. In the case of thermal spray process, a process map would result from understanding the linkage between process/torch/feedstock variables and the resultant coating characteristics. The large number of operational parameters, wide particle size distributions and the stochastic associated with the phase changes (melting and solidification), taking place at very short time scales (in the orders of milli-seconds), have made the development of such maps very difficult for plasma spray. However, over the last decade, particle-flame interactions have been investigated extensively, resulting in the development of commercial instruments to study the in-flight particle diagnostics, allowing the characterization of the spray stream in terms of the particle velocity, temperature, size and trajectory. These new tools and capabilities have allowed the examination of the process, enabling generation of advanced maps for both scientific development and industrial practice.

Figure 3-2 presents an illustrative description of the proposed process map concept. The entire process has been subdivided into two zones. The interaction between feedstock powder and the thermal spray device results in a spray stream whose attributes can be manipulated through changes in powder characteristics (size, morphology), processing hardware (torch type, gun nozzle, powder injection type, etc.) and processing parameters (gun current, gas flow, etc.). Our ability to quantitatively characterize the spray stream will allow characterization of the process at this stage. We refer to this sub-step as the first-order process map. The first order process maps provide a logical strategy to identify regions of interest for coating development and add considerable degrees of freedom for process manipulation. Linkage between the observed coating properties and the spray stream characteristics can be referred to as a second –order process map. The second order process maps are designed to link the particle state to the splat build-up and coating microstructure, and the resultant coating properties and performances.

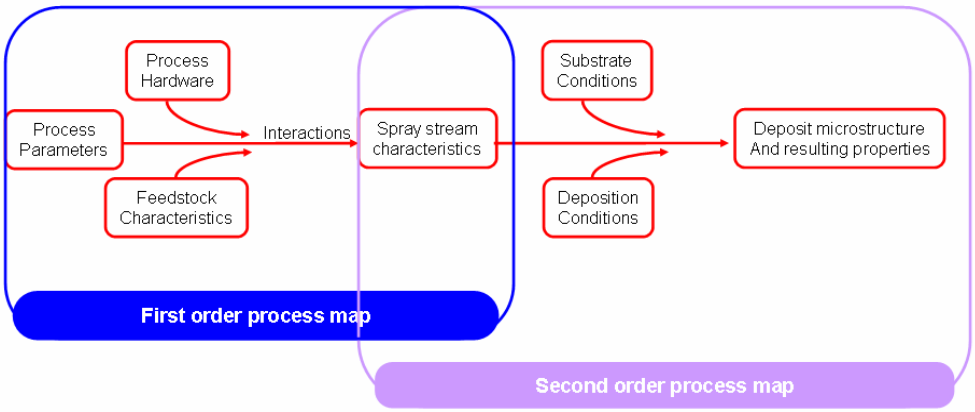

Figure 3-2, schematics of the process links and significant variables at each stage of the process.

3.4.1.1. First-order process map

A first-order process map is a projection of the 3D experimental design (part (a) of Figure 3-3) space on to a 2D temperature-velocity (or Melting Index and Reynolds number)

plane, as illustrated by Figure 3-3. Associated with T-V data in Figure 3-3 for the eight outer cube corner conditions is the vector illustrating effects of the key process parameters on the overall T-V response. These maps allow for a quantitative description of the process input and response output relations, providing significant value from the point of process optimization, control and fundamental understanding of the complexities. They are useful in tracking instabilities and examining process reproducibility.

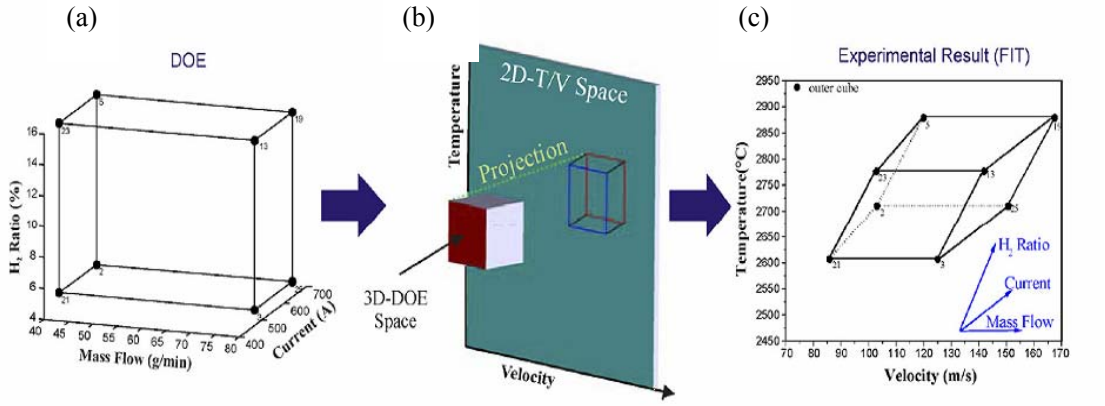

Figure 3-3, an illustrative description of the linkage between torch parameter and the first-order process map.

The particle – spray stream interaction is unique to materials. Since such study has not been conducted before on ferrite, it is very important for us to understand the behavior of ferrite particles in plasma spray streams.

3.4.1.2. Second-order process map

The first-order process maps described earlier is a description of the particle T-V relationships for a given torch/nozzle/material combination. However, to utilize such maps from a coating design and microstructural tailoring perspective, it is important to combine, coating properties with the particle output. Second-order process maps are a set of measured microstructural characteristics and coating properties as well as performances overlaying on the average particle T-V space or MI-Re space. These linkages provide insights in both scientific understanding of the physics of materials and knowledge in engineering practices. For example, the relationships between the oxygen loss or zinc loss of MnZn ferrite and the particle temperature can complement our understanding of the thermodynamics and kinetics of such reactions. Figure 3-4 is an example of a second-order process map of plasma sprayed yittria-stablized zirconia (YSZ) for thermal barrier coating (TBC) applications.

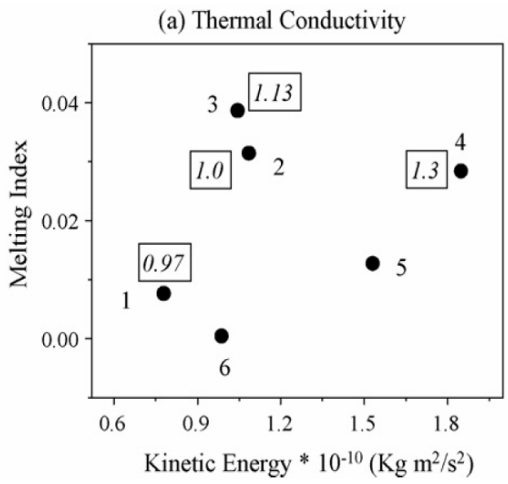

Figure 3-4, an illustration of second-order process map. Through-thickness thermal conductivity of plasma sprayed YSZ coating in the MI-KE (kinetic energy) space.

3.4.2. The introduction of dimensionless numbers of Melting Index and Reynolds number into ferrite process maps

The particle temperature measured from pyrometric sensors only provides access to the particle surface temperature instead of information on the bulk temperature of an entire particle. Most sensors measure temperature at a given location and does not take into account the in-flight time for a traveling particle. To more accurately assess the melting status of ferrite, a dimensionless number, *Melting Index* (M.I.) is proposed. The concept of melting index was first introduced by Vaidya et al [114], to describe the molten state of a given particle by normalizing the measured surface temperature with the dwell time and size. In its simplest rendition this is assessed as:

$$M.I. = \frac{T\Delta t_{fly}}{D} \qquad \text{(Equation 3-1)}$$

where T is the measured particle surface temperature, D is the particle size, and ΔT_{fly} is the particle in-flight time which is estimated as:

$$\Delta t_{fly} = \frac{2L}{V} \qquad \text{(Equation 3-2)}$$

by assuming that the molten particles are traveling with a constant acceleration. Here L is the spray distance and V is the particle velocity. Since this equation does not contain information of a material's melting point and other properties, it does not reveal whether or when a particle will start to melt. Zhang et. al. [115] significantly enhanced the scientific description of melting index through the thermal resistance and energy balance analysis. They define M.I. as the ratio of particle residence time in the flame, ΔT_{fly} , to the total melting time (the total time needed to melt the particle), ΔT_{melt} , as

$$M.I. = \frac{\Delta t_{fly}}{\Delta t_{melt}} = \frac{24k}{\rho h_{fg}} \cdot \frac{1}{1+4/Bi} \cdot \frac{(T_f - T_m) \cdot \Delta t_{fly}}{D^2} \quad \text{(Equation 3-3)}$$

where k is the thermal conductivity, ρ is the density of the material in liquid state, , h_{fg} is the enthalpy of fusion, and T_f is the flame temperature near the in-flight particle, T_m is the melting point of the material, D is the particle size, and Bi is the Biot number, defined as:

$$Bi = \frac{hL_c}{k} \quad \text{(Equation 3-4)}$$

Where h is the heat transfer coefficient and L_c is the characteristic length which is commonly defined as the volume of the body divided by the surface area of the body. h is usually assumed to be 1500 W/m^2•K for all powders in thermal spraying. The newly defined M.I. is dimensionless therefore allowing for cross-comparison of melting state among a range of materials. From this equation, it can be seen that, if the flame temperature is higher than the melting point of the material, the particle begins to melt and a positive M.I. will be obtained. A M.I. value of 1 means that the in-flight time equals to the time needed for fully melting.

Similar to M.I., Vaidya et al [116] also used particle *Reynolds number* as another nondimensional parameter for describing the kinetic state of a particle.

$$\mathrm{Re} = \frac{\rho v D}{\mu} \quad \text{(Equation 3-5)}$$

Where v and μ are the velocity and the fluid viscosity of molten droplets.

It has been shown both experimentally and theoretically that Re has significant effect on particle impact, spreading and splat formation during thermal spray due to the fact that the parameter considers both the particle in-flight status and the material properties essential to droplet impact and splat flattening [117] [118-121]. This number is dimensionless and non-material-specific, therefore it is a powerful approach to compare among multiple materials and processes. It does, however, require knowledge or estimation of material viscosity in the melting state, which can be obtained from handbooks and open publications. Deposition efficiency (DE) and splat and coating qualities are significantly affected by molten status. It is essential to represent particle status at impact using the material viscosity in the molten state due to the fact that the studied object in this case is the molten particles, i.e. the fluid that is moving with a certain speed.

In this dissertation research, we will seek to use these dimensionless numbers that characterize the melting status and kinetic energy to understand the processing effects on coating microstructures and properties.

Chapter 4 Experiments

In this chapter, the experimental techniques used in the composite studies are discussed. A brief description of the physical principle is given, together with details of actual experimental procedure.

4.1. Thermally sprayable powder

As stated in chapter 2, the particle size greatly affects the particle velocity and temperature, the degree of zinc loss (for MnZn ferrite) as well as the splat morphology. Usually fine particles result in dense coating while coarse particles result in porous coating. However, if the particles are too fine, the surface tension as well as the magnetostatic force will result in sticky powder which will tend to clog the powder feeder or the feed line. Therefore, particle size needs to be carefully selected.

Two kinds of Co ferrite powder were used in this study; one is spray dried stoichiometric $CoFe_2O_4$ powder (Inframat Advanced Materials, Willington, CT), the other was prepared by sintering chemically co-precipitated Co-Fe hydroxides. The co-precipitated Co ferrite powder is nonstoichimetric due to the phase segregation during precipitation. The synthesis of $CoFe_2O_4$ powder will be briefly discussed in the following section.

In the study of MZF-NiFe composite, the MnZn ferrite (MZF) powder with average composition of $Mn_{0.52}Zn_{0.48}Fe_2O_4$ (Steward Ferrite FLP1510, Steward Corp. Chattanooga, TN) was mixed with $Ni_{80}Fe_{20}$ powder according to designated volumetric percentage.

While in constructing the process map and making MnZn ferrite-NiCo composites, MnZn ferrite powder with average composition of $Mn_{0.50}Zn_{0.51}Fe_{1.99}O_4$ (Steward Ferrite FLP17035-1) was used. NiCo powder is of composition $Ni_{80}Co_{20}$ (Praxair Surface Technology, Indianapolis, IN).

4.1.1. Synthesis of Co Ferrite by co-precipitation

Calculated quantities of $Co(NO_3)_2 \cdot 6H_2O$ (Cobalt nitrate hexahydrate) and $Fe(NO_3)_3 \cdot 9H_2O$ (Iron nitrate nonahydrate) were weighted and dissolved in pure water separately. Then the nitrate solutions were mixed together. Magnetic stirrer was used to enhance mixing during the dissolving and mixing process to ensure the formation of homogeneous solution. Ammonium hydroxide was slowly added into the solution to form brownish precipitates. During precipitation, the pH value of the solution was monitored by checking the pH value using pH paper in a short interval. The pH value was maintained at 11 during the precipitation process. During filtration, the precipitated gel was washed several times to remove ammonium nitrate residuals. The gel was collected and dried in an oven in a fume hood at 150°C. The raw dried powder was black.

Thermal analysis on the dried raw powder showed that from 100 to 200°C, the main reaction was associated with hydrate evaporation, from 200 to 600°C; the main reaction was mainly about the decomposition of ammonium nitrate. Spinel ferrite started to form above 600°C. X-ray diffraction study showed that powders calcined at temperature below 1100°C were mixtures of spinel and hematite (Fe_2O_3), powder calcined above 1100°C showed monophase of spinel. So the dried raw powder was finally calcined at 1100°C for 10 hours to form homogeneous spinel powder. The calcined powder was ground to some degree to get particle size suited for plasma spray. The powder synthesis will be given a more detailed description and discussion in Chapter 6.

4.1.2. Powder characterization

The particle size distribution was measured by a Beckman Coulter particle size analyzer. This instrument employs techniques based on the concept that when a coherent source of light (such as a laser) with a known frequency is directed at the moving particles, the light is scattered at a different frequency [122]. The change in the scattered frequency is quite similar to the change in frequency or pitch one hears when an ambulance with its wailing siren approaches and finally passes. For the purposes of particle size measurement, the shift in light frequency is related to the size of the particles.

The particle size distributions of MnZn ferrite, Co ferrite are shown in Figure 4-1 to Figure 4-4.

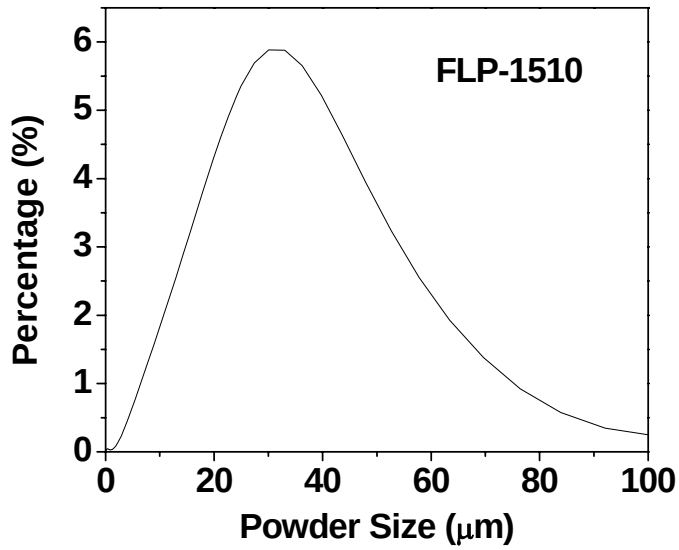

Figure 4-1, particle size distribution of MnZn ferrite FLP-1510.

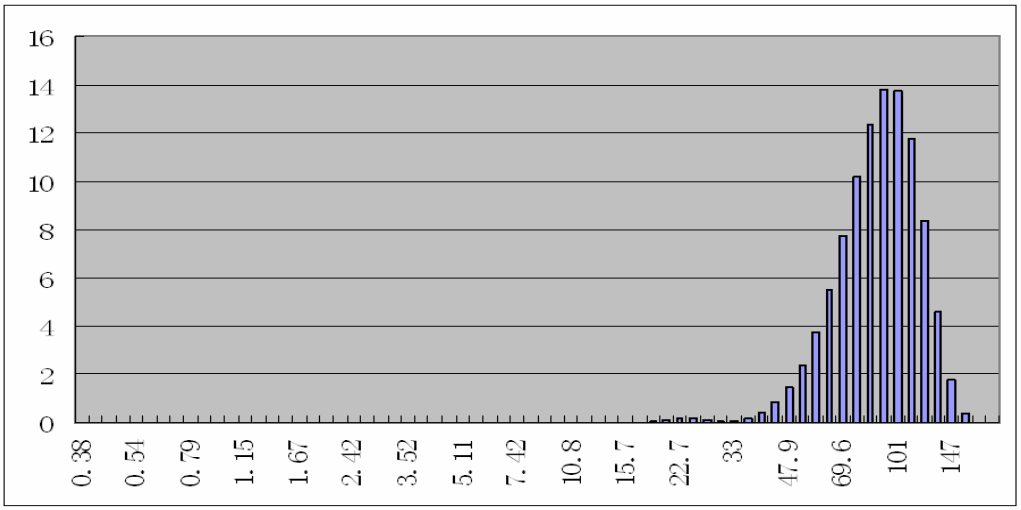

Figure 4-2, particle size distribution of MnZn ferrite 17469-1.

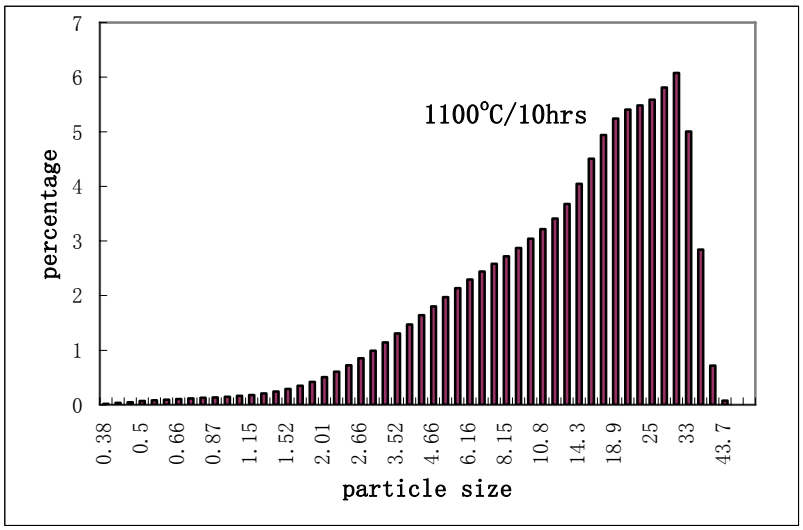

Figure 4-3, Particle size distribution for cobalt ferrite powder sintered in air at 1100°C for 10 hours followed by a lightly grinding using pestle and mortar.

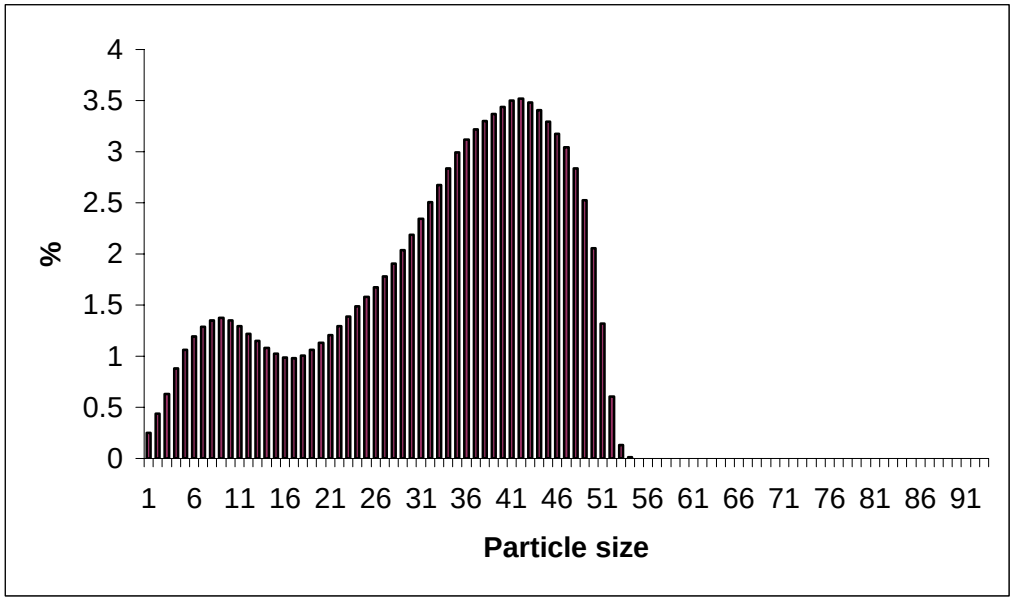

Figure 4-4, particle size distribution of Inframat spray dried Co ferrite.

4.2. Spraying process

4.2.1. Spray distance and substrates

In this study, the stand-off distance [123] (the distance between the nozzle and the substrates) were set to be in the range from 100 mm to 220 mm. Thus the substrate temperature is greatly reduced, which enable the choices of a variety of substrates, i.g. aluminum, stainless steel, alumina, PC board and magnesium/yttrium stabilized zirconia. Free-standing thick films can be made by peeling them off from metallic substrates. Ceramic insulating substrates are preferred during the fabrication of ferrite devices due to their high resistivity.

4.2.2. Power input and plasma gas component

During the deposition, the current and voltage are typically set to be 400 A~650 A and 50 V~77 V respectively depending on gun and plasma gas components. The power input is a critical issue that affects the particle temperature. Sufficient power is necessary to melt the injected powder [124], which enhances the bonding strength between substrate and sprayed film [125]. However, high power (high particle temperature) can cause oxygen loss, rapid quenching, and subsequent metastable phase, random cation distribution, cracking of the coating, etc. Normally, it is necessary to consider such factors as plasma gas components, the stand off distance and powder feeding rate to determine the values of currents and voltage. In spraying MZF-NiFe composites and co-precipitated Co ferrites, the stand-off distance is set up to be 120 mm and the plasma gas was a mixture of Ar:He:H_2=60:40:2 cm^3/min, the current and voltage was set to be 500 A and 72 V. In spraying MZF for process map study and making MZF-NiCo composites, the spraying system was set up as N_2 and H_2 as the

primary gases, while spraying spray dried Co ferrite; the primary gas was mixture of Argon and Hydrogen. The components of plasma gas were chosen by the availability of spray booth. The current were varied between 470 A and 620 A for plasma spraying process to study the relationship between gun current and particle temperature and velocity. In making MZF/NiCo composites, the set to be 470 A and 60 V, while in spraying spray-dried Co ferrite, the current and voltage were set to be 400 A and 56 V, the stand-off distances were both 120 mm.

4.2.3. Plasma Gun and diagnostic of spray process

The plasma guns used in this study were the Plasma Technik F4 and the Metco 7MB. The feeding rate in the deposition of the ferrite films was typically 16 g/min.

The in-flight particle characteristics including particle size, temperature and velocity, were examined by a Tecnar DPV 2000 Online Diagnostic System [126] and a Tecnar AccuraSPRAY sensor. The former system measures over 10,000 particles in a specified section of the plasma plume. The setup [127, 128] is a robust easy-to-use optical sensor allowing measurement of the particles' temperature prior to their impact by using a fast two-color pyrometer. The velocities are measured by a time-of-flight technique. An optical-fiber linear array, located in the same sensor head, is used to monitor the hot jet particles. The radiation from the hot particles is detected by a camera that permits the measurement of the orientation and width of the particle jet relative to the plasma gun.

4.3. Sample fabrication

4.3.1. Coating deposition

The gun was moved from left to right and up and down to cover the substrate area at a certain raster speed. The thickness of composite films were in the range of 100~300 μm after tens of cycles. Free-standing thick films were made by peeling the coatings off the substrate. Before spraying, the substrates were preheated by plasma plume without powder injection for a few cycles to increase the substrate temperature to about 200°C to ensure better adhesion between the coatings and the substrates. During spraying, the substrates were cooled by cooling air to enhance better heat dissipation, avoiding the overheating of substrates.

4.3.2. Splats collection

The substrate temperature greatly affects the morphology of splats. Increasing the substrate temperature to 200°C results in contiguous, disk shaped splats [129] while the splats deposited on cold substrates is highly splashed. Single splat samples can be made by reducing the powder feeding rate (1 or 2 rpm) and traversing the spray gun rapidly across the surface of the substrate. Substrates were attached to a substrate heater heated up to about 200 °C during the deposition of splats in order to get round-disk shaped, thickness-wise homogeneous splats.

4.3.3. Bulk sintered counterparts

To compare with plasma sprayed composites, MZF-NiCo bulk composites were also made from Steward Ferrite FLP17035-1 powder by conventional pressing and sintering technique. The hydraulic pressure for pressing is 1.5×10^5 psi. To avoid the oxidation of the metallic phase, the pressed pellet was sintered in nitrogen gas in a tube furnace. However, to minimize the deoxidation of MZF in low oxygen partial pressure at high temperature and oxidation/reduction reactions at the MZF/NiCo interface, the sintering temperature could not be very high. Therefore, a heat treatment temperature of 800°C was selected.

To compare with plasma sprayed Co ferrite, Co ferrite pellets was also made from Inframat spray dried powder by conventional pressing and sintering technique, using the same pressure. The sintering was done in air and the temperatures were 800°C and 1000°C.

4.4. Thermal analysis

The heat treatment temperature and duration of as-synthesized powder and as-deposited coating were examined by the Thermal Gravimetric Analysis (TGA), Differential Scanning Calorimetry (DSC) and Differential Thermal Analysis (DTA) carried out with a NETZSCH STA 449C system. Before each measurement, an empty crucible was used to obtain a correction file containing the background signal. The correction file is used after the measurements of the real samples to subtract the background signal.

To examine the phase transition temperature, a full temperature scan starting from room temperature to 1500°C, the highest capacity of the NETZSCH system, were carried out at 5°C or 10°C per minute. For ferrite coatings, the TGA results from full temperature scan will show a sharp mass change at some temperature ranges, so the annealing temperature will be selected at these temperatures.

4.5. Annealing

Annealing process of plasma-sprayed MnZn ferrite-NiFe composites, MnZn ferrites-NiCo composites as well as Co ferrite was carried out in air. In air annealing, temperature can vary from 300°C to 1500°C, in inert gas annealing, temperature can vary from 300°C to 900°C limited by quartz tube.

4.6. Structural characterization

4.6.1. Phase identification and compositional determination

4.6.1.1. X-ray diffraction

The atomic planes of a crystal cause an incident beam of X-rays (if wavelength is approximately the magnitude of the inter-atomic distance) to interfere with one another as they leave the crystal. The interaction of x-ray with the reciprocal lattices is governed by the Bragg Law [130]:

$$\lambda = 2d\sin\theta \qquad \text{(Equation 4-1)}$$

where λ is the wavelength of the x-ray, d is the spacing between the lattice planes and θ is the diffraction angle. The diffraction patterns can reveal the information about the crystal lattice. X-ray diffraction is a useful tool for materials characterization, allowing the

identification of phase and determination of phase content, grain size [131] and material stress(this will be discussed in GADDS/residual stress section) [132]. Although theoretically the information of cation distribution within the crystalline lattice can be examined by x-ray diffraction with Rietveld refinements [133], this procedure can not be performed on MnZn ferrites or Co ferrites because the atomic scattering factors for Mn, Fe, Zn, and Co are too similar. However, neutron-scattering lengths of these atoms are very different. Thus the site distribution of cations in plasma-sprayed MnZn ferrite films can be examined by neutron diffraction [134].

According to the sample sizes, geometry and the purpose of study, two x-ray machines have been used in this study: a SCINTAG/PAD-V diffractometer and a Bruker GADDS (General Area Detector Diffractometer system) micro-diffractometer. The SCINTAG/PAD-V diffractometer is suitable for the phase analysis of bulk materials. The x-ray beam in the Bruker GADDS system can be collimated to the range of 20~500μm. This type of diffractometer is suitable to examine the phases in small sized samples, e.g. a single splat. One more benefit of using GADDS is that it has multiple axis of rotation which allows the rotation of sample and hence the measurement of residual stress. SCINTAG/PAD-V system has a very good spatial resolution so it is good for structural refinement experiments. The voltage and current are 40 kV and 30 mA respectively in the operation of both x-ray instruments.

4.6.1.2. Diffraction analysis: Rietveld Refinements

General Structure Analysis System (GSAS) [135] was employed in the crystalline structure refinements on the neutron data. This program is produced by the Los Alamos National Laboratory. It can analyze powder diffraction data from a mixture of phases by refining structural parameters for each phase. It also can supply information about the molar or weight ratios of each phase, the cation distribution and the lattice constants of each phase. For examining the ordering of cation distribution within the crystalline lattice, the neutron diffraction works well for an interstitial site that is co-occupied by less than or equal to two elements, e.g. $CuFeS_2$ [136]. For an interstitial site that is co-occupied by more than three elements, it can not determine the site occupancy of each element without other information. Figure 4-5 ([134]) is an example of GSAS refinement of neutron diffraction or X-ray diffraction data, where the cross dots are the experimental data, fitted curve on the cross dots is the simulated result based on refined structural parameters, and the lower curve shows the standard deviation of the simulated result from the experimental data. The flatter the line, the better the refinement result.

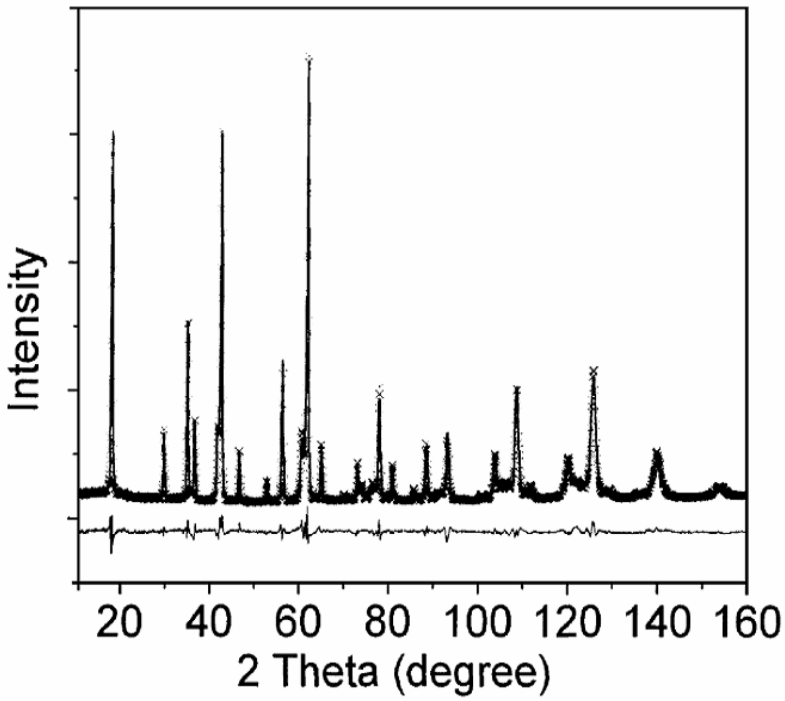

Figure 4-5, The neutron diffraction data of as-sprayed plasma-sprayed MnZn ferrites. The cross dots are the measured data and the solid line is the fit to the data. The difference line beneath the fitted data shows the excellence of agreement between the simulation and the data.

4.6.2. Microscopy: SEM and EDAX

The Scanning electron microscopy is defined as use of an electron microscope in which a finely focused electron beam is electrically or magnetically moved across the specimen; the reflected and emitted electron intensity is measured and displayed, sequentially building up an image with great depth of field. The microstructure of the cobalt ferrite and other materials were all examined by Scanning Electron Microscopy (LEO 1550 with a field emission gun). Observation of both cross-section and top view are carried out. Cross-section samples were prepared by polishing the coating mounted in epoxy. The electron energy is set to be 15 keV. In metallic-ceramic two phase mixtures, the two phases have very significant difference in average atomic weight, resulting in great contrast in backscattered electron images, therefore backscattered electrons were collected to construct the 3-D image of coating structure.

The composition of the ferrites has been analyzed by Energy Dispersive X-ray Spectroscopy (EDAX). The EDAX detector (JEOL JSM6400) is built into the SEM system. When the primary electron beam strikes the specimen, a number of different emissions and absorption processes may occur as is illustrated by Figure 4-6 [137]. Considering X-ray emission from the bombardment by electrons, there are two types of x-ray. One is a continuum or spread of wavelengths called white radiation or Bremsstrahlung, the other is a series of discrete wavelengths forming characteristic emission spectrum of that particular

element. The excited X-ray photons are collected by nearby solid-state detector and converted to voltage signals. Thus the peaks at energy characteristic of the specimen within the excitation volume can be identified and the concentrations of the specimen can be calculated. The diameter of the excitation volume depends on the atomic number of the elements and the electron energy, which is normally in the range of 0.1 μm to several microns.

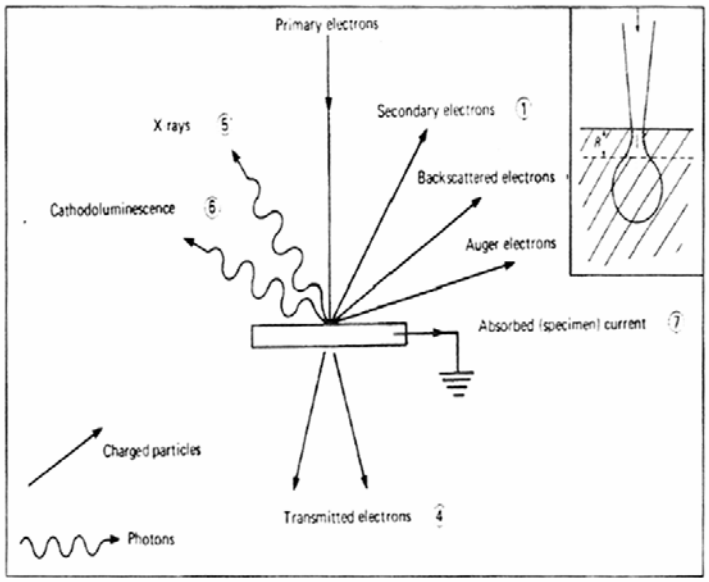

Figure 4-6, the different emission and absorption process occur when the primary electron beam strikes the specimen in the SEM, after reference [137]. The inlet illustrates the excitation volume.

4.6.3. Zygo 3D surface profilometer and splat mapping

The thickness of splats, typically less than 1 μm and the diameter of splats is typically around 20~120 μm. The three dimensional configuration of a single splat can't be imaged by macroscopic techniques. Therefore, a scanning white light interferometer (Zygo New View 200 non-contact surface profiler) [138] was used to characterize the three dimensional profile of splats. Scanning White Light Interferometry is a sophisticated and advanced microscopy in which light is split from a single source, transmitting one beam to a precise internal surface and the other to the sample. The reflected beams recombine inside the interferometer, resulting in optical path differences and producing a fringe pattern that is converted into a three dimensional (3-D) image by software.

After the 3-D image is obtained, the thickness can be obtained from the cross-section images, as illustrated by the right part of Figure 4-7. Moreover, the volume of the splat can be determined by the following procedures: (1) Choose three points on the substrate to determine a reference plane. (2) Determine a mask area within which all the volume above the reference plane will be integrated into the sample volume (the volume of the splats).

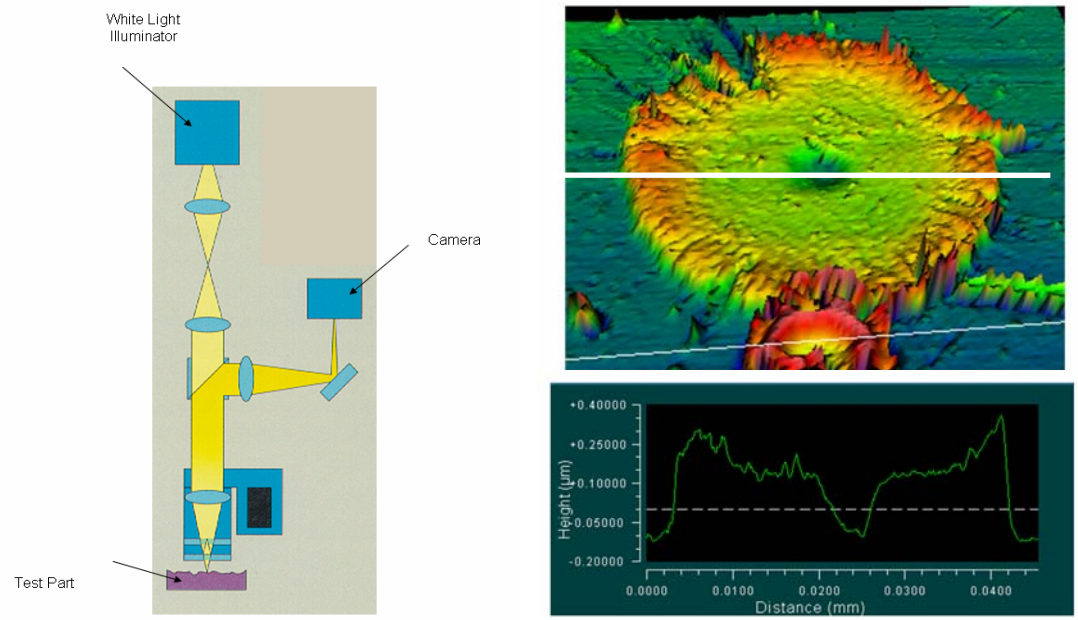

Figure 4-7, left, schematic diagram of a Zygo New View 200 non-contact surface profiler; upper right, a 3-D Ni splat under Zygo profiler; lower right, a 2-D vertical profile of Ni splat when draw a line (as indicated by the white line in the upper right image) on the 3-D profile.

4.7. Composition study and Image analysis

Due to different deposition efficiency resulted from difference in particle size, density, degree of wetting on the substrate, etc., the composition of the final deposit can deviate from the initial design. To determine the volume percentage of the two phase mixture, two techniques are used in this study, one is X-ray analysis in which the peak intensities of the two phases can be used to calculate the composition of the mixture, and the other is image analysis. Under optical microscope, metallic phase is more conductive and reflects more light so it looks brighter than the ceramic phase. In SEM backscattering images, since the average molecular weight of metallic phase is smaller than that of ferrite phase, therefore, it absorbs fewer electrons resulting in brighter images. In both cases, the two phases have brightness contrast in their microscopic images. Using image tools, we can separate the two phases and count the area of the two phases as well as the pores. Assuming the area ratio is equal to volume ratio by taking statistically enough sampling, we can exactly determine the true volume fraction of the composites as well as their porosities.

4.8. Magnetic characterization by VSM

The hysteresis loops of the composites at ambient temperature were measured by using a vibrating sample magnetometer (***VSM, DMS model 880***). As shown by Figure 4-8, the magnetic field is provided by iron core electromagnet, which can generate field up to 10,000 Oe. The samples are normally cut into 5mm by 5mm shapes and are mounted onto a high purity quartz glass rod. The glass rod is vibrating vertically at a preset frequency (75 Hz).

The applied magnetic field can magnetize the samples. A pair of sensing coils are placed close to the samples. The change of the magnetic flux within the sensing coils due to vibration of the samples induces a voltage in the sensing coils. This induced voltage is then fed into a lock-in amplifier together with a reference signal of sample vibrating frequency. The amplitude of output signal from the lock-in amplifier is proportional to the magnetization of the measured samples.

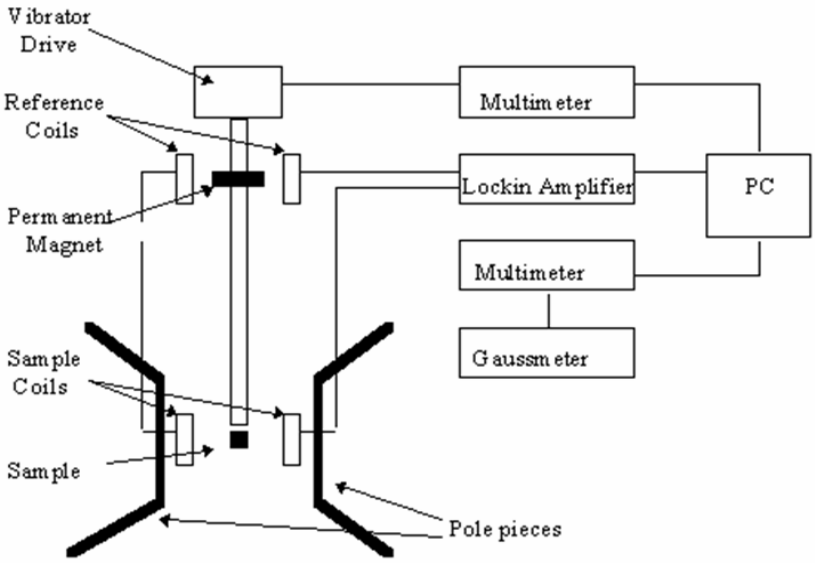

Figure 4-8, schematic of VSM.

The VSM system needs to be calibrated with a standard sample, e.g. Ni, with known magnetic moment. The ratio between the measured saturation magnetization of this Ni standard and the labeled saturation magnetization value can be calculated and noted down. The ratio is used to multiply the measured magnetization values of other samples.

4.9. Exchange coupling study and SQUID measurements

The exchange coupling studies is usually done by measuring the hysteresis loops of the two phase mixture after being cooled in the presence of magnetic field. In this study, the magnetic measurements in low temperature were carried out in a Superconducting Quantum Interference Device (SQUID, ***Quantum Design MPMS***) due to its capability in providing a wide range of measuring temperature (from 400K to 1.8K) and a higher magnetic field (5 Telsa) compared to VSM DMS 880.

Although, in this study, the SQUID was used due to its capability in low temperature and high magnetic field measurements, it is more famous for its capability in measuring extremely low magnetic moments. The SQUID consists of two superconductors separated by thin insulating layers to form two parallel Josephson junctions [139]. The great sensitivity of the SQUID devices is associated with measuring changes in magnetic field associated with one flux quantum. One of the discoveries associated with Josephson junctions is that flux is quantized in units

$$\Phi_0 = \frac{2\pi\hbar}{2e} = 2.0678\times10^{-15} Tesla\cdot m^2$$

(Equation 4-2)

If a constant biasing current is maintained in the SQUID device, the measured voltage oscillates with the changes in phase at the two junctions, which depends upon the change in the magnetic flux. Counting the oscillations allows the evaluation of the flux change which has occurred. The schematic of SQUID is shown in Figure 4-9.

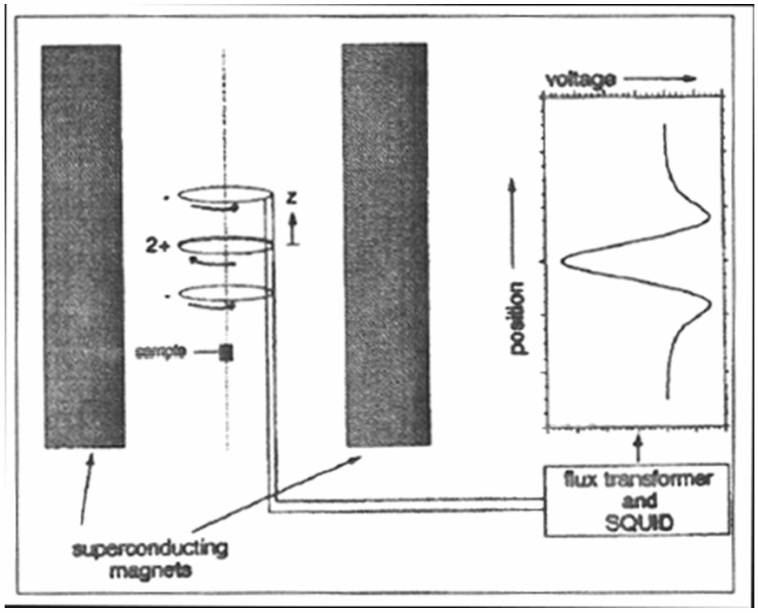

Figure 4-9, schematic of SQUID.

4.10. Electrical characterization

Electrical resistivity of ferrite coatings and splats were measured using four-point-probe method. Four point contacts can eliminate the effects of contact resistance resulting in a more accurate measurement.

Figure 4-10 shows a common setup of four-point-probe measurement, the four probes are equally spaces, i.e. $S_1=S_2=S_3$, a constant current flows through contact A and D, the voltage drop between contact B and C is measured by a digital voltmeter. The resistance of the sample between probes B and C is the ratio of the voltage registering on the digital voltmeter to the value of the output current of the power supply. The high impedance of the digital voltmeter minimizes the current flow through the portion of the circuit comprising the voltmeter. Thus, since there is no potential drop across the contact resistance associated with probes B and C, only the resistance associated with the samples between probes B and C is measured. Then the resistivity of thin film is given by:

$$\rho = \frac{\pi W}{\ln 2}\frac{V}{I},$$

Here W is the thickness of thin film, V and I are the voltage drop and current between contacts B and C.

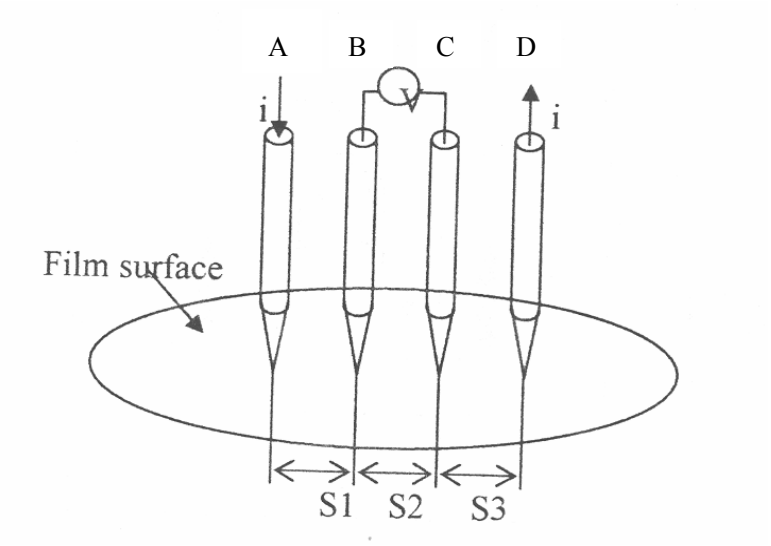

Figure 4-10, Diagram of a four probe system. Electrodes A and D are for flowing current, a voltage drop is measured between electrodes B and C.

But a more general measurement is the Van der Pauw method (shown in Figure 4-11), where the thin film can be treated as a semi-infinite 2-dimensional substance. A, B, C, D are four contacts on the thin film, the resistance R_{ABCD} is the defined as voltage measured between A and B divided by the current measure between C and D.

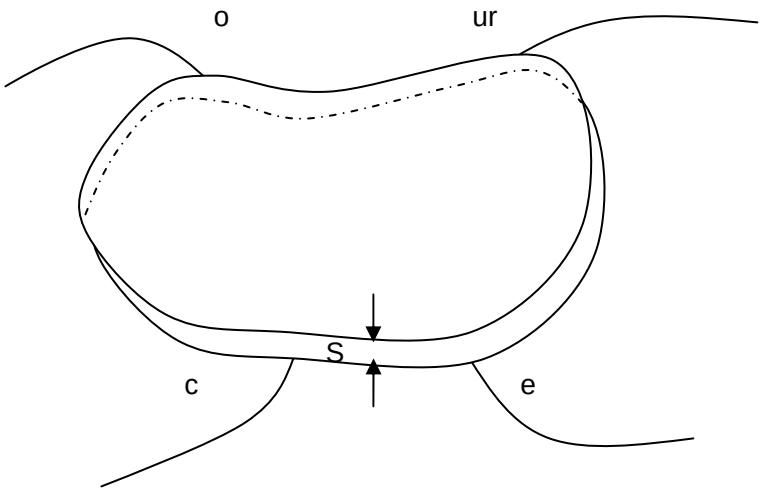

Figure 4-11, uniform plane lamella with line contacts on its edges presenting the ideal geometry for measuring resistivity by the "Van der Pauw" method.

The resistivity of thin film is derived to be

$$\rho = \frac{\pi W}{\ln 2}\{\frac{R_{ABCD} + R_{BCDA}}{2}\} f(\frac{R_{ABCD}}{R_{BCDA}}) \qquad \text{(Equation 4-3)}$$

here f is a function depends only on the ration $Q = \frac{R_{ABCD}}{R_{BCDA}}$.

The sheet resistance of the ferrite films has been measured by (1) a FPP-5000 four point probe system, and (2) a homemade testing circuit automated by a LabView program. In this circuit, a constant current source, Keithley 238 or Keithley 224, is used to provide current ranging from 1pA (in the case of Keithley 238) or 5nA (in the case of Keithley 224) up to 100mA, an HP34401 digital multimeter is used to measure the voltage drop. The FPP-5000 system utilizes a probe-up configuration, which assures repeatable probe pressure in each test. Its digital computation allows the direct display of sheet resistance in Ω/square from 1.1 mΩ/square to 450 kΩ/square. The homemade testing setup can measure beyond the lower and upper limit of the FPP-5000 system. The thickness of the ferrite films can be measured independently by a micrometer. Thus the sheet resistance of the ferrite films can be converted into resistivity as

$$\rho = R_s W = \frac{\pi W}{\ln 2} \cdot \frac{V}{I} \qquad \text{(Equation 4-4)}$$

where R_s is the measured sheet resistance.

4.11. Impedance measurements

The impedance is the total opposition by a circuit to the alternating current flow. It is a vector sum of all resistance, capacitance and inductance in a circuit, with a unit in ohms. The impedances of the ferrite films were measured by a impedance network analyzer [140]. Figure 4-12 shows the circuit diagram of the Auto-Balancing-Bridge method. In order to perform precise impedance measurements, the voltage applied to the devices under test (DUT), and the current, which flows through the DUT, need to be accurately measured. The voltage applied to the DUT is detected as "V_1" at the High-Potential (Hp) terminal of the instrument. The terminal is isolated from the High-Current (Hc) terminal, which is a signal output terminal. This isolation enables accurate detection of the voltage applied to the DUT. The current, which flows through the DUT, goes to the Low-Current (L_c) terminal. The Low terminal is kept near the voltage level of ground. This is called a "Virtual Ground", and it is functionally dependent on a feedback loop. The feedback loop is called a "null-loop" amplifier. This circuit maintains the virtual ground at the L_p terminal, and pulls the current to a range resistor. By detecting the voltage of the range resistors, the current, which flows through the DUT, is measured. Impedance analyzers usually have several range resistors in order to achieve high-resolution for various current measurements. By detecting the voltage of the range resistors, the current, which flows through the DUT, is measured. Impedance analyzers usually have several range resistors in order to achieve high-

resolution for various current measurements.

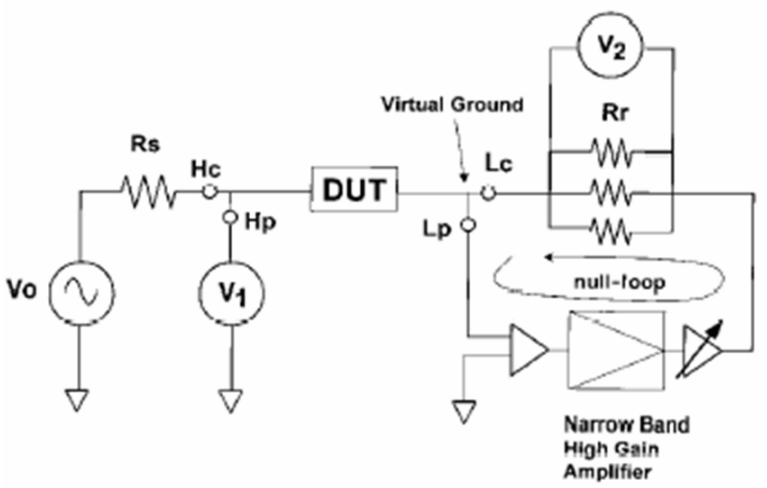

Figure 4-12, schematic of an Impedance Analyzer.

Two types of measurements are carried out on the composite films: (1) the permeability and (2) the complex impedance curves.

In the inductance measurements, a closed loop inductor was made by drilling a hole in the center of the sample and winding a few turns of insulating copper wire around it. The inductance is measured by connecting the two heads of the insulating copper wire in the frequency range of 40 Hz to 110 MHz. The permeability is calculated by the following equation:

$$L = \frac{\mu_0 \mu N^2 A}{l} \quad [141] \qquad \text{(Equation 4-5)}$$

Since the energy loss can not be measured directly due to lack of facilities, the Q factor is measured as an indirect parameter to judge the power loss. The Q factor is defined as:

$$Q = \frac{\text{Energy}_{\text{stored}}}{\text{Energy}_{\text{loss}}} \quad [142] \qquad \text{(Equation 4-6)}$$

The impedance measurements have been conducted on freestanding composite films. Silver paint is applied on both surfaces to form electrodes. The effects of cables and wires for connection are carefully calibrated and subtracted. The impedance spectroscopy of the as-sprayed and annealed MZF samples is measured with an HP 4294A impedance analyzer in the frequency range from 40 Hz to 110 MHz.

4.12. Magnetostriction Measurements

The magnetostriction of the cobalt ferrite films was measured by (1) using the laser deflection method and (2) strain gage method.

In the cantilever technique, bimorph cantilever samples in rectangular shape, 3cm×2cm,

with ferrite films on nonmagnetic titanium substrates or aluminum substrates were subjected to a uniform magnetic field area produced by a pair an iron core electromagnet. The DC magnetic field is measured by a Bell gauss meter 7010. As the magnetic field increased, the magnetization of the ferrite films expanded/contracted, creating a stress on the substrates which caused the substrates and films to bend. The cantilever sample is clamped on one end and a He-Ne laser beam was reflected off of the free end. A UDT SLC-5D linear position sensor, 1.0 meters away from the cantilever samples, monitored the reflected beam position change and is capable of detecting beam displacement of 2 μm. The sensor output current is sent to a position-to-voltage converter, which produces an output voltage linearly proportional to the beam position that was measured using a HP 34401A digital multimeter. The meastturement is carried out at ambient temperature. Due to the limited space between the pole pieces of the electromagnet, the cantilever samples are fixed with their surfaces perpendicular to the applied DC field. The experimental setup is illustrated in Figure 4-13.

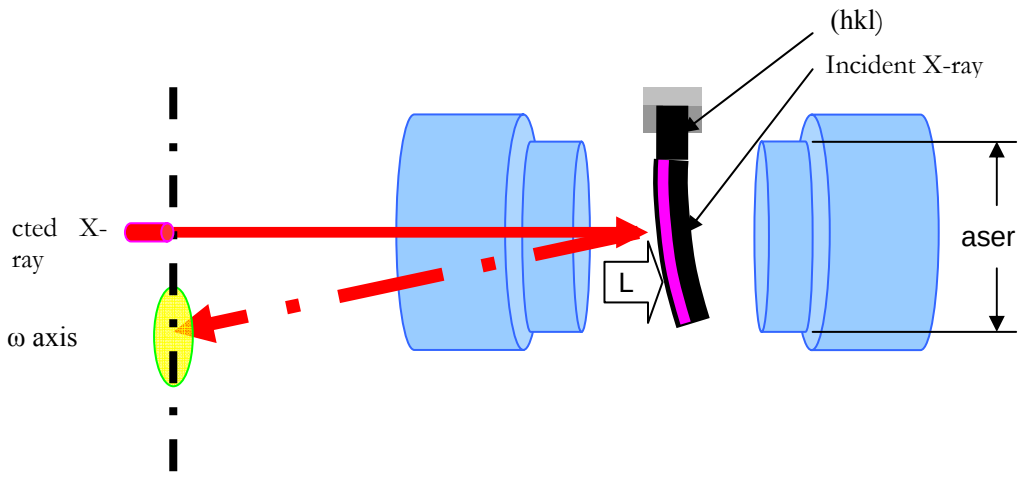

Figure 4-13, schematic of magnetostriction measurement setup.

The deflection of the sample, Y, is converted to the in-plane strain by using the Stoney equation:

$$e = \frac{Yt_s^2 E_s(1-\nu_f)}{2t_f L^2 E_f(1-\nu_s)} \text{ [11]} \qquad \text{(Equation 4-7)}$$

where t_s and t_f are the thickness of the substrate and film respectively, E_s and E_f are the modulus of the substrate and film respectively, ν_s and ν_f are the Poisson ratio of the substrate and film respectively, Y the defection of the sample at distance L from the clamped end. According to the formula: $e=\frac{3}{2}\lambda_s(\cos^2\theta-\frac{1}{3})$ [11], where λ_s is the saturation magnetostriction and e is the strain measured at an angle θ relative to the saturation magnetization direction, the strain measured in this experiment is the strain perpendicular to the direction of the magnetization with $\theta=90°$. Thus the saturation magnetostriction is deduced to be $\lambda_s=2e_\perp$.

The Stoney formula is deduced based on the assumption of infinite bilayer system is

free to curve without any constraint. However, in our experimental setup, the bilayer is finite with one end fixed across the surface [143-145]. Therefore, by minimizing the total energy of the system, the magneto-strain is more appropriately expressed as:

$$e = \frac{t_s^2}{t_f}\frac{Y}{L^2}\left[\frac{2}{3}\frac{E_s/(1-\upsilon_s)}{E_f/(1-\upsilon_f)}\frac{1}{1+\upsilon_s} + 4\frac{t_f}{t_s}\frac{1-\upsilon_f}{1+\upsilon_f}\right] \qquad \text{(Equation 4-8)}$$

The stain gage technique is often used to measure magnetostriction of bulk samples or free standing films. Stain gages are glued to the clean sample surface by suitable high temperature cement (e.g. polyimide adhesive, PLD 700, BLH Electronics), they can be used over a temperature range from liquid helium temperature to 670K [11]. The metal foil embedded inside plastic tape forms a serpentine pattern with elongated legs in the direction in which strain is to be measured. Metals with temperature insensitive coefficient ($\partial \ln R / \partial T$), such as certain NiCr alloys, are often used to make strain gages. When subjected to a uniaxial strain ε, the length of the metal foils are either elongated or shrunk, accompanying the shrinkage or enlargement of the cross sectional area for current flow, respectively, resulting in change in the electrical resistance of the metal foils. The change in resistance is related to the strain by the gage factor G by $\frac{\Delta R}{R} = G\varepsilon$. Metal foil strain gages typically have $G \approx 2.0$. Semiconductor strain gages can have gage factors of a few hundred, but their performance is strongly dependent on temperature. The resistance of metal foil changes not only from strain caused by the magnetostriction but also from the magnetoresistance of the metal foil under the testing magnetic field. Therefore, a similar strain gage or so called "dummy gage" is arranged parallel along active gage, but is not fixed to any surface, so that this dummy strain gage only measures the magnetoresistance effect of strain gage.

In our experiments, cantilever method is used to measure magnetostriction of as-sprayed coatings on nonmagnetic aluminum or titanium substrates. After annealing, the metallic substrates are partially oxidized and the mechanical properties such as elastic modulus have changed, therefore it is not appropriate to use the cantilever method to measure the magnetostriction of annealed coatings. Strain gage method can be used to measure the magnetostriction of both as-sprayed and annealed coatings, but this method is less accurate than the first one, due to the fact that the largest source of error comes from the bonding between the gage and the coating.

4.13. Magnetoresistance measurement

The resistances of MnZn ferrite/NiCo composites under magnetic field are measured by using a four-probe technique. Four copper wires are connected to the coating surface by silver epoxy and wired to the experimental setup for resistance measurement. Addition to the resistance measurement setup, magnetic field up to 3000 Oe is supplied by a water-cooled electromagnet. The measurements are carried out in three orientations: (1) parallel (//), in which the field is in the plane of the coating and parallel to the applied current, (2) traverse (⊤), in which the field is in plane while perpendicular to the current, (3) perpendicular (⊥), in which the field is perpendicular to plane and to the current.

4.14. Residual Stress Measurements

The stress level in these ferrite films is determined by means of x-ray diffraction, which is based on the measurements of changes in crystalline lattice spacing. From a set of lattice spacing in different orientations, an elastic strain tensor is constructed, which is then converted to a stress tensor using Hooke's law. The formula deduction starts from the Bragg law. Differentiating Bragg Law gives:

$$\frac{\Delta d}{d} = -\frac{\cot\theta \Delta 2\theta}{2} \qquad \text{(Equation 4-9)}$$

An angle ψ is defined as the angle between normal of the atomic plane of a crystal and the normal of the sample surface. The relationship between d and $\sin^2\psi$ is given by:

$$\frac{\Delta d}{d} = \frac{1+\nu}{E}\sigma \sin^2\psi \qquad \text{(Equation 4-10)}$$

where ν is the Poisson ratio of the material, E is the Young's modulus and σ is the stress. Combining equation 4-1 and 4-2, it becomes

$$\sigma = \frac{E \cdot \cot\theta}{2(1+\nu)\sin^2\psi}\Delta 2\theta$$

By measuring a set of values of $\Delta\theta$ vs. $\sin^2\psi$, the value of σ can be calculated. The technique is called "$\sin^2\psi$" method.

The assumptions have been made that the in-plane stress state is characteristic of the typical equi-biaxial stress state away from free edges, and stress in the direction perpendicular to the film surface is zero. The X-ray measurements are performed on a Bruker GADDS micro-diffractometer with Cu Kα radiation (as shown in Figure 4-14). The in-plane stress is estimated from the average of the stress measured at several points.

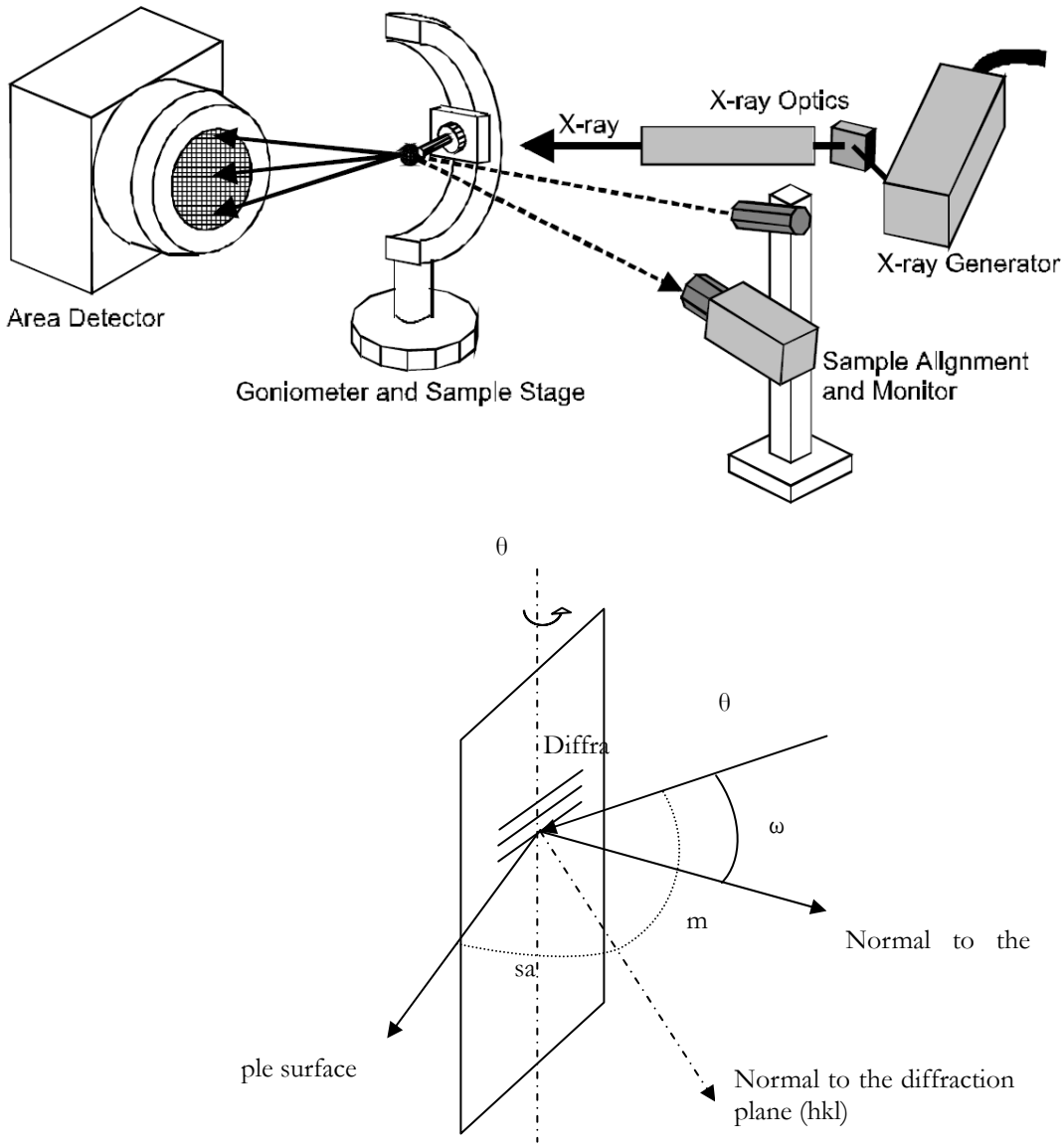

Figure 4-14, a schematic of GADDS system (upper part) and the relationship between the three angles: θ, ψ and ω (lower part).

Chapter 5 Composite design and percolation study

As the non-percolating composites are favored in the application of magnetic composites, understanding the percolation phenomenon and especially knowing the percolation threshold is critical for composite design. In this chapter, the relationship between composition and the electrical and magnetic properties of plasma sprayed composites will be studied. A physically based effective medium approximation model is proposed to understand the percolation phenomenon in plasma sprayed composites.

5.1. Percolation threshold in plasma sprayed magnetic ferrites

The in-plane electrical conductivities of the as-sprayed MnZn ferrite and NiFe composites are plotted in Figure 5-1. The electrical conductivities of these composites are very high (about 10^4 $\Omega^{-1}.m^{-1}$), suggesting that the compositions being studied are well above the percolation threshold. Figure 5-2 shows the cross-section MZF/permalloy composite films. It can be seen from Figure 5-2 (a) that the some of the Permalloy splats are connected to each other thus forming a conducting path for current. In this present study, the $Ni_{80}Fe_{20}$ volume fraction is above the percolation threshold. To increase the resistivity for application in the high frequency range, lower concentrations of Permalloy should be studied.

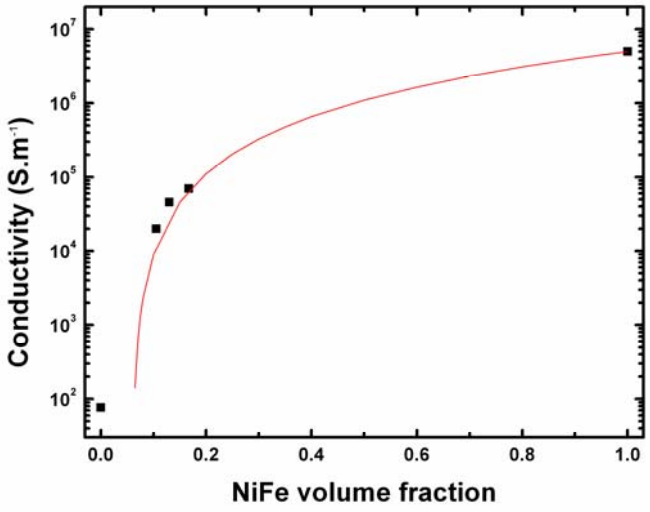

Figure 5-1, electrical resistivity of as-sprayed MnZn ferrite – NiFe composites vs. NiFe volume fraction. The solid line represents the effective conductivity calculated from equation I with NiFe volume fraction above the percolation threshold. The parameters ϕ_c, t used here are: 0.065 and 2.0.

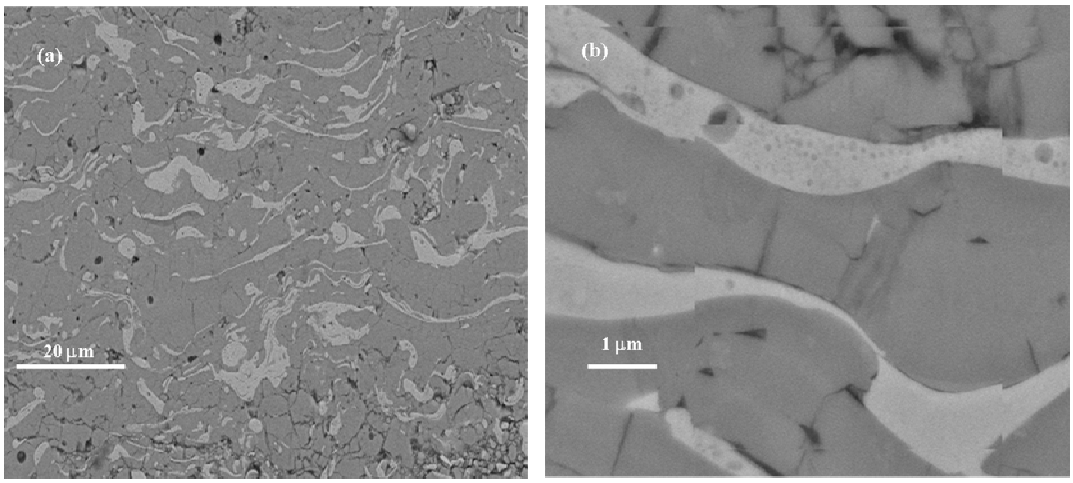

Figure 5-2, (a) and (b) SEM images of plasma sprayed MZF- 10 vol% permalloy composite.

Since the classical percolation equation is given as [57]:

$$\sigma_{eff} = \sigma_2 (\frac{\phi - \phi_c}{1 - \phi_c})^t, \phi > \phi_c$$

(Equation 5-1)

$$\sigma_{eff} = \sigma_1 (\frac{\phi_c - \phi}{\phi_c})^{-s}, \phi < \phi_c$$

where σ_{eff} is the effective conductivity of a two-phase composite, σ_1 and σ_2 are the conductivities of the insulator and conductor, respectively, ϕ is the volume fraction of the conductor. Three fitting parameters ϕ_c , s and t are percolation threshold, critical exponents characterizing the conductivity in the conducting region and insulating region, respectively [57]. It is believed that the critical exponents are universal and depend only on the dimensions of the problem [58]. The most widely accepted universal values of s and t in three dimension problems are s=0.87 and t=2.00 [57]. The percolation threshold ϕ_c can be calculated to be 6.5 vol% by fitting the experimental data, as illustrated by the solid line in Figure 5-1.

Figure 5-3 shows the electric conductivity of plasma sprayed MZF-NiCo coatings with various compositions. The conductivity changes about an order of magnitude in a narrow range from 3 vol% to 10 vol% of NiCo. This suggests that the percolation threshold of plasma sprayed metal-ferrite composite falls within this range. Using equation 5-I, the percolation threshold ϕ_c can be calculated to be 6.4 vol% by fitting the experimental data, as illustrated by the solid and dash lines in Figure 5-3.

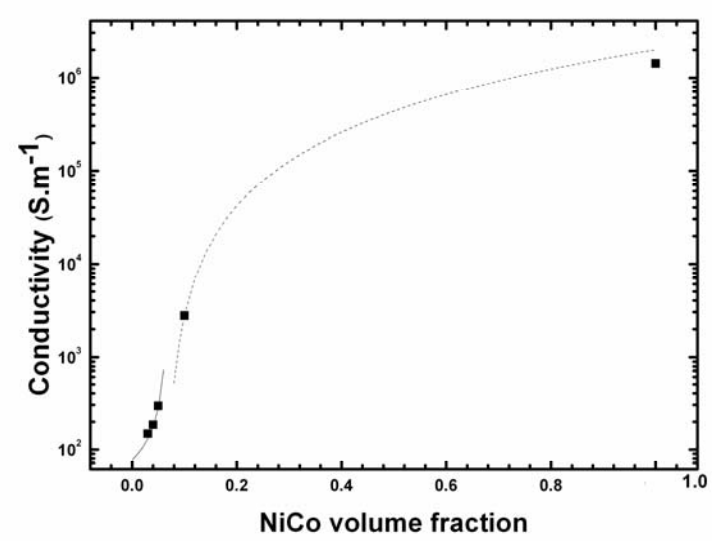

Figure 5-3, electrical conductivity of plasma sprayed MZF-NiCo composites as a function of NiCo volume fraction. The solid and dash lines represent the effective conductivity calculated from equation I with NiCo volume fraction below and above the percolation threshold, respectively. The parameters ϕ_c, s and t used here are: 0.064, 0.87, and 2.0.

Figure 5-4 shows the electrical conductivity of pressed-sintered MZF-NiCo composites with various compositions. The conductivity changes about two orders of magnitude in the range from 30 to 40 volume percent of NiCo. In sharp contrast to the 3% to 10vol% range for the plasma sprayed coatings, the percolation threshold ϕ_c can be calculated to be 33 vol% by fitting the experimental data, as illustrated by the solid and dash lines in Figure 5-4.

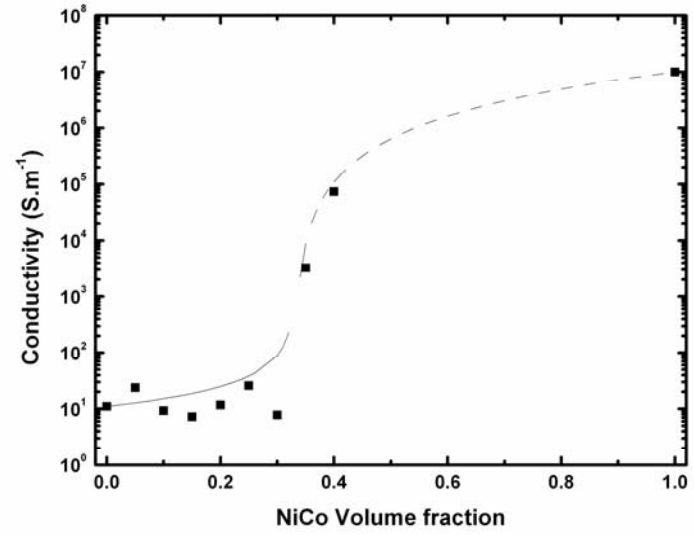

Figure 5-4, Electrical conductivity of pressed-sintered MZF-NiCo composites as a function of NiCo volume fraction. Solid line represents effective conductivity below percolation threshold, while the dash line represents effective conductivity above percolation threshold. The parameters ϕ_c, s and t used here are: 0.33, 0.87 and 2.0, respectively.

5.2. Effective medium approximation study

A thermal sprayed conductor-insulator composite coating can be considered as a network in which disk-shaped conductor splats randomly embedded into a matrix also made up by disk-shaped insulator splats, as illustrated by Figure 5-5 (a). The splats are highly oriented with the symmetric axis highly confined to the sprayed direction (Figure 5-5 (b)).

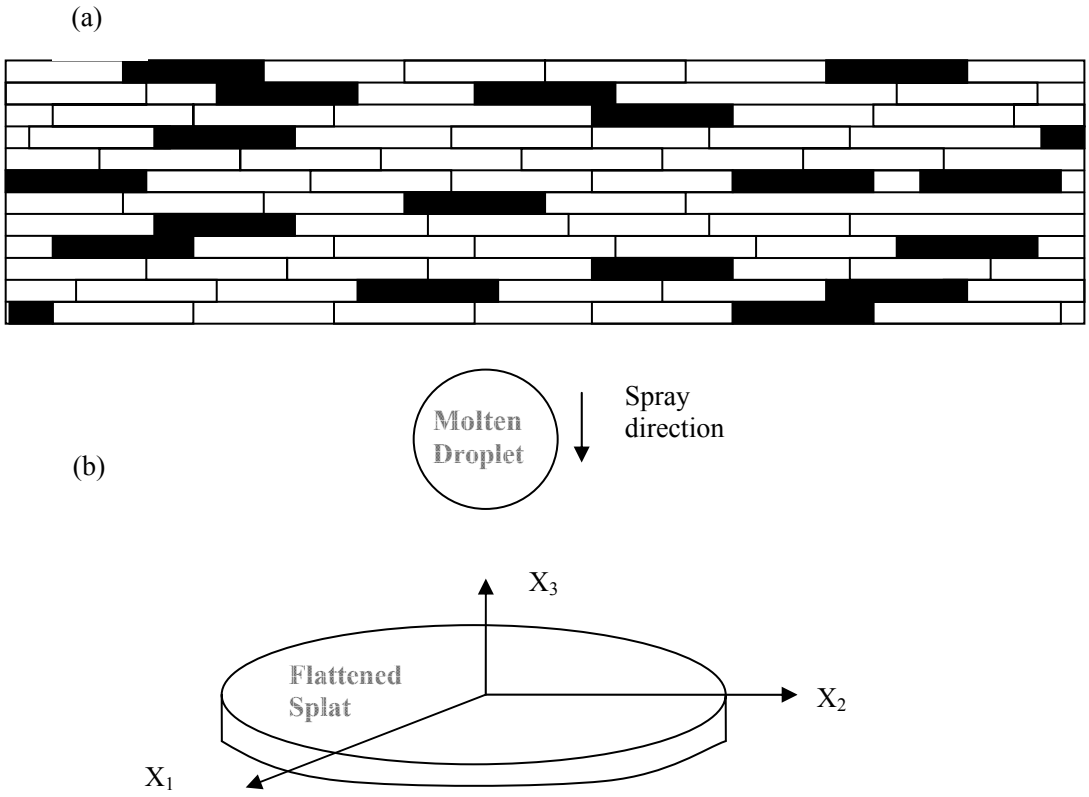

Figure 5-5, (a) An illustration of the cross sectional appearance of a thermal sprayed two phase network. The dark bricks represent the conductor fillers and the bright bricks represent insulator matrix. (b) The orientation of splats.

For simplicity, these disk-shaped splats can be modeled as ellipsoids. According to an effective medium model of a macroscopically anisotropic composite consisting of M different types of unidirectionally aligned isotropic ellipsoidal inclusions of the same shape,

an equation can be deduced as [62]:

$$\sum_{j=1}^{M} \phi_j (\sigma_j - \sigma_e) \cdot R^{(je)} = 0 \qquad \text{(Equation 5-2)}$$

Where

$$R^{(je)} = [I + A^* \cdot \sigma_e^{-1} \cdot (\sigma_j - \sigma_e)]^{-1}$$

The definitions of the parameters have been described in chapter 2 and are not repeated here. Using the conductivity data for bulk MZF and $Ni_{80}Co_{20}$, by solving equation 5-2, the effective conductivity can be expressed as a function of conductor volume fraction ϕ. Figure 5-6 (a) shows the calculated effective conductivity of a MZF-NiCo splats network as a function of the volume fraction of NiCo phase. The percolation threshold is about 6 vol% which is close to our experimental result. For the case of MZF-NiCo spheroid system, as shown by Figure 5-6 (b), the numerical model predicts 33 vol% for the percolation threshold, again, agreeing well with our experimental data.

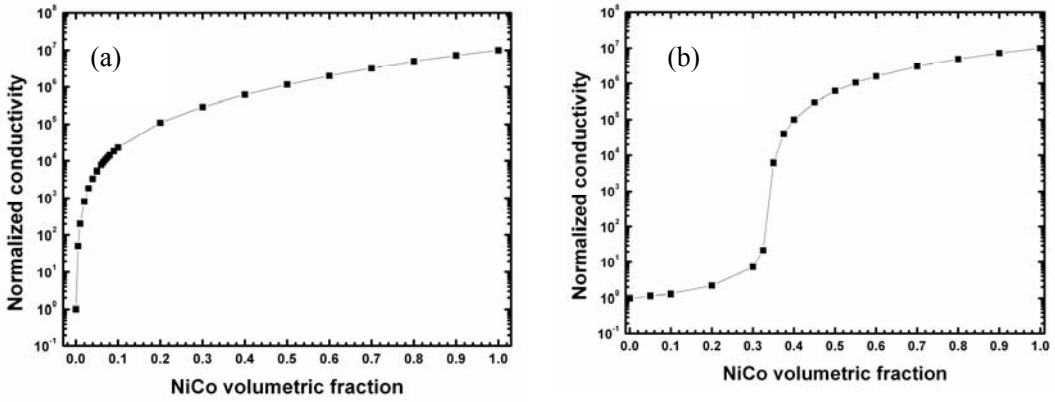

Figure 5-6, numerical models predicting the effective conductivity as a function of NiCo volumetric fraction in a MZF-NiCo splats network (a) and a MZF-NiCo spheroid network (b).

By calculating the effective conductivity as a function of metal volume fraction at a series of aspect ratio (Figure 5-7), we can calculate the percolation threshold as a function of aspect ratio (Figure 5-8). The aspect ratio can be related to splat flattening ratio by $A = 1.5FR^3$ (A is aspect ratio and FR is flattening ratio) by using the rule of conservation of volume (Figure 5-9). Therefore, we can predict the percolation threshold for different flattening ratios, as shown by Figure 5-10.

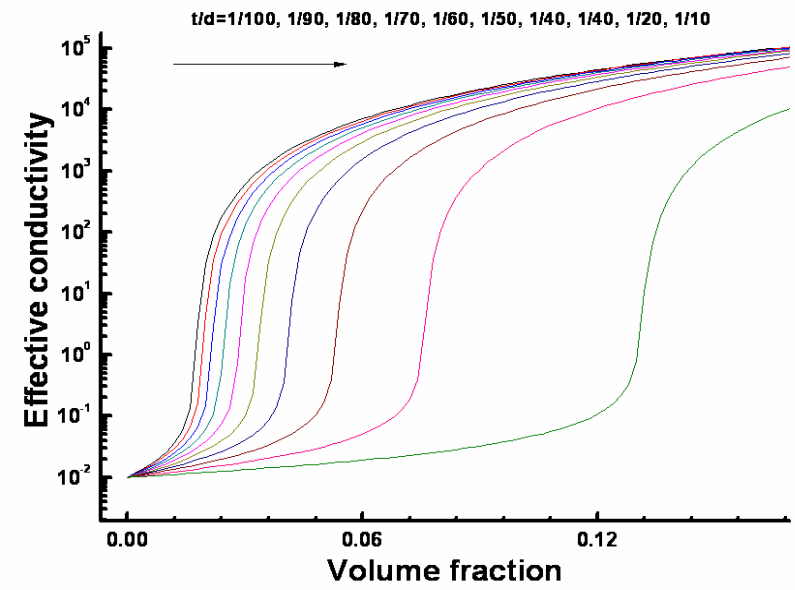

Figure 5-7, effective conductivity as a function of metal volume fractions at a number of aspect ratios.

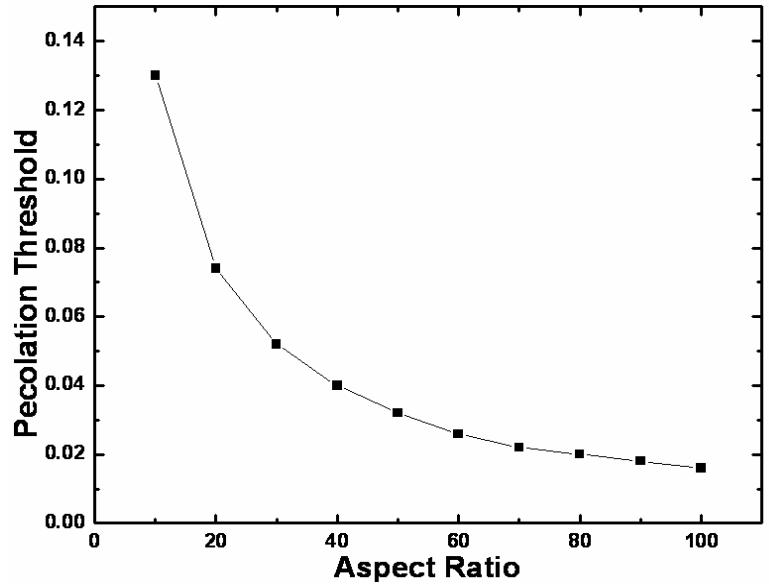

Figure 5-8, percolation thresholds as a function of aspect ratio.

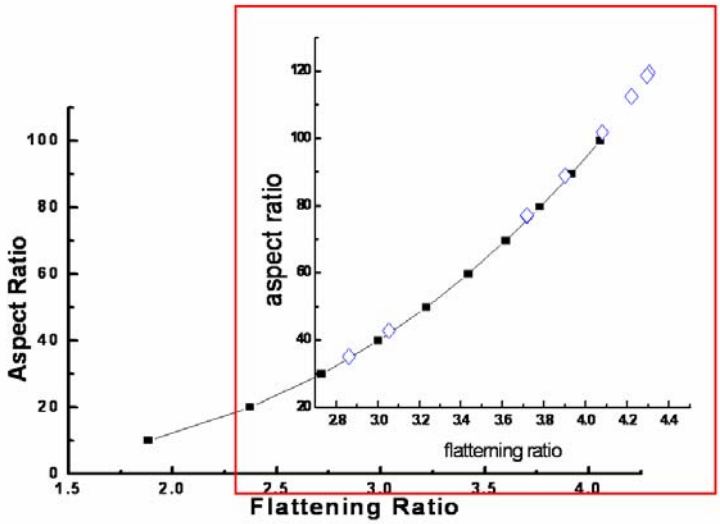

Figure 5-9, aspect ratio as a function of flattening ratio, the outer plot is obtained by calculation, the blue dots in the red inset are from splat data measured using Zygo profiler.

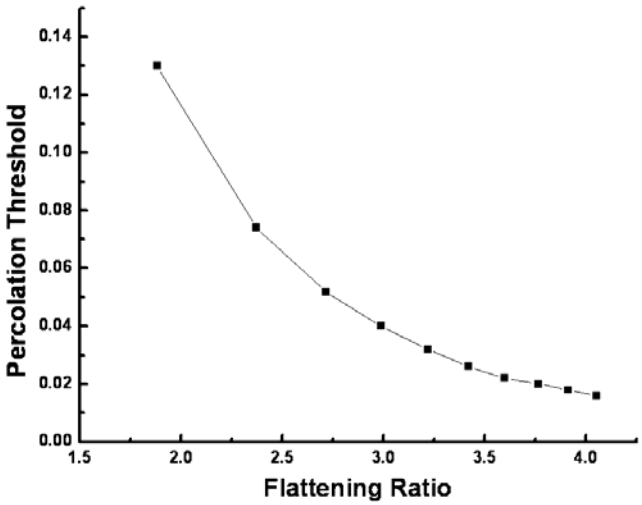

Figure 5-10, percolation threshold vs. flattening ratio.

To verify this model, we have made Al_2O_3-Ni composites by high velocity oxygen fuel (HVOF) spraying. In HVOF spraying, particles generally have high velocities (in this study, the typical velocity is about 800 m/s) and larger Reynolds number than plasma spraying, resulting in higher splat flattening ratio. The electrical conductivity of Al_2O_3-Ni composites has been measured in both in-plane and through-thickness directions and presented in Figure 5-11. In both directions, the percolation is taking place at about 5 vol% of Ni.

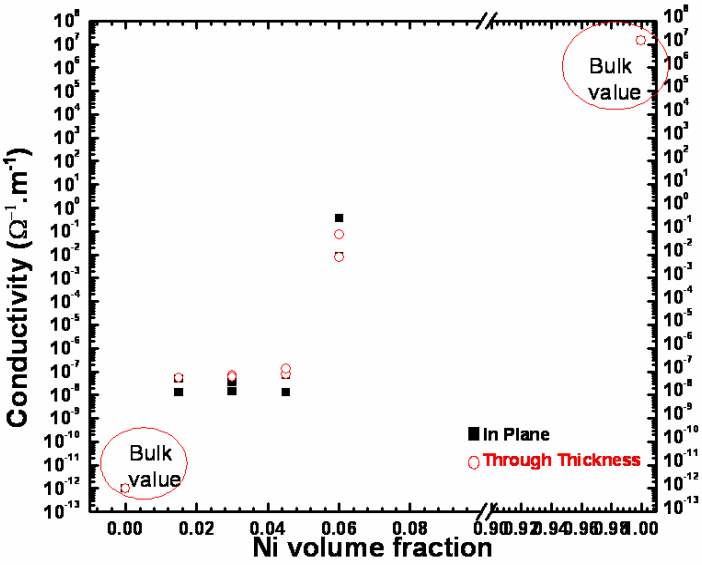

Figure 5-11, percolation threshold vs. flattening ratio.

The average flattening ratio of NiCo splats made by plasma spraying is determined to be 2.3, according to Figure 5-12, the percolation threshold is about 7 vol%. This value agrees well with our experiments. The flattening ratio of Ni splats made by HVOF spraying is determined to be 3.3, according to Figure 5-10, the percolation threshold should be 3 vol%. This prediction is smaller than our experimental data, suggesting the model can be improved. It is also possible that as the flattening ratio increases, the splat becomes thinner, and the contact between splats in in-plane direction becomes worse. However, the trend is correct that HVOF composites with larger flattening ratio have smaller percolation threshold than plasma sprayed composites which have smaller flattening ratio.

The electrical anisotropy $\frac{\rho_{TT}}{\rho_{IP}}$ (ρ_{TT} and ρ_{IP} are through-thickness and in-plane resistivity, respectively) is plotted against Ni volume fraction in Figure 5-12. It is observed that below percolation threshold, the anisotropy is smaller than 1, meaning that the coating is more resistive in in-plane direction; above percolation threshold, anisotropy is larger than 1, meaning the coating is more resistive in through-thickness direction. This is because the true contact area between splats are larger in through-thickness direction than in in-plane direction [111], the resistivity in through-thickness direction is smaller than in-plane direction. That is true when metallic phase is below percolation threshold. However, when metallic particles are connected above percolation threshold, they are connected hand-in-hand in the in-plane direction; electrons have to find a zigzag short circuit path when applied current perpendicular to plane direction, therefore, the through-thickness resistivity is larger than the in-plane resistivity.

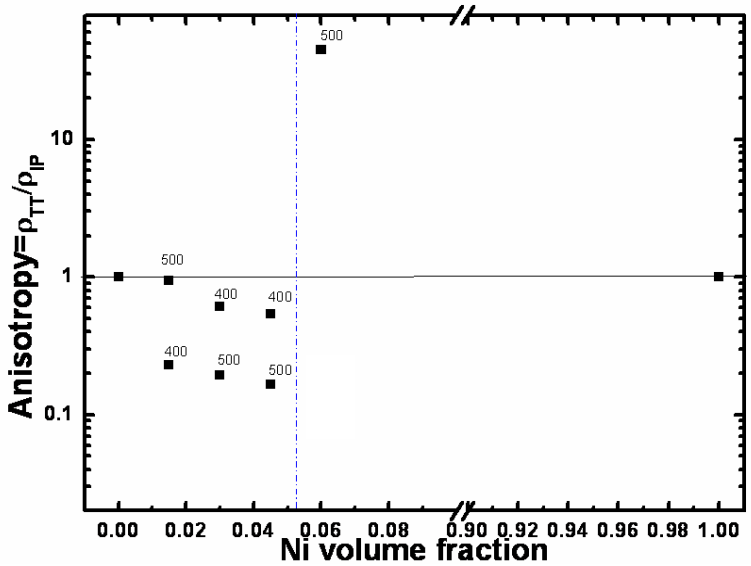

Figure 5-12, electrical anisotropy vs. Ni volume fraction. The horizontal line at 1 means isotropic.

5.3. Magnetoresistance transition across the percolation threshold

In the study of the magnetoresistance effect of the MZF-NiCo composite coatings and bulk counterparts, we found that the plasma sprayed MZF-NiCo coating with less than or equal to 5 vol% NiCo shows negative magnetoresistance in all three orientations, i.e. parallel, traverse and perpendicular directions, as illustrated in Figure 5-13 (a). This is a typical giant magnetoresistance (GMR) effect [46]. Plasma sprayed composite coatings with 10 vol% NiCo or more shows positive magnetoresistance in parallel orientation while negative magnetoresistance for traverse and perpendicular orientations (Figure 5-13 (b)). This is a typical anisotropic magnetoresistance (AMR) effect. For the pressed-sintered counterparts, composites with less than or equal to 30 vol% NiCo show GMR effect while above that composition show AMR effect. Figure 5-14 (a) and (b) shows the magnetoresistance of parallel orientation as a function of composition. Comparing to Figure 5-3 and Figure 5-4, it is found that the magnetoresistance changes signs across the percolation threshold, where below the percolation threshold, magnetoresistance is in the regime of GMR, above the percolation threshold, magnetoresistance is in the regime of AMR. To explain this GMR-AMR transition across the percolation threshold, we propose that the two distinctive magnetic phases contributes differently to magneto transport phenomenon. Since pure MZF shows GMR effect while pure NiCo shows AMR effect, it is believed that below the percolation threshold where the metallic NiCo phase regions are not connected to from a conductive path, the resistance and therein the magnetoresistance comes from the dominating MZF phase. When the NiCo phase percolates, the resistance comes from the NiCo phase, therefore the magnetoresistance is dominated by AMR effect. In this study, MZF shows weak GMR which is unusual. We speculate that the spins in the grain boundary are disordered while the spins in the grain cores are well aligned, therefore forming like a core-shell ferromagnetic-antiferromagnetic particle, analogous to surface spin disorder in ferrite nanoparticles [146, 147]. When magnetic field is applied, the disorder spins are forced

to align with the field direction, resulting in less electron-scattering in the ferromagnetic-antiferromagnetic interfaces and subsequently reduction in resistance.

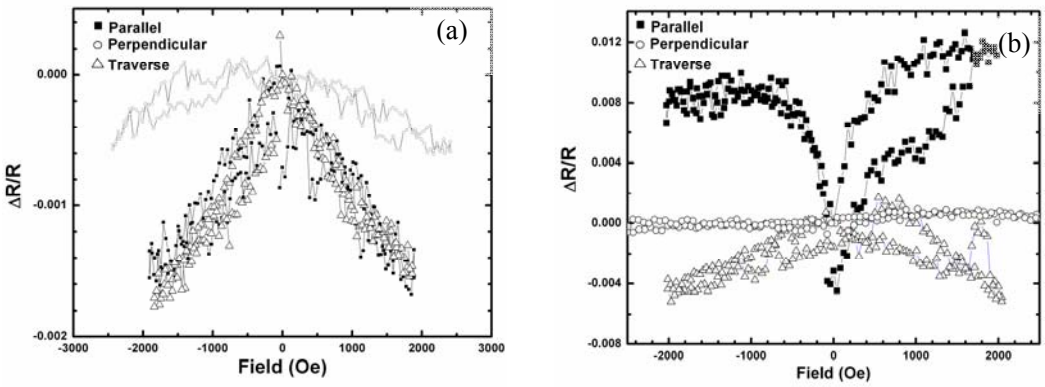

Figure 5-13, magnetoresistance of (a) as-sprayed 4 vol% NiCo-MZF coating, (b) as-sprayed NiCo coating.

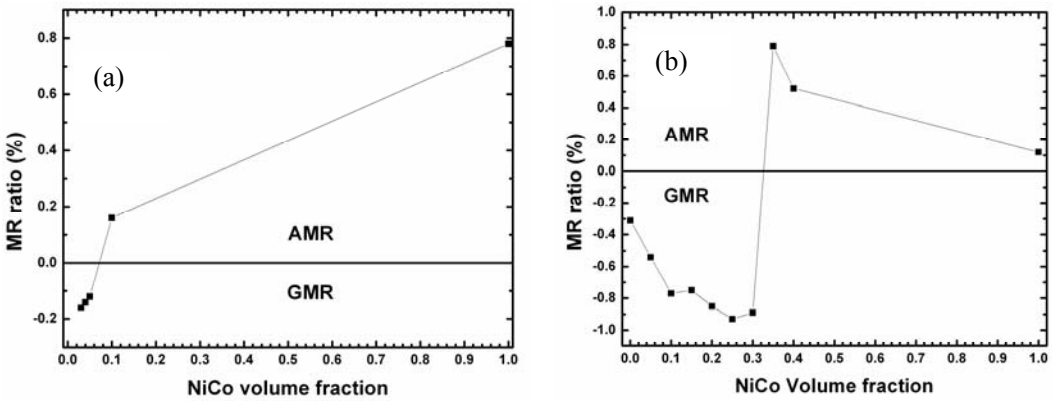

Figure 5-14, magnetoresistance under parallel orientation as a function of composition. (a) Plasma sprayed MZF-NiCo coatings, (b) pressed-sintered MZF-NiCo pellets.

Chapter 6 Properties of plasma sprayed magnetic composites

In this chapter, three types of magnetic ferrite/ ferrite composites are made by plasma spraying. Important issues including the formation of secondary phases, degradation of functional properties and properties improvement by annealing are given detailed discussion.

6.1. Plasma Sprayed MnZn ferrite-Permalloy Composites

6.1.1. Structural studies

The XRD patterns of the feedstock powder for spraying and MZF films (as-sprayed and annealed) are presented in Figure 6-1. The feedstock powder (pattern (a)) is spinel, FeO wuestite in the as-sprayed films (shown in pattern (b)) forms due to oxygen loss during spraying at high temperature, the wuestite phase is a metastable phase resulting form rapid quenching of the molten MZF droplet [80]. Since FeO wuestite is a metastable phase below 560°C [91], during annealing under this temperature in air, FeO dissociated into Fe and $FeFe_2O_4$ and Fe is oxidized to Fe_2O_3. In pattern (c), samples annealed in air at 400°C for 1 hour, peaks of MZF spinel and small peaks of FeO wuestite and small peaks of Fe_2O_3 hematite are present, the $FeFe_2O_4$ peaks overlap with those of MZF due to the same spinel structure, the absence of the peaks of Fe is due to the oxidation of Fe into Fe_2O_3. Annealing at 600°C (shown in pattern (d)) for 1 hour transforms the metastable FeO wuestite phase fully into $FeFe_2O_4$ magnetite and Fe_2O_3 hematite. Pattern (e) (sample heat treated at 1000°C for 1 hour but quenched) doesn't show too much difference in peak positions except that the intensity of the hematite peaks increases. However, when the MZF film is annealed in air at 1000°C for 1 hour and then slowly cooled down to room temperature (XRD pattern shown in pattern (f)), the Fe_2O_3 hematite peaks disappear and the MZF peaks are shifted to larger Bragg angles, which is a result of Fe_2O_3 going into MZF and changing the chemical composition as well as the lattice constant of the MZF. Calculation shows that the starting powder has a lattice constant of 8.410 Å and the lattice constants of the MZF phase in the as-sprayed, 400°C/1h annealed, 600°C/1h annealed and 1000°C/1h heat-treated then quenched samples are 8.420Å, while the lattice constant of the MZF phase in the 1000°C/1h annealed and slowly cooled samples is 8.320Å. The lattice constant of $FeFe_2O_4$, $ZnFe_2O_4$ and $MnFe_2O_4$ are 8.396Å, 8.441Å, and 8.499Å respectively [JCPDS 19-629, 22-1012, 10-0319]. It can be seen that the lattice constant increase from feedstock powder to as-sprayed coating can be attributed to the zinc loss during spraying and the formation of FeO wuestite [148]. The smaller lattice constant of slowly cooled MnZn ferrite is a result of the formation of solid solution of $FeFe_2O_4$, $ZnFe_2O_4$ and $MnFe_2O_4$.

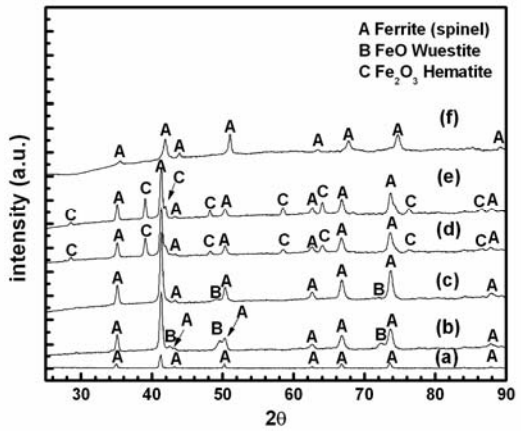

Figure 6-1, XRD patterns of MZF (a) feedstock powder, (b) as-sprayed coatings, (c)-(e) heat treated in air at 400°C, 600°C and 1000°C for 1 hour, quenched, respectively, (f) heat treated in air at 1000°C for 1 hour, slowly cooled.

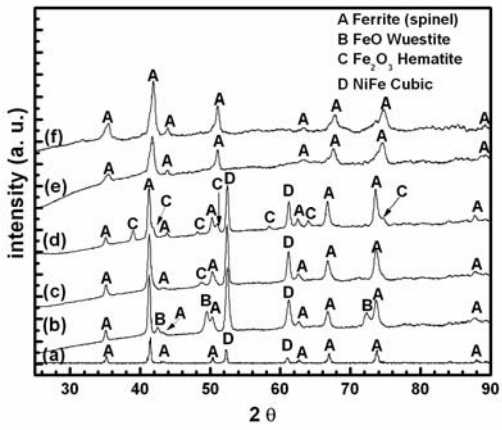

Figure 6-2, XRD patterns of MZF-20 wt%$Ni_{80}Fe_{20}$ (a) feedstock powder, (b) as-sprayed coatings, (c)-(e) heat treated in air at 400°C, 600°C and 1000°C for 1 hour, quenched, respectively, (f) heat treated in air at 1000°C for 1 hour, slowly cooled.

The XRD patterns of the feedstock powder for spraying and MZF/permalloy films with MZF:$Ni_{80}Fe_{20}$=0.8:0.2 (weight percentage) are presented in Figure 6-2. Similar to the MZF coatings, the as-sprayed coating (b) shows FeO wuestite peaks and FeO wuestite is transformed into Fe_2O_3 hematite after annealing in air at and below 600°C (pattern (c) and (d)). However, annealing at 1000°C for 1 hour doesn't shown any Fe_2O_3 hematite as in the MZF counterparts and the $Ni_{80}Fe_{20}$ peaks disappear upon annealing at 1000°C. The only peaks presents in the 1000°C/1h annealed films belong to the cubic spinel phase. This suggests that the $Ni_{80}Fe_{20}$ is oxidized into Ni ferrite with cubic spinel structure, and the Ni ferrite forms solid solution with MZF forming MnZnNi ferrite. The lattice constant of the cubic spinel phase changes from 8.410Å of starting powder to 8.420Å of the as-sprayed coating and remains about the same in 400°C/1h and 600°C/1h annealed coatings but decreases to 8.347Å of 1000°C/1h annealed, quenched coating and to 8.330Å of the 1000°C/1h annealed, slowly cooled coating. The increase of lattice constant in as-sprayed coating is due to the compositional change resulting from zinc loss and the formation of FeO [148]. The decrease of lattice constant in 1000°C annealed coatings is largely due to the formation of MnZnNi ferrite in which the Ni ferrite contributes a smaller lattice constant ($NiFe_2O_4$, a=8.338Å, [JCPDS 74-2081], $ZnFe_2O_4$, a=8.441Å, $MnFe_2O_4$, a=8.499Å [JCPDS 22-1012, 10-0319]).

6.1.2. Magnetic properties

Hysteresis loops of MZF and MZF/permalloy films before and after annealing were measured at room temperature. For comparison, feedstock powders are also characterized by VSM. Table 6-1 summarizes the corresponding values of saturation magnetization (M_s), in-plane coercivity ($H_c^{//}$) (magnetic field parallel to the in-plane direction), and through-thickness coercivity ($H_c^{\perp}$) (field perpendicular to the in-plane direction) for different samples.

Table 6-1, Magnetic properties of MnZn ferrite films and MnZn ferrite/$Ni_{80}Fe_{20}$ composite films, annealing conditions are air annealing.

Sample composition	Heat treatment condition	Ms (emu/g)	$H_C^{//}$ (Oe)	$H_C^{\perp}$ (Oe)	Heat treatment condition	Ms (emu/g)	$H_C^{//}$ (Oe)	$H_C^{\perp}$ (Oe)
MZF	Powder	64.3						
	As-sprayed	44.8	87.3	114.4				
	400°C/1h, quenched	65.8	87.0	100.1	400°C/1h, slowly cooled	77.8	76.0	101.9
	600°C/1h, quenched	65.1	50.8	62.5	600°C/1h, slowly cooled	60.8	45.5	54.2
	1000°C/1 h, quenched	14.1	5.0	7.5	1000°C/1h, slowly cooled	43.6	14.2	30.2
MZF/ 15 wt% Permalloy	Powder	66.1						
	As-sprayed	52.5	76.4	100.9				
	400°C/1h, quenched	62.4	66.07	91.0	400°C/1h, slowly cooled	61.5	65.8	84.4
	600°C/1h, quenched	69.2	42.9	79.4	600°C/1h, slowly cooled	68.4	43.8	52.4
	1000°C/1 h, quenched	52.2	19.4	26.0	1000°C/1h, slowly cooled	44.0	9.5	15.8
MZF/ 20 wt% Permalloy	Powder	68.0						
	As-sprayed	47.5	86.6	116.5				
	400°C/1h, quenched	58.3	81.5	105.4	400°C/1h, slowly cooled	58.8	80.3	107.9
	600°C/1h, quenched	71.9	47.2	69.4	600°C/1h, slowly cooled	70.4	44.9	53.5
	1000°C/1 h	48.5	11.4	12.7	1000°C/1h, slowly cooled	45.5	12.2	24.8
MZF/ 25 wt% Permalloy	Powder	68.0						
	As-sprayed	45.6	81.0	111.6				
	400°C/1h	54.8	75.4	116.9	400°C/1h, slowly cooled	56.8	78.3	101.2
	600°C/1h	63.2	43.5	62.8	600°C/1h, slowly cooled	67.4	46.2	57.3
	1000°C/1 h	49.1	18.5	29.0	1000°C/1h, slowly cooled	45.3	16.8	32.8

The saturation magnetizations of as-sprayed coatings are smaller than the corresponding feedstock powder for all compositions. The low Ms of as-sprayed MZF film is attributed to the random distribution of cation in the tetrahedral sites (A) or octahedral sites (B) resulting from the rapid quenching from the molten droplet (about 2000°C) to substrate temperature (about 200°C) in about 10ms, which limits the equilibrium cation distribution. This can also be seen from the difference between the Ms of 1000°C/1h annealed, quenched MZF film (*Ms*=14.1emu/g) and that of 1000°C/1h annealed, slowly cooled MZF film (*Ms*=43.6emu/g). Annealing in air up to 600°C can improve the *Ms* and decrease the coercivity. For MZF/permalloy composites, low temperature annealing can result in even higher *Ms* than the starting powder. The increase in *Ms* is believed to be due to the cation ordering in MZF during low temperature annealing [148]. Annealing above 1000°C gives a drop in Ms for both MZF and MZF/permalloy composite films. For the case of 1000°C/1h annealed, slowly cooled MZF film, which has more Fe in the MZF, the excessive B-site preferring Fe^{2+} expels Fe^{3+} into A site, so the antiparallel A-B interaction decreases the net magnetic moment per formula. For the case of 1000°C/1h annealed MZF/permalloy films which forms MnZnNi Ferrite, since Ni^{2+} ($2\mu_B$) and Mn^{3+} ($4\mu_B$) prefer B site, Fe^{3+} ($5\mu_B$), cations are expelled to A site, the magnetic moment increase in B site form Ni^{2+} and Mn^{3+} can not counteract the magnetic moment increase in A site from Fe^{3+}, the net magnetic moment decreases. The coercivity drops as the annealing temperature increases, the drop in coercivity after annealing in air is attributed to two facts [148]. One is that annealing makes the inhomogeneous composition resulting from preferential Zinc evaporation during spraying more homogenous. As the crystalline anisotropy constant is strongly compositional dependent, the compositional discontinuity presents a barrier to domain wall motion [5]. Second, the grain volume increases resulting from phase transformation of FeO wuestite to Fe_2O_3 hematite during annealing, filling up the porosity and cracks which also are barriers to domain wall motion [5].

6.1.3. Electrical properties

Resistivity measurement are done on as-sprayed films and 600°C/1h air annealed films which have the highest *Ms*. Results are summarize in Table 6-2. The resistivity of MZF and 15%$Ni_{80}Fe_{20}$ composite are increased by an order of magnitude after annealing, while the composites with higher $Ni_{80}Fe_{20}$ concentration only increase several times. The electrical conductivities of as-sprayed composites are also plotted against NiFe volume fraction converted from weight percentage, as shown in Figure 5-1. From this plot, we can see that the percolation is below 10 vol%. Further study on percolation of plasma sprayed composites was discussed in Chapter 5.

Table 6-2, bulk resistivity of MZF/permalloy composite films before and after annealing

Bulk resistivity (Ω.m) / Heat-treatment Condition	MZF	MZF-15 wt% $Ni_{80}Fe_{20}$	MZF-20 wt% $Ni_{80}Fe_{20}$	MZF-25 wt% $Ni_{80}Fe_{20}$
As-sprayed	0.013	$4.99x10^{-5}$	$2.180\ x10^{-5}$	$1.429\ x10^{-5}$
600°C/1h annealed	0.614	$7.33\ x10^{-4}$	$8.99\ x10^{-5}$	$3.10\ x10^{-5}$

The increase of resistivity in MZF/permalloy films can be related to the formation of the insulating hematite in the grain boundaries and partial oxidation of the $Ni_{80}Fe_{20}$. The EDAX analysis on the $Ni_{80}Fe_{20}$ phase before and after annealing shows an increase of oxygen content. Figure 6-3 shows the cross-section MZF/permalloy composite films. It can be seen from (a) that the some of the Permalloy splats are connected to each other thus forming a conducting path for current. In this present study, the $Ni_{80}Fe_{20}$ volume fraction is above the percolation threshold. To increase the resistivity for application in the high frequency range, lower concentrations of Permalloy will be studied. It is worth-noting that the Permalloy is in round disk shape with average thickness of about 1 μm (shown in fig. 5-26(b)). This is comparable to multilayered laminated permalloy/ferrite films [29].

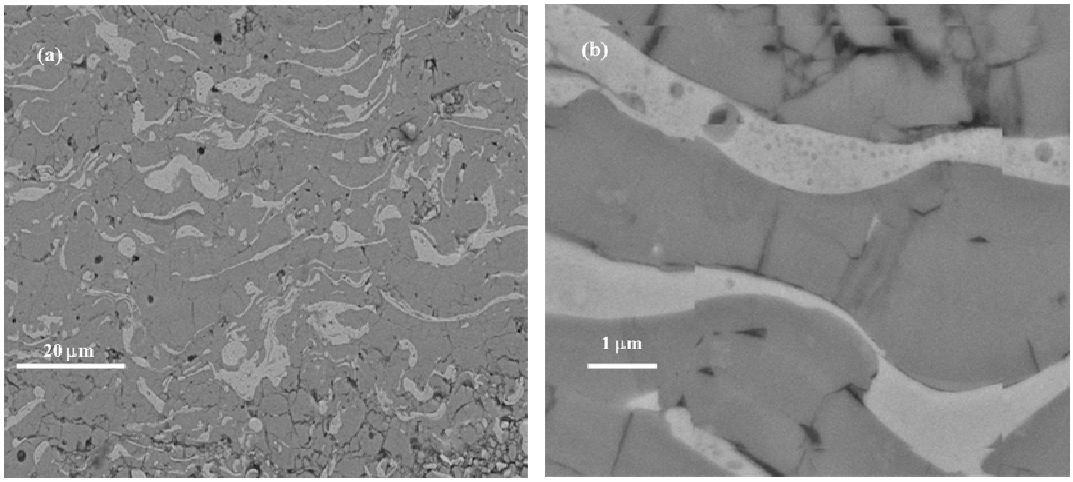

Figure 6-3, (a) and (b) SEM images of plasma sprayed MZF-permalloy composite.

6.2. Plasma Sprayed MnZn ferrite-NiCo Composites

6.2.1. Microstructures

Powder XRD patterns of as-sprayed NiCo coating and MZF-NiCo composite coating with 10 Vol% of NiCo are shown in Figure 6-4. As evidenced by the XRD results, NiCo partially oxidized during plasma spraying and formed a solid solution of NiO-CoO. The lattice constant of this oxide phase is 4.197Å. By extrapolating between lattice constants of NiO (4.177Å, JCPDS #9-402) and CoO (4.260Å, JCPDS #4-835), this solid solution is estimated to be $Ni_{0.75}Co_{0.25}O$. The as-sprayed composite consists of four phases, NiCo metal,

rocksalt structured (Ni,Co)O, MZF spinel and FeO wuestite (4.307Å, JCPDS #6-615). FeO wuestite forms due to deoxidation of MZF at high temperature and low oxygen partial pressure environment during spraying. FeO wuestite is a metastable phase at room temperature, however it is preserved due to the rapid quenching process during spraying. The FeO wuestite is located in the outer shell of the grains or in the grain boundary region in the as-sprayed MZF coatings [109].

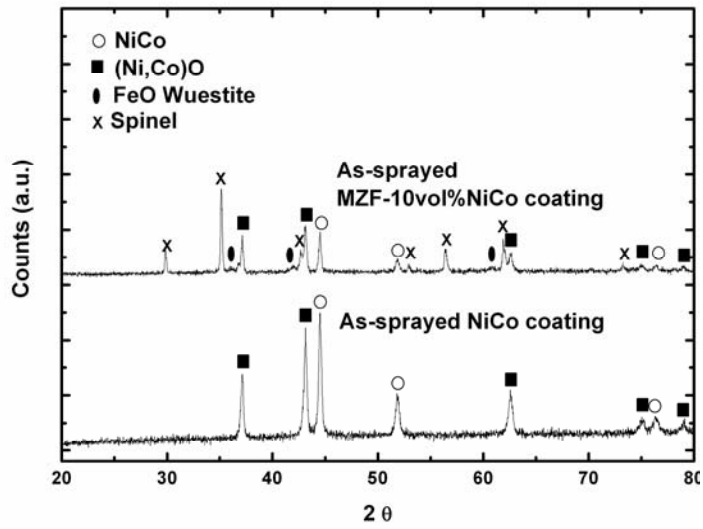

Figure 6-4, Powder XRD patterns of as-sprayed NiCo coating and MZF-10 vol% NiCo composite coating.

The as-sprayed composite coatings have low magnetization and low resistivity due to random cation distribution and the existence of conductive wuestite phase, respectively. These functional properties can be improved by low temperature annealing[108]. To select the appropriate annealing temperature, as-sprayed NiCo coating and MZF-10 vol% NiCo coating were heated in air at 10°C/min from room temperature to 1200°C for DTA/TGA measurements. Figure 6-5 shows the DTA/TGA results of these two coatings. From room temperature to 400°C, there is no significant weight change, from 400°C to 600°C, weights of the coatings start to increase, and the weight change increases drastically above 600°C. Therefore, as-sprayed NiCo coatings and MZF-NiCo composite coatings were annealed in air at 400°C and 600°C. The XRD patterns of as-sprayed and annealed NiCo and MZF-10vol% NiCo coatings are shown in Figure 6-6 and Figure 6-7 respectively. For the case of NiCo, during low temperature air annealing, the oxidation of NiCo is not significant. For the case of composite, FeO wuestite peaks disappear after annealing in air at 400°C. According to the Fe-O phase diagram, since FeO wuestite is a metastable phase below 560°C[91], annealing under this temperature in air, FeO resolves into Fe and $FeFe_2O_4$ and Fe is again oxidized to Fe_3O_4. Fe_3O_4 has the same crystal structure as that of MZF and very close lattice constant, its XRD peaks overlap with those of MZF, therefore, it is difficult to differentiate small amount of Fe_3O_4 from MZF. Fe_3O_4 oxidizes and forms Fe_2O_3 hematite at higher temperature, which is shown in Figure 6-7, pattern (c). The metallic phase is still preserved even after heat treatment at 600°C for 1 hour, as can be seen from Figure 6-6 (c) and Figure 6-7 (c).

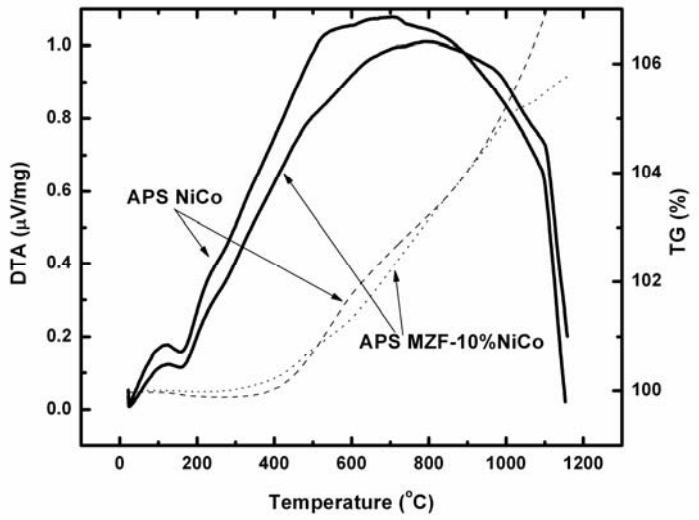

Figure 6-5, DTA and TGA result of as-sprayed NiCo coating and MZF-10vol%NiCo composite coating. Solid lines represent DTA results, dash lines represent TGA results.

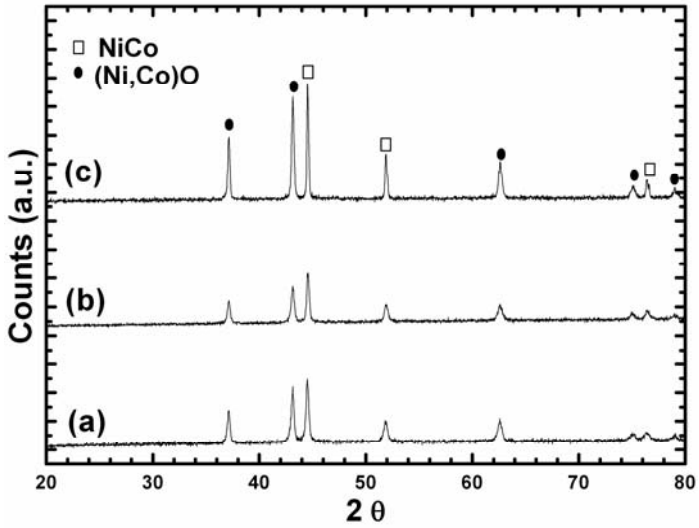

Figure 6-6, XRD patterns of plasma sprayed NiCo coating after different heat treatments. (a) as-sprayed, (b) annealed in air at 400°C for 1 hour, (c) annealed in air at 600°C for 1 hour.

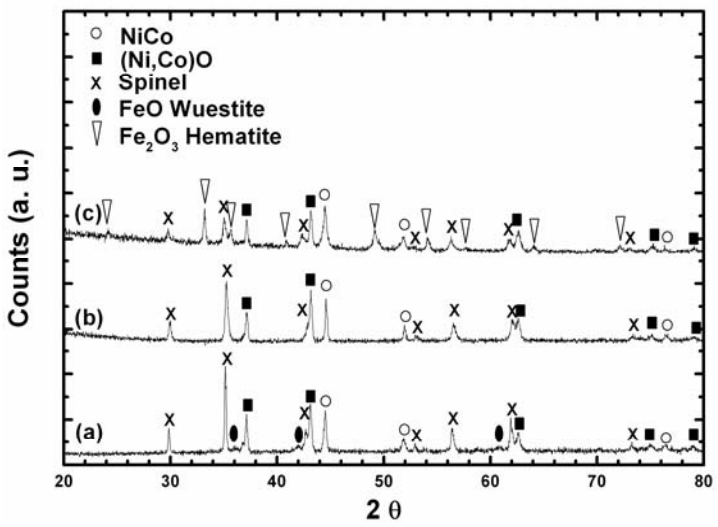

Figure 6-7, XRD patterns of plasma sprayed MZF-10 vol% NiCo composite coating after different heat treatments. (a) as-sprayed, (b) annealed in air at 400°C for 1 hour, (c) annealed in air at 600°C for 1 hour.

6.2.2. Magnetic Properties

Hysteresis loops of NiCo and MZF/NiCo composites films before and after annealing were measured at ambient temperature. Saturation magnetization (Ms) and in-plane coercivity (Hc) are plotted in Figure 6-8. The as-sprayed NiCo has a low saturation magnetization of 261 emu/cm^3 compared to 1326 emu/cm^3 of bulk $Ni_{80}Co_{20}$.This low saturation magnetization is mostly due to the formation of the antiferromagnetic NiO-CoO solid solution. The Néel temperature of the NiCoO solid solution is estimated to be 467K by interpolating between the Néel temperature of NiO an CoO (525K and 293K, respectively [149]) .

Annealing in air oxidized NiCo to form additional NiO-CoO solid solution, therefore the saturation magnetization slightly decreases. As-sprayed NiCo metallic coatings have very high coercivity compared to a few Oersteds of bulk alloy. The antiferromagnetic exchange coupling between (Ni,Co)O and NiCo does not contribute significantly to this increase in coercivity, as will be shown that in the pressed-sintered NiCo pellet, although there exists NiCoO solid solution, the coercivity is still as low as a few Orsteds. Reasons for high coercivity are chemical inhomogeneity and microstructural defects. NiCo particles have different degrees of oxidation during spraying, resulting in varying Ni/Co ratio in individual particles either in metallic phase or in antiferromagnetic oxide phase. Magnetocrystalline anisotropy depends critically on the chemical composition of the alloy and oxide. Therefore, difference in composition among individual particles presents a barrier to domain wall motion [5]. Also as can been seen from Figure 6-9 (a), the as-sprayed NiCo coating has more granular pores, interlaminar pores and more cracks, all these microstructural defects also presents barriers to domain wall motions [5]. The coercivity drops as the annealing temperature increases, this drop is attributed to two factors [150]. First is that annealing makes the composition more homogenous. Second, as evidenced by Figure 6-9 (b), the grain

volume increases resulting from further oxidation of NiCo to (Ni,Co)O, filling up the porosity and cracks. For as-sprayed MZF/NiCo composite coatings, the saturation magnetizations are low. Annealing in air at 400°C increases the saturation magnetization. As studied by neutron diffraction[150], the low saturation magnetization in the as-sprayed coating is due to the random cation distribution resulting from rapid solidification during plasma spray deposition. During low temperature annealing, cations receive sufficient kinetic energy to move to their equilibrium sites, resulting in an increase of magnetic moment. However, the saturation magnetization decreases after annealing in air at 600°C. Energy Dispersive X-ray (EDX) analysis results provide evidence that there are some Ni and Co elements in the MZF phase which may be the result of diffusion at elevated temperature. Since Ni^{2+} and Co^{2+} have smaller magnetic moments (2μB and 3 μB, respectively) than those of Mn^{2+}, Fe^{2+} and Fe^{3+} (5 μB, 4 μB and 5 μB, respectively), the presence of Ni^{2+} and Co^{2+} cations in MnZn ferrite will lower its magnetic moment. Due to the preferential Zinc evaporation during spraying, the composition of MZF phase can be very inhomogeneous [81], and due to the porous microstructure of as-sprayed composite coating, the coercivities of as-sprayed composite coatings are also very high. Annealing in air can reduce the coercivity by making the coating chemically and microstructurally more homogeneous, resulting in the decrease in coercivity.

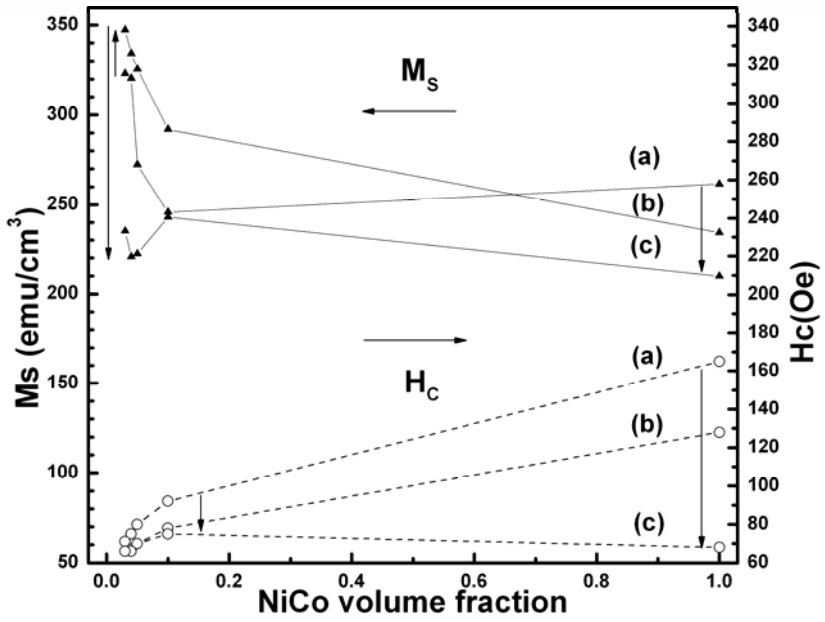

Figure 6-8, saturation magnetization and in-plane coercivity of MZF-NiCo composite coatings at (a) as-sprayed, (b) annealed in air at 400°C for 1 hour, and (c) annealed in air at 600°C for 1 hour. Solid triangles represent saturation magnetization while open circles represent coercivity. The lines are guides to the eye. Arrows indicate the change of M_s and H_c from as-sprayed state to annealed state.

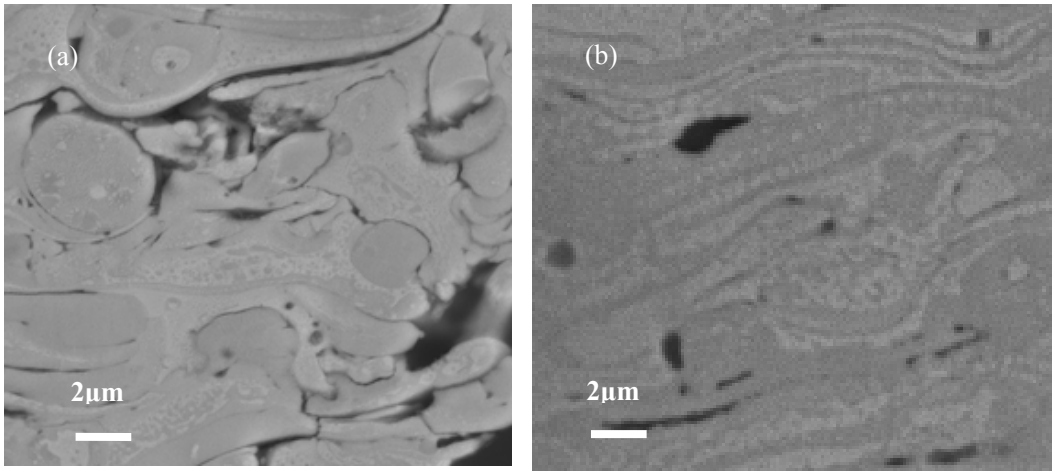

Figure 6-9, Back scattering SEM micrographs of the cross sectional (a) as-sprayed and (b) 600ºC annealed NiCo coating.

6.2.3. Sintered counterparts

The XRD patterns of pressed-sintered MZF-NiCo composite pellets are shown in Figure 6-10. Although the pellets were sintered under protective gas, some degree of oxidation has still taken place in the metal phase by trace impurities in the N_2 or by the oxidation/reduction reaction between MZF and NiCo. As shown by the XRD pattern of sintered NiCo pellet, a minor oxide phase with lattice constant of 4.233Å forms. This suggests that the oxide is a solid solution of NiO and CoO with more Cobalt concentration compared to the solid solution formed by plasma spraying. By extrapolating the lattice constants of NiO and CoO, the solid solution is estimated to be 32 mol%NiO-68mol%CoO. The Gibbs free energy of the formation of CoO is more negative than that of the formation of NiO at temperatures ranging from room temperature to about 2200ºC [151, 152], which is the typical particle temperature of molten droplets under the current spraying condition, so it is easier to form CoO when the oxygen partial pressure is low. Therefore, the Ni/Co ratio in the oxide solid solution formed during spraying is close to that of metal powder due to sufficient oxygen for the oxidation of NiCo (however insufficient to maintain MnZn Ferrite) in the plasma plume. However, at sintering, the oxygen partial pressure is low, so that the formation of CoO is more favored and the solid solution has more Co content. In the composite pellets, due to low oxygen partial pressure, MZF was partially reduced to form FeO wuestite. FeO, NiO and CoO share the same rocksalt structure, and interdiffusion may take place in the grain boundary region to form a (Ni,Co,Fe)O solid solution, thus the XRD pattern only shows a single rocksalt phase.

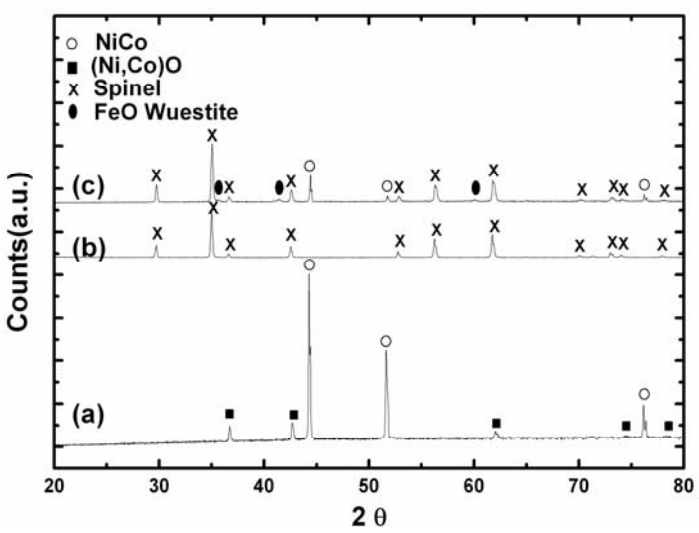

Figure 6-10, XRD patterns of (a) NiCo, (b) MZF and (c) MZF-30 vol% NiCo pellets after heat treatment at 800°C in N_2.

Hysteresis loops of samples of MZF/NiCo composites with varying compositions were measured at ambient temperature. Saturation magnetization (Ms) and coercivity are plotted in Figure 6-11. Compared to plasma sprayed composite coatings, pressed-sintered pellets have higher saturation magnetization and much lower coercivity. It is noteworthy that the saturation magnetization of NiCo-MZF composites does not increase monotonically with the increase of NiCo volume fraction as expected for a simple physical mixture. EDX on NiCo particles shows some amount of Mn and Fe elements which could be from the diffusion from surrounding MnZn Ferrite particles. EDX on MnZn ferrite particles also shows some amount of Ni and Co. The diffusion between NiCo phase and MZF phase could change the chemistry of the ferrite and the alloy whose magnetic moments depends critically on chemical composition. Further experiments and calculations are needed to explain this abnormality.

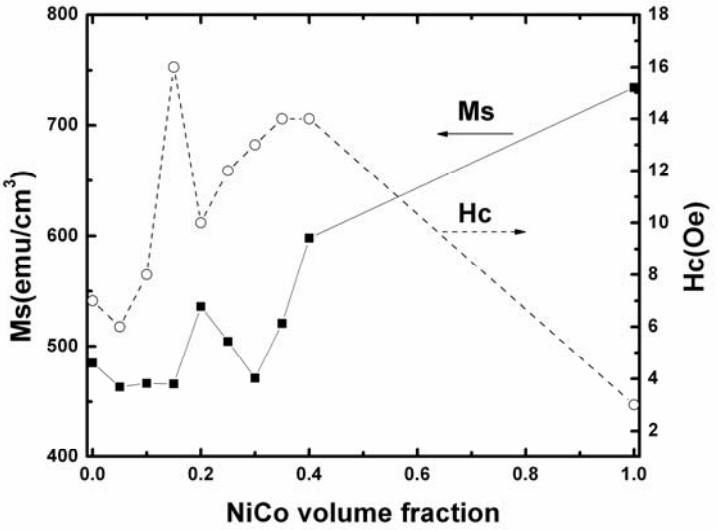

Figure 6-11, Saturation magnetization and in-plane coercivity of MZF-NiCo composite pellets. Solid squares represent saturation magnetization while open circles represent coercivity. The lines are guides to the eye.

6.2.4. Electrical properties

The resistivities of plasma sprayed MZF-NiCo composites are shown in Figure 2-1. The resistivity of as-sprayed NiCo metallic coating is 70 μΩ•cm which several times higher than bulk NiCo (10 μΩ•cm). This is due to the formation of insulating (Ni,Co)O. This oxide seems to form a separate smaller splat sitting on the top of the NiCo metallic splat instead of to form a layer enclosing the metallic splats due to different crystallization in quenching (this is possible as a focus ion beam study [153] on the thermally sprayed NiAl splat showed that Al_2O_3 layer formed on the top of the NiAl splat due to the smaller density of Al_2O_3). Therefore, the metallic splats are still connected to form a conductive path. After annealing, NiCo is partially oxidize, this time, the oxide is formed outside the metallic splats, forming a scale enclosing the metallic grains, therefore, the resistivity increases as the annealing temperature increases. The resistivities of MZF/NiCo composites also increase after annealing in air, partially due to the formation of insulating (Ni,Co)O, partially due to the formation of insulating Fe_2O_3 hematite.

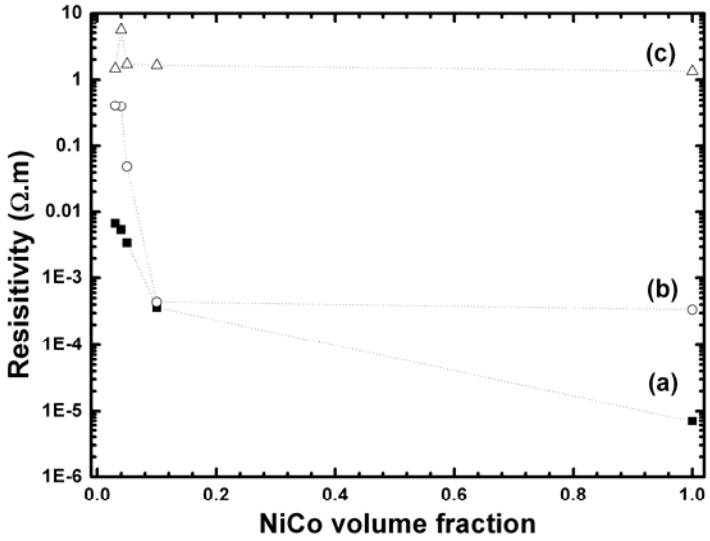

Figure 6-12, resistivities of MZF-NiCo composites, (a) as-sprayed, (b) 400°C annealed, and (c) 600°C annealed.

6.3. Plasma Sprayed Co ferrite-Co Composites

6.3.1. Co ferrite made from Co-precipitated powders

6.3.1.1. Powder characterization

Figure 6-13 shows the DTA/TGA results on as-precipitated gel, the heating rate is 5°C/min in air. It can be seen that the most weight loss is taking place below 200°C associating with an endothermic peak. This phenomenon is typical hydrate dissociation.

Figure 6-14 shows DTA/TGA results on powder dried in an oven at 150°C for 10 hours. The experiment was conducted in air at the heating rate of 1°C/min. It can be seen that there are 3 steps in weight loss, the first one is from room temperature to 200°C, the second on is from 200°C to 400°C, the third one is from 550°C to 600°C. Assuming the co-precipitate is a fine mixture of Cobalt hydroxide and Iron hydroxide, the final product is $CoFe_2O_4$, so the reaction should be:

$$CoFe_2(OH)_8 = CoFe_2O_4 + 4H_2O$$

For this reaction, the weight loss of the reaction should be 23.5%, however, the weight loss in the TG measurement only shows a maximum weight loss of 10.8%. This could suggest that during the low temperature drying process, the mix hydroxide has partially decomposed as can be seen from the huge weight loss (93.2%) in TGA experiment on the wet gel.

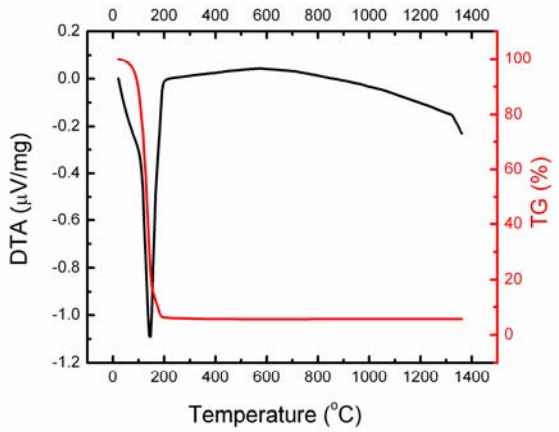

Figure 6-13, DTA and TG results on as-precipitated gel.

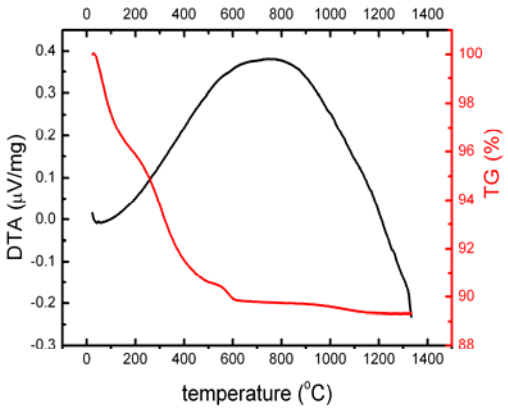

Figure 6-14, DTA and TG results on dried co-precipitate powder.

The first weight loss is associated with loss of water, the second weight loss is the dissociation of ammonium nitrate, and this is confirmed by the observation of brownish smoke when the temperature reaches around 300°C to 400°C during the calcinations of dried powder in a box furnace. The third weight loss is believed to be associated with the decomposition of iron-cobalt hydroxide which will results in the formation of cobalt ferrite. From 600°C to 1000°C, the weight of sample remains constant which suggests the dissociation of cobalt iron hydroxide may have finished before 600°C. It can also be noticed that there is a small weight loss from 1000°C to 1120°C. This weight loss can be attributed to oxygen loss at high temperature. X-ray results support this conclusion and will be discussed

later.

According to the TGA analysis, heat treatment temperature was selected to be above 600°C to form spinel ferrite. X-ray powder diffraction study was carried out on the dried powder and heat-treated powder to examine the completeness of ferrite formation. The results are shown in Figure 6-15.

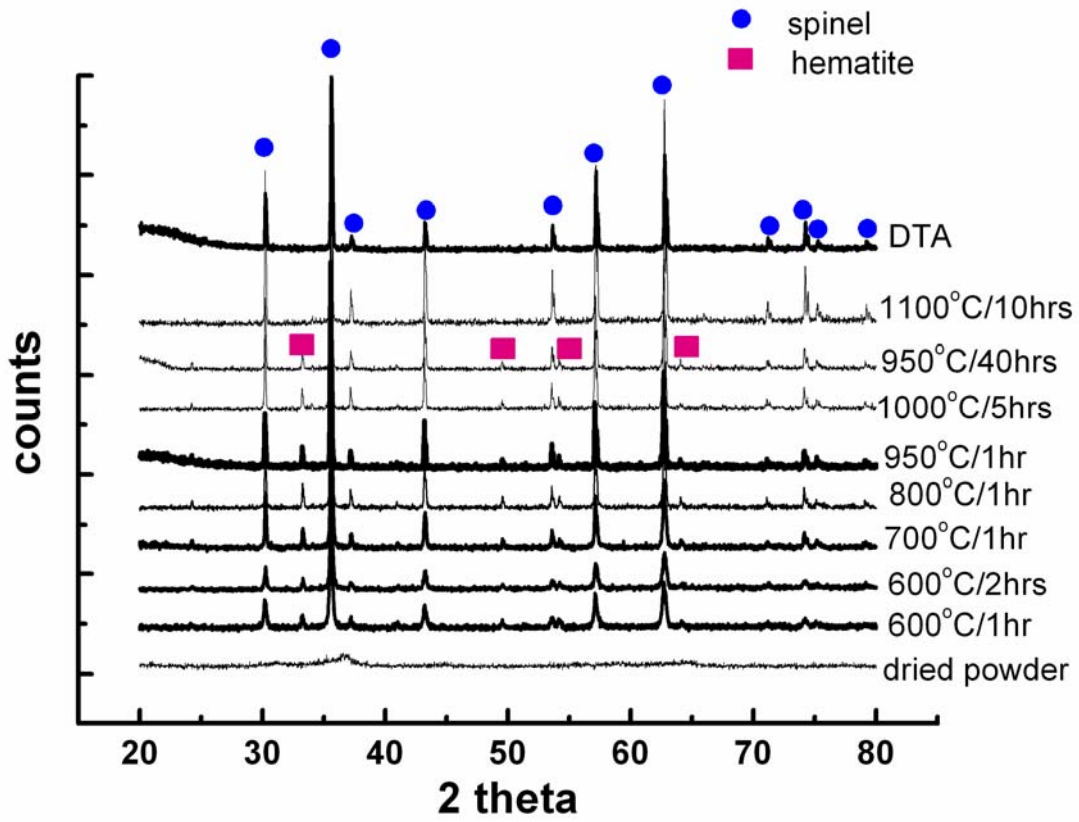

Figure 6-15, XRD patterns of dried powder and heat-treatd powder in air at different temperatures.

From Figure 6-15, it can be seen that the dried powder from the precipitate is amorphous. Powder heat-treated at temperatures ranging from 600°C to 950°C shows a mixture of spinel and hematite. Powder heat-treated in air at 1100°C for 10 hours or the remaining powder after the previous DTA/TGA experiment at 1°C/min heating rate to 1400°C show only spinel structure. Calculation of lattice constant shows that the unit cell length of powder heat-treated below 950°C is 8.39Å, while it is 8.37Å for powder heat-treated at above 1100°C. The reference lattice constant is 8.392 Å for sample made by heating co-precipitated hydroxides at 950°C for 40 hours (JCPDS 22-1086) or 8.377 Å for sample made by fusion of co-precipitated hydrates (JCPDS 3-864). This means that the powder heat-treated below 950°C may preserve $CoFe_2O_4$ stoichiometry. According to the binary phase diagram of Fe-O [91] (Figure 2-21), the mixture of magnetite and hematite can form magnetite by increasing temperature or reducing oxygen, so combining the lattice constant drop and weight loss in the thermal gravimetric experiment, it can be concluded that the hematite phase decomposes into Fe_3O_4 magnetite which has the spinel structure with lattice constant 8.396 Å (JCPDS 19-629) or 8.374 Å (JCPDS 3-864) and the magnetite

forms a solid solution with $CoFe_2O_4$, resulting a change in both the chemical stoichiometry and unit cell parameter.

The existence of hematite can be explained by the phase separation during precipitation. It was observed that the filtered solution can further precipitate some green gel, the green color is a typical color for $Co(OH)_2$. The explanation is that the precipitation rate for Co^{2+} and Fe^{3+} is not stoichiometric so that there is some loss of cobalt and the excess iron forms $Fe(OH)_3$. The iron hydroxide forms hematite during heat treatment.

The lattice constants and phase ratio between Fe_2O_3 hematite and cobalt ferrite are calculated by Rietveld refinement analysis. The results are listed in Table 6-3. It can be seen that increase temperature above 950°C causes more loss of oxygen and the amount of Fe_2O_3 decreases while the magnetite increases, and as a result, the lattice constant of spinel phase drops.

Table 6-3, Physical properties of cobalt ferrite sintered under several conditions.

Heat-treatment	Lattice constant of spinel phase (Å)	Fe_2O_3/ $CoFe_2O_4$ (molar ratio)	Magnetic moment (emu/g)	Corrected magnetic moment (emu/g)	Coercivity (Oe)
950°C/1hr	8.392	0.249	51.7	60.5	85
950°C/40hrs	8.393	0.237	50.3	58.4	5
1000°C/5hrs	8.383	0.231	53.0	61.3	532
1100°C/10hrs	8.374	0	59.2	59.2	420
25→1400°C @1°C/min	8.374	0	59.3	59.3	229

Since hematite is theoretically an antiferromagnet (T_N=950K), so at room temperature the hematite phase does not contribute to the magnetic moment, hence the measured magnetic moment should be corrected for the spinel phase only. The saturation magnetization for all powders is lower than the literature value (80emu/g). It is found that cobalt ferrite nano-particles usually have lower Ms (~60emu/g) due to superparamagnetism (the critical size is estimated by[11] $r_o^{1yr} \approx (\frac{10K_BT}{K_u})^{1/3}$, for cobalt ferrite at room temperature, it is 2nm). The particle size in this study is typically 20μm which is beyond the superparamagnetic regime, therefore the Co ferrite particle is not superparamagnetic. The low measured magnetic moment may be caused by canted spins in the grain boundary regions.

From the above results, 1100°C was chosen as the heat treatment temperature to form single phase spinel. Ten hours heat treatment duration was selected to allow for enough grain growth to achieve 20-50μm optimum plasma spray particle size. The particle distribution is shown in Figure 4-3, d_{50} is 16.23μm, d_{90} is 32.4μm. The particle size can be increased by longer sintering.

The morphology of the powder heat treated at 1100°C for 10 hours is shown in Figure 6-16. A particle consists of hundreds of equiaxed single crystallites. The chemical composition is determined to be $Co_{0.9}Fe_{2.1}O_4$ by EDAX analysis, confirming that the ferrite is Iron rich and there is Cobalt loss during co-precipitation.

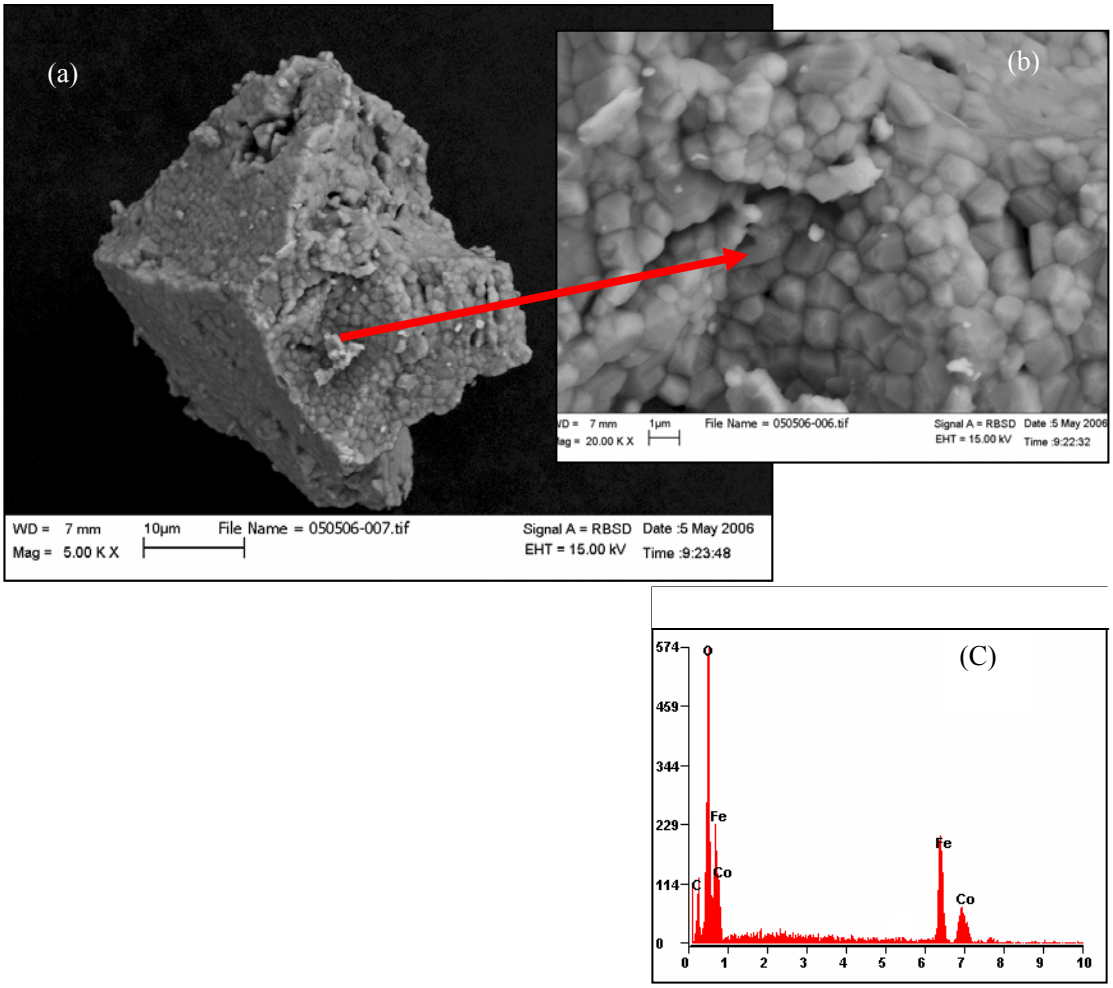

Figure 6-16, SEM backscattered image of cobalt ferrite powder at 5K magnification (a), and 20K magnification (b). EDAX result is obtained under 20KeV electron excitation (c).

6.3.1.2. Selection of spraying condition

Splats were made under a few conditions. Microstructural analysis is conducted to select the best condition to make coating.

The as-sprayed splats on silicon substrates were used to do the X-ray microdiffraction. Figure 6-17 shows the XRD patterns of as-sprayed cobalt ferrite splats with stand-off distance fixed at 120mm while the hydrogen flow rate ranges from 0 to 4 L/min. With increasing hydrogen flow, the crystallinity of splats decreases. It is known that hydrogen flow can increase the particle temperature rendering more quenching and consequently the degradation in crystallinity.

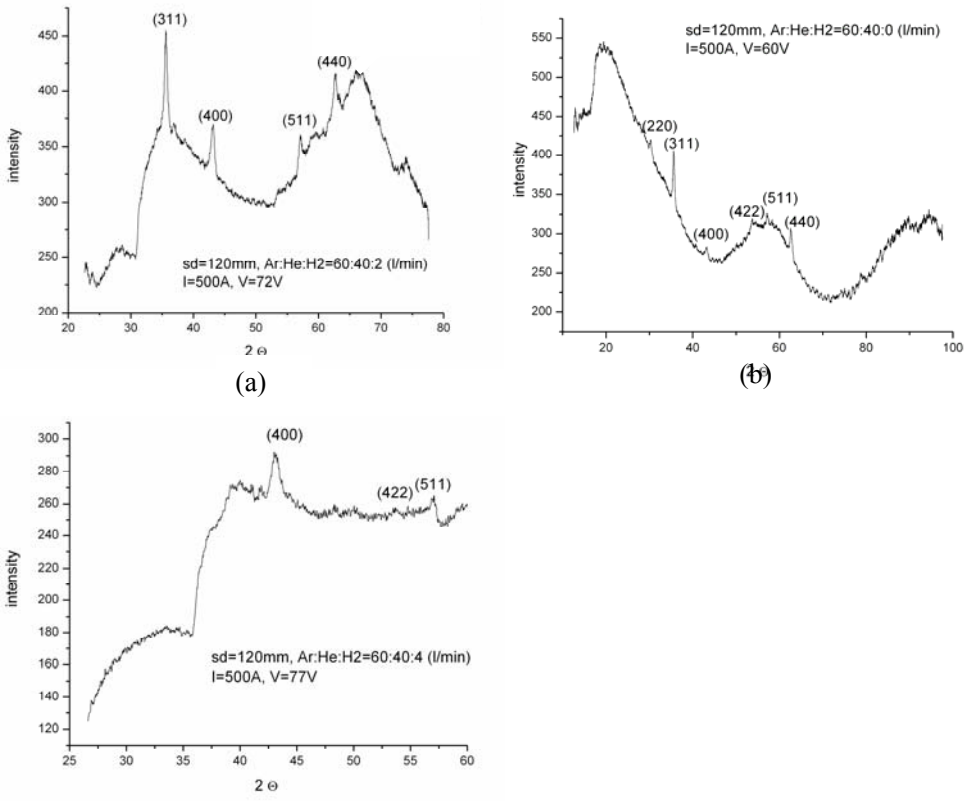

Figure 6-17, X-ray diffraction patterns on as-sprayed cobalt ferrite powder with (a) 0, (b) 2 and (c) 4 L\min hydrogen flow.

So it is also expected to find wuestite in the as-sprayed splats, however in the above XRD patterns, the wuestite peaks are absent. This could be due to the small volume of splats resulting in only a small amount of photons diffracted, making it hard to see the secondary phase.

The lattice constants for splats are listed in Table 6-4. The minor discrepancy in lattice constant between splats and coating comes from different instruments used. Compared to the feed stock powder for spraying previously heat-treated at 1100°C for 40 hours, the lattice constant increases from 8.37Å to 8.39Å. We have concluded that the lattice constant drop from lower temperature to higher temperature heat treatment is a result of the formation of Iron rich Co ferrite, therefore the lattice increase from feed stock powder to as-sprayed coating should come from the dissociation of Iron rich Co ferrite to stoichiometric Co ferrite and FeO wuestite.

Table 6-4, lattice constants of cobalt ferrite sintered powder, splats and coating.

Sample name	Diffractometer	Lattice constant
Powder heat-treated in air at 950°C for 40 hours	SCINTAG/PAD-V	8.393Å
Powder heat-treated in air at 1100°C for 40 hours	SCINTAG/PAD-V	8.374Å
Splats sprayed without hydrogen gas	Bruker GADDS	8.39Å

Splats sprayed with 2L\min hydrogen gas	Bruker GADDS	8.39Å
Splats sprayed with 4L\min hydrogen gas	Bruker GADDS	8.39Å

Figure 6-18 shows optical microscopic image of splats on silicon wafer (waferuniversity.com, (100) oriented). (a)-(c) are taken at 100x magnification for splats deposited under 120mm stand-off distance and 0, 2, 4L\min hydrogen flow, respectively. It can be seen that with increase hydrogen flow, the splat density increases which means the deposition efficiency increases. However, for 220mm stand-off distance, the particle on silicon wafer does not show a typical disk shape splat morphology, suggesting the particles has resolidified before impinging the substrate.

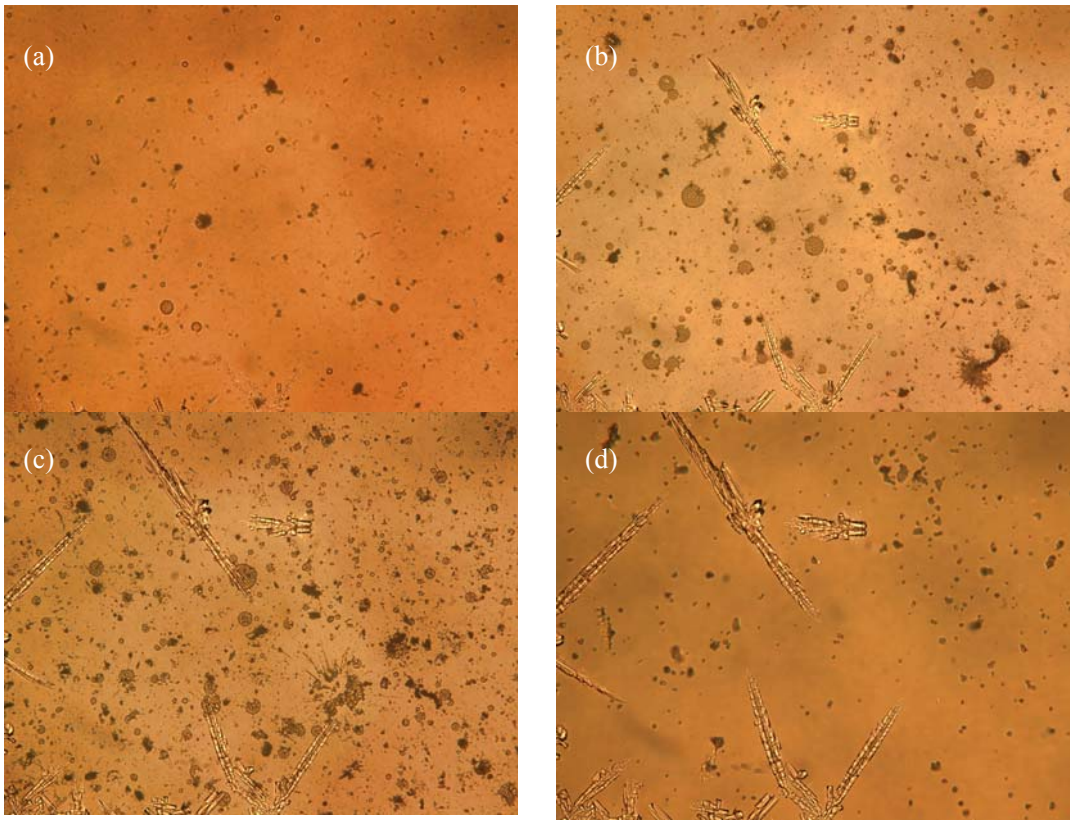

Figure 6-18, Optical microscopy image of cobalt ferrite on silicon wafer. (a) SD=220mm, H_2=0 L\min, (b) SD=220mm, H_2=2 L\min, (c) SD=220mm, H_2=4, L\min. The magnification is 1000x for all images.

Increasing the hydrogen flow rate can increase the temperature, then the difference between substrate temperature and molten particle temperature increases, introducing more quenching stress which can be released by cracking. This explains the increase in the degree of fragmentation as the hydrogen flow increases (shown in Figure 6-19).

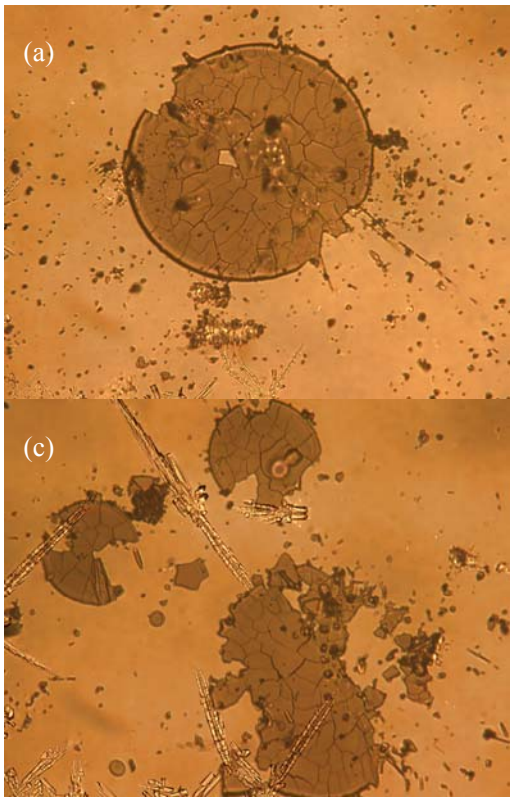

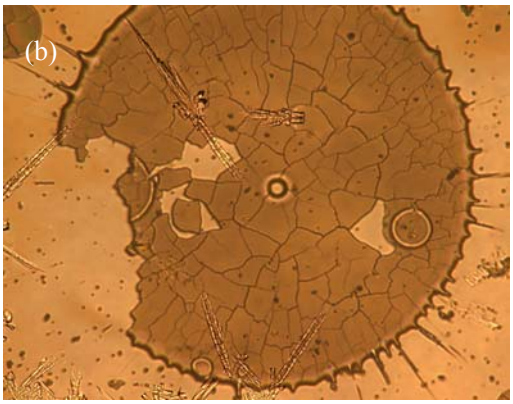

Figure 6-19, Optical microscopy image of cobalt ferrite on silicon wafer. (a) SD=120mm, H_2=0 L\min, (b) SD=120mm, H_2=2 L\min, (c) SD=120mm, H_2=4 L\min. The magnification is 1000x for all images.

Based on the study of the morphology and structure of splats, an optimum condition of gun current and voltage is selected as 500 A and 55 V. The plasma gas component is set as Ar:N_2:H_2=60:40:2 (liter/min) and the powder feeding rate is 16 g/min using compressed air as the powder carrier gas. The distance from the gun nozzle to substrate was 120 mm.

6.3.1.3. Coating characterization

6.3.1.3.1. Structural characterization

The as-sprayed coating has a spinel structure, as shown Figure 6-20 (a). The presence of alumina peaks is from the alumina substrate. The thickness of cobalt ferrite coating (10 μm) is low so the coating is not very continuous. The typical surface roughness of plasma sprayed coating is about 10 to 20 μm. Again, we still do not see a minor wuestite phase as we have expected. The lattice constant of as-sprayed and 500°C annealed cobalt ferrite is determined to be 8.39 Å., which is close to that of stoichiometric Co ferrite.

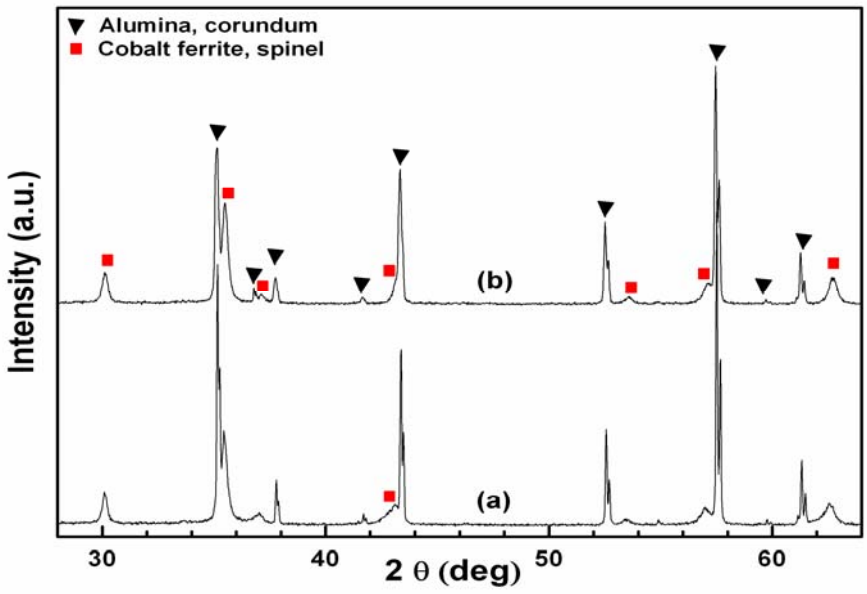

Figure 6-20, X-ray diffraction patterns on as-sprayed cobalt ferrite coating (a) and 500°C annealed coating.

6.3.1.3.2. Electrical resistivity

The electrical resistivity of as-sprayed cobalt ferrite films on alumina is 30Ω·cm; the resistance of coatings annealed in air at 500°C for 1 hour exceeds the upper limit (5KΩ) of the four point probe system indicating the coating is insulating. The resistivity of $CoFe_2O_4$ varies from 1 Ω·cm to 100 Ω·cm depending on the cation distribution as reported by Na et. al. [23].

6.3.1.3.3. Residual stress

Residual stress of cobalt ferrite coating sprayed under 2L/min Hydrogen flow on Titanium substrate was also measured. The calculated residual stress is -297 ± 51 MPa, corresponding to $-(0.2 \pm 0.04)\%$ strain. This is comparable to the residual stress of MnZn ferrite on Titanium substrate (-220 ± 30 MPa)[90]. This stress comes majorly from the thermal mismatch between the substrate and the coating. Assuming the coating and the substrate were cooling from 200°C to 25°C, the thermal mismatch strain is:

$(\Delta\alpha_{CFO} - \Delta\alpha_{Ti}) \cdot \Delta T \approx -0.24\%$.

6.3.1.3.4. Magnetic property

The magnetic hysteresis loops of as-sprayed coating and 500°C annealed coating are shown in Figure 6-21. It is observed that the saturation magnetizations are far below the literature value (420 emu/cm^3), this could be more related to the inaccurate measurement of the coating volumes due to the coating thickness is about the surface roughness range.

However, it is important to notice that the magnetic moment drops from 57 emu/cm^3 to 54 emu/cm^3 while the coercivity increases from 1270 Oe to 3270 Oe after annealing. The drop in saturation magnetization is a direct result of cation redistribution since an ordered cobalt ferrite has a lower magnetic moment [154]. According to a domain wall pinning theory [155], the coercivity in a magnetic material with sharp defects is $H_c=h_c \cdot H_k /2$. Therefore the increase in coercivity can be explained by the increase in magnetocrystalline anisotropy energy which depends critically on the cation distribution. The large magnetocrystalline anisotropy energy of cobalt ferrite originates from the spin-orbit interaction of Co^{2+} in an octahedral site where the trigonal crystal electric field (CEF) is responsible for the partially quenched orbital momentum [12]. Here, it is estimated that the annealed coating has a completely ordered cation distribution having $K_1=2.7\times10^6$ erg/cm^3 [5], while the as-sprayed coating has a completely random cation distribution, having $K_1=1.8\times10^6$ erg/cm^3 (a linear extropolation by assuming that Co^{2+} in A site does not have any anisotropy). The saturation magnetizations of ordered and disordered $CoFe_2O_4$ are approximately 426 emu/cm^3 (3.4μB/formula) and 552 emu/cm^3 (3.9 μB/formula) [154]. Thus the effective anisotropic fields, H_k, are 12676 Oe and 7361 Oe for ordered and disordered phases, respectively. Assuming hc≈1.6, then the change in coercivity due to the increase in magnetocrystalline anisotropy energy and decrease in saturation magnetization, is estimated to be 4252 Oe.

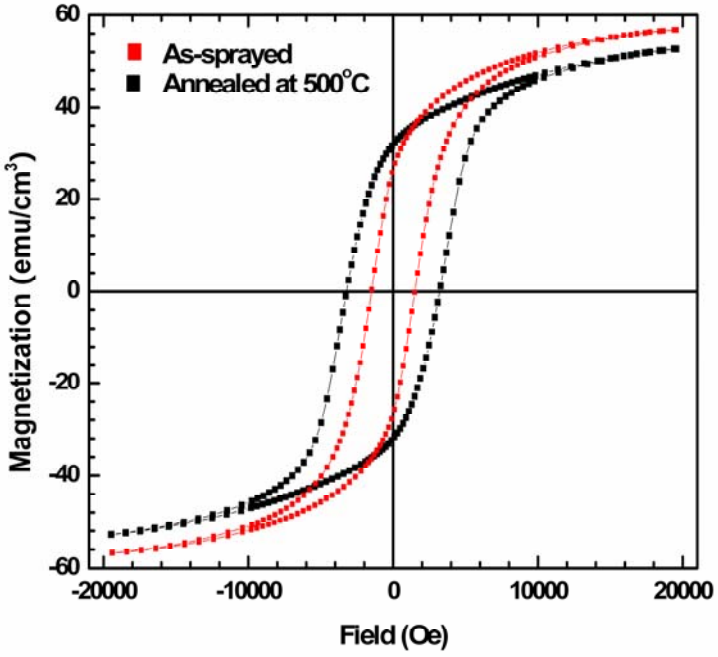

Figure 6-21, magnetic hysteresis loops of as-sprayed cobalt ferrite coating and 500°C annealed coating. (Hysteresis loops were conducted by Dr. Tang, RPI)

6.3.1.3.5. Magnetostriction

The magnetostriction of as-sprayed cobalt ferrite coating is measured by laser deflection technique. The result is presented in Figure 6-22. The highest magntostriction achieved in

this measurement is -73 ppm at 4530 Oe. The strain derivative (dλ/dH) is -2.1×10^{-10} $A^{-1}\cdot m$. The magnetization process in the perpendicular direction is characteristic of domain wall rotation from the in-plane direction to the field direction, therefore the magnetization is linear with field up to saturation. Therefore the saturation magnetostriction can be linearly extrapolated to the saturation field using the same strain derivative. As shown by Figure 6-23, the saturation field is 13,500 Oe. Then the saturation magnetostriction is extrapolated to -217 ppm. Cobalt ferrite synthesized by ceramic sintering methods has a saturation magnetostriction of -220 ppm at a field of about 750 KA/m (9424Oe) and the strain derivative (dλ/dH) is -1×10^{-9} $A^{-1}\cdot m$ [156].

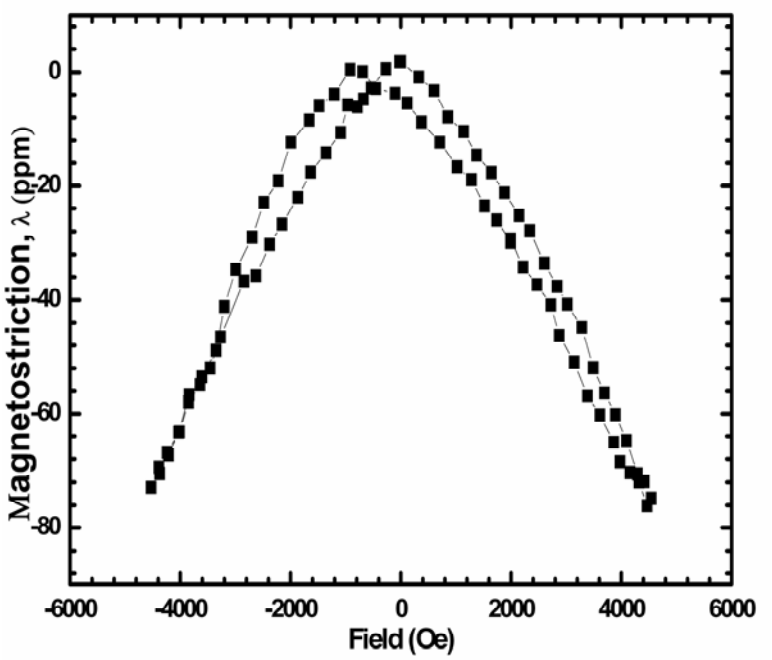

Figure 6-22, magnetostriction of as-sprayed Co ferrite coating on Ti substrates.

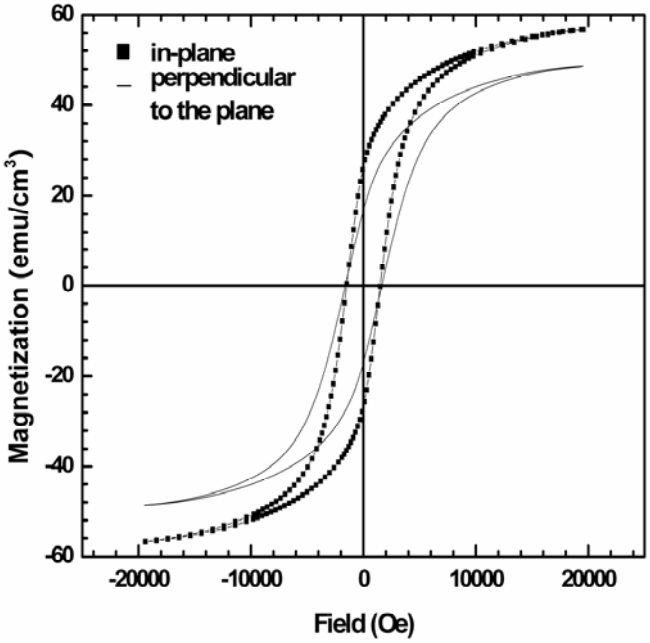

Figure 6-23, magnetic hysteresis loops of as-sprayed Co ferrite in both plane and perpendicular directions.

6.3.2. Ferrite made from spray dried powder

6.3.2.1. Powder characterization

Nanoparticles are bound by a polymer binder and agglomerate in a spray drier. The powder is of spherical shape and the mean particle size d_{50} is 18 μm. The SEM image of spray dried powder is shown in Figure 6-24.

XRD analysis shows that the spray dried powder is of spinel structure (Figure 6-25). The lattice constant is 8.359 Å. The saturation magnetization is 27.8 emu/g which is much smaller than the bulk value (80 emu/g).

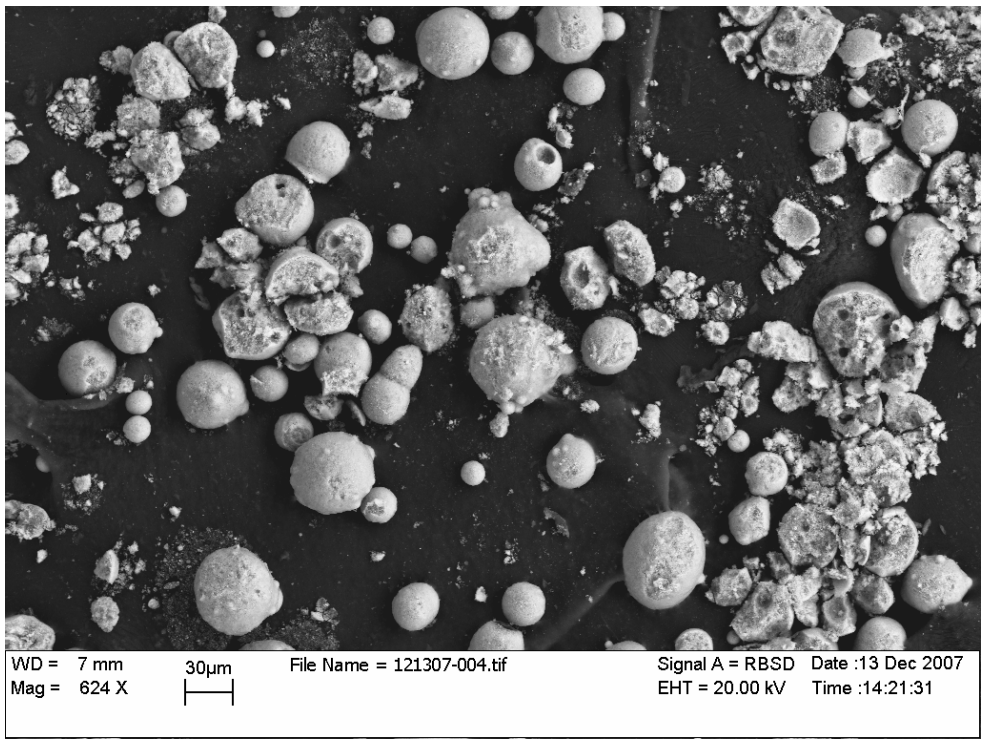

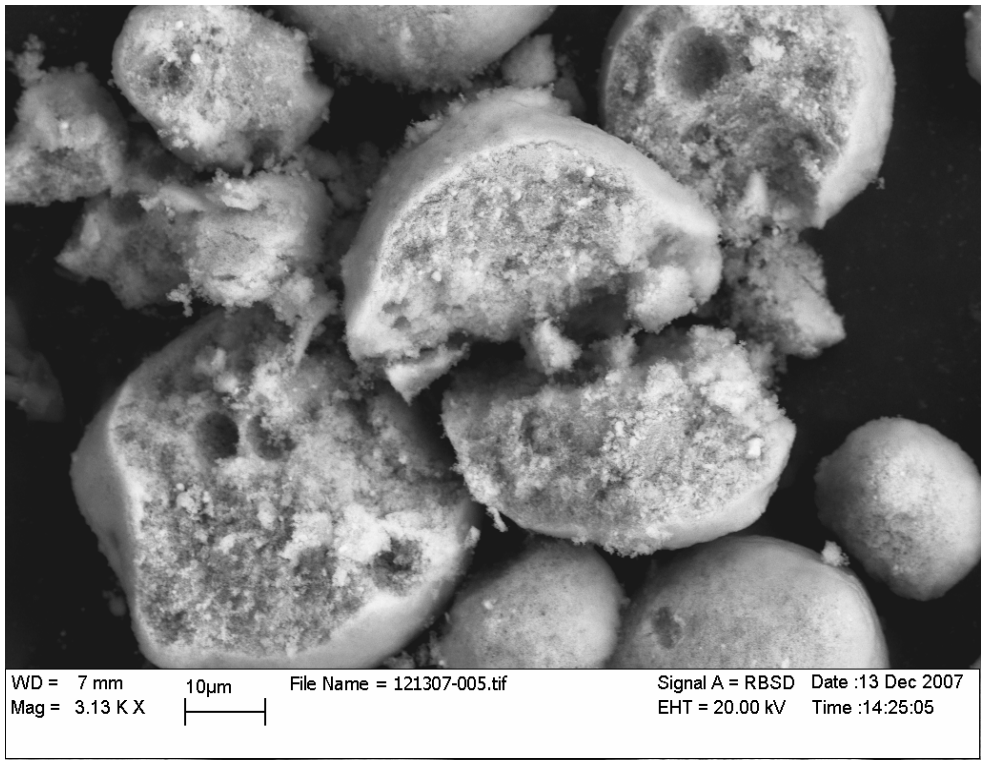

Figure 6-24, SEM microscope picture of spray dried powders.

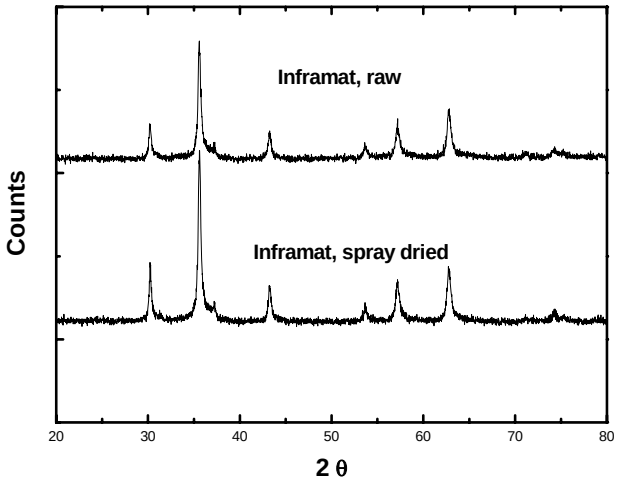

Figure 6-25, XRD patterns of Co ferrite powder before and after spray drying.

6.3.2.2. Spraying conditions and diagnostics

Two conditions have been used to make Co ferrite coatings. They are listed in Table 6-5. The gun current and H_2 volume fraction are already at the lower limit of the plasma gun, otherwise the plasma flame won't be stable and will extinguish during experiments. The only differences between the two conditions are the nozzle size and H_2 flow rate.

Table 6-5, spraying conditions of Co ferrite.

	Nozzle diameter (mm)	Current (A)	Voltage (V)	Ar (cm^3/min)	H_2 (cm^3/min)	Carrier gas	Standoff distance (cm)	Feed rate (g/min)
Run884	8	400	55	46	0.6	air	120	15
Run885	6	400	55	46	0.5	air	120	15

Figure 6-26 shows the histograms of the temperature and velocity of 10,000 monitored in-flight particles at 120 mm away from plasma gun. The average temperature is about 1760±180°C, which is 190°C higher than the melting temperature of $CoFe_2O_4$. The average velocity is 193±49m/s when the molten droplets are impacting the substrate. At this temperature, $CoFe_2O_4$ is partially reduced to divalent oxide such as CoO and FeO. The extent of deoxidation depends on temperature, the partial pressure of O_2 and duration of heating. To optimize the spraying process, we need to lower the temperature while increase the velocity to reduce the particle flight duration. This is not possible in the current plasma spraying system. HVOF should be tried to increase the particle velocity and decrease the temperature.

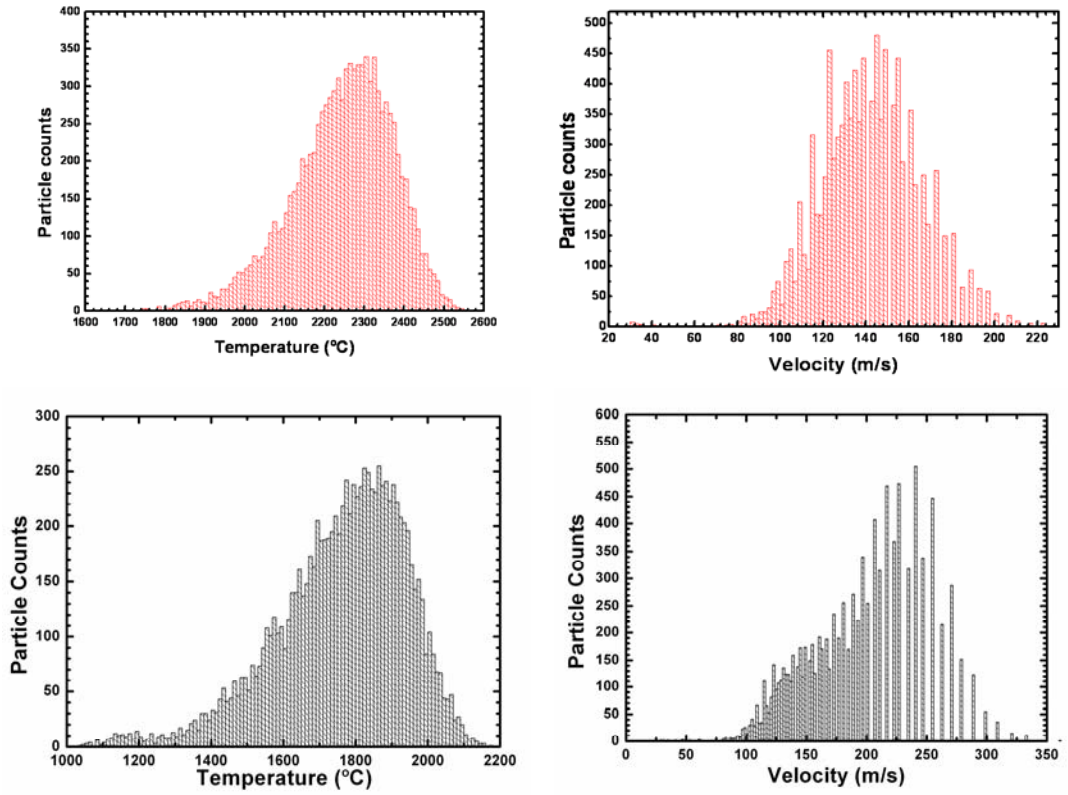

Figure 6-26, temperature histogram (left) and velocity histogram (right) of 10,000 Co ferrite particles during spraying experiments run 884 (up) and run 885 (down).

6.3.2.3. Structural study

The XRD patterns of feed-stock powder for spraying, as-sprayed $CoFe_2O_4$ coating and 600°C and 800°C annealed coatings are shown in Figure 6-27. The feed-stock powder is of spinel structure. The as-sprayed cobalt ferrite coating has two phases, spinel and rocksalt. Rocksalt phase is still present after annealing in air at 600°C and 800°C, but its ratio to cobalt ferrite is greatly reduced. The lattice constants of rocksalt phase in as-sprayed coatings are 4.248 Å, 4.267 Å, and 4.274 Å for as-sprayed, 600°C annealed and 800°C annealed coatings, respectively. By comparing with the lattice constants of CoO (4.260 Å, JCPDS #9-402) and FeO (4.307 Å, JCPDS #6-615), it is believed that the rocksalt phase in as-sprayed coating is mostly CoO. According to the Co-Fe-O system [157] (Figure 6-28), the stable phases above 900°C for the composition of Co/(Co+Fe)=1/3 is spinel and CoO solid solution. Therefore, quenching from a liquid state, Co ferrite spinel and CoO both precipitate and reserve in the final deposit. The enlargement of the rocksalt crystal structure may suggest that the composition of the rocksalt phase is changing during annealing, possibly due to diffusion of Fe from Co ferrite. During annealing, divalent cobalt oxide oxidizes to form mixed divalent-trivalent oxide such as Co_3O_4, which is also of spinel structure, and through diffusion, the newly formed spinel merges with the original spinel to form a single spinel phase. After annealing in air at 800°C for 10 hours, there is only $CoFe_2O_4$ spinel phase present for run 885, but the 800°C annealed coating of run 884, there is another spinel with lattice constant of a=8.128 Å. This spinel could be Co_3O_4 or Fe doped Co_3O_4 because its lattice constant is

very close to that of Co_3O_4 (8.084 Å, JCPDS 9-418). As we shall see later, that the run 884 as-sprayed coating has more CoO, therefore, it is possible that the excessive Co_3O_4 is not incorporated into the Co ferrite phase.

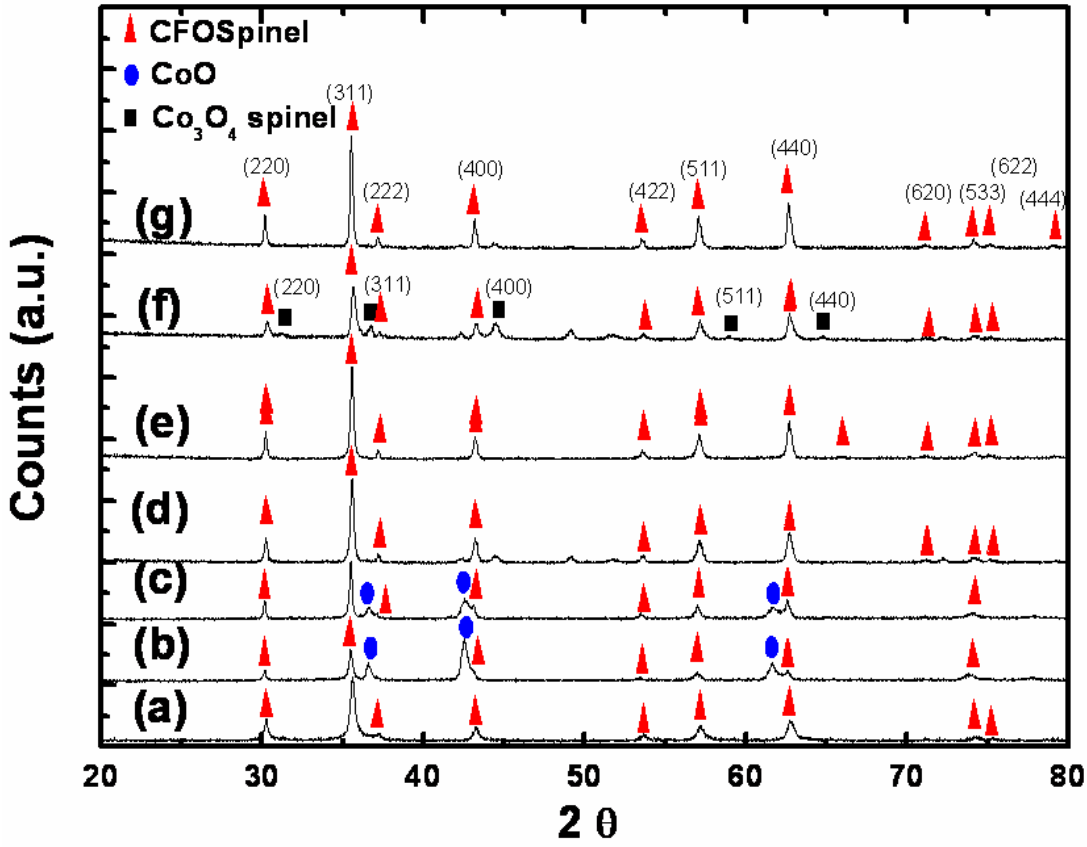

Figure 6-27, XRD patterns of (a) feed-stock cobalt ferrite powder, (b) as-sprayed coating of run 884, (c) as-sprayed coating of run 885, (d) 600°C annealed coating of run 884, (e) 600°C annealed coating of run 885, (f) 800°C annealed coating of run 884, (g) 800°C annealed coating of run 885.

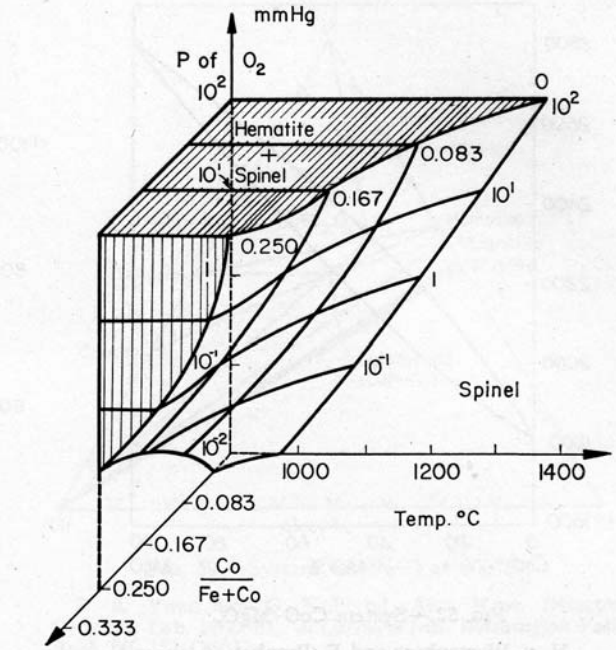

FIG. 49.—System Fe–Co–O; schematic. For isothermal diagrams at 1000°, 1100°, 1200°, and 1300°C, see B. D. Roiter and A. E. Paladino, *J. Am. Ceram. Soc.*, **45** [3] 132 (1962).

Shuichi Iida, *J. Phys. Soc. Japan*, **11**, 847 (1956).

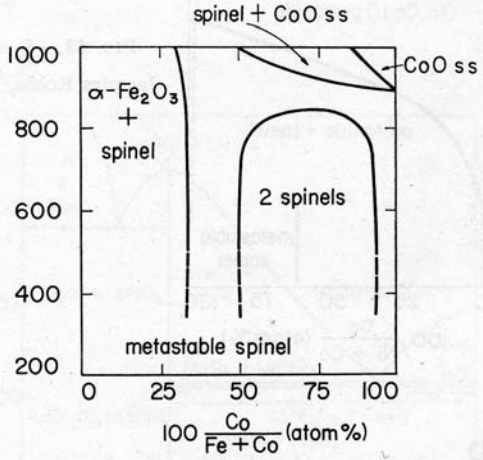

FIG. 50.—System CoO–Fe_2O_3 at 1 atm. pressure.

Jacques Robin, *Ann. chim.* (*Paris*), **10**, 393 (1955).

Figure 6-28, phase diagram of Co-Fe-O system.

The lattice constants of spinel phase in feed-stock powder, as-sprayed coating, 600°C annealed coating and 800°C annealed coating are 8.359 Å, 8.391 Å, 8.376 Å, 8.380 Å, respectively. The formation of CoO leaves the remaining cobalt ferrite Fe rich, so the lattice

constant of cobalt ferrite in as-sprayed coating is larger than that of feed-stock powder and annealed coatings.

To determine the fraction of rocksalt phase in the as-sprayed coating, the as-sprayed coatings are heated in air from room temperature to 1150°C, the maximum temperature of DTA/TGA instrument, for three cycles. Figure 6-29 shows the mass change of the cobalt ferrite coating in air for run 885. The weights of sample increase by 3.12% and 2.29% after heating up to 1150°C for run 884 and 885, respectively. Since the weight gain is presumably due to the reaction of $CoO+Co_{1-x}Fe_2O_{4-4/3x}+x/6O_2=CoFe_2O_4$, the weight fraction of CoO in the as-sprayed coating can be determined to be about 35 wt% and 31 wt% under current spraying condition for run 884 and run 885, respectively, leaving the remaining ferrite to be ferrous ferrite, Fe_3O_4. This also explains that the remaining ferrite in as-sprayed coating has a larger lattice constant, closer to that of Fe_3O_4 magnetite (8.396Å, JCPDS #19-629) than that of $CoFe_2O_4$ (8.377Å, JCPDS #3-864). After annealing, since the ferrite gains Cobalt through diffusion, the lattice constant is closer to that of stoichiometric $CoFe_2O_4$.

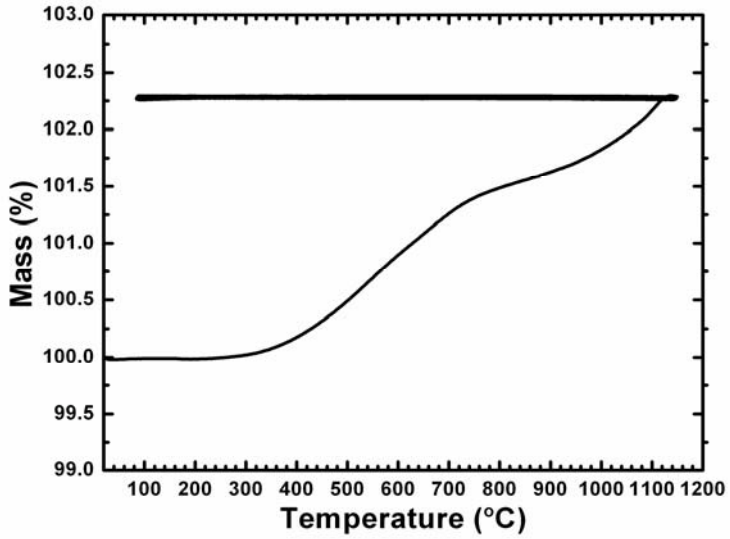

Figure 6-29, TGA of Co ferrite coating sprayed under condition run 885.

Figure 6-30 shows the microstructure of polished cross-section of as-sprayed and annealed cobalt ferrite coatings. The as-sprayed coating has a typical plasma sprayed coating microstructure, containing splats, splat boundaries, unmelted particles, cracks, globular pores and inter-laminar pores. After annealing in air at 600°C, most of the cracks and small pores disappear, resulting from the volume change from the oxidation of CoO. It is noteworthy that there are bright dots of around 100 nm emerging in the positions of former cracks, interlaminar pores and splat boundaries. EDAX results show that these dots have a much higher Co/Fe ratio (1.2) compared to an average value of 0.5 in the other regions. Since this is a backscattered electron image, the brightness contrast comes from the atomic number difference. The bright dots are speculated to be pure cobalt metal instead of oxide. Cobalt metal comes from the reaction $4CoO+1/2O_2=Co_3O_4+Co$, cobalt is further oxidized to form Co_3O_4; therefore only small amount of cobalt is remaining and not detectable by XRD. After annealing in air at 800°C, cobalt particles are completely oxidized and there is only cobalt ferrite phase, therefore the bright dots disappear.

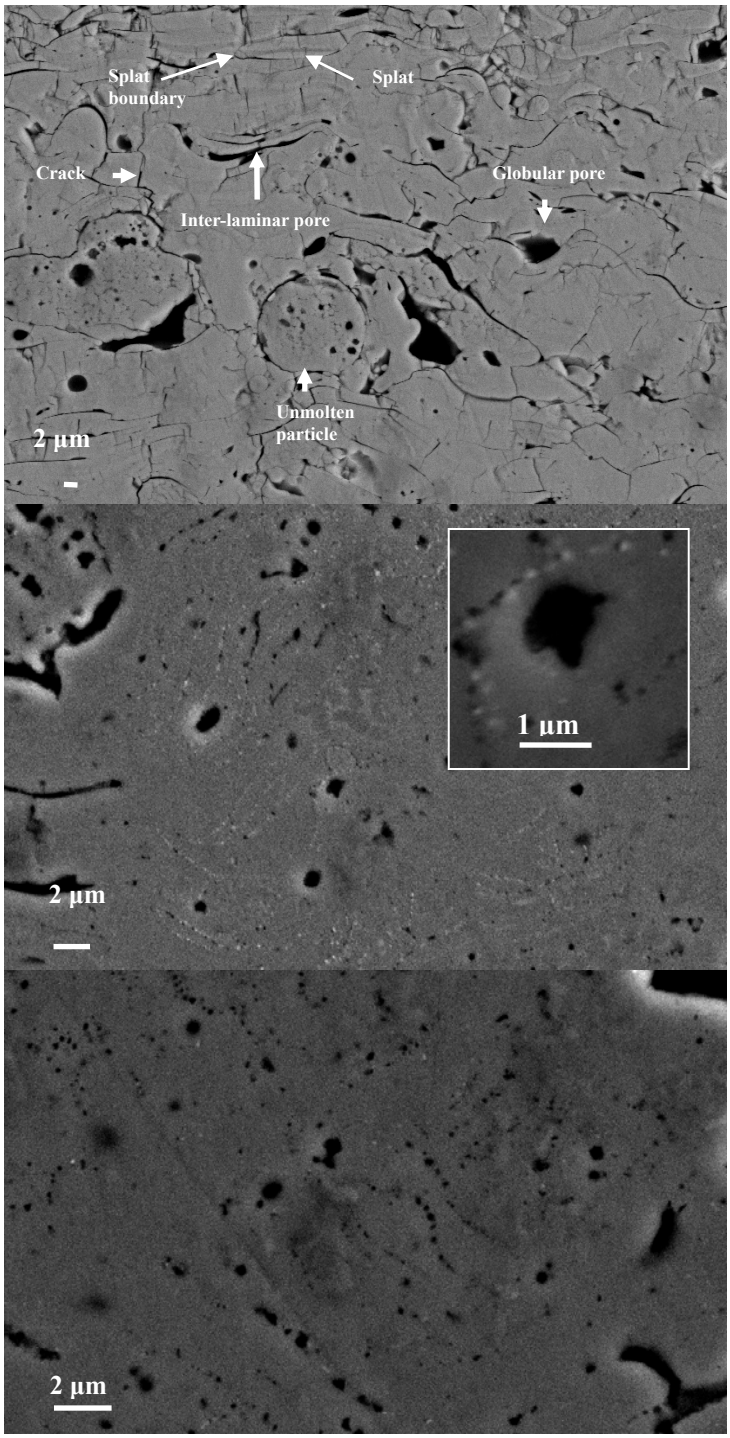

Figure 6-30, back scattered SEM cross sectional micrograph of plasma sprayed cobalt ferrite coatings, (a) as-sprayed, (b) 600°C annealed, (c) 800°C annealed.

6.3.2.4. Electrical resistivity

The electrical resistivities of cobalt ferrite coatings before and after annealing are

tabulated in Table 6-6. The resistivity increases several times after annealing at 600°C. This increase can be attributed to the cation redistribution. However, the resistivity increases a few orders of magnitude after annealing at 800°C. The reported electrical resistivity of Co_3O_4 is 10^3-10^4 Ω•cm [158], the formation of more insulating Co_3O_4 layer can be a possible reason for the increase in resistivity.

Table 6-6, resistivity of as-sprayed and annealed Co ferrite coatings.

	As-sprayed (Ω•cm)	600°C annealed (Ω•cm)	800°C annealed (Ω•cm)
Run884	2.74	11.06	83155
Run885	3.42	40.4	53000

6.3.2.5. Magnetic properties

Figure 6-31 shows the saturation magnetization and coercivity of as-sprayed and annealed coatings. Compared to reported value of sintered cobalt ferrite (80 emu/g), the as-sprayed coatings has very low saturation magnetization, due to the presence of anti-ferromagnetic phase of CoO. CoO not only does not contribute to magnetization but reduce the magnetization of ferrite phase by negative exchange. After annealing, CoO phase diminishes, so the saturation magnetization increases. The presence of CoO phase can present as a domain wall motion barrier, therefore the as-sprayed coating has a high coercivity. For run 885, after annealing in air at 600°C, the coercivity increases from 650 Oe to 800 Oe. There are two competing factors contributing to the coercivity, one is the presence of domain wall pinning antiferromagnetic phase, the other is the intrinsic coercive force of the ferrite. After annealing, the amount of CoO phase reduces, the coercivity due to this factor also reduces. However, annealing also modifies the cation distribution in the crystal lattice. Due to rapid solidification, the cations in as-sprayed coating are randomly distributed, during annealing; the cations gain enough kinetic energy to migrate to their equilibrium sites. Our previous calculation and other reference points out that the as the site occupancy goes from random to equilibrium, the magnetocrystalline energy increases so the coercivity increases. Therefore, the increase in coercivity after annealing at 600°C is due to that the increase of coercivity resulted from the increase of magnetocrystalline anisotropy energy can't be compensated by the decrease of coercivity resulted from the diminishing of CoO. CoO disappears after annealing at 800°C, so the coercivity drops. For comparison, the magnetization and coercivities of sintered pellets are also plotted in Figure 6-31. The magnetization of 800°C and 1000°C sintered pellets have the same saturation magnetization, but the 800°C sintered pellet has a much lower coercivity compared to that of 1000°C sintered sample. As can be seen from SEM micrographs (Figure 6-32), the 800°C sintered pellet consists of 100 nm diameter crystallites, while the 1000°C sintered pellet consists of tens of microns diameter grains.

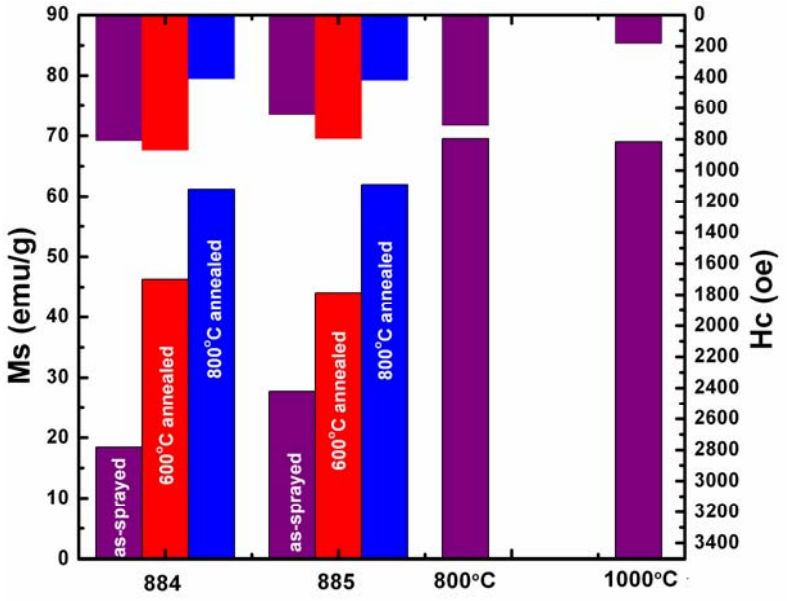

Figure 6-31, saturation magnetization (upward bars) and in-plane coercivity (downward bars) of as-sprayed (purple), 600°C annealed (red), and 800°C annealed (blue) for run 884 and 885 coatings and for 800°C and 1000°C sintered pellets.

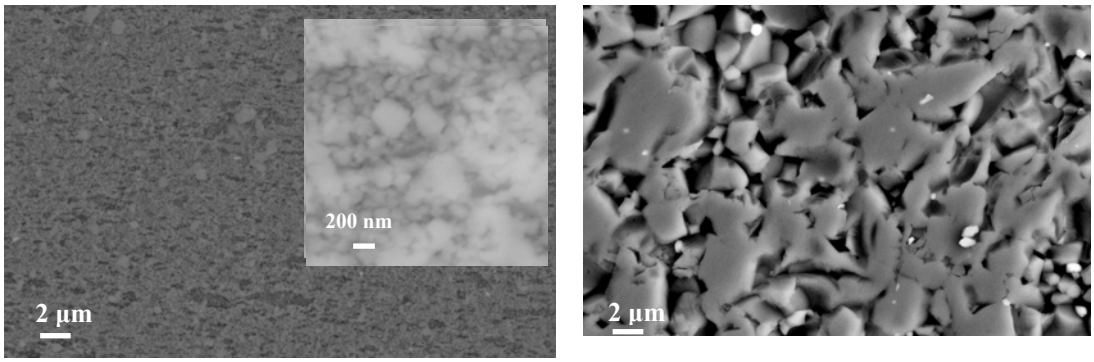

Figure 6-32, SEM cross sectional micrograph of pressed-sintered cobalt ferrite, (a) sintered at 800°C for 10 hours, (b) sintered at 1000°C for 10 hours.

6.3.2.6. Exchange bias study

Since the run 884 as-sprayed coating has a greater amount of antiferromagnetic rocksalt phase, the exchange bias effect can be more pronounced, also since there is another antiferromagnetic phase Co_3O_4 after annealing at 800°C in run 884 coating which is also interesting effect to look at, therefore only a set of run 884 samples are used to conduct the exchange bias study. Figure 6-33 shows the magnetization as a function of temperature when cooling down from 300K to 5k in the presence of 1T magnetic field. For the case of as-sprayed cobalt ferrite, from 300K to 283K, the magnetization increases as the temperature decreases, but starts to drop below 283K. The magnetization decrease is a result of antiferromagnetic exchange coupling. The as-sprayed cobalt ferrite coating is actually a

mixture of ferrimagnetic phase and antiferromagnetic phase. The temperature dependence of the magnetization of ferrite follows the classical Brillouin function as is the case for sintered Co ferrite pellet shown by the top panel of Figure 6-33. Above the Néel temperature, the antiferromagnetic $Co_xFe_{1-x}O$ is paramagnetic therefore does not contribute to the magnetization of the mixture. As the temperature decreases, the magnetization of cobalt ferrite increases as a classical ferromagnet. When the antiferromagnetic material cooled below its Néel temperature in the presence of an external magnetic field, the antiferromagnetism is turned on, therefore in the interface region, the spin of ferrite is antiferromagnetically coupled to the spin of (Co,Fe)O, resulting in the net magnetization decrease. The Néel temperature is estimated to be 283K in the as-sprayed cobalt ferrite coating. This Néel temperature is close to the reported value of CoO. The magnetization of 600°C annealed coating increases as temperature drops from 300K to 214K then starts to decrease from 214K down to 5K. This suggests that the Néel temperature of the antiferromagnetic phase is 214K. In the previous discussion, we have known that the lattice constants of the rocksalt phase in the as-sprayed coating and 600°C annealed coating are 4.248 Å and 4.267 Å, respectively. The lattice constant change suggests the compositional change in the rocksalt phase. Due to the interdiffusion with the ferrite phase, CoO becomes solid solution of CoO and FeO with more Fe content. The Néel temperature of CoO and FeO are 290K [158] and 198 K [159], respectively. By linear interpolation, we estimate the rocksalt phase to be $Co_{0.2}Fe_{0.8}O$ from Néel temperature. The magnetization of the 800°C annealed coating increases from 300K to 77K then decreases from 77K to 5K. This tells us that the Néel temperature of the dominant antiferromagnetic phase in this coating is about 77K. This phase should be the Fe doped Co_3O_4 spinel with lattice constant of 8.128 Å. The Néel temperature of pure Co_3O_4 is 40K [158], if the Co_3O_4 is doped with Fe^{2+} or Fe^{3+}, the Néel point can be higher.

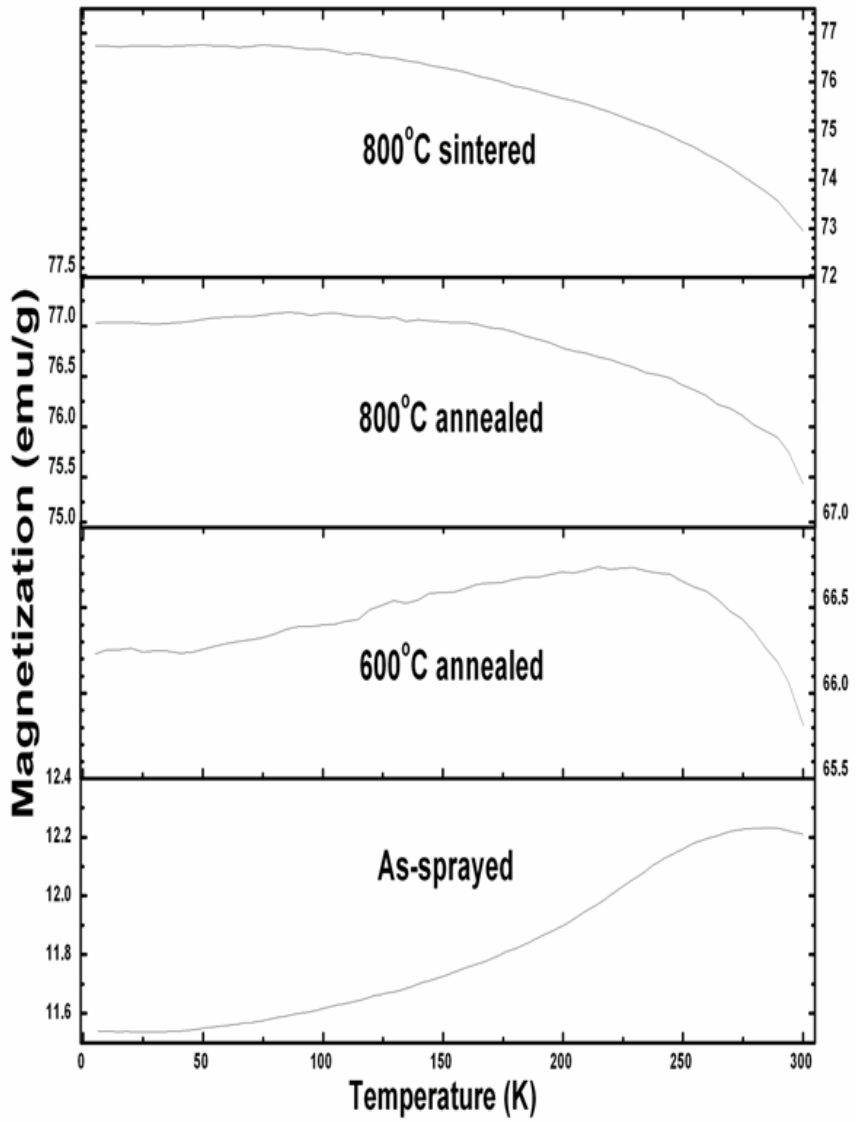

Figure 6-33, magnetization of as-sprayed cobalt ferrite coating, 600°C annealed, 800°C annealed coating and 800°C sintered pellet, from bottom to top, at 10,000 Oe as temperature decreases from 300K to 5K.

Figure 6-34 displays a few hysteresis loops of field cooled as-sprayed coating. As temperature decreases, the coercivity decreases and the hysteresis loop is biased toward the field cooling direction. Accompanying with exchange bias, H_{ex} (horizontal shift of the symmetric axis of the hysteresis loop), the hysteresis loop is also offset from the x-axis, this is called vertical shift, δM (the offset of the vertical symmetric axis). As illustrated by Figure 6-35, H_{ex} is calculated by $H_{ex} = \frac{H_C^{\downarrow} + H_C^{\uparrow}}{2}$, where $H_C^{\uparrow}$ and $H_C^{\downarrow}$ are upward coercivity and

downward coercivity, respectively. δM is calculated by $\delta M = \frac{M_S^{\uparrow} + M_S^{\downarrow}}{2}$, where $M_S^{\uparrow}$ and $M_S^{\downarrow}$ are the upward saturation magnetization and downward saturation magnetization, respectively. The exchange bias (H_{ex}), coercivity (Hc) and relative vertical shift ($\frac{\delta M}{M_s}$) of as-sprayed coating, 600°C annealed and 800°C annealed coatings as well as the 800°C sintered pellet are plotted in Figure 6-36.

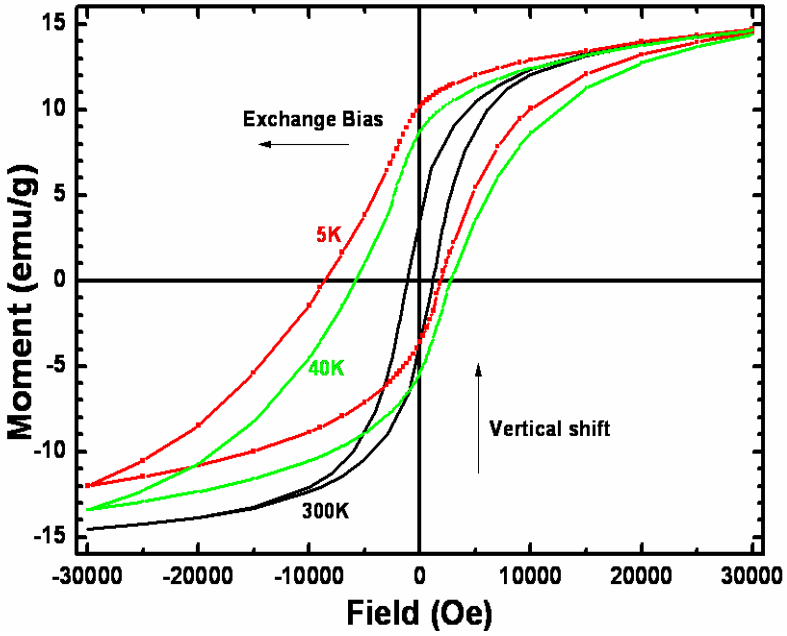

Figure 6-34, magnetic hysteresis loops of as-sprayed run 884 coating after being field cooled from room temperature to 5K. The cooling field is 10,000 Oe.

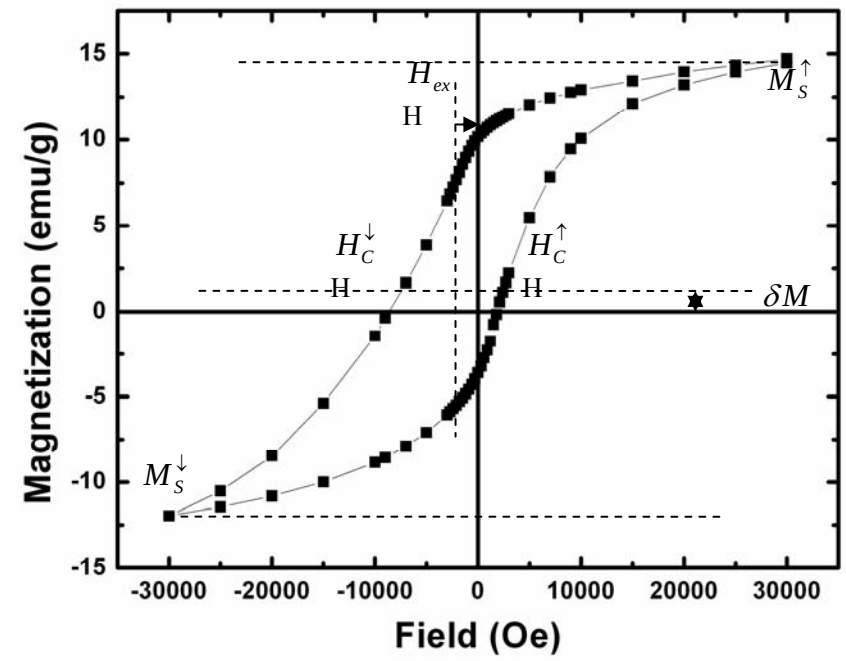

Figure 6-35, magnetic hysteresis loops of as-sprayed run 884 coating measured at 5K after being field cooled from room temperature to 5K. The cooling field is 10,000 Oe.

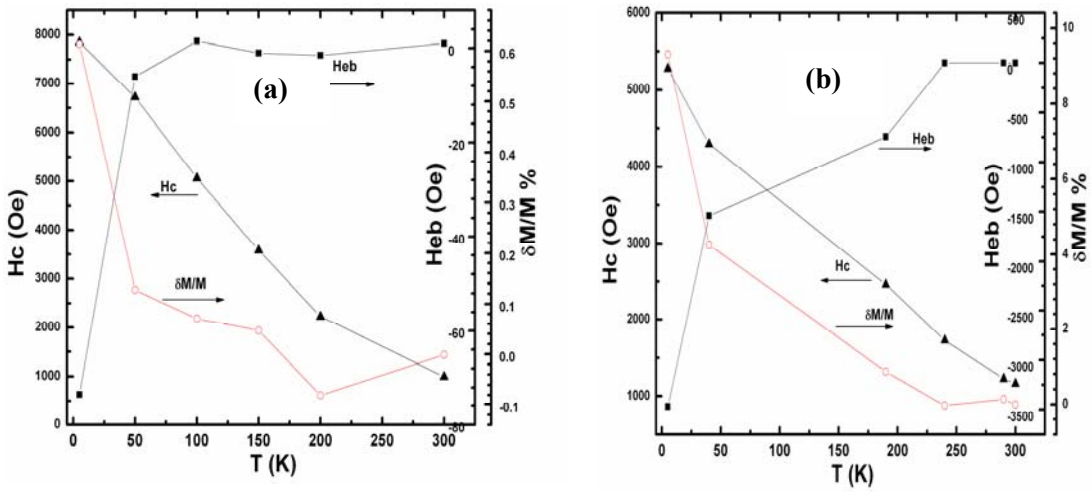

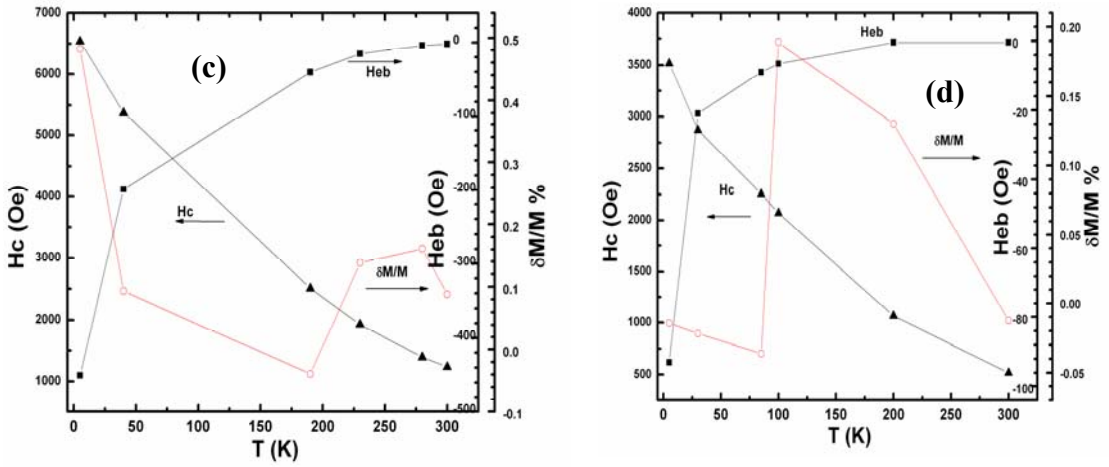

Figure 6-36, exchange bias, coercivity and vertical shift of (a) pressed-sintered Co ferrite at 800°C, (b) as-sprayed, (c) 600°C annealed and (d) 800°C annealed run 884 coating after being field cooled from room temperature to 5K. The cooling field is 10,000 Oe.

From Figure 6-37, it can be noticed that the coercivity in all samples increases almost linearly with the decrease of temperature; this is a direct result of increased magnetocrystalline anisotropy. As studied by Shenker [160], the magnetocrystalline anisotropy constant K_1 for Co ferrite can be expressed as $K_1 = 19.6\times10^6 \exp\left(-1.90\times10^{-5}T^2\right) ergs/cm^3$ from 0K to 340K. Since coercivity can be estimated by $H_c = \frac{h_c \bullet K_u}{M}$ [11], and since the saturation magnetization of ferrite at low temperature range does not change significantly as indicated by figure 5-68, the coercivity can be approximately expressed as $log\left(Hc\right) \propto -T^2$. Figure 5-72 confirms such relationship between coercivity and temperature.

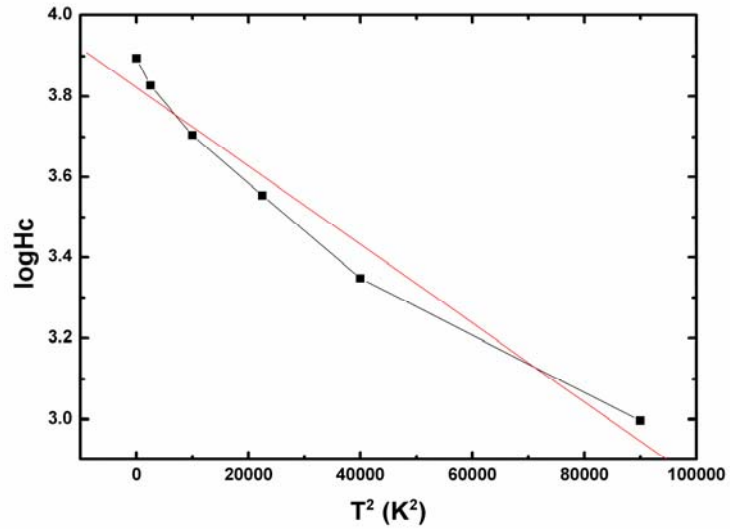

Figure 6-37, $\log(H_c)$ vs. T^2, for 800°C sintered pellet.

The exchange bias of pressed-sintered Co ferrite is very small until below 50K. This is consistent with the XRD result, for there exist only single phase of ferrimagnetic Co ferrite. The exchange bias for as-sprayed Co ferrite coating at room temperature is zero, meaning that the Néel temperature of antiferromagnetic phase is below room temperature. As the temperature decreases, the exchange coupling turned on, and the ferromagnetic particle is exchanged biased by the antiferromagnetic particles, which is CoO in this case. Similar to coercivity, the magnitude of exchange bias also depends on temperature as the result of the temperature dependence of the anisotropic energy of antiferromagnetic phases. For 600°C annealed coating, the exchange bias is much smaller than that of as-sprayed coating at corresponding temperature. As studied by XRD and magnetic cooling curve, the antiferromagnetic phase in this case is (CoFe)O, whose magnetocrystalline anisotropy is smaller than that of pure CoO (K_1=5×10^6 erg/cm^3 or 1.1×10^8 erg/cm^3 by different references, [161]), therefore the exchange coupling effect is greatly reduced. For strong antiferromagnet, the exchange bias can be expressed as $H_{ex} = -\frac{J}{M_s t_F}$, where J is the exchange energy per unit area of the interface coupling, M_s is the saturation magnetization of the ferromagnetic phase and t_F is the thickness of ferromagnetic layer [11]. The exchange bias decreases after 600°C annealing due to three effects: the decrease of exchange energy, the increase of magnetization and the increase of ferrite particle size. There is an obvious positive vertical shift in as-sprayed coating. The positive vertical shift has been reported to be due to the induced magnetic moments in the antiferromagnetic phase are pinned to the cooling field direction [162]. So in this case, the interfacial magnetic spin of CoO is aligned with the cooling field direction which is the magnetization of B site cations. Since the exchange coupling in oxides are antiferromagnetic super-exchange, the Co^{2+} in CoO is antiparallel exchange with Fe^{3+} in the A site of Co ferrite in order to be parallel to the magnetic field direction in which direction B site spins are taking. The exchange coupling is sketched in Figure 6-38. In 600°C annealed coating, the vertical shift is also positive below Néel temperature, suggesting that the induced magnetic moment is again pinned to the field cooling direction.

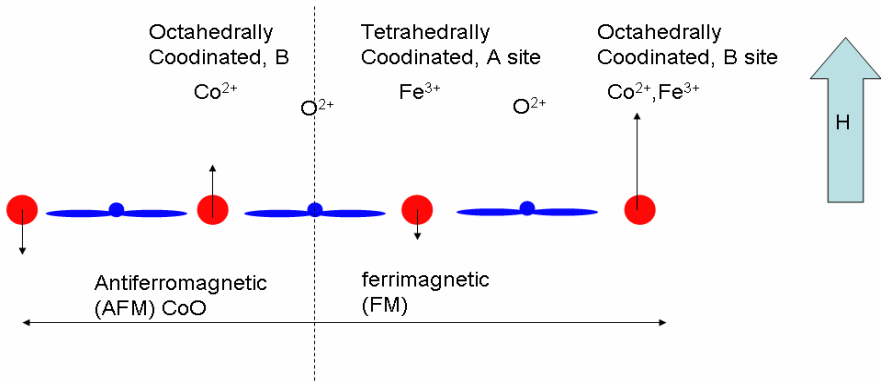

Figure 6-38, exchange coupling model for CoO and Co ferrite.

For 800°C annealed coating, the exchange bias is further decreased. As indicated by XRD study and cooling field magnetic curve, the dominant antiferromagnetic phase is

Co_3O_4. The vertical shift below Néel point is negative. But it is very small, so it is not sure this is within measurement accuracy, therefore we should not jump to conclude that the induced magnetic moments are pinned opposite to the cooling field direction in this case. As-sprayed $CoFe_2O_4$ has by far the largest exchange bias (-3500 Oe) and the largest $\frac{\delta M}{M}$ (9%) of the four process conditions displayed in Figure 6-36. Therefore, CoO is the best antiferromagnet for exchange bias compared to CoO-FeO and Co_3O_4.

6.3.2.7. Magnetostriction

The magnetostriction of as-sprayed Co ferrite coating on alumina substrate has been measured by laser deflection technique. Magnetostriction is also measured by strain gage in three directions (1) field parallel to film and strain gage (parallel), (2) field parallel to film and perpendicular to strain gage (traverse), and (3) field perpendicular to film and strain gage (perpendicular). In perpendicular orientation, the coating/substrate bilayer is subjected to a uniaxial stress/strain, therefore $\varepsilon_{zz} = -2\left(\varepsilon_{xx} + \varepsilon_{yy}\right) * \frac{\upsilon_s}{\left(1-\upsilon_s\right)}$ with $\varepsilon_{xx} = \varepsilon_{yy}$. Then we can calculate the strain in z direction (i.e. field direction) and compare the result to laser deflection experiment. The result is shown in Figure 6-39. The magnetostriction measured by strain gage is smaller than that obtained from laser deflection measurement, most likely due to poor bonding between the strain gage and sample. However, we could not make a better bonding because larger pressure to bond the strain gage will crack the fragile sample.

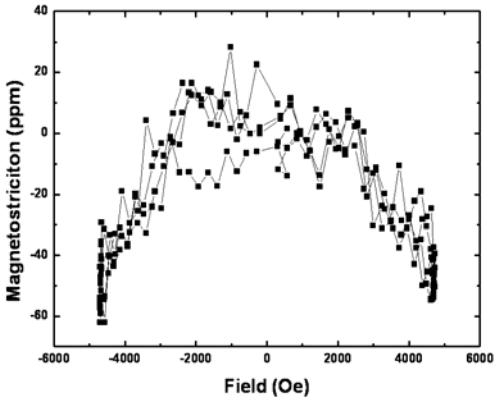

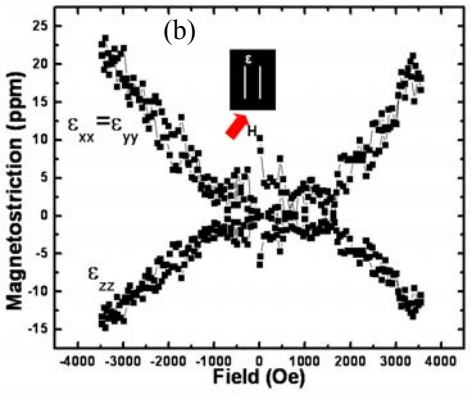

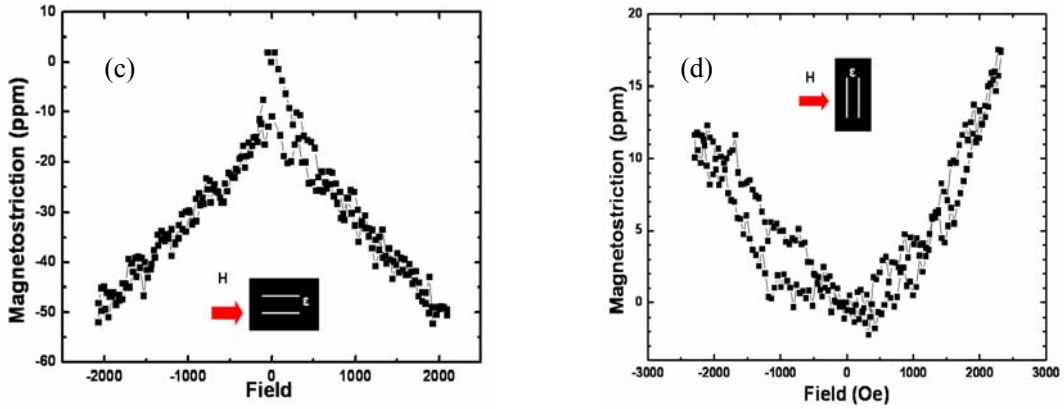

Figure 6-39, magnetostriction of as-sprayed run 885 Co ferrite measured by laser deflection with field perpendicular to film (a), strain gage with field perpendicular to film (b), field parallel to film and strain gage (c), and field parallel to film yet perpendicular to strain gage (d).

The strain derivative $\frac{d\lambda}{dH}$ of as-sprayed run 885 Co ferrite coating calculated as the slope of strain-field curve from the laser deflection technique is $1.55\times10^{-10}A^{-1}\bullet m$. This value is almost an order of magnitude lower than that of press sintered cobalt ferrite ring ($1.0\times10^{-9}A^{-1}\bullet m$). In our experimental setup, the Co ferrite coatings are not saturated yet, therefore to estimate the saturation magnetostriction, we extrapolate the magnetostriction data obtained from perpendicular orientation to saturation field of 15,000 Oe obtained from hysteresis loop measurement. Thus an estimated saturation magnetostriction λ_s is -186 ppm. This value is slightly deviated from the literature value of -210 ppm and previously obtained λ_s in plasma sprayed co-precipitated Co ferrite coatings. Since the rocksalt phase is CoO, then the ferrite phase is Fe-rich Co ferrite, whose K_1 value should be larger than that of stoichiometric Co ferrite (K_1 values of $Co_{0.8}Fe_{2.2}O_4$, $CoFe_2O_4$, and $Co_{1.1}Fe_{1.9}O_4$ are 3.9×10^6 erg/cm^3, 2.7×10^6 erg/cm^3, and 1.8×10^6 erg/cm^3, respectively [163]), the magnetostriction should be larger than that of stoichiometric ferrite. Therefore the reduction in λ_s is not able to be explained by change in magnetocrystalline anisotropic energy. A possible explanation could be that the uncompensated spins in rocksalt phase are exchange coupled with Co ferrite phase even above its Néel temperature; CoO has a small positive magnetostriction [164] which will offset the negative magnetostriction of Co ferrite. In the previous plasma sprayed co-precipitated Co ferrite, there is less CoO, therefore, its λ_s (-217 ppm) is much closer to the literature value.

For comparison, magnetostriction of pressed sintered Co ferrite at 800°C is also measured by strain gage method and the result is presented in Figure 6-40. Again, due to the poor bonding between the strain gage and Co ferrite pellet, the measured magnetostriction is still far below its literature value. It can be noted that the λ_s-H curves of plasma sprayed deposits do not show hysteresis. The hysteresis does exist in M-H curves (Figure 6-41) in both parallel and perpendicular magnetizations.

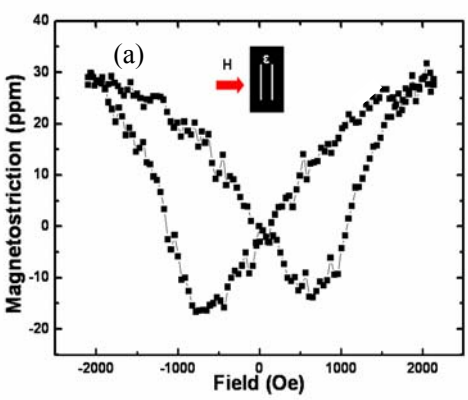

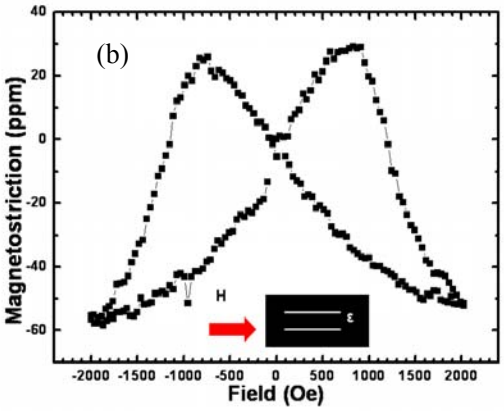

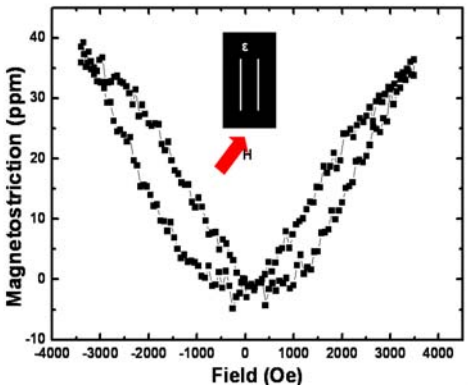

Figure 6-40, magnetostriction of 800°C sintered Co ferrite pellet measured by strain gage in three directions: (a) traverse, (b) parallel, and (c) perpendicular.

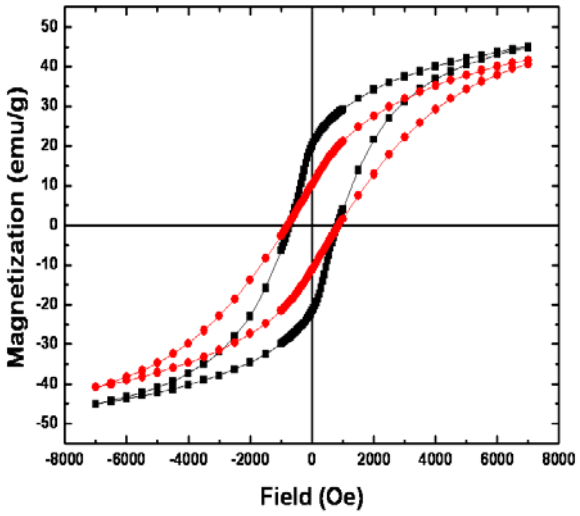

Figure 6-41, M-H curves of as-sprayed run 885 Co ferrite coating. The black symbol and line represent in-plane magnetization, while the red symbol and line represent the perpendicular magnetization.

The magnetostriction of annealed coatings has been measured on 600°C annealed run 885 coatings by laser deflection method. The result is presented in Figure 6-42. The

annealing time is only 30 minutes to avoid too much oxidation of the metallic substrate. It seems that the magnetostriction of annealed coating has not changed significantly, maybe due to the annealing time is not long enough.

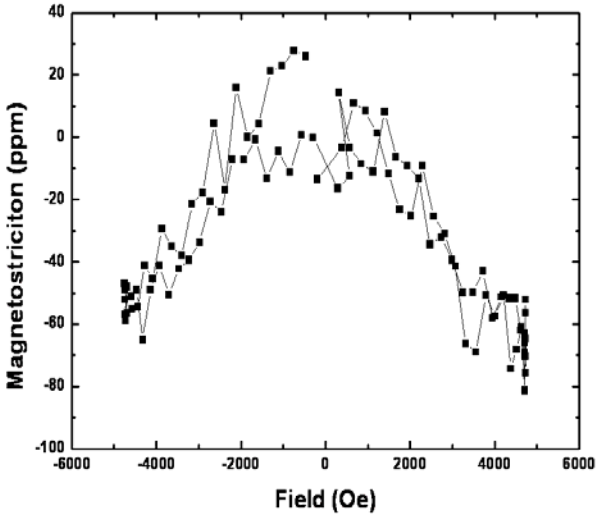

Figure 6-42, magnetostriction of 600°C annealed run 885 Co ferrite measured by laser deflection with field perpendicular to film.

Chapter 7 Ferrite process maps—an integrated study of the relationship between process, microstructure and properties

7.1. Ferrite process map study

In this study, we aim to build a relationship mapping the process conditions to microstructure and properties of ferrite coatings. The plasma spraying process is a very complex processing method; a lot of variables can affect the particle history in the flame resulting in different deposits, such as gun current, gun traverse speed, nozzle type and size, the composition of gas mixture, the choice of carrier gas, the flow rate of each gas, the powder feeding rate, the powder injection angle, the temperature of substrates, the surface roughness of the substrates, etc. These conditions, except for those related to the substrate, will change the particle state which includes the melting condition and fly trajectory of the particle, and the particle state will eventually determine the coating microstructure and physical properties. So we first try to relate the process parameters with the most important particle state variables such as temperature and velocity, or alternatively, the Melting Index and the Reynolds number. This correlation is called the first order process map. Then we try to relate the particle state with the splat morphology, the microstructure of the coating, the physical properties and functional performances of the coating, which is the second order process map.

In this study, we change three important spraying parameters to tune the particle temperature and velocity; they are gun current, total mass flow and volume percentage of H_2. The material used for process map study is MnZn ferrite (FLP17035-1). The selection of the material is based on three concerns: (1) MnZn ferrite is used to make composites with NiFe and NiCo in the later studies, a better understanding of the process of plasma spraying ferrite will be a good starting point for the better understanding of the process of composites, (2) the physical properties such as melting temperature, heat capacity, thermal conductivity of Co ferrite is very similar to those of MnZn ferrite, so the melting behavior of Co ferrite is very close to that of MnZn ferrite, and (3) the large commercial use and availability of MnZn ferrite powders.

7.1.1. Design of experiments (DoE)

An extended central composite experimental design was used to generate a carefully controlled parameter set so as to produce a range of process conditions. Three main process variables were chosen, that is: total mass flow of the plasma gas (N_2+H_2), volume ratio of H_2 with respect to the primary gas, and gun current. The volume representation of the DoE is presented in Figure 7-1. The corners of the cube and the body center of the cube represent a total of 9 spray experiments. The center condition was repeated two times (at the beginning and the end) throughout the measurement sequence.

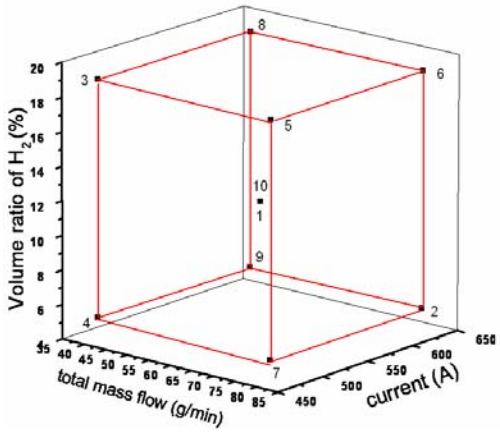

s

Parameter	Lower limit (-a)	Center (0)	Upper limit (a)
Gas flow (g/min)	40	60	80
H_2 volume ratio (%)	0.050	0.105	0.160
Arc current (A)	466	550	634

Figure 7-1, visual representation of the design of experiments (DoE) layout identifying the maximum operating range of each variable. The appended table provides specific values for the upper and lower limit.

7.1.2. First order process maps

As shown in Figure 7-1, ten experiments with nine different experimental conditions have been conducted to collect the particle state data. Experiment No.1 and No.10 are of the same conditions, they are repeated to test the stability of process conditions. Figure 7-2 shows the average particle temperature and velocity of these ten experiments, collected from AccuraSpray sensor. The average temperature and velocity of experiment No. 1 and No. 10 are different, meaning that even for the same process parameters; the particle state can drift over time which is a drawback of plasma spraying process. The vectors on the upper part of Figure 7-2 indicate how the three variables affect the particles response. It can be noticed that increase of H_2 ratio increases the temperature significantly while slightly decreases the velocity. Increase of the total mass flow will significantly increase the particle velocity while slightly decrease the temperature. Current input increases both the particle momentum and temperature. The effects of H_2 percentage on average particle temperature and total mass flow on average particle velocity are also visualized in Figure 7-3 and Figure 7-4, respectively. As illustrated by the dotted circles in Figure 7-3 and Figure 7-4, it is clear to see that for the same H_2 percentage and total mass flow, the higher the current, the larger the particle temperature and velocity.

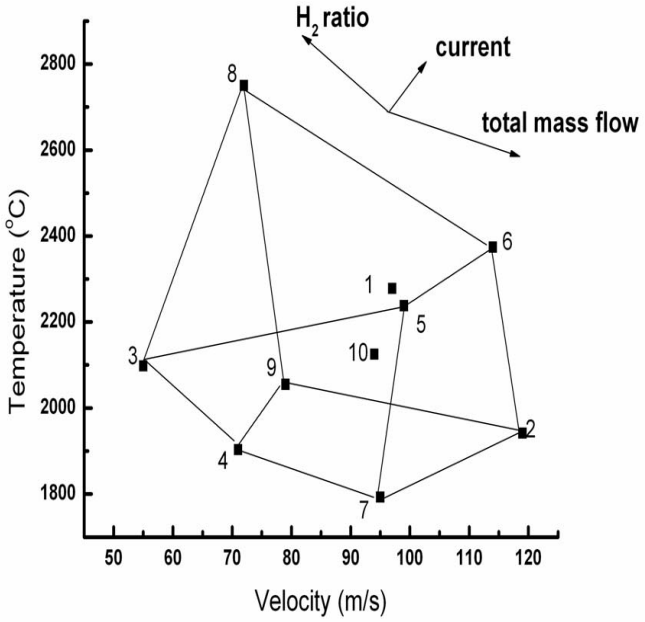

Figure 7-2, average temperature and velocity of process map study.

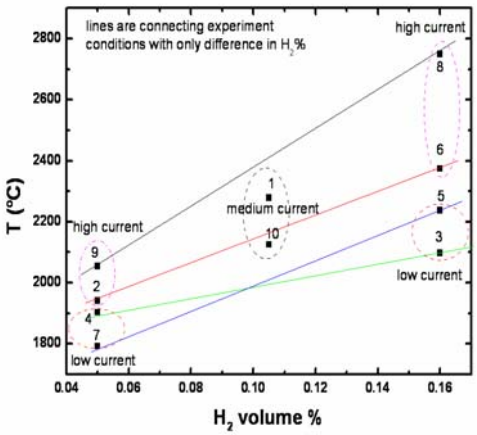

Figure 7-3, the effect of H_2 volume percentage on temperature. Lines are drawn between two experiments with all other experimental conditions the same except the volume ratio of H_2 gas.

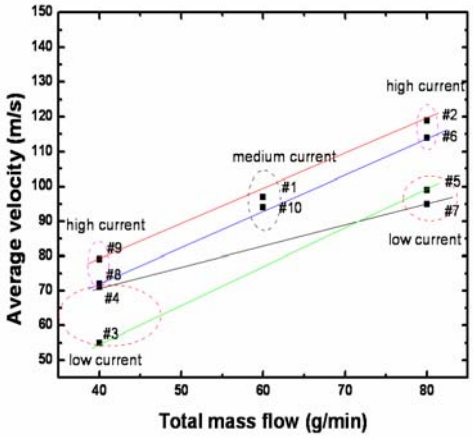

Figure 7-4, effect of total mass flow rate on the average velocity. Lines are drawn between two experiments with all other experimental conditions the same except the total gas flow.

We can see that the average temperatures of the above experiments are all higher than the melting point of MnZn ferrite (~1570°C), however the excess of temperature doesn't necessarily mean that the powders are fully molten. The degree of melting depends on (1) the temperature difference between the melting temperature and the particle surface temperature which can be measured by DPV or AccuraSPRAY sensors, (2) the duration of

particle in plasma flame, (3) how fast the heat can be transferred from the surface to the core of the particle which is determined by the thermal conductivity of the material, (4) the density of the material, (5) the latent heat of melting, and (6) the size of the particle. Therefore, a new concept, Melting Index (MI) is introduced by Vaidya [116] and Zhang [165] characterize the melting state of the particle, expressed as:

$$M.I. = \frac{\Delta t_{fly}}{\Delta t_{melt}} = \frac{24k}{\rho h_{fg}} \cdot \frac{1}{1+4/Bi} \cdot \frac{(T_f - T_m) \cdot \Delta t_{fly}}{D^2}$$

With Bi is another dimensionless number called the Biot number and defined as:

$$Bi = \frac{hL_c}{k}$$

The definition of the above mentioned parameters have been discussed in Chapter 3. If the melting index is smaller than 0, it means that the particle is totally not molten, if the MI is equal to 1, it means that the particle is fully molten, if the MI is somewhere in between 0 and 1, it means that the particle is partially molten. The greater the MI value, the better the melting condition of particles.

Also, in addition to melting index, Reynolds number is used to replace particle velocity to represent the momentum of the particle. It is defined as:

$$\mathrm{Re} = \frac{\rho v D}{\mu}$$

Where v and μ are the velocity and the fluid viscosity of molten droplets.

For each process condition, DPV sensor collects temperature and velocity data of 10,000 particles. Using appropriate thermal physical property data of MnZn molten droplet, we can plot the histogram of MI and Re number over 10,000 particles, as shown in Figure 7-5 (a) and (b). The average MI and Re values are obtained by taking the mean value of the 10,000 particles, they are plotted to build the first order process map, as shown in Figure 7-6. Again, we can see that for experiment No. 1 and No. 10 have very different MI and Re values despite the fact that they have the same operating conditions. Similar to the T-V plot, the H_2 volume percentage increase the Melting Index and decrease the Reynolds number, the total mass flow increase the Reynolds number while decrease the Melting Index, the current increase both the Melting Index and Reynolds number.

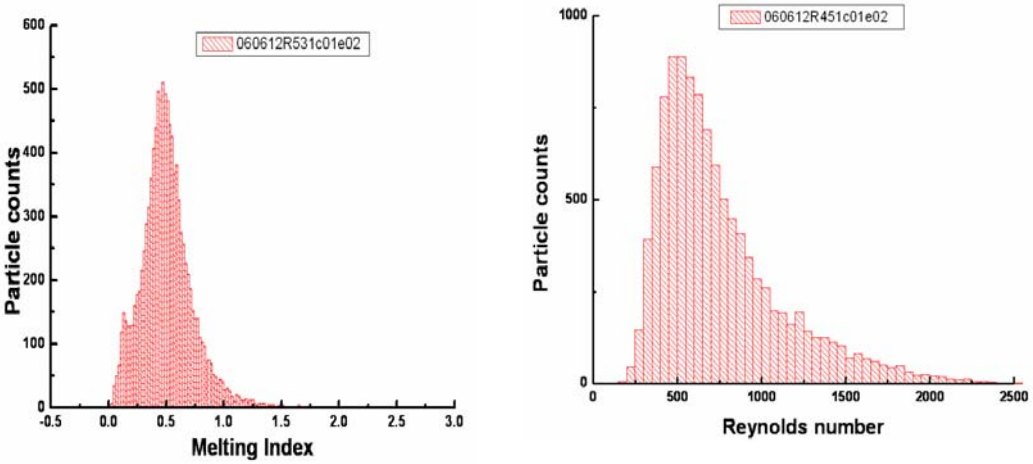

Figure 7-5 (a), histogram of MI for 10,000 particles in experiment No. 1. (b), histogram of Re for 10,000 particles in experiment No. 1.

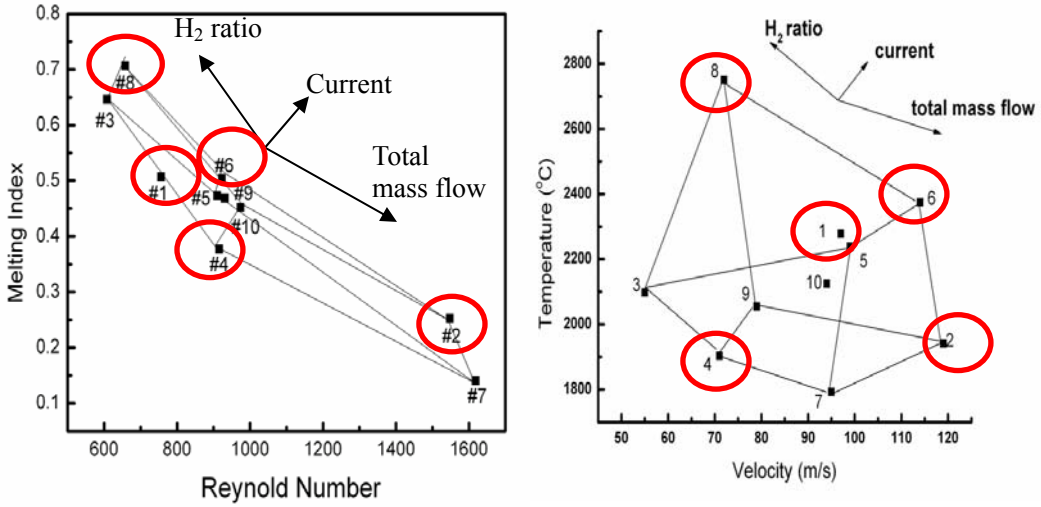

Figure 7-6, left, average melting index (MI) and Reynolds number; right, comparison with T-V first process map. The red circles indicate the deposition experiments which are conducted later.

7.1.3. Second order process maps

Among the nine previous conditions, we selected 5 of them for splat and coating deposition and further characterizations. They are experiment conditions No. 4, 2, 1, 6 and 8, and the experiment run numbers are 452, 453, 454, 455 and 456, respectively, as indicated by the red circles in Figure 7-6. These conditions are basically the four extreme conditions (No. 4, 2, 6 and 8) and one medium condition (No. 1) in the T-V or MI-Re first process map, representing low T (MI) and low V (Re), low T (MI) and high V (Re), high T (MI) and high V (Re), high T (MI) and low V (Re), and medium T (MI) and V (Re) extremes. In the following sections, we will present the physical properties and microstructures under these five spraying conditions. The relationship between these properties and particle histories are correlated.

7.1.3.1. Splat morphology and microstructure

The optical microscope images of splats collected on polished stainless steel substrates under the five conditions are shown in Figure 7-7. The splats all have cracks which are a result from the quenching stress and thermal mismatch between the MnZn ferrite and stainless steel. It is noteworthy that the splats under high Reynolds number have very significant splashing due to the strong impact on the substrates. Using the Zygo profiler, we have measured the diameters and thickness of 20 MnZn splats of each sample. They are used to calculate the splat flattening ratio defined as:

$$FR = D / d$$

Where D is the diameter of the splat and d is the diameter of the original molten

droplet. d is equal to $\sqrt[3]{\frac{3}{2}D^2t}$ by assuming that the volume is conserved. The average flattening ratio is plotted in Figure 7-8. The dotted lines are sketched to speculate the lines with equal flattening ratio. It seems that the combination of large MI and Re value gives a large flattening ratio. It is intuitive to explain that particles with high temperature or melting index but with low velocity or Reynolds number are not easy to spread on the substrate due to small mechanical impact, on the other hand, particles of opposite situations are not easy to spread on the substrate due to the low viscosity at lower temperature.

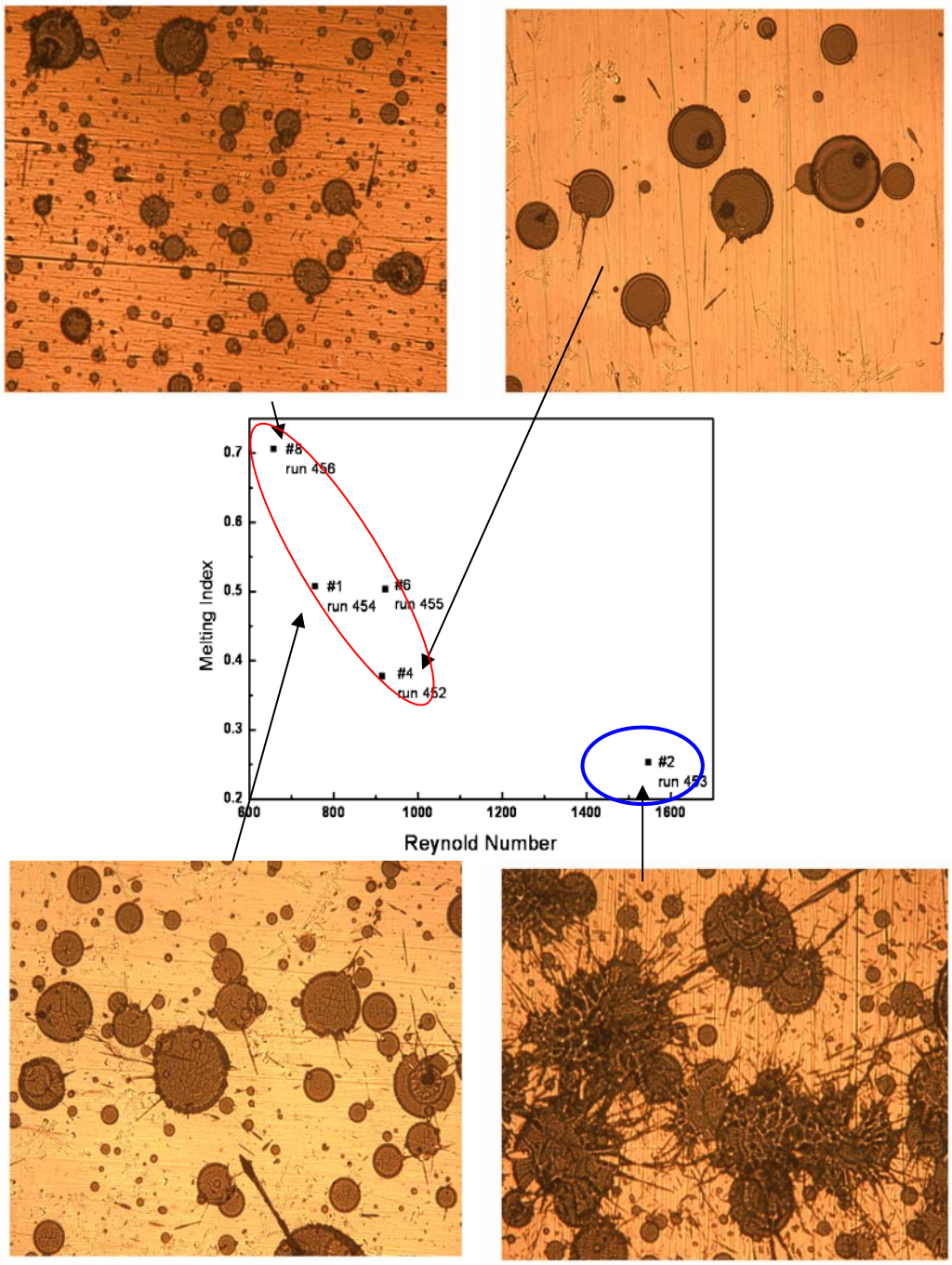

Figure 7-7, optical microscopic images of splats collected in run 452, 453, 454 and 456. These splats are all on polished stainless steel substrates. Splats of run 452, 454, 456 do not show significant splashing while splats of run 453 have significant splashing.

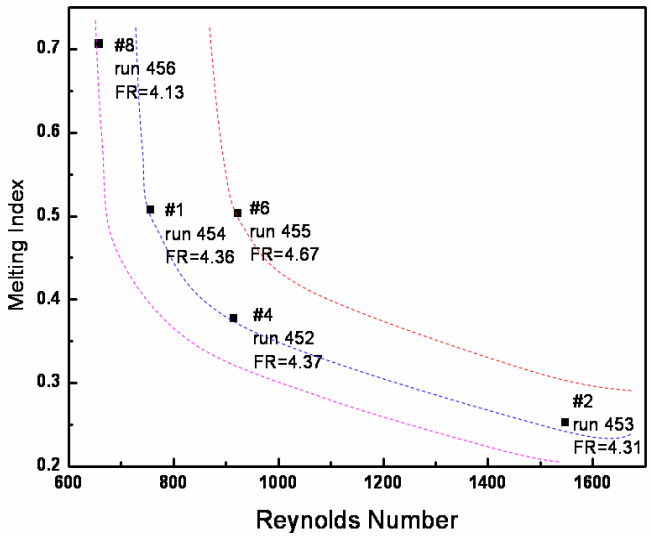

Figure 7-8, flattening ratio (FR) on the MI-Re plot, dotted lines are sketched to simulate the iso-lines for flattening ratio.

Optical microscope images of polished cross section of as-sprayed MnZn ferrites are shown in Figure 7-9. Images have been taken over 20 different locations of each sample, and average porosities are therein calculated by image analysis method. The relationship between average porosity and MI, Re values and flattening ratio is shown in Figure 7-10. The porosities of these five coatings are very close, ranging from 18.9 to 22.2%. It doesn't seem that there is a clear correlation between melting index or Reynolds number or the flattening ratio with the total porosity. If we don't consider coating run 454 which may seem a little abnormal in the trend, as shown in the Figure 7-9, by throwing the data point out, we might find that in the inner part of the MI-Re space, one might find a denser coating, while in the outer part of the MI-Re space, one might find a porous coating. This is reasonable, since higher melting index and Reynolds number may result in both splat fragmentation and splashing which may in turn result in loose splat packing.

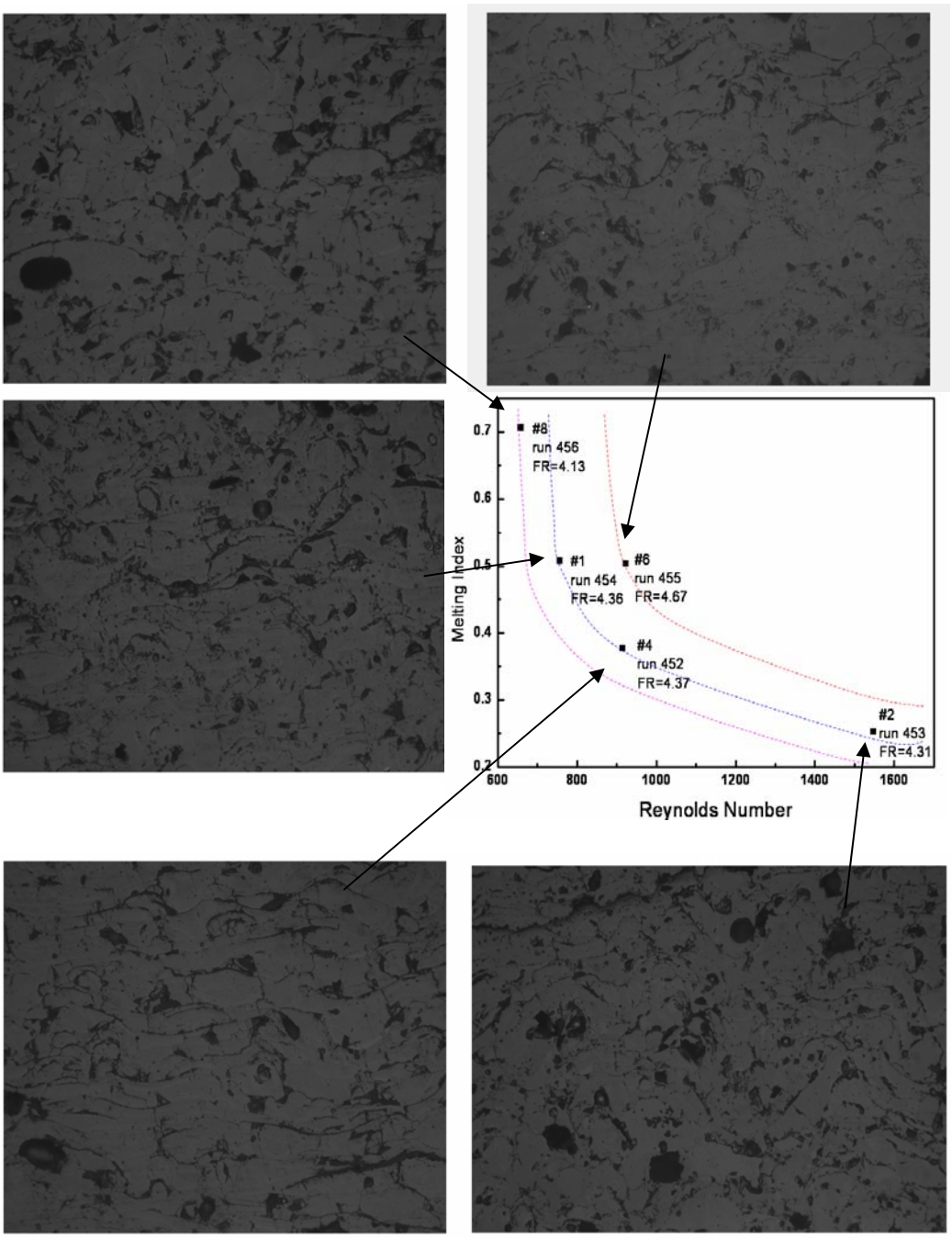

Figure 7-9, optical microscope images of polished cross section of as-sprayed MnZn ferrites. These images are all of 500 magnifications.

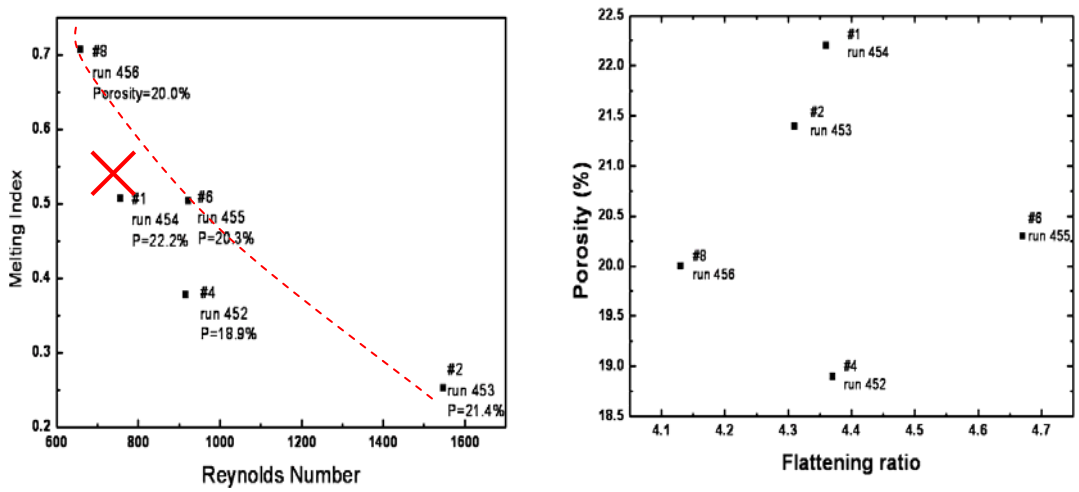

Figure 7-10 (a), porosity vs. MI-Re numbers. (b), porosity vs. flattening ratio.

7.1.3.2. FeO decomposition

XRD experiments are conducted on the feed stock powder for spraying and the surface of the as-sprayed coatings as well as corresponding crushed powders of the five as-sprayed deposits. There is no difference in the XRD patterns obtained from the surface of as-sprayed coatings and their crushed powders, indicating no significant texture in the coating structure. The powder XRD patterns are shown in Figure 7-11. The powder for spraying is of purely MnZn ferrite spinel structure with the lattice constant of 8.440 Å. However after spraying, the coatings all have a secondary phase of wuestite phase. This lattice constant of wuestite is 4.305 Å, comparing to that of FeO (Fm3m, 4.307 Å, JCPDS 6-615), this wuestite is most likely to be FeO rather than MnO (Fm3m, 4.445Å, JCPDS 7-230) or their solid solution. The wuestite phase is developed due to deoxidation in the plasma plume as a result of high temperature and low oxygen partial pressure. The oxygen loss resulting in a oxygen deficient ferrite and this non-stoichiometric ferrite solidifies into ferrite and wuestite similar to that of Fe_3O_{4-x} which is shown in Fe-O phase diagram [91]. The lattice constant of MnZn ferrite under each spraying conditions are: 8.454 Å, 8.452 Å, 8.453 Å, 8.454 Å, and 8.455 Å for run 452, 453, 454, 455, and 456, respectively. The lattice constants of as-sprayed ferrites are larger than that of the starting powder. This can be explained by the change of chemistry of the ferrite, the ferrite becomes Mn rich than the starting powder due to Zinc loss and Fe separation from the ferrite. The lattice constant of $FeFe_2O_4$, $ZnFe_2O_4$ and $MnFe_2O_4$ are 8.396 Å, 8.441 Å, 8.499 Å respctively [JCPDS 19-629, 22-1012, 10-0319]. The ratio between the peak intensities of the major peaks of each phase agree well with standard powder XRD patterns, therefore, the ratio between the strongest peak of ferrite (311) and the strongest peak of FeO (200) is used to determine the weight percentage of FeO phase and ferrite phase.

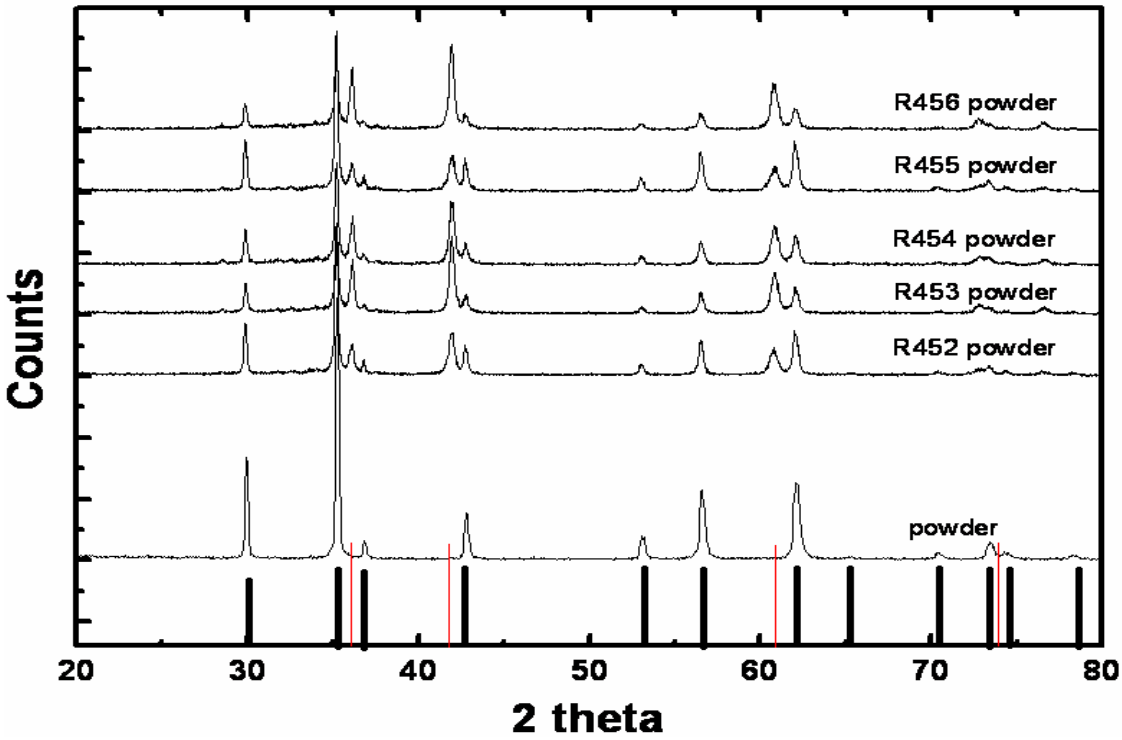

Figure 7-11, XRD patterns of MnZn ferrite powder (FLP17035-1), surface of as-sprayed coating run452 and crushed powders of as-sprayed coating run 452 to 456. The black lines in the bottom indicate the peak positions for MnZn ferrite spinel; red lines indicate the peak positions of FeO wuestite.

The weight percentages of FeO wuestite in the as-sprayed coatings are: 22%, 46%, 38%, 18% and 54% for run 452, run 453, run 454, run 455 and run 456, respectively. These percentages are plotted as a function of average particle temperature and in-flight time (in-flight time is inversely proportional to particle velocity (Figure 7-12) and as a function of average melting index and Reynolds number (Figure 7-13), seeking to bulid the relationship between particle history and secondary phase formation.

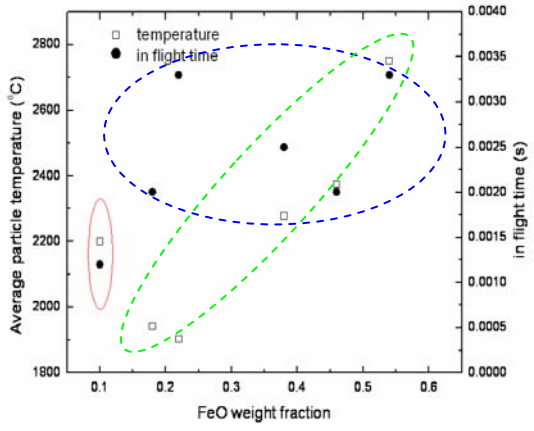

Figure 7-12, FeO weight fractions in as-

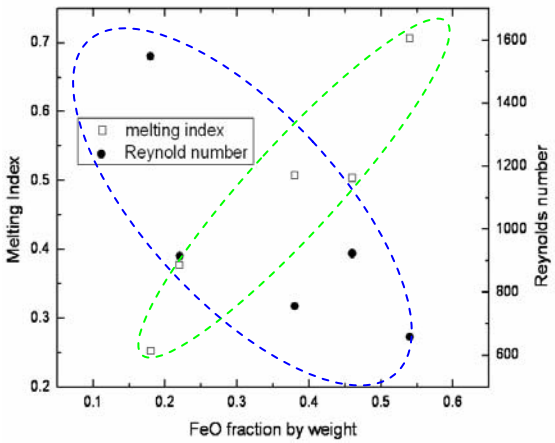

Figure 7-13, FeO weight fractions in as-

sprayed MnZn ferrite coatings vs. average particle temperatures and velocities. The data in red circle is from previous study by Yan [80].

sprayed MnZn ferrite coatings vs. average melting indices and Reynolds numbers.

From Figure 7-12, we can see that the FeO weight fraction is almost positively correlated to the particle temperature. If we assume during spraying, oxygen loss is like $Fe_3O_4 = Fe_3O_{4-x} + \frac{x}{2}O_2$, and the liquid Fe_3O_{4-x} forms FeO and Fe_3O_4 when recystallizing. Then the oxygen loss is proportional to the amount of FeO wuestite. If we assume that the rate of reaction of $Fe_3O_4 = Fe_3O_{4-x} + \frac{x}{2}O_2$ depends on temperature according to the Arenius equation as $A \bullet \exp\left(\frac{-\Delta G}{RT}\right)$ (A is a constant and G is the activation energy), then as temperature increases, the decomposition increases too. Although we should expect that the longer the particle is in the flame, the more FeO formation, but we don't see such a clear trend in the FeO% vs. in-flight time plot, as illustrated as the scattered points in the blue circle. Maybe the dependence on the in-flight time is obscured by the more evident difference in temperature (more than 900°C) compared to the small difference in in-flight time (just a millisecond). When the particle velocity is rearranged to the dimensionless numbers of Reynolds number, the dependence is clearer (as show by the blue circle in Figure 7-13). The weight fraction of FeO is inversely proportional to the Reynolds number.

Since the FeO wuestite is a metastable phase in air under 560°C according to the Fe-O phase diagram, the reaction $4FeO = Fe_3O_4 + Fe$ is taking place when the coating is subject to annealing in the air. Therefore the FeO peaks diminish as after annealing in the air at 400°C for an hour, as shown in Figure 7-14. The Fe is further oxidized to from Fe_3O_4 adding to the formation of Fe_3O_4 from phase forming from the reaction $4FeO = Fe_3O_4 + Fe$. Fe_3O_4 magnetite is also a spinel structure and its lattice constant is very close to that of MnZn ferrite, their peaks overlap with each other, therefore we can only see the spinel peaks. The weight fraction of the FeO phase is also calculated from the peak intensity ratio between the spinel (311) peak and wuestite (200) peak. The weight percentages of FeO are 9%, 17%, 13%, 8% and 21% in the 400°C air annealed coatings for run 452 to 456, respectively.

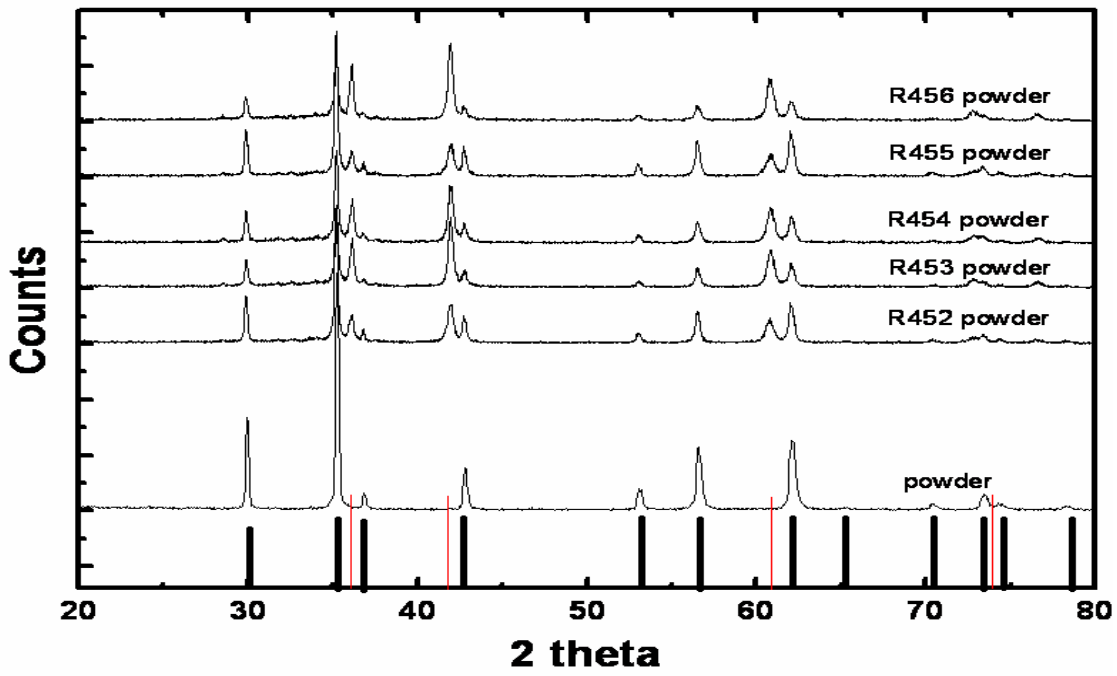

Figure 7-14, XRD patterns of plasma sprayed MnZn ferrite annealed in the air at 400°C for an hour. The black lines in the bottom indicate the peak positions for MnZn ferrite spinel; red lines indicate the peak positions of FeO wuestite.

Annealing in the air at higher temperature (>560°C but <800°C) will oxidize Fe_3O_4 into Fe_2O_3 hematite, as shown in Figure 7-15. At the other hand, at higher temperatures, getting enough kinetic energy, Fe in Fe_3O_4 phase can diffuse into MnZn ferrite phase, changing the composition of the MnZn ferrite at the as-sprayed state. The percentages of Fe_2O_3 hematite is again calculated by taking the ratio between ferrite (311) peak, and the hematite (104) peak. The weight fractions of nonmagnetic Fe_2O_3 hematite phase in the 600°C air annealed coatings are: 10%, 14%, 12%, 7% and 13% for run 452 to 456, respectively.

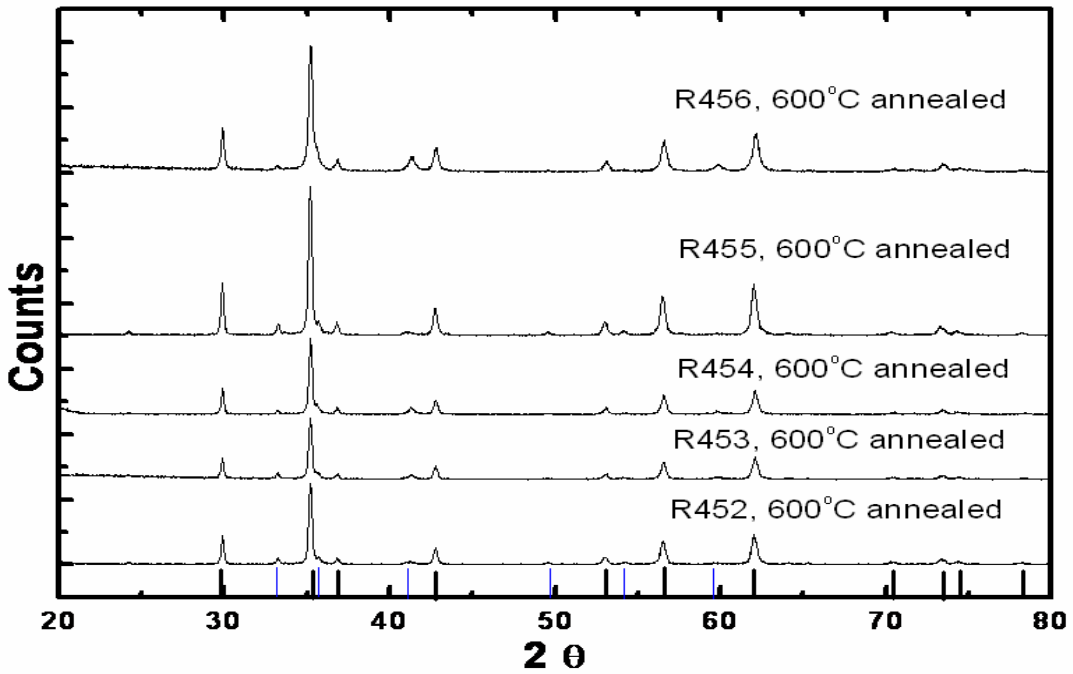

Figure 7-15, XRD patterns of plasma sprayed MnZn ferrite annealed in the air at 600°C for an hour. The black lines in the bottom indicate the peak positions for MnZn ferrite spinel; blue lines indicate the peak positions of Fe_2O_3 hematite.

7.1.3.3. Zinc loss

The composition of starting powder for spraying is obtained by EDAX analysis on the powders. The composition varies from particle to particle due to the zinc evaporation resulting from different particle size. The value of $Mn_{0.50}Zn_{0.51}Fe_{1.99}O_4$ averaging over 10 particles is used to represent the starting composition. In the as-sprayed plasma sprayed MnZn ferrites, besides MnZn ferrite, there is a secondary phase of FeO. EDAX on as-sprayed coating shows the presence of four elements: Mn, Zn, Fe and O, among them, Fe and O come from both the MnZn ferrite phase and the FeO wuestite phase. Therefore then the amount of Fe in MnZn ferrite phase is the total amount of Fe in the coating subtracted by the amount of Fe in FeO whose weight or molar fraction of FeO can determined by XRD analysis. Then we can determine the real composition of MnZn ferrite in the as-sprayed coatings. 10 EDAX spectra were obtained during low magnification SEM scanning. Using low magnification, we are scanning over a relatively large area (20×20μm), then the compositional variation from splat to splat can be overcome.

The average compositions of MnZn ferrite in as-sprayed state are: $Mn_{0.6886}Zn_{0.4227}Fe_{1.8887}O_4$, $Mn_{1.0709}Zn_{0.4590}Fe_{1.4701}O_4$, $Mn_{0.9283}Zn_{0.4003}Fe_{1.6714}O_4$, $Mn_{0.6622}Zn_{0.4835}Fe_{1.8543}O_4$, and $Mn_{1.4546}Zn_{0.3901}Fe_{1.4886}O_4$, respectively for run 452, 453, 454, 455 and 456 respectively. The lattice constant of $FeFe_2O_4$, $ZnFe_2O_4$ and $MnFe_2O_4$ are 8.396 Å, 8.441 Å, 8.499 Å, respectively [JCPDS 19-629, 22-1012, 10-0319]. By extrapolating between the three ferrites, the above composition ferrites should have lattice constant of 8.455 Å, 8.451 Å, 8.450 Å, 8.453 Å and 8.453 Å for run 452, 453, 454, 455 and 456, respectively.

These estimations are in quite good agreement with the XRD analyses discussed above.

The zinc loss is expressed as the relative change of Zinc molar ratio in the ferrite phase. For example, the molar ratio of Zinc in the starting powder is $\frac{Zn}{Zn+Mn+Fe}=\frac{0.51}{0.51+0.50+1.99}=0.17$, the zinc molar ratio in ferrite phase of the as-sprayed coating of run 452 is $\frac{Zn}{Zn+Mn+Fe}=\frac{0.4227}{0.4227+0.6886+1.8887}=0.1409$, therefore the zinc loss is 0.0291 or 2.91%. The zinc losses of run 453 to 456 are 1.7%, 3.66%, 0.89% and 6.3%, respectively. The zinc loss is plotted against average particle temperature and velocity, as well as against melting index and Reynolds number, as shown by Figure 7-16 and Figure 7-17. Clearly, as the temperature increases, the zinc loss increases. The longer the particle travels in the hot zone of plasma plume, the larger the zinc loss.

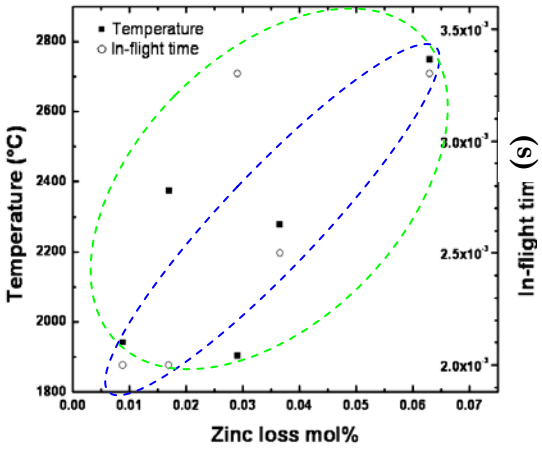

Figure 7-16, zinc loss vs. temperature and in-flight time. Blue and green circles represent the trend of the relationship between particle temperature and zinc loss, and relationship between inflight time and zinc loss, respectively.

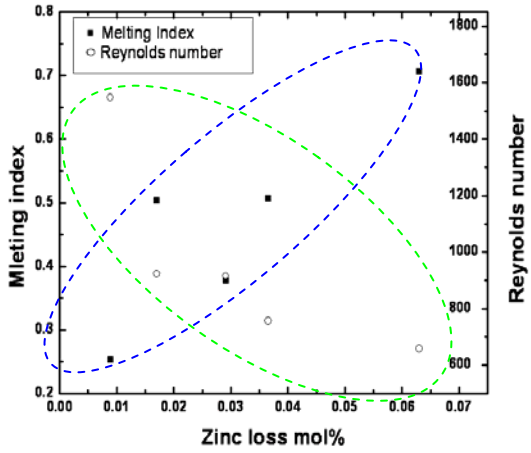

Figure 7-17, zinc loss vs. melting index and Reynolds number. Blue and green circles represent the trend of the relationship between average melting index and zinc loss, and relationship between avererage Reynolds number and zinc loss, respectively.

The molar concentration of Zinc at the final moment before impacting on the substrate is assumed to be equal to the zinc concentration in the as-sprayed coating, as the zinc evaporation during quenching process is small compared to that in the flight and thus neglected. The molar concentration of zinc is expressed as:

$$Zn_{final}(mole)\% = \frac{C_{Zn}V - \Delta M_{Zn}}{(C_{Zn}+C_{Mn}+C_{Fe})V - (\Delta M_{Zn}+\Delta M_{Mn}+\Delta M_{Fe})},$$

The values of C_{Zn}, C_{Mn} and C_{Fe} are calculated from the powder composition provided by the supplier and are confirmed by the EDS measurements (C_{Mn}=3721 mole/m^3, C_{Zn}=3743 mole/m^3, C_{Fe}=14640 mole/m^3). ΔM_{Fe}, ΔM_{Zn} and ΔM_{Mn} are the mole loss of Fe, Zn and Mn individually. Since the molar percentage changes of Fe and Mn after spraying is small (noted in Figure 2-20), implying that ΔM_{Fe} and ΔM_{Mn} can be neglected. Using equation 2-18, and

assuming the particles are having same particle size (d_{50}=94.6 μm), the average evaporation rates for these five experimental conditions are calculated and tabulated in Table 7-1.

Table 7-1, zinc evaporation rates and oxygen loss rates

	452	453	454	455	456
N_{Zn} $(mole \cdot s^{-1} \cdot m^{-2})$	14.22	32.41	27.38	16.30	26.25

We can write $N_{Zn} = A_1 \bullet \exp\left(\frac{-\Delta G_1}{RT}\right)$ with G_1 is the activation energy for the reactions of zinc evaporation. Then, we will have $\ln(N_{Zn}) \propto -\frac{1}{T}$. Figure 7-18 shows this inverse linear relationship between the logarithm of N_{Zn} and 1/T. By linear fitting the data, we can calculate the activation energy of the zinc evaporation as 46 KJ/mol.

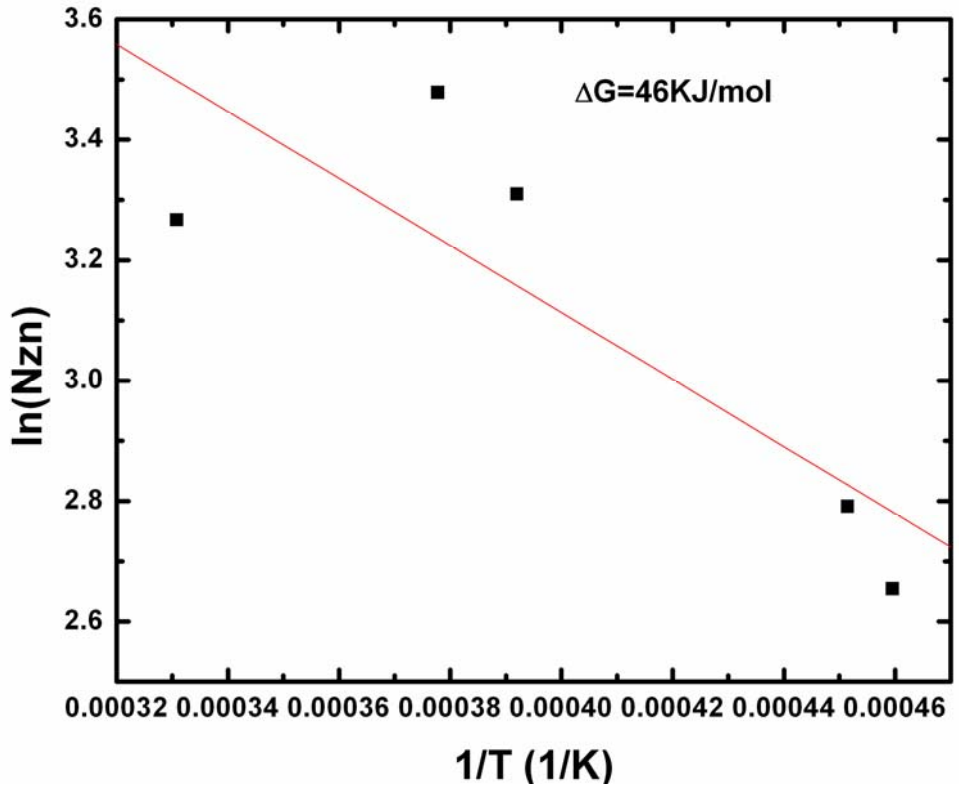

Figure 7-18, zinc loss vs. temperature and in-flight time.

7.1.3.4. Saturation magnetization and coercivity

The saturation magnetization and coercivity data for as-sprayed MnZn ferrite coatings are superimposed on the T-V space (Figure 7-19) and the MI-Re space (Figure 7-20). The

red dash lines in Figure 7-19 are presumptive

contour lines for saturation magnetization in T-V space. The red lines and blue lines in Figure 7-20 are presumptive contour lines for saturation magnetization and coercivity in MI-Re space, respectively. It is obvious that high particle temperature and low resistivity result in loss of magnetization and increase in coercivity. Since the accompanying effects with high particle temperature such as the formation of antiferromagnetic wuestite phase, the change of composition resulting from zinc evaporation and oxygen loss, and random cation distribution, will eventually lead to a low magnetization state. It is also clear that the spraying conditions with high melting index and high Reynolds number will result in low magnetization and high coercivity, because under these conditions, compositional inhomogeneity caused by preferential oxygen loss and zinc evaporation, and structural inhomogeneity such as splat boundaries, pores and cracks are more likely to take place.

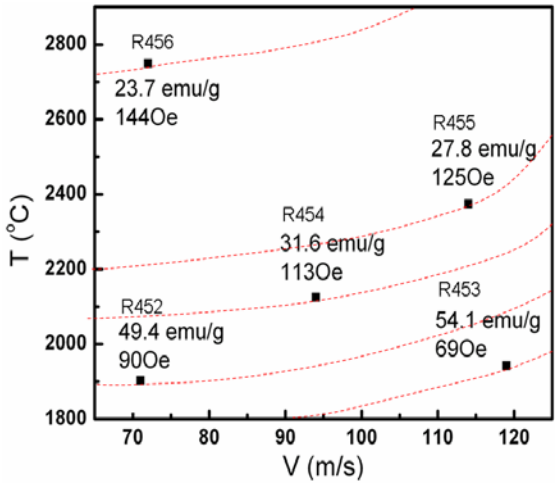

Figure 7-19, saturation magnetization and in-plane coercivity on T-V space. Red dash lines are presumptive contour lines for magnetization.

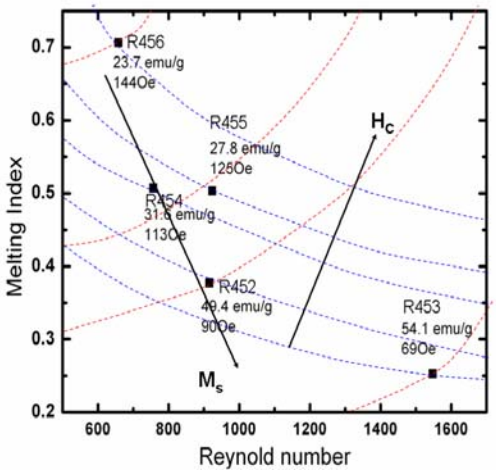

Figure 7-20, saturation magnetization and in-plane coercivity on MI-Re space. Red dash lines are presumptive contour lines for magnetization.

The magnetic properties can be improved by low temperature annealing. As can be seen from Figure 7-21, the saturation magnetization increases and the coercivity decreases after annealing in air. After annealing, the non-magnetic phase is reduced therefore more atoms contribute to the magnetization. Also cations are able to take their equilibrium sites thus increase the magnetic moment ferrite per formula. The calculated magnetic moments for random and ordered state of MnZn ferrite with the same composition of the as-sprayed state are shown in Figure 7-22, line (e) and (f), we can see that ordered state does have larger magnetic moment than the random state. As for coercivity, magnetocrystalline anisotropy depends critically on the chemical composition. Therefore, difference in composition among individual particles presents a barrier to domain wall motion [5]. Also as can been seen from Figure 7-9, the as-sprayed MnZn coating has a lot of granular pores, interlaminar pores and more cracks, all these microstructural defects also presents barriers to domain wall motions [5]. After annealing, the coercivity drops, and this drop is attributed to two factors[150]. First is that annealing makes the composition more homogenous. Second, the grain volume increases resulting from oxidation of FeO, filling up the porosity and cracks.

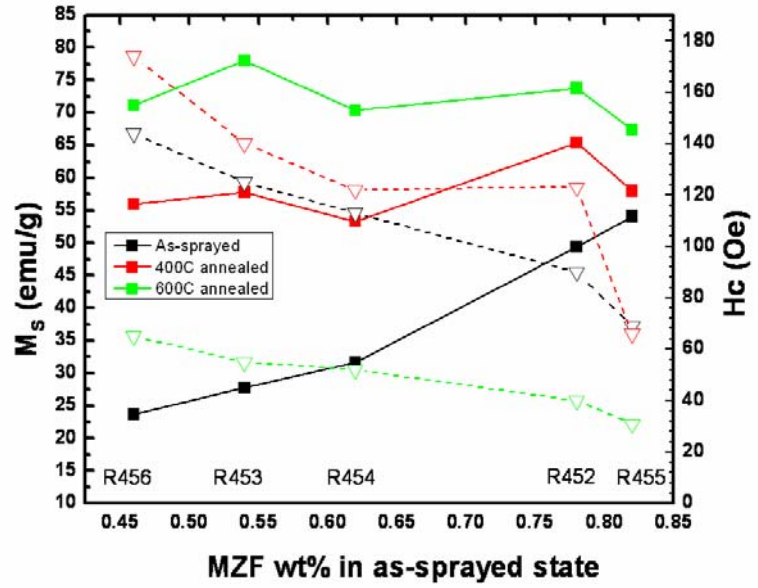

Figure 7-21, saturation magnetization and in-plane coercivity of the as-sprayed coatings, 400°C annealed coatings and 600°C annealed coatings. Solid lines and solid squares represent Ms, dash lines and open triangles represent coercivity.

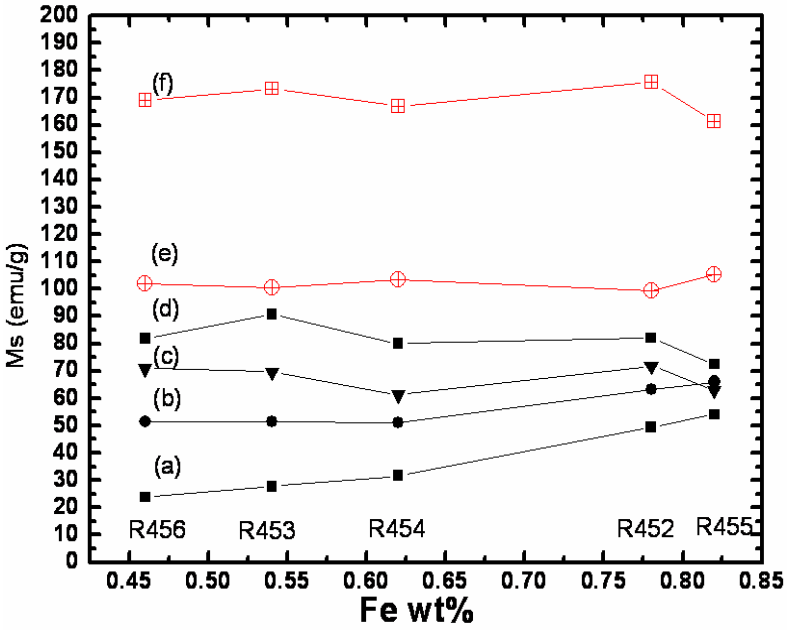

Figure 7-22, saturation magnetization of the as-sprayed coatings (a), ferrite phase in the as-sprayed coatings (b), ferrite phase in the 400°C annealed coatings (c), ferrite phase in the 600°C annealed coatings (d), calculated saturation magnetization of ferrite with same composition and random cation distribution (e), and calculated saturation magnetization of ferrite with same

composition and ordered cation distribution (f).

Chapter 8 Conclusions

The functional properties of plasma-sprayed ferrites composites have been investigated. The research focuses on the composition design, effects of the process related issues such as oxygen deficiency, zinc volatilization and disordered cation distribution; improvement from both process optimization and post-deposition heat treatment. This study can contribute to both the scientific understanding of such a non-equilibrium material system and further improvements of the engineering process, i.e. plasma spraying of magnetic oxides.

The methodology consists of multi-scale experimental techniques, including phase analysis, microstructure observation, magnetic properties measurements, and electrical properties measurement.

8.1. Percolation

Using the effective medium approximation, we have calculated the effective conductivity against different aspect ratios of the metallic phase, and we are able to predict the percolation threshold if we know the splat flattening ratio. Composites with three different aspect ratios are tested. The MZF-NiCo sintered composites with spherical particles (aspect ratio is 1) have a percolation threshold of 33 vol%. For plasma sprayed MZF-NiCo composites (the average flattering ratio is 2.3, corresponding to aspect ratio of 20), the percolation threshold drops to 6.7 vol%. For HVOF sprayed Al_2O_3-Ni composites (the average FR is 3.3, corresponding to aspect ratio of about 45), the percolation threshold is about 5 vol%. These experimental results are in quite good agreement with simulation results. We have found that for the MZF-NiCo composites has a GMR-AMR transition at the percolation threshold. And for Al_2O_3-Ni composites, we found that the type of electrical anisotropy changes at the percolation threshold.

8.2. Functional magnetic composites

The as-sprayed MZF/permalloy composite films has FeO wuestite in the outer shell of the MZF grains and has a low saturation magnetization, when the as-sprayed films are annealed in air up to 600°C, the FeO wusetite phase transforms into Fe_2O_3 hematite phase, forming insulating grain boundaries which is mainly responsible for the drop in electric conductivity after annealing. The increase in saturation magnetization after annealing is due to the cation ordering in the lattice sites. The drop in coercivity is a result of the compositional homogenization and refinement of the microstructure. Annealing at or above 1000°C will give rise to the formation of MnZnNi ferrite with a lower magnetic moment, explaining the drop of magnetization. Resistivity measurements have shown that annealing can increase the resistivity of the composite films, which is essential for high frequency application. The composite samples have been studied are above the percolation threshold.

We have examined the magnetic and electrical properties of plasma sprayed MZF-NiCo thick film composites and compared with that of sintered bulk counterparts of similar compositions. As-sprayed coatings have low magnetization and high coercivity, annealing can increase the magnetization as well as decrease the coercivity by the mechanism of cation ordering, structural and compositional homogenization. The pure MnZn ferrite and low

NiCo concentration composites show a typical GMR effect, while NiCo and high NiCo concentration composites show a typical AMR effect. Although we didn't find an enhance AMR in the composites as we expected, due to the GMR effects in the ferrite phase. However, we do find a GMR-AMR transition at the percolation threshold due to the fact that the two magnetic phases contribute differently to the magnetoelectrical transport phenomenon. This is the first time that a sign change in MR at a percolation threshold has been detected.

CoO forms in plasma spraying of Co ferrite, as a result of oxygen loss. The as-sprayed coatings have poor magnetic properties due to the formation of CoO. Through annealing in air, CoO is oxidize to form Co_3O_4, and though cation diffusion, the Co_3O_4 is partially merges with Co ferrite. The saturation magnetization increases after being annealed due to the decease of the amount of CoO phase. The coercivity increases after annealing in air 600°C as a result of an increase of magnetocrystalline anisotropic energy. The coercivity decreases after annealing in air at 800°C as a result of coating densification and reduction of domain wall motion barrier presented by CoO phase. Very large exchange bias effect has been found in the as-sprayed and annealed coatings. When cooling in a magnetic field, the magnetization of as-sprayed and annealed ferrite coatings first increase and then decrease after their respective Néel temperature. However, the magnetization of pressed-sintered ferrite pellet increases as the temperature decreases, following the classical Brillion function. The Néel temperature change is related to the phase evolution during annealing. Magnetic hysteresis loops at various temperatures after field cooling have been conducted to extract the exchange bias and magnetization vertical shift information. The exchange bias of annealed coating is much smaller than that of as-sprayed coating, suggesting the decrease of exchange energy and increase of grain size of the ferrite phase. The positive vertical shift in magnetization curve suggests that the CoO is negative exchange coupled with A site cations of the Co ferrite. The magnetostriction of as-sprayed and 600°C annealed Co ferrite have been measured; the estimated saturation magnetostriction is about -186 ppm, which is close to bulk value. The deviation from the bulk value could be related to exchange coupling between the antiferromagnetic phase and the Co ferrite phase. The strain derivation is about an order of magnitude lower than that of cobalt ferrite ring fabricated from sintering method.

8.3. Process optimization

Using processing diagnostic sensors, we have measured the in-flight characteristics of molten particles. We have constructed the first order process maps correlating the process condition such as gun current, H_2 volume fraction and total mass flow with particle temperature, velocity, melting index and Reynolds number. We found that increasing the gun current will increase both the particle temperature and velocity, increasing H_2 percentage will increase the temperature but decrease the velocity; increasing total mass flow will increase the velocity but decrease the temperature.

Composition, structure and magnetic properties are measured and second order process maps are drawn to relate these properties to the particle history, i.e. T, V, MI and Re. We found that the splats tend to spread better with medium MI and Re values. Low MI and high Re will result in splat fragmentation. It also seems that coatings deposited in high Re and low MI region are more porous. We have measured the zinc loss and the fraction of FeO phase which is a result of oxygen loss. The smaller the particle velocity, the longer the particle has

to travel in the flame, the more zinc loss and oxygen loss. We calculated the zinc evaporation rate, it is related to the temperature by Arenius equations $N = A \bullet \exp\left(\frac{-\Delta G}{RT}\right)$. The activation energy for zinc evaporation is estimated to be 46 KJ/mol. Understanding the kinetics of zinc evaporation in thermal spraying, we can design the process condition as well as pre-compensate the zinc concentration in MnZn ferrite to achieve desired final composition as well as magnetic properties.

The saturation magnetization and coercivity are mapped on the T-V or MI-Re plots. We found that low MI, high Re tend to produce coatings with higher Ms and lower Hc. This region is also the region with least zinc loss and oxygen loss. The only trade-off is that coatings tend have more structural defects in this region. The region with low MI, low Re also tends to produce coatings with good magnetic properties, and the coatings are denser in this region. Therefore, in the later coating fabrications, we should try to spray under these conditions.

Chapter 9 Suggestions on successive future work

9.1. HVOF process

The ratio of undesired wuestite phase to spinel ferrite is still large in the above studied ferrite samples. To reduce the wuestite formation, we might want to shorten the flight time and reduce the temperature of plasma gas. Further lowering the gun current or increase total mass flow is not possible in the current laboratory spraying systems. An alternate route is to seek HVOF spraying.

Yan [80] has done a small study on HVOF spraying MnZn ferrite, he found that compared to plasma spraying, the HVOF sprayed MnZn ferrite had a higher saturation magnetization due to lower particle temperature. But the coercivity is similar to that of plasma sprayed sample. HVOF tends to produce a denser coating which is good for getting a low coercivity coating, but since the splats are thinner, there are more splat boundaries that can act as pinning force in domain wall motion.

A preliminary study of HVOF Co ferrite has been carried out. The problem has encountered so far is the powder injection. As can be seen from Figure 6-24, a spray dried Co ferrite particle is composed by thousands of nanoparticles. In HVOF, the powder is injected co-axially with combustion flame. The powders are broken up by back pressure in HVOF nozzle and clog the nozzle. Adjusting the pressure of HVOF gun is needed to solve the feeding problem.

9.2. Deposition efficiency and phase segregation

The powder trajectory in the plasma plume depends on the density and size of the particles. Particles with higher density tend to penetrate deeper in the plasma plume resulting in two distinct streams in the plasma plume. For ferrite – metal composites in the present study, the density of ferrite is about 5.2 g/cm^3, while the density of metal is about 8.9 g/cm^3. It is intuitive to think that the metal will deposit more in the lower band of the substrate while the ferrite will deposit more in the upper band of the substrate.

We have used HI-Watch sensor to visualize the particle streams in plasma plume. As can be seen from Figure 9-1, the NiCo particles (panel a) forms a much more confined stream than that of MnZn ferrite (panel b) particles. We can see from Figure 9-2, there are more MnZn ferrite splats in the top of the substrate while there are more NiCo splats in the bottom of the substrate. But the segregation of stream is not severe; we have not observed segregation from the cross sectional images of MnZn ferrite composites.

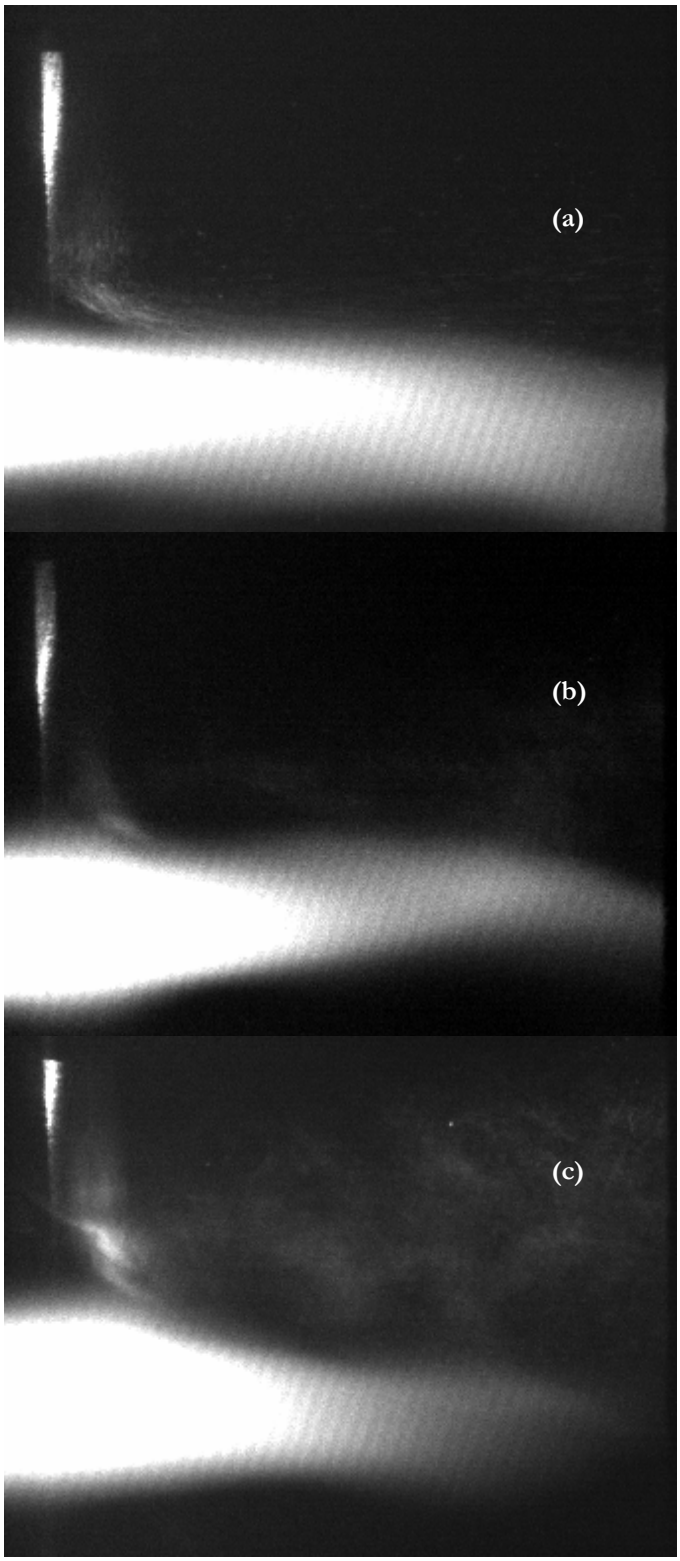

Figure 9-1, particle streams observed by Hi-Watch, (a) NiCo powder, (b) MnZn ferrite powder, and (c) MnZn ferrite-10 vol% NiCo powder.

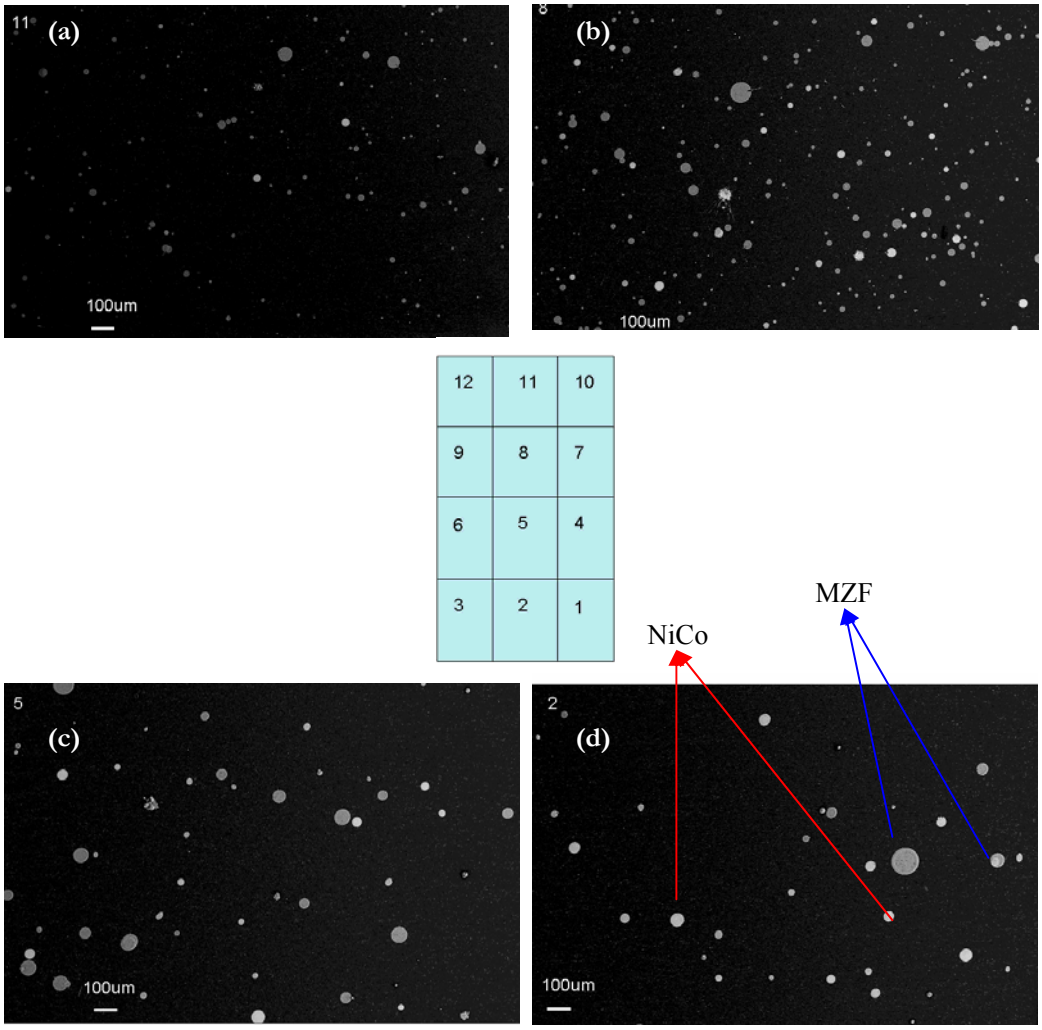

Figure 9-2, splats on silicon substrates. The substrate is divided into 4 bands from top to bottom. Figure (a) is corresponding to region (11) which is the top. Figure (b) and (c) are corresponding to region 8 and 5. Figure (d) is corresponding to region 2 which is the bottom of the substrate. The white splats are NiCo, the grey splats are MnZn ferrite.

However, for plasma spraying Al_2O_3-Ni composites, the segregation is very severe, the coating actually forms a banded structure, as shown in Figure 9-3 (b). This results in that even at a very low composition; the Ni splats are already "percolated", as shown by the electrical conductivity measurement in Figure 9-4.

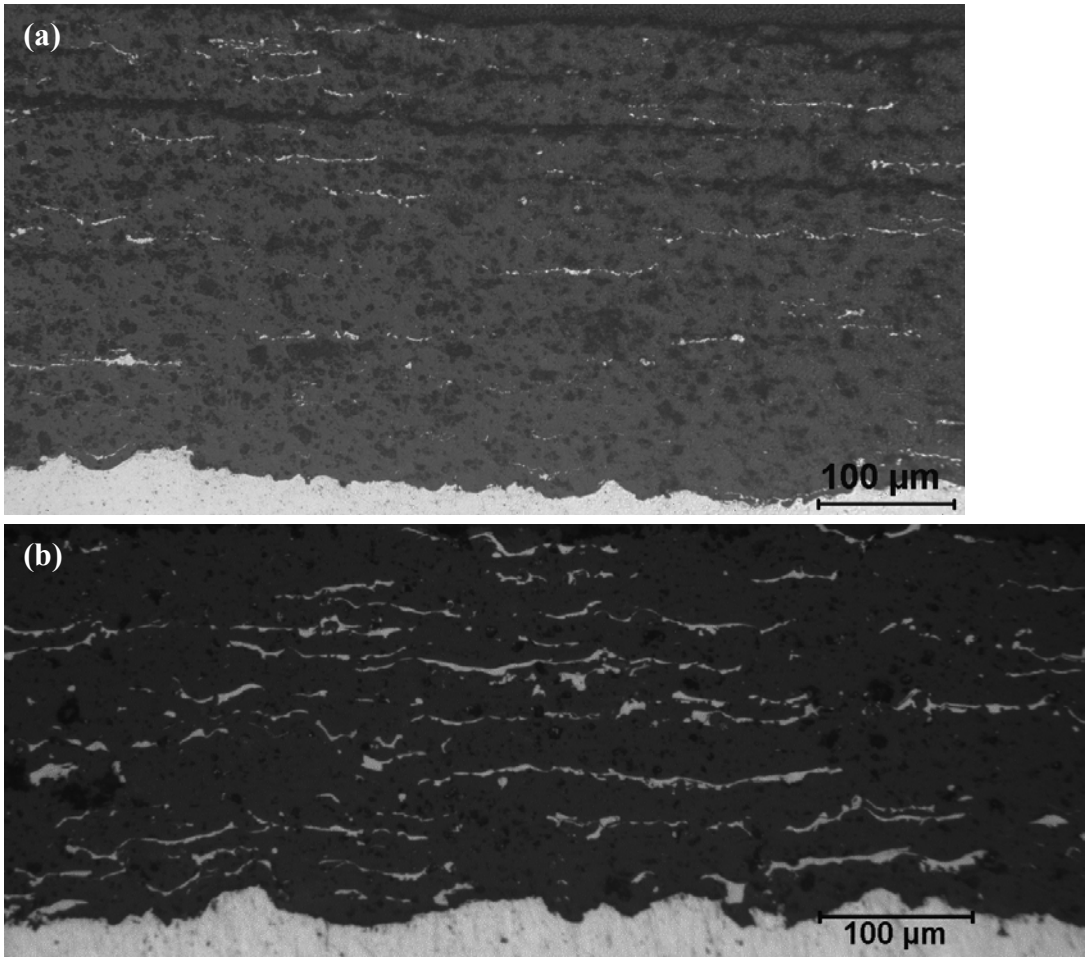

Figure 9-3, cross sectional optical microscope of (a) plasma sprayed. (b) HVOF sprayed and Al_2O_3 – 3 vol% Ni composites.

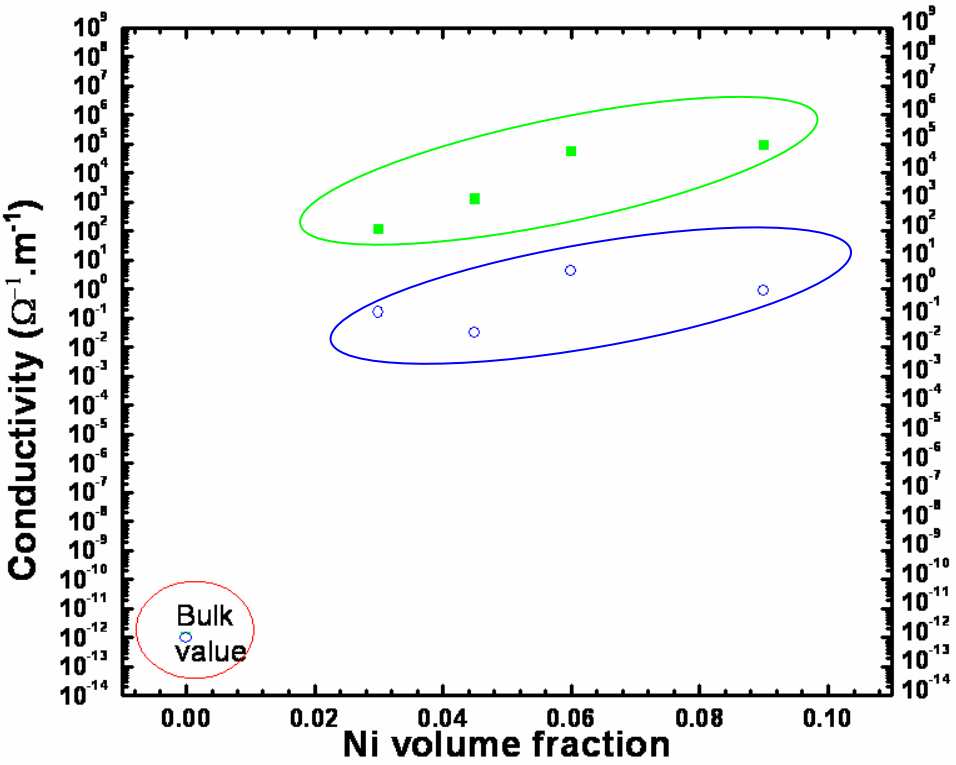

Figure 9-4, electrical conductivity of plasma sprayed MnZn ferrite and Ni composites. Data in green circle is in-plane conductivity while data in blue circle is through-thickness resisitivity.

The above preliminary results address the importance to study the two phase mixture behavior in the plasma spraying process. The deposition efficiency of metal and ceramic may be different; this will result in departure from the nominal composition. This also needs to be elaborated.

9.3. Co ferrite composites

We haven't completed the goal of making Co ferrite – Co composites. This should be done when we have better control over the processing conditions to minimize oxygen loss. Because on one hand, Co ferrite decomposes to form CoO, on the other hand Co oxidize to form CoO. There will be too much CoO phase which is detrimental to the functional properties of composites. We should try to lower the particle temperature by using Argon+Helium+Hydrogen plasma gas to achieve this goal.

Since a magnetostrictive sensor is used at a wide temperature range, it is important to investigate the magnetostriction of plasma sprayed Co ferrite at various temperatures. At low temperature, the CoO phase is also magnetostrictive; it might also contribute to magnetostriction through exchange coupling. All these effects should be studied in the future.

.

9.4. Magnetic annealing

Annealing in the presence of a strong magnetic field at sufficiently high temperature (high enough for atom mobility yet still lower than the Curie temperature) can result in preferred direction of magnetization in a sample by rearranging atoms on a local scale in such a way as to favor magnetization in a given direction. It is reported that a sintered Co ferrite disk annealed at 300oC in air for 36 hours in a vibrating sample magnetometer with a furnace under a DC field of 4 kOe applied in the sample plane, the magnetostriction along the easy axis and hard axis increased by 20% and 26%, and the corresponding maximum strain derivative increase by 126% and 163% under hard axis applied fields, respectively [33]. For plasma sprayed magnetic composites, annealing has been proved to be able to improve the degraded magnetic properties, annealing in the presence of magnetic field may be another technique to improve the magnetic properties. Since plasma sprayed magnetic coatings generally have an in-plane anisotropy due to the shape. Applying a magnetic field in the in-plane direction during low temperature annealing may result in enhanced in-plane anisotropy. This may be useful to increase the in-plane permeability for inductor applications, and increase the magnetostriction level and strain-stress response in the hard axis magnetization.

References

1. Baibich, M.N., J.M. Broto, A. Fert, F.N. Van Dau, et al., *Giant Magnetoresistance of (001)Fe/(001)Cr Magnetic Superlattices.* Physical Review Letters, 1988. **61**(21): p. 2472.
2. Srinivasan, G., E.T. Rasmussen, J. Gallegos, R. Srinivasan, et al., *Magnetoelectric bilayer and multilayer structures of magnetostrictive and piezoelectric oxides.* Physical Review B, 2001. **64**(21): p. 214408.
3. Sampath, S., J. Longtin, R.J. Gambino, H. Herman, et al., *Direct-Write Thermal Spraying of Multilayer Electronics and Sensor Structures*, in *Direct-Write Technologies for Rapid Prototyping : Applications to Sensors, Electronics, and Passivation Coatings*, D. Chrisey, Editor. 2002, Academic Press. p. 261-302.
4. Goldman, A., *Handbook of Modern Ferromagnetic Materials*. 1999, Dordrecht: Kluwer Academic.
5. O'Handley, R.C., *Modern Magnetic Materials Principles and Applications*. 2000, New York: Wiley.
6. Na, J.G., T.D. Lee, S.J. Park, Y.J. Tang, et al., *Effects of cation distribution on superexchange interaction incobalt ferrites.* IEEE Transactions on Magnetics, 1995. **31**(6): p. 3970.
7. Prince, E., *Neutron Diffraction Observation of Heat Treatment in Cobalt Ferrite.* Physical Review, 1956. **102**(3): p. 674.
8. Gorter, E.W., *Saturation Magnetization and Crystal Chemistry of Ferrimagnetic Oxides.* Philips Research Reports, 1954. **9**(6): p. 403-443.
9. Anderson, P.W., *2 Comments on the Limits of Validity of the Weiss,P.R. Theory of Ferromagnetism.* Physical Review, 1950. **80**(5): p. 922-923.
10. Keizo, O., *Magnetocrystalline Anisotropy and Magnetic Permeability of Mn-Zn-Fe Ferrites.* Journal of the Physical Society of Japan, 1963. **18**(5).
11. O'Handley, R., *Modern Magnetic Materials, Principles and Applications*. 2000: John Wiley & Sons, Inc.
12. Slonczewski, J.C., *Origin of Magnetic Anisotropy in Cobalt-Substituted Magnetite.* Physical Review, 1958. **110**(6): p. 1341-1348.
13. Slonczewski, J.C., in *Magnetism*, G. Rado and H. Suhl, Editors. 1963, Academic Press: New York.
14. Friedberg, R. and D.I. Paul, *New Theory of Coercive Force of Ferromagnetic Materials.* Physical Review Letters, 1975. **34**(19): p. 1234.
15. Paul, D.I., *General theory of the coercive force due to domain wall pinning.* Journal of Applied Physics, 1982. **53**(3): p. 1649-1654.
16. Borzorth, R.M., E.F. Tilden, and E.T. Williams, *Anisotropy and Magnetostriction of Some Ferrites.* Physics Review, 1955. **99**(6): p. 1788.
17. Inaba, H., T. Abe, Y. Kitano, and J. Shimomura, *Mechanism of core loss and the grain-boundary structure of niobium-doped manganese-zinc ferrite.* Journal of Solid State Chemistry, 1996. **121**(1): p. 117-128.
18. Jeong, W.H., Y.H. Han, and B.M. Song. *Effects of grain size on the residual loss of Mn--Zn ferrites*. 2002: AIP.
19. Tung, M.J., W.C. Chang, C.S. Liu, T.Y. Liu, et al., *Study of Loss Mechanisms of Mn-Zn Ferrites in the Frequency from 1 Mhz to 10 Mhz.* Ieee Transactions on Magnetics, 1993. **29**(6): p. 3526-3528.
20. Hemeda, O.M. and M.M. Barakat, *Effect of hopping rate and jump length of hopping electrons on the conductivity and dielectric properties of Co-Cd ferrite.* Journal of Magnetism and Magnetic Materials, 2001. **223**(2): p. 127-132.
21. Guillaud, C., *Elementary mechanisms of magnetization in mixed oxides of Iron and Cobalt.* Reviews of Modern Physics, 1953. **25**(1): p. 64.
22. Newnham, R.E., *Electroceramics.* Reports on Progress in Physics, 1989. **52**(2): p. 123-156.
23. Na, J.G., T.D. Lee, and S.J. Park, *Effects of Cation Distribution on the Magnetic and Electrical-Properties of Cobalt Ferrite.* Ieee Transactions on Magnetics, 1992. **28**(5): p. 2433-2435.
24. Zheng, H., J. Wang, S.E. Lofland, Z. Ma, et al., *Multiferroic BaTiO3-CoFe2O4 nanostructures.*

Science, 2004. **303**(5658): p. 661-663.
25. Taylor, D., *Thermal expansion data, VI Complex Oxides, AB2O4, the spinels.* Transaction of British Ceramics Society, 1985. **84**: p. 121.
26. Zheng, H., J. Wang, S.E. Lofland, Z. Ma, et al., *Multiferroic BaTiO3-CoFe2O4 Nanostructures* 2003.
27. Chien, C.L., *Magnetism and Giant Magneto-transport Properties in Granular Solids.* Annu. Rev. Mater. Sci., 1995. **25**: p. 129-160.
28. Beach, G.S.D. and A.E. Berkowitz, *Co-Fe metal/native-oxide multilayers: A new direction in soft magnetic thin film design II. Microscopic characteristics and interactions.* IEEE Transactions on Magnetics, 2005. **41**(6): p. 2053-2063.
29. Yamamoto, S., S. Horie, N. Tanamachi, H. Kurisu, et al., *Fabrication of high-permeabilityferrite by spark-plasma-sintering method.* Journal of Magnetism and Magnetic Materials, 2001. **235**: p. 218.
30. Kim, D., M. Ohnishi, N. Matsushita, and M. Abe, *Magnetic cores usable in gigahertz range: Permalloy/Ni-Zn ferrite microcomposite made by low-temperature wet process.* Ieee Transactions on Magnetics, 2003. **39**(5): p. 3181-3183.
31. Naoe, M. and N. Matsushita, *Deposition of single-layer CoFe2O4 and multilayer CoFe2O4/alpha-Fe2O3 with large 4 pi M(s) and high H-c using vacuum arc evaporation.* Journal of Magnetism and Magnetic Materials, 1996. **155**(1-3): p. 216-218.
32. Paulsen, J.A., A.P. Ring, C.C.H. Lo, J.E. Snyder, et al., *Manganese-substituted cobalt ferrite magnetostrictive materials for magnetic stress sensor applications.* Journal of Applied Physics, 2005. **97**(4): p. -.
33. Lo, C.C.H., A.P. Ring, J.E. Snyder, and D.C. Jiles, *Improvement of magnetomechancial properties of cobalt ferrite by magnetic annealing.* Ieee Transactions on Magnetics, 2005. **41**(10): p. 3676-3678.
34. Lee, E.W., *Magnetostriction and Magnetomechanical Effects.* Rep. Prog. Phys., 1955. **18**: p. 184.
35. Lacheisserie, E.d.T.d., *Magnetostriction, Theory and Applications of Magnetoelasticity*. 1993: CRC Press.
36. R. Becker, M.K., Z. Phys., 1934. **88**: p. 634.
37. Jin, X., C.O. Kim, Y.P. Lee, and Y. Zhou, *In-situ measurement of magnetostrictive coefficient and elastic properties for thin film during growth.* Journal of Vacuum Science and Technology, 2002. **A 20**(3): p. 612.
38. Gumen, N.M., *Variation of Magnetostriction in Heat-Treated Cobalt Ferrite.* Soviet Physics Jetp-Ussr, 1966. **22**(2): p. 251-&.
39. Pines, B.Y. and N.M. Gumen, *X-ray determination of the magnetostriction constants of iron-cobalt ferrites.* Soviet Physics, Solid State, 1964. **5**(12): p. 2557.
40. Jones, F.J. and B.k. Tanner, *A double axis X-ray diffractometer for magnetostriction measurements.* Journal of Physics, E: Scientific Instruments, 1980. **13**: p. 1183.
41. Merz, K.M., *X-ray study of ferromagnetic domains in cobalt zinc ferrite.* Journal of Applied Physics, 1960. **31**(1): p. 147.
42. Pettifer, R.F., O. Mathon, S. Pascarelli, M.D. Cooke, et al., *Measurement of fermtometre-scale atoimc displacements by X-ray absorption spectroscopy.* Nature, 2005. **435**: p. 78.
43. Smith, A.B. and R.V. Jones, *Magnetostriction in Nickel Ferrite and Cobalt -Nickel Ferrite.* Journal of Applied Physics, 1966. **37**(3): p. 1001.
44. Gambino, R.J., M.M. Raja, S. Sampath, and R. Greenlaw, *Plasma-sprayed thick-film anisotropic magnetoresistive (AMR) sensors.* IEEE Sensors Journal, 2004. **4**(6): p. 764-767.
45. Webpage. 2002 [cited; Available from: w3.rz-berlin.mpg.de/~michaeli/member/MaterialsScienceLectures/GMR-2.pdf
46. Chien, C.L., J.Q. Xiao, and J.S. Jiang, *Giant Negative Magnetoresistance in Granular Ferromagnetic Systems.* Journal of Applied Physics, 1993. **73**(10): p. 5309-5314.
47. Chien, C.L., J.Q. Xiao, and J.S. Jiang. *Giant negative magnetoresistance in granular ferromagnetic systems (invited).* in *37th Annual conference on magnetism and magnetic materials*. 1993. Houston, Texas (USA): AIP.
48. von Helmolt, R., J. Wecker, B. Holzapfel, L. Schultz, et al., *Giant negative magnetoresistance in perovskitelike La2/3Ba1/3MnOx ferromagnetic films.* Physical Review Letters, 1993. **71**(14): p. 2331.

49. Jin, S., T.H. Tiefel, M. McCormack, R.A. Fastnacht, et al., *Thousandfold Change in Resistivity in Magnetoresistive La-Ca-Mn-O Films.* Science, 1994. **264**(5157): p. 413-415.
50. Meiklejohn, W.H. and C.P. Bean, *New Magnetic Anisotropy.* Physical Review, 1956. **102**(5): p. 1413.
51. Mauri, D., H.C. Siegmann, P.S. Bagus, and E. Kay, *Simple model for thin ferromagnetic films exchange coupled to an antiferromagnetic substrate.* Journal of Applied Physics, 1987. **62**(7): p. 3047-3049.
52. Malozemoff, A.P., *Random-field model of exchange anisotropy at rough ferromagnetic-antiferromagnetic interfaces.* Physical Review B, 1987. **35**(7): p. 3679.
53. Koon, N.C., *Calculations of Exchange Bias in Thin Films with Ferromagnetic/Antiferromagnetic Interfaces.* Physical Review Letters, 1997. **78**(25): p. 4865.
54. Mackaya, T.G. and A. Lakhtakiab, *Percolation thresholds in the homogenization of spheroidal particles oriented in two directions.* Optics Communications, 2006. **259**(2).
55. Last, B.J. and D.J. Thouless, *Percolation Theory and Electrical Conductivity.* Physical Review Letters, 1971. **27**(25): p. 1719.
56. Stroud, D., *The effective medium approximations: Some recent development.* Superlattices and Microstructures, 1998. **23**(3/4).
57. Cai, W., S. Tu, and J. Gong, *A Physically Based Percolation Model of the Effective Electrical Conductivity of Particle Filled Composites.* Journal of Composite Materials, 2006. **40**(23): p. 2131-2142.
58. Stauffer, D. and A. Aharony, *Introduction to Percolation Theory*. 1992, London: Taylor and Francis.
59. Smith, L.N. and C.J. Lobb, *Percolation in Two-dimensional Conductor-insulator Networks with Controlled Anisotropy.* Physical Review B, 1979. **20**(9): p. 3653-3658.
60. Yi, Y.B., C.W. Wang, and A.M. Sastry, *Two-Dimensional vs. Three-Dimensional Clustering and Percolation in Fields of Overlapping Ellipsoids.* Journal of The Electrochemical Society, 2004. **151**(8): p. 1292-1300.
61. Jones, S.B. and S.P. Friedman, *Particle shape effects on the effective permittivity of anisotropic or isotropic media consisting of aligned or randomly oriented ellipsoidal particles.* Water Resources Research, 2000. **36**(10).
62. Torquato, S., *Random Heterogeneous Materials: Microstructure and Macroscopic Properties*. 2002, New York: Springer-Verlag.
63. Doyle, W.T. and I.S. Jacobs, *The influence of particle shape on dielectric enhancement in metal-insulator composites.* Journal of Applied Physics, 1992. **71**(8): p. 3926-3936.
64. Ferretti, A., R.J. Arnott, E. Delaney, and A. Wold, *Cobalt ferrite single crystals.* Journal of Applied Physics, 1961. **32**(5): p. 905.
65. Ostorero, J. and M. Guillot, *High-Field Magnetization of Aluminum-Doped Cobalt Ferrite Single-Crystals.* Journal of Applied Physics, 1990. **67**(9): p. 4935-4937.
66. Chen, Y., J.E. Snyder, C.R. Schwichtenberg, K.W. Dennis, et al., *Metal-bonded Co-ferrite composites for magnetostrictive torque sensor applications.* IEEE Transactions on Magnetics, 1999. **35**(5): p. 3652-3654.
67. Okuno, S.N., S. Hashimoto, and K. Inomata, *Preferred Crystal Orientation of Cobalt Ferrite Thin-Films Induced by Ion-Bombardment during Deposition.* Journal of Applied Physics, 1992. **71**(12): p. 5926-5929.
68. Na, J.G., *Fabrication and magnetic properties of metal/cobalt ferrite composite thin films.* Journal of Applied Physics, 1996. **79**(8): p. 4893-4895.
69. Gu, B.X., *Magnetic properties and magneto-optical effect of Co0.5Fe2.5O4 nanostructured films.* Applied Physics Letters, 2003. **82**(21): p. 3707.
70. Gillies, M.F., R. Coehoorn, J.B.A. van Zon, and D. Alders, *Structure and soft magnetic properties of sputter deposited MnZn-ferrite films.* Journal of Applied Physics, 1998. **83**(11): p. 6855-6857.
71. Dorsey, P.C., P. Lubitz, D.B. Chrisey, and J.S. Horwitz, *CaFe2O4 thin films grown on (100)MgO substrates using pulsed laser deposition.* Journal of Applied Physics, 1996. **79**(8): p. 6338-6340.
72. Suzuki, Y., G. Hu, R.B. van Dover, and R.J. Cava, *Magnetic anisotropy of epitaxial cobalt ferrite thin films.* Journal of Magnetism and Magnetic Materials, 1999. **191**(1-2): p. 1-8.
73. Roy, R.W., K.F. Etzold, and J.J. Cuomo, Materials Research Society Symposium Proceedings, 1992. **200**: p. 179.

74. Sato, T., T. Iijima, M. Seki, and N. Inagaki, *magnetic properties of ultrafine ferrite particles.* Journal of magnetism and magnetic materials, 1987. **65**: p. 252.
75. Lee, J.G., J.Y. Park, Y.J. Oh, and C.S. Kim, *Magnetic properties of CoFe2O4 thin films prepared by a sol-gel method.* Journal of Applied Physics, 1998. **84**(5): p. 2801-2804.
76. Harris, D.H., R. Janowiec, C.E. Semler, M.C. Willson, et al., *Polycrystalline Ferrite Films for Microwave Applications Deposited by Arc-Plasma.* Journal of Applied Physics, 1970. **41**(3): p. 1348-&.
77. Andrews, C.W.D. and B.A. Fuller, *The Effects of Substrate Materials and Powder Type on the Properties of Plasma Sprayed Ferrite.* Journal of Materials Science, 1975. **10**: p. 1771-1778.
78. Preece, I. and C.W.D. Andrews, *Plasma Spray of Ferrites.* Jouranl of Materials Science, 1973. **8**: p. 964-967.
79. Varshney, U., B.D. Eichelberger, J.A. Neal, R.J. Churchill, et al. *Monolithic Magnetic Modules for DC-DC Power Converters*. in *Colloque C1, Supplement au Jounal de Physique III de mars*. 1997.
80. Yan, Q., *Magnetic Functional Oxide by Plasma Spray---MnZn Ferrites*, in *Department of Materials Science and Engineering*. 2004, State University of New York, Stony Brook: Stony Brook.
81. Yan, Q., R.J. Gambino, S. Sampath, L.H. Lewis, et al., *Effects of zinc loss on the magnetic properties of plasma-sprayed MnZn ferrites.* Acta Materialia, 2004. **52**(11): p. 3347-3353.
82. Janisson, S., E. Meillot, A. Vardelle, J.F. Coudert, et al. *Meeting the Challenges of the 21st Century*. in *ASM International*. 1998. Materials Park, OH.
83. Leger, J.M., P. Fauchais, A. Grimaud, M. Vardelle, et al. *International Advances in Coating Technology*. in *ASM International*. 1992. Materials Park, OH.
84. Wang, X.Y., H. Zhang, L.L. Zheng, and S. Sampath, *An integrated model for interaction between melt flow and non-equilibrium solidification in thermal spraying.* International Journal of Heat and Mass Transfer, 2002. **45**(11): p. 2289-2301.
85. Sampath, S. and X. Jiang, *Splat formation and microstructure development during plasma spraying: deposition temperature effects.* Materials Science and Engineering a-Structural Materials Properties Microstructure and Processing, 2001. **304**: p. 144-150.
86. Bhat, H., *Characterization of plasma-sprayed iron- and nickel- based alloy coatings*, in *Materials Science and Engineering*. 1984, Stony Brook University: Stony Brook.
87. Bhat, H. and H. Herman, *Plasma-Spray-Quenched Martensitic Stainless-Steel Coatings.* Thin Solid Films, 1982. **95**(3): p. 227-235.
88. Matejicek, J. and S. Sampath, *Intrinsic residual stresses in single splats produced by thermal spray processes.* Acta Materialia, 2001. **49**(11): p. 1993-1999.
89. Kuroda, S., T. Fukushima, and S. Kitahara, *Generation Mechanisms of Residual-Stresses in Plasma-Sprayed Coatings.* Vacuum, 1990. **41**(4-6): p. 1297-1299.
90. Yan, Q.Y., R.J. Gambino, and S. Sampath, *Magnetostriction and stress measurements in plasma-sprayed MnZn ferrite films.* Journal of Applied Physics, 2005. **97**: p. 10G102
91. Darken, L.S. and R.W. Gurry, *The System Iron Oxygen .2. Equilibrium and Thermodynamics of Liquid Oxide and Other Phases.* Journal of the American Chemical Society, 1946. **68**(5): p. 798-816.
92. Hastings, J.M. and L.M. Corliss, *Neutron Diffraction Studies of Zinc Ferrite and Nickel Ferrite.* Review of Modern Physics, 1953. **25**(1): p. 114.
93. Sampath, S. and H. Herman, *Rapid solidification and microstructure development during plasma spray deposition.* Journal of Thermal Spray Technology, 1996. **5**(4): p. 445-456.
94. Jiang, X.Y., Y.P. Wan, H. Herman, and S. Sampath, *Role of condensates and adsorbates on substrate surface on fragmentation of impinging molten droplets during thermal spray.* Thin Solid Films, 2001. **385**(1-2): p. 132-141.
95. Jiang, X.Y., S. Sampath, and H. Herman, *Grain morphology of molybdenum splats plasma-sprayed on glass substrates.* Materials Science and Engineering a-Structural Materials Properties Microstructure and Processing, 2001. **299**(1-2): p. 235-240.
96. Zhang, H., H.B. Xiong, L.L. Zheng, and X.Y. Jiang. *Melting Behavior of In-flight Particles and Its Effects on Splat Morphology in Plasma Spraying*. in *Proceedings of 2002 ASME International Mechanical Engineering Congress and Exposition*. 2002. New Orleans.
97. Sampath, S., X.Y. Jiang, J. Matejicek, A.C. Leger, et al., *Substrate temperature effects on splat formation, microstructure development and properties of plasma sprayed coatings Part I: Case*

study for partially stabilized zirconia. Materials Science and Engineering a-Structural Materials Properties Microstructure and Processing, 1999. **272**(1): p. 181-188.
98. Ilavsky, J., C.C. Berndt, and J. Karthikeyan, *Mercury intrusion porosimetry of plasma-sprayed ceramic.* Journal of Materials Science, 1997. **32**(15): p. 3925-3932.
99. Prchlik, L., J. Pisacka, and S. Sampath, *Deformation and strain distribution in plasma sprayed nickel-aluminum coating loaded by a spherical indenter.* Materials Science and Engineering a-Structural Materials Properties Microstructure and Processing, 2003. **360**(1-2): p. 264-274.
100. Baldha, G.J., R.V. Upadhyay, and R.G. Kulkarni, *On the Substitution of Calcium in Cobalt Ferrite.* Journal of Materials Science, 1988. **23**(9): p. 3357-3361.
101. Harris, D.H., Janowiec.Rj, C.E. Semler, M.C. Willson, et al., *Arc-Plasma Sprayed Thick Films - Ferrites and Dielectrics.* American Ceramic Society Bulletin, 1970. **49**(4): p. 417-&.
102. Jeyadevan, B., K. Tohji, K. Nakatsuka, and A. Narayanasamy, *Irregular distribution of metal ions in ferrites prepared by co-precipitation technique structure analysis of Mn-Zn ferrite using extended X-ray absorption fine structure.* Journal of Magnetism and Magnetic Materials, 2000. **217**(1-3): p. 99-105.
103. Matejicek, J., S. Sampath, P.C. Brand, and H.J. Prask, *Quenching, thermal and residual stress in plasma sprayed deposits: NiCrAlY and YSZ coatings.* Acta Materialia, 1999. **47**(2): p. 607-617.
104. Porter, D.A. and K.E. Easterling, *Phase Transformation in Metals and Alloys*. second ed. 2000: Stanley Thorness Ltd.
105. Inaba, H. and T. Matsui, *Vaporization and diffusion of manganese-zinc ferrite.* Journal of Solid State Chemistry, 1996. **121**(1): p. 143-148.
106. Paul, D.I., *General-Theory of the Coercive Force Due to Domain-Wall Pinning.* Journal of Applied Physics, 1982. **53**(3): p. 1649-1654.
107. Ghate, B.B., *Boundary Phenomena in Soft Ferrites - a Review.* American Ceramic Society Bulletin, 1980. **59**(3): p. 336-336.
108. Yan, Q.Y., R.J. Gambino, and S. Sampath, *Low-temperature annealing effect on plasma sprayed MnZn ferrite for planar transformers of high-frequency applications.* IEEE Transactions on Magnetics, 2003. **39**(5): p. 3106-3108.
109. Yan, Q.Y., R.J. Gambino, and S. Sampath, *Plasma-sprayed MnZn ferrites with insulated fine grains and increased resistivity for high-frequency applications.* IEEE Transactions on Magnetics, 2004. **40**(5): p. 3346-3351.
110. Lin, K.-W. and R.J. Gambino, *Enhanced Anisotropic Magnetoresistance of Ion-Beam-Deposited Ni80Fe20–NixFe1-xO Composite Films.* Japanese Journal of Applied Physics, 2005. **44**(9(A)): p. 6522-6566.
111. Sharma, A., R.J. Gambino, and S. Sampath, *Anisotropic electrical properties in thermal spray metallic coatings.* Acta Materialia, 2006. **54**(1): p. 59-65.
112. Sharma, A., A. Gouldstone, S. Sampath, and R.J. Gambino, *Anisotropic electrical conduction from heterogeneous oxidation states in plasma sprayed TiO2 coatings.* Journal of Applied Physics, 2006. **100**(11): p. 9.
113. Vaidya, A., V. Srinivasan, T. Streibl, M. Friis, et al., *Process maps for plasma spraying of yttria-stabilized zirconia: An integrated approach to design, optimization and reliability.* Materials Science and Engineering: A, 2008. **497**(1-2): p. 239-253.
114. Vaidya, A., T. Streibl, L. Li, S. Sampath, et al., *An integrated study of thermal spray process-structure-property correlations: A case study for plasma sprayed molybdenum coatings.* Materials Science and Engineering: A, 2005. **403**(1-2): p. 191-204.
115. Xiong, H.-B., L.-L. Zheng, L. Li, and A. Vaidya, *Melting and oxidation behavior of in-flight particles in plasma spray process.* International Journal of Heat and Mass Transfer, 2005. **48**(25-26): p. 5121-5133.
116. Vaidya, A., G. Bancke, S. Sampath, and H. Herman, *Influence of Process Variables on the Plasma Sprayed Coatings: An Integrated Study*, in *International Thermal Spray Conference*. 2001. p. 1345-1349.
117. Salimijazi, H., L. Pershin, T. Coyle, J. Mostaghimi, et al., *Effect of Droplet Characteristics and Substrate Surface Topography on the Final Morphology of Plasma-Sprayed Zirconia Single Splats.* Journal of Thermal Spray Technology, 2007. **16**(2): p. 291-299.
118. Fukumoto, M., E. Nishioka, and T. Nishiyama, *New criterion for splashing in flattening of thermal sprayed particles onto flat substrate surface.* Surface and Coatings Technology, 2002. **161**(2-3): p.

103-110.
119. Escure, C., M. Vardelle, and P. Fauchais, *Experimental and Theoretical Study of the Impact of Alumina Droplets on Cold and Hot Substrates.* Plasma Chemistry and Plasma Processing, 2003. **23**(2): p. 185-221.
120. Li, C.-J., H.-L. Liao, P. Gougeon, G. Montavon, et al., *Experimental determination of the relationship between flattening degree and Reynolds number for spray molten droplets.* Surface and Coatings Technology, 2005. **191**(2-3): p. 375-383.
121. Shinoda, K., T. Koseki, and T. Yoshida, *Influence of impact parameters of zirconia droplets on splat formation and morphology in plasma spraying.* Journal of Applied Physics, 2006. **100**(7): p. 074903-6.
122. Weiss, E.L. and H.N. Frock, *Rapid Analysis of Particle-Size Distributions by Laser-Light Scattering.* Powder Technology, 1976. **14**(2): p. 287-293.
123. Sun, L.M., C.C. Berndt, and C.P. Grey, *Phase, structural and microstructural investigations of plasma sprayed hydroxyapatite coatings.* Materials Science and Engineering a-Structural Materials Properties Microstructure and Processing, 2003. **360**(1-2): p. 70-84.
124. Cheang, P. and K.A. Khor, *Thermal Spraying of Hydroxyapatite (Ha) Coatings - Effects of Powder Feedstock.* Journal of Materials Processing Technology, 1995. **48**(1-4): p. 429-436.
125. Lu, S.P. and O.Y. Kwon, *Microstructure and bonding strength of WC reinforced Ni-base alloy brazed composite coating.* Surface & Coatings Technology, 2002. **153**(1): p. 40-48.
126. Fauchais, P., A. Vardelle, and B. Dussoubs, *Quo vadis thermal spraying?* Journal of Thermal Spray Technology, 2001. **10**(1): p. 44-66.
127. Moreau, C., P. Gougeon, M. Lamontagne, V. Lacasse, et al. *Thernal Spray Industrial Applications*. in *ASM International*. 1994. Materials Park, OH.
128. Moreau, C., P. Gougeon, A. Burgess, and D. Ross. *Thermal Spray Science and Technology*. in *ASM International*. 1995. Materials Park, OH.
129. Wan, Y.P., H. Zhang, X.Y. Jiang, S. Sampath, et al., *Role of solidification, substrate temperature and Reynolds number on droplet spreading in thermal spray deposition: Measurements and modeling.* Journal of Heat Transfer-Transactions of the Asme, 2001. **123**(2): p. 382-389.
130. Cullity, B.D., *Elements of X-ray Diffraction*. 1978, Reading, MA: Addison Wesley Publishing. 81-143.
131. Alexander, L. and H.P. Klug, *Determination of Crystallite Size with the X-Ray Spectrometer.* Journal of Applied Physics, 1950. **21**(2): p. 137-142.
132. Noyan, I.C. and J.B. Cohen, *Residual-Stresses in Materials.* American Scientist, 1991. **79**(2): p. 142-152.
133. Scott, H.G., *The Estimation of Standard Deviations in Powder Diffraction Rietveld Refinements.* Journal of Applied Crystallography, 1983. **16**(APR): p. 159-163.
134. Yan, Q.Y., R.J. Gambino, S. Sampath, and Q. Huang, *Neutron diffraction and ferromagnetic resonance studies on plasma-sprayed MnZn ferrite films.* Journal of Applied Physics, 2005. **97**(3): p. 033902-7.
135. Robinson, R.A., A.C. Lawson, A.C. Larson, R.B. Vondreele, et al., *Rietveld Refinement of Magnetic-Structures from Pulsed-Neutron-Source Powder-Diffraction Data.* Physica B, 1995. **213**: p. 985-989.
136. Woolley, J.C., A.M. Lamarche, G. Lamarche, M. Quintero, et al., *Low temperature magnetic behaviour of CuFeS2 from neutron diffraction data.* Journal of Magnetism and Magnetic Materials, 1996. **162**(2-3): p. 347-354.
137. Watt, I.M., *The Principle and Practice of Electron Microscopy*. 1985: Cambridge University Press.
138. Deck, L. and P. Degroot, *High-Speed Noncontact Profiler Based on Scanning White-Light Interferometry.* International Journal of Machine Tools & Manufacture, 1995. **35**(2): p. 147-150.
139. Fulton, T.A. and R.C. Dynes, *Interpretation of Quantum Interference Properties of Double Josephson Junctions.* Bulletin of the American Physical Society, 1970. **15**(6): p. 837-&.
140. Henriquez, T.A. and C.M. Ruggiero, *An Algorithm for the Efficient Measurement of Immittance Using the Hp-4192a Impedance Analyzer.* Journal of the Acoustical Society of America, 1985. **78**(1): p. 264-266.
141. Mohri, K., *Accurate Ac Demagnetizing Method Using a Linear Inductance for High Permeability Cores.* Ieee Transactions on Magnetics, 1976. **12**(4): p. 385-389.
142. Lee, J.M., T.W. Lee, S.H. Park, B.G. Min, et al., *Comparison of frequency responses of spiral*

inductors with different figures. Semiconductor Science and Technology, 2001. **16**(2): p. 66-71.
143. Watts, R., M.R.J. Gibbs, W.J. Karl, and H. Szymczak, *Finite-element modelling of magnetostrictive bending of a coated cantilever.* Applied Physics Letters, 1997. **70**(19): p. 2607-2609.
144. Marcus, P.M., *Magnetostrictive bending of a cantilevered film-substrate system.* Journal of Magnetism and Magnetic Materials, 1997. **168**(1-2): p. 18-24.
145. du Trémolet de Lacheisserie, E. and J.C. Peuzin, *Magnetostriction and internal stresses in thin films: the cantilever method revisited.* Journal of Magnetism and Magnetic Materials, 1994. **136**(1-2): p. 189-196.
146. Kodama, R.H., A.E. Berkowitz, E.J. McNiff, and S. Foner, *Surface spin disorder in ferrite nanoparticles (invited).* Journal of Applied Physics, 1997. **81**(8): p. 5552-5557.
147. Lin, D., A.C. Nunes, C.F. Majkrzak, and A.E. Berkowitz, *POLARIZED NEUTRON STUDY OF THE MAGNETIZATION DENSITY DISTRIBUTION WITHIN A COFE2O4 COLLOIDAL PARTICLE .2.* journal of magnetism and magnetic materials, 1995. **145**(3): p. 343-348.
148. Yan, Q.Y., R.J. Gambino, S. Sampath, and Q. Huang, *Neutron diffraction and ferromagnetic resonance studies on plasma-sprayed MnZn ferrite films.* Journal of Applied Physics, 2005. **97**(3): p. -.
149. Lewis, F.B. and N.H. Saunders, *The thermal conductivity of NiO and CoO at the Neel temperature.* Journal of Physics C: Solid State Physics, 1973. **6**(15): p. 2525-2532.
150. Yan, Q.Y., R.J. Gambino, S. Sampath, and Q. Huang, *Neutron diffraction and ferromagnetic resonance studies on plasma-sprayed MnZn ferrite films.* Journal of Applied Physics, 2005. **97**(3): p. 7.
151. *NIST-JANAF Thermodynamical Tables*, ed. M.w. Chase Jr.: American Chemical Society, American Institute of Physics.
152. Hemingway, B.S., *Thermodynamic Properties for Bunsenite, NiO, Magnetite, Fe3O4, and Hematite Fe2O3, with Comments on Selected oxygen Buffer Reactions.* American Mineralogist, 1990. **75**: p. 781-790.
153. Wu, Y., M. Qu, L. Gianuzzi, S. Sampath, et al., *Focused Ion Beam Study of Ni5Al Single Splat Microstructure*, in *Materials Research Society Symposium Proceedings*. Fall, 2006: Boston, MA.
154. Sawatzky, G.A., Vanderwo.F, and A.H. Morrish, *Cation Distributions in Octahedral and Tetrahedral Sites of Ferrimagnetic Spinel Cofe2o4.* Journal of Applied Physics, 1968. **39**(2P2): p. 1204-&.
155. Paul, D.I., *General theory of the coercive force due to domain wall pinning.* Journal of Applied Physics, 1982. **53**(3): p. 1649.
156. McCallum, R.W., K.W. Dennis, D.C. Jiles, J.E. Snyder, et al., *Composite magnetostrictive materials for advanced automotive magnetomechanical sensors.* Low Temperature Physics, 2001. **27**(4): p. 266-274.
157. Robins, J., Ann. Chim., 1955. **10**.
158. Rao, C.N.R. and G.V.S. Rao, *Transition Metal Oxides*
Crystal Chemistry, Phase Transition and Related Aspects. 1974.
159. Samsonov, G.V., *The oxide handbook*. 1973: IFI/Plenum. 214.
160. Shenker, H., *Magnetic Anisotropy of Cobalt Ferrite (Co1.01Fe2.00O3.62) and Nickel Cobalt Ferrite (Ni0.72Fe0.20Co0.08Fe2O4).* Physical Review, 1957. **107**(5): p. 1246.
161. Tracy, J.B., D.N. Weiss, D.P. Dinega, and M.G. Bawendi, *Exchange biasing and magnetic properties of partially and fully oxidized colloidal cobalt nanoparticles.* Physical Review B (Condensed Matter and Materials Physics), 2005. **72**(6): p. 064404-8.
162. Nogues, J., C. Leighton, and I.K. Schuller, *Correlation between antiferromagnetic interface coupling and positive exchange bias.* Physical Review B, 2000. **61**(2).
163. Bozorth, R.M., E.F. Tilden, and A.J. Williams, *Anisotropy and Magnetostriction of Some Ferrites.* Physical Review, 1955. **99**(6): p. 1788.
164. Nakamichi, T., *Magnetostrictive Behavior of Antiferromagnetic CoO Single Crystal in Magnetic Field.* Jouranl of the Physical Society of Japan, 1965. **20**.
165. Zhang, H., H.B. Xiong, L.L. Zheng, A. Vaidya, et al., *Melting Behavior of In-flight Particles and Its Effects on Splat Morphology in Plasma Spraying*, in *International Mechanical Engineering Congress and Exposition*. 2002, ASME International: New Orleans, Louisiana, USA. p. 1-8.